



**HAL**  
open science

# Probing AC electronic compressibility of 3D HgTe and Bi<sub>2</sub>Se<sub>3</sub> topological insulators at high electric fields : evidence for excited massive surface states

Andreas Inhofer

## ► To cite this version:

Andreas Inhofer. Probing AC electronic compressibility of 3D HgTe and Bi<sub>2</sub>Se<sub>3</sub> topological insulators at high electric fields : evidence for excited massive surface states. Physics [physics]. Université Paris sciences et lettres, 2017. English. NNT : 2017PSLEE016 . tel-01615846

**HAL Id: tel-01615846**

**<https://theses.hal.science/tel-01615846>**

Submitted on 12 Oct 2017

**HAL** is a multi-disciplinary open access archive for the deposit and dissemination of scientific research documents, whether they are published or not. The documents may come from teaching and research institutions in France or abroad, or from public or private research centers.

L'archive ouverte pluridisciplinaire **HAL**, est destinée au dépôt et à la diffusion de documents scientifiques de niveau recherche, publiés ou non, émanant des établissements d'enseignement et de recherche français ou étrangers, des laboratoires publics ou privés.

# THÈSE DE DOCTORAT

de l'Université de recherche Paris Sciences et Lettres  
PSL Research University

Préparée au Laboratoire Pierre Aigrain  
à l'École Normale Supérieure

Probing AC electron compressibility of 3D HgTe and Bi<sub>2</sub>Se<sub>3</sub>  
topological insulators at high electric fields: Evidence for excited massive surface states

Étude de la compressibilité AC des isolants topologiques 3D HgTe et Bi<sub>2</sub>Se<sub>3</sub>  
aux forts champs électriques : Mise en évidence d'états massifs excités de surface

**Ecole doctorale n° 564**

Physique en Île-de-France

**Spécialité** Physique de la matière condensée

## COMPOSITION DU JURY :

M. COMBESCOT, Roland  
ENS Paris, Président du jury

M. BERNEVIG, Andrei Bogdan  
Princeton University, Rapporteur

M. TEPPE, Frédéric  
Université de Montpellier, Rapporteur

Mme. QUAY HUEI LI, Charis  
Université Paris Sud, Membre du jury

M. SCHÖNENBERGER, Christian  
Universität Basel, Membre du jury

M. BUHMANN, Hartmut  
Universität Würzburg, Membre du jury

M. PLAÇAIS, Bernard  
ENS Paris, Directeur de thèse

M. BOCQUILLON, Erwann  
ENS Paris, Membre invité

**Soutenu par**  
**ANDREAS INHOFER**  
**le 05 avril 2017**

Dirigée par **Bernard PLAÇAIS**



# ÉCOLE NORMALE SUPÉRIEURE

Université de recherche Paris Sciences et Lettres

PSL Research University

Département de Physique

Laboratoire Pierre Aigrain

THÈSE de DOCTORAT de L'ÉCOLE NORMALE SUPÉRIEURE

École doctorale: "Physique en Île-de-France" (ED 564)

présentée par

**Andreas INHOFER**

Pour obtenir le titre de  
DOCTEUR de L'ÉCOLE NORMALE SUPÉRIEURE

Sujet de la thèse :

**Probing AC electronic compressibility of 3D HgTe and Bi<sub>2</sub>Se<sub>3</sub>  
topological insulators at high electric fields: evidence for excited  
massive surface states**

Étude de la compressibilité AC des isolants topologiques 3D HgTe et Bi<sub>2</sub>Se<sub>3</sub> aux forts  
champs électriques : Mise en évidence d'états massifs excités de surface

Soutenue le 5 avril 2017 devant le jury composé de :

M.	Roland COMBESCOT	Président du jury
M.	Bogdan Andrei BERNEVIG	Rapporteur
M.	Frédéric TEPPE	Rapporteur
Mme.	Charis QUAY HUEI LI	Examinatrice
M.	Christian SCHÖNENBERGER	Examinateur
M.	Hartmut BUHMANN	Examinateur
M.	Bernard PLAÇAIS	Directeur de thèse
M.	Erwann BOCQUILLON	Membre invité



*In Erinnerung an Sarah.*



# Abstract

This thesis discusses the electronic compressibility of two representative three dimensional topological insulators: Strained mercury telluride (HgTe) and bismuth selenide ( $\text{Bi}_2\text{Se}_3$ ). I present low temperature phase-sensitive electron admittance data over a broad frequency range. This allows to extract the quantum capacitance related to the density of states and the resistivity of the investigated materials. We show that the response of an intrinsic topological insulator is dominated by topological surface states over a large energy range exceeding the bulk material's transport gap. This regime, named "Dirac screening" is characterized by an electron compressibility proportional to the surface Fermi level and a high mobility. Subsequently, we investigate the limits of this regime. At high energy and large perpendicular electric fields we observe the population of excited massive surface states. Experimentally, these manifest themselves in multiple signatures: A drop in the electronic diffusion constant, a peak in the conductivity, appearance of a second carrier type in magneto-transport and meta-stability in the charge-voltage relation. A theoretical model based on a quasi-relativistic treatment of the surface Hamiltonian is presented. It allows to identify the electric field and energy dependence of the massive surface states. This thesis is complemented by experimental results on  $\text{Bi}_2\text{Se}_3$  crystals grown on boron nitride for which we demonstrate the importance of clean surfaces for the study of electronic properties in topological insulators.



# Résumé

Dans cette thèse, j'étudie la compressibilité électronique de deux isolants topologiques tridimensionnels : Le tellurure de mercure (HgTe) sous contrainte et le sélénure de bismuth ( $\text{Bi}_2\text{Se}_3$ ). Je présente des mesures d'admittance électronique à basse température résolues en phase sur une large gamme de fréquence. Cela permet d'extraire la capacité quantique associée à la densité d'états et la résistivité des matériaux étudiés. Nous montrons qu'un isolant topologique intrinsèque présente une réponse dominée par les états de surface topologiques sur une large gamme d'énergie qui s'étend au-delà du gap de transport du matériau massif. Ce régime, appelé « écrantage de Dirac », est caractérisé par une compressibilité électronique proportionnelle à l'énergie de surface et une haute mobilité. Dans la suite, nous nous intéressons à la limite de ce régime. Nous observons qu'à haute énergie et sous l'influence de forts champs électriques perpendiculaires, des états excités massifs de surface sont peuplés ce qui se manifeste expérimentalement de différentes façons : Une chute dans la constante de diffusion électronique, un pic de conductivité ainsi que l'apparition d'un deuxième type de porteurs en magnéto-transport et de métastabilité dans la relation charge-tension. Un modèle théorique basé sur un traitement quasi-relativiste du Hamiltonien de surface est présenté. Il permet d'identifier la dépendance en énergie et champ électrique des états massifs de surface. Cette thèse est complétée par des résultats expérimentaux sur des cristaux de  $\text{Bi}_2\text{Se}_3$  obtenus par croissance sur nitrure de bore mettant en évidence l'importance de la pureté des interfaces d'isolants topologiques.



# Acknowledgements

I thank Andrei B. Bernevig and Frédéric Teppe for accepting to review this thesis. I thank Charis Quay Huei Li, Christian Schönenberger, Hartmut Buhmann, Roland Combescot and Erwann Bocquillon to be members of the Jury and to evaluate my work.

Il y a beaucoup de gens qui ont contribué directement et indirectement à ce travail de plusieurs années. En premier lieu, je remercie Bernard Plaçais de m'avoir accueilli au sein de l'équipe méso. Il a été un directeur de thèse extrêmement impliqué dans mon travail, apportant de nouvelles idées à un rythme (presque) journalier, enrichissant ainsi la discussion physique et rayonnant d'un optimisme qui m'impressionne de jour en jour. Je tiens également à remercier tous membres actuels et anciens du Laboratoire Pierre Aigrain et en particulier ceux de la "team P13". Tout mon intérêt pour la physique mésoscopique a commencé en 2011 pendant un stage d'un mois dans cette salle mythique. L'accueil de Gwendal, Erwann, Emiliano et Andi n'aurait pu être meilleur. Ceci m'a donné envie de revenir pour la thèse ...Et j'avais raison: L'esprit d'entraide qui règne dans cette équipe est exceptionnel. Arrivant au LPA après un master théorique, je remercie en particulier Quentin qui m'a appris beaucoup de choses en salle blanche et du côté expérimental. Merci également à Arthur, Mohamed, Wei, Holger, Rémi, Pablo et Anshu pour la bonne ambiance et les multiples discussions que nous avons eu au labo et en dehors. Un très grand merci s'adresse à Badih pour toutes les discussions en P12 qui ont fortement amélioré ma culture des isolants topologiques. Les résultats sur le  $\text{Bi}_2\text{Se}_3$  présentés dans cette thèse n'auraient pas pu être obtenus sans sa persévérance de construire un four de croissance TI au département. Dans ce contexte, je remercie également Jack Duffy qui a nettement contribué à mettre ce four en marche. Je remercie également Yves Guldner, Louis-Anne de Vaultier et Thanya Phuphachong de m'avoir donné la possibilité de m'impliquer dans les discussions de magnéto-optique et de m'associer à leur travail. Je remercie Jean-Marc Berroir et Robson Ferreira pour les discussions concernant les aspects théoriques des bandes du HgTe. Pour leur apport théorique, je remercie Serguei Tchoumakov et Mark-Oliver Görbig ainsi que David Carpentier et Victor Jouffrey. Le développement du modèle effectif a fortement contribué au développement d'une image physique permettant à mieux comprendre nos résultats

---

expérimentaux. J'espère que vous avez pris autant de plaisir que moi dans cette collaboration. Ein ganz besonderer Dank gilt der Molenkamp-Gruppe aus Würzburg, die uns hervorragende Quecksilber-Tellurid Proben zur Verfügung stellte. Dort möchte ich insbesondere Kalle, David, Hartmut Buhmann und Laurens Molenkamp für den freundlichen Empfang in Würzburg und die effektive Zusammenarbeit danken. Ich hoffe, dass die Zusammenarbeit in Zukunft noch viele Früchte tragen wird. Je tiens à remercier Erwann Bocquillon pour avoir ouvert la porte à cette collaboration. Je remercie également Alan Durnez du LPN pour la croissance des couches de  $\text{HfO}_2$ . Je tiens à remercier tous les collaborateurs à Grenoble (Benjamin Sacépé, Katrin Zimmermann et Kévin Le-Calvez), à Dresden (Joseph Dufouleur, Romain Giraud, Louis Veyrat), à l'INSP (Massimiliano Marangolo, Mahmoud Eddrief, Paola Atkinson) et à HKUST (Xu Shuigang et Ning Wang) de nous avoir donné des échantillons. Merci à Michael et José pour m'avoir formé en salle blanche et leur aide dans le développement de processus de fabrication. Je remercie tous les membres des équipes d'électronique et d'ingénierie du LPA et du département de physique: Pascal, Claude, Anne, David et Philippe ainsi qu'Olivier, Aurélien et Florent du service de cryogénie. Je remercie également Anne, Olga et Fabienne pour leur efficacité dans les tâches administratives ainsi que Yann Collin pour le support informatique. Cette thèse s'est déroulée dans une phase de rénovation du département. Merci beaucoup à M. Courtiade, Célia et Catherine pour tous les déménagements de nos manips pendant cette période. Si en troisième année de thèse, quand les résultats expérimentaux commencent enfin à devenir plus clair, le cryostat – élément central aux mesures – tombe en panne, heureux est celui qui peut compter sur le service de soudure de Georges et José. Sans eux, le système serait resté en panne encore plus longtemps et je n'aurais pas pu réaliser une bonne partie de cette thèse. Je leur en suis infiniment reconnaissant. Puis, je remercie tous les membres du LPA, en particulier les "Takis-boys and -girls" Matthieu, Matthieu et Matthieu, Jérémie, Laure, Tino et Lauriane, ainsi que Takis et Audray. Merci également à Benjamin, Omblin, Simon, Adrien, Sarah, Danijela et pardon à ceux que j'oublie ici. Je remercie tous les amis de Paris: Antoine, Bruno, Camille, Tommy, Thibaud, Charlotte ainsi que Pauline, Rookie, Mathilde, Valentine, Adèle, ... und aus Freiburg: Matze, Christian, Clarissa, Nils, Andi, Ruben, Laura, Robert, Felix, Laura, Anni, Domi, ...

Ein ganz besonderer Dank gilt meinen Eltern für die langjährige Unterstützung, obwohl sie sich sorgen, dass mir "irgendwann noch alles um die Ohren fliegt". Außerdem möchte ich meiner (neuen) Familie, Vincent, Marie-Agnès, Gabriele, Anne-Charlotte, Sigi, Birgitta, Louis, Jonathan, Lara, Laurent, Silvia, Guillaume, Valentine und Juliette danken.

Zu guter Letzt, vielen Dank an Angeline. Du warst immer an meiner Seite, hast mich aufmuntern können, akzeptiert, wenn ich mal wieder bis spät in die Nacht gemessen habe, nie die Geduld verloren und mir stets neue Kraft gegeben. Vielen Dank!

# Abbreviations

TI – topological insulator  
TSS – topological surface states  
MSS – massive surface states  
DoS – Density of states  
MITI – Metal-insulator-topological insulator  
MOM – Metal-oxide-metal  
MIS – Metal-insulator-semiconductor  
MOS – Metal-oxide-semiconductor  
Cap – Capacitor(s)  
CBE – Conductance band edge  
VBE – Valence band edge  
CVD – Chemical vapor deposition  
SVD – Solid vapor deposition  
SVT – Solid vapor transport  
MBE – Molecular beam epitaxy  
CdTe – Cadmium telluride  
HgTe – Mercury telluride  
Bi<sub>2</sub>Se<sub>3</sub> – Bismuth selenide  
CPW – Coplanar waveguide  
RF – radio frequency  
LHe – liquid helium  
LN<sub>2</sub> – liquid nitrogen  
hBN – hexagonal boron nitride  
VNA – Vector Network Analyzer  
THRU – Through-line (used for de-embedding)  
DuT – Device under test  
L – length  
W – width  
D — dimension(al)

(I)QHE – (integer) Quantum Hall Effect

SdH – Shubnikov-de Haas

QL – Quintuple layer

DIW – Deionized water

C-V – Capacitance-voltage

DC – Direct current

AC – Alternating current

*tg* – topgate

*bg* – backgate

# Contents

<b>1</b>	<b>Introduction</b>	<b>1</b>
1.1	A simple picture of electron conduction in a solid . . . . .	1
1.1.1	Electronic compressibility . . . . .	2
1.2	Topological insulators . . . . .	5
1.2.1	A historical approach . . . . .	6
1.2.2	Properties of topological surface states . . . . .	8
1.3	Other topological phenomena in physics . . . . .	10
1.4	Scope and outline of this thesis . . . . .	12
<b>2</b>	<b>3D TI HgTe and Bi2Se3 – a short review</b>	<b>15</b>
2.1	Methods for characterizing topological insulators . . . . .	15
2.1.1	Theoretical band-structure calculations . . . . .	16
2.1.2	ARPES . . . . .	16
2.1.3	Magneto-transport . . . . .	17
2.1.4	Quantum transport . . . . .	19
2.1.5	(Quantum) Capacitance . . . . .	20
2.2	Materials . . . . .	21
2.2.1	Mercury telluride . . . . .	21
2.2.2	Bismuth selenide . . . . .	28
2.3	Summary of HgTe and Bi2Se3 properties . . . . .	34
<b>3</b>	<b>The metal-insulator-topological insulator capacitor</b>	<b>37</b>
3.1	Equilibrium . . . . .	39
3.2	Electron compressibility and the surface potential . . . . .	40
3.3	cQ in 2D systems and the DoS . . . . .	43
3.4	Surface compressibility for 3D conductors. . . . .	46
3.4.1	A first rough estimate for the bulk response . . . . .	47
3.4.2	Dimensional analysis . . . . .	49
3.4.3	Exact result for a degenerate semi-conductor . . . . .	49
3.4.4	Comment on finite temperature effects . . . . .	53
3.5	Dirac screening and its signatures in capacitance . . . . .	54
3.6	Conclusion . . . . .	54
<b>4</b>	<b>Sample fabrication and experimental techniques</b>	<b>57</b>
4.1	Sample fabrication . . . . .	58
4.1.1	Topological insulator synthesis . . . . .	58
4.1.2	Device fabrication of RF MITI capacitors . . . . .	64

4.2	Experimental techniques . . . . .	78
4.2.1	Small signal response of a metal-insulator-TI Capacitor . . . . .	78
4.2.2	The cryogenic probe station and measurement equipment . . . . .	80
4.2.3	RF measurements, scattering and admittance parameters . . . . .	82
4.2.4	Deembedding . . . . .	85
<b>5</b>	<b>Topological confinement in 3D HgTe and its evolution under E-fields</b>	<b>89</b>
5.1	Introduction: Two samples and focus of this work . . . . .	90
5.2	Low frequency capacitance spectroscopy . . . . .	92
5.2.1	Capacitance-voltage characteristic . . . . .	92
5.2.2	Surface chemical potential and electric fields . . . . .	94
5.2.3	Interpretation and discussion . . . . .	96
5.3	Scattering process revealed by high frequency capacitor admittance . . . . .	100
5.3.1	Einstein-Boltzmann relation, diffusion constant, Thouless time . . . . .	101
5.3.2	Radio-frequency spectra and extracted parameters . . . . .	103
5.3.3	Larger gate range . . . . .	108
5.4	DC transport confirms sub-band scattering . . . . .	110
5.5	Metastability . . . . .	114
5.6	Summary intrinsic 3D TI . . . . .	118
5.7	The n-type sample . . . . .	120
5.7.1	Capacitance . . . . .	121
5.7.2	Resistance . . . . .	121
5.7.3	Robustness of the phenomenology . . . . .	124
5.7.4	DC measurements . . . . .	126
5.7.5	Conclusions . . . . .	126
5.8	A relativistic model . . . . .	127
5.8.1	Presentation of the model . . . . .	127
5.8.2	Summary of qualitative theoretical predictions . . . . .	132
5.8.3	Relation to experiment – Choice of variables . . . . .	134
5.8.4	Relation to experiment – Procedure . . . . .	137
5.9	Estimation of topological confinement fields . . . . .	139
5.9.1	The topological confinement fields . . . . .	139
5.9.2	Background contributions . . . . .	144
5.10	Conclusions . . . . .	148
<b>6</b>	<b>Bi<sub>2</sub>Se<sub>3</sub> – Compressibility, scattering, room temperature Dirac physics</b>	<b>151</b>
6.1	Sample characteristics . . . . .	152
6.2	Low temperature radio-frequency admittance . . . . .	154
6.2.1	The capacitance . . . . .	154
6.2.2	Resistance and conductivity . . . . .	156
6.3	Phonon scattering . . . . .	162
6.4	Dual-gated room temperature measurements . . . . .	165
6.5	Conclusions and outlook . . . . .	169
<b>7</b>	<b>Conclusions and Outlook</b>	<b>171</b>

---

<b>A</b>	<b>Finite temperature expressions for 2D Quantum capacitances</b>	<b>175</b>
A.1	Linear dispersion - Graphene-like systems . . . . .	175
A.2	Quadratic Dispersion - Quantum well - 2DEG-like systems . . . . .	176
A.3	Massive Dirac system . . . . .	176
<b>B</b>	<b>Capacitance in depletion regime</b>	<b>179</b>
<b>C</b>	<b>1D model for the RF-admittance of a distributed RC-line</b>	<b>183</b>
<b>D</b>	<b>Y matrix corrections due to wave propagation and cross-talk</b>	<b>187</b>
<b>E</b>	<b>Supplementary (low frequency) measurements for the HgTe samples</b>	<b>191</b>
<b>F</b>	<b>Change of variables in the model</b>	<b>195</b>



# Chapter 1

## Introduction

### 1.1 A simple picture of electron conduction in a solid

Most physical properties of electronic transport in (crystalline) solids can be understood within the so-called band theory; it is based on the quantum mechanical description of particles moving in periodic potentials [1]. The usual classification of the conducting properties that prevailed throughout almost the entire twentieth century knew metals, insulators, semi-conductors, ferromagnets and superconductors. If we leave ferromagnets and superconductors aside, the other phases can be predicted for a given material by calculating the energy dispersion as a function of electronic pseudo-momentum for a single electron  $E(k)$ . It turns out that the energy spectrum forms *bands*, i.e. broad energy ranges that do present electronic states. However, there exist also so-called *gaps*, i.e. energy windows, in which no electronic states exist. The calculation of these bands can often be accurately carried out in a single-electron picture, i.e. neglecting electron-electron interactions [2]. This is somewhat surprising, as in a real material each atom yields typically one electron. These occupy the energy levels up to a characteristic energy  $\mu$  – the *Fermi level*. Note that due to Pauli’s exclusion principle each level can only be singly occupied. For a metal, the Fermi level lies within a band, whereas for insulators, the Fermi level lies within a so-called band-gap. According to this simple criterion, a semi-conductor is just a certain kind of insulator; i.e. a system in which thermal excitations are sufficient to populate a small portion of an electronic band, rendering the system conductive. The connection between band-structure, Fermi level position and conductivity can be understood in a simplified picture as follows: In order to pass an electric current, i.e. transport electrons through the system, low energy electrons need to be fed into the system through one lead and flow out of the system through another lead. As electrons are Fermions and as such subject to Pauli’s exclusion principle, the

additional electrons needed for conduction need to occupy an unoccupied energy level. If there are no energy levels available in vicinity to the Fermi level, the electron cannot flow into the system, i.e. it is an insulator, whereas in the metallic case, a large number of states are available, resulting in a finite conductivity.

### 1.1.1 Electronic compressibility

From this simple picture, we can readily conclude that the number of available states in close vicinity to the Fermi energy – called *Density of states* (DoS), defined as  $DoS = \partial n / \partial \mu$  – is an important quantity for the determination of electronic conduction. The above picture can be reformulated as follows: If an extra electron is put in the system, how does the Fermi level change? Obviously, this question is somewhat ill-formulated, as it does not specify any other external parameters that might affect the answer, like temperature, external electro-magnetic fields, etc. We note that this question can be treated in the framework of thermodynamics. Indeed, for the involved thermodynamic variables in a homogeneous system, the thermodynamic identity is written using the Helmholtz free energy as

$$dF(n, T, \mathbf{E}, \mathbf{B}, \dots) = -pdV - SdT + \mu dn - \mathbf{D}d\mathbf{E} + \mathbf{H}d\mathbf{B} + \dots, \quad (1.1)$$

with the electric field  $\mathbf{E}$ , magnetic field  $\mathbf{B}$  and the corresponding conjugate variables  $\mathbf{D}$  and  $\mathbf{H}$ . The inverse electron compressibility at fixed electromagnetic field, temperature and volume is usually defined as [3]

$$1/\kappa = n^2 \left. \frac{\partial \mu}{\partial n} \right|_{T, V, \mathbf{E}, \mathbf{B}}, \quad (1.2)$$

with the particle density  $n = N/V$ . We observe that compressibility  $\kappa$  and density of states are closely related. In chapter 3 I will show that the measurements presented in this thesis probe the (surface) DoS. As a slight abuse of terminology we will therefore use the term compressibility to designate the quantity  $\chi$  defined as

$$\chi(n, T, \mathbf{E}, B, \dots) = \left( \frac{\partial n}{\partial \mu} \right)_{T, \mathbf{E}, B, \dots}, \quad (1.3)$$

whereas the term *density of states* is used to designate this compressibility at zero-temperature. We note that  $\chi$  can explicitly depend on the electric field, a feature that will turn out to be of great importance in this work.

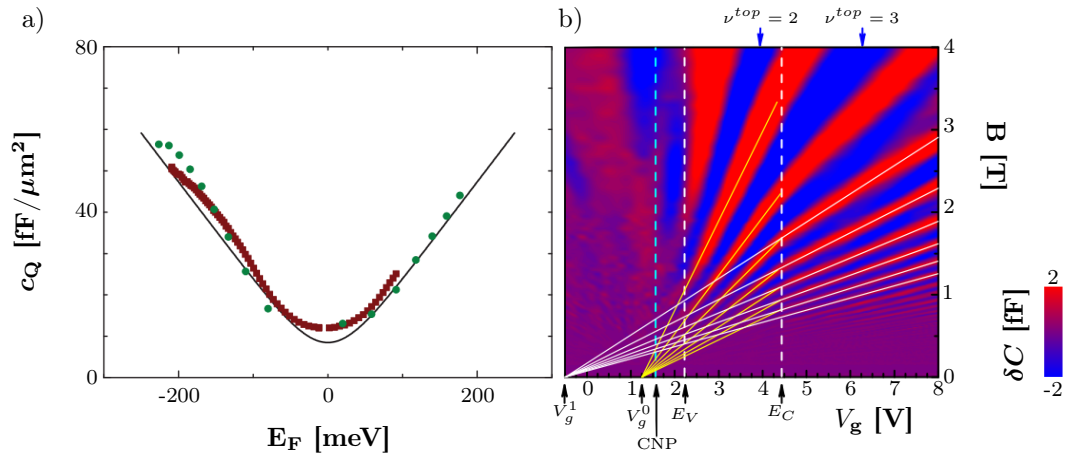


FIGURE 1.1: a) Quantum capacitance of graphene as a function of chemical potential measured at LPA. Adapted from Ref. [15]. b) Oscillations in capacitance as a function of gate voltage and  $B$ -field for a 3D strained HgTe TI sample. Adapted from Ref. [16].

We highlight that the above line of thought allows us in principle to distinguish between conductors and insulators based on the thermodynamic quantity  $\chi$ . However, it does not account for scattering processes limiting conduction.

We shall now discuss how  $\chi$  can be determined experimentally. Already in 1968, Kaplit and Zemel [4] observed that the capacitance of a two-dimensional electron gas (2DEG), is affected by strong magnetic fields due to Landau quantization. In particular they observed strong suppressions of the measured “small-signal space charge capacitance” when the system was driven in between two Landau levels. Smith *et al.* [5] showed that these capacitance features are directly related to the density of states of the 2DEG up to a factor of  $e^2$ . Luryi coined the term “quantum capacitance” for this phenomenology and pointed out that 2D charge carrier distributions screen electric fields only partly [6]. Since these first experimental and theoretical efforts, quantum capacitance measurements were used to probe the electron compressibility of different low dimensional systems. As examples, Eisenstein, Pfeiffer and West revealed a negative electron compressibility due to electron-electron interactions in ultra-clean 2DEGs [7, 8]. Similarly Ilani *et al.* [9] investigated the role of electron-electron interactions in carbon nanotubes, i.e. in a one dimensional system. For graphene, Fang *et al.* [10] calculated the quantum capacitance for an infinite sheet and nano-ribbons. Shortly after, the quantum capacitance with and without quantizing magnetic fields was measured by several groups [11–14].

In order to probe the electron compressibility via capacitance measurements, one usually measures the current in response to a small voltage excitation at finite frequency while an external parameter is varied. This parameter can be a gate voltage, allowing to change the Fermi level or a magnetic field. A common issue in this approach lies in the correct disentanglement of resistive and capacitive effects at finite frequencies [5, 17]. Pallecchi

*et al.* showed how a phase-sensitive microwave admittance measurement probes simultaneously capacitance and conductivity variations in graphene [15]. Importantly, as will be recalled in more detail in chapter 5 of the present thesis, simultaneous measurement of capacitance and conductivity allows us furthermore to determine the electronic diffusion constant  $D$ .

The capacitive method successfully used to measure the electron compressibility in low dimensional systems, must be handled more carefully when three-dimensional systems are investigated. This comes from the fact that the *local* compressibility as defined in eq. (1.3) cannot directly be probed in a capacitance measurement. Indeed, the screening effects in a 3D material lead to a space dependent electron density and a space-dependent chemical potential. In this case, the experimentally accessible quantity is the (electronic) *surface* compressibility  $\chi_s = \partial n_{tot} / \partial \mu_s$ , where  $n_{tot}$  is the *total integrated charge* of the 3D structure and  $\mu_s$  the *surface* chemical potential. This quantity can yield valuable quantitative information about the band-bending properties of bulk states [18].

In this thesis, we are going to employ capacitance measurements on three-dimensional (3D) topological insulator (TI). These materials have a rich electronic phenomenology as discussed in section 1.2.2 below. In particular, 2D topological surface states (TSS) can coexist with “trivial” bulk electrons. A more detailed discussion of the combined capacitive response in this case is given in chapter 3. First magneto-capacitance studies on the TI  $\text{Bi}_2\text{Se}_3$  were carried out by Xiu *et al.* [19]. There has been considerable theoretical effort on magneto-capacitance in TIs, focusing on the effects of strain [20], Zeeman splitting [21], quadratic corrections in the TSS band-structure and electron-electron interactions [22] as well as hexagonal warping [23]. Kernreiter *et al.* [24] proposed quantum capacitance measurements as a tool to characterize the topological phase transition of HgTe-based quantum wells as function of well thickness. Kozlov *et al.* [16] presented combined magneto-capacitance and -conductivity measurements on strained (3D) HgTe films. I will further comment on these measurements in chapter 2.

Most measurements of electronic (surface) compressibility rely on a change of the electron density via a (DC) gate electrode. Inevitably this implies the creation of electric fields in the insulating layer between the investigated material and the gate electrode. For several materials, e.g. double layer graphene [25–27], black phosphorus [28–30] and phosphorene [31], an explicit electric field dependence of the band gap has been calculated theoretically and partly been observed experimentally. Also in the case of topological matter, some effort has been made into this direction. As an example, the effect of electric fields on strained 2D HgTe quantum well systems were studied: In this system, a renormalization of the Fermi velocity and the inversion of the band-gap was theoretically predicted under strong external electric fields [32–34]. Recently, Krishtopenko *et al.* [35]

predicted a topological phase transition in two tunnel-coupled HgTe quantum wells when the electric field between the double-well structure is varied.

The role of topology in thermodynamics has been less considered so far [36, 37]. Under this aspect, compressibility measurements could eventually help to establish a stability phase diagram. As a simple example consider the  $(p - V)$  compressibility  $\kappa_T = -(1/V)\partial V/\partial p|T$  that diverges at the liquid-gas critical point. In the context of topological matter, measurements of local compressibility have been proposed to identify, e.g. the normal- to topological  $p$ -wave superconducting phases of a nanowire (candidate for hosting Majorana fermions, see below in section 1.3) [38] or a “topological to trivial”-phase transition of superfluid states in ultracold Fermi gases [39]. Interestingly, the thermodynamics of the trivial to topological insulator transition are far less studied, perhaps due to the fact that for topological transitions no *local* order parameter can be defined [40]. Very recently, it has been shown however that such a phase transition in a  $d$ -dimensional TI is of order  $d$  in the boundary and of order  $d + 1$  in the bulk using Hill’s thermodynamics, cf. Refs. [36, 37]. Hence, a third order phase transition, i.e. a discontinuity in the derivative of a 3D TI’s TSS-compressibility with respect to chemical potential is predicted to occur. In these seminal papers, the driving parameter for the phase transition is the effective electron mass, hardly continuously variable in an experiment. It is part of this thesis to raise the question (without answering it) whether strong electric fields could drive such a phase transition.

Generally, to our knowledge, little attention has been paid to the role of strong electric fields on the electronic properties of 3D TI materials in the context of quantum capacitance so far. Calculations on the evolution of the electronic bands in the strained 3D HgTe TI system were carried out by Baum *et al.* [41]. In this work, quantum capacitance effects were however explicitly neglected. It is a central aim of this work to investigate the effects of strong electric fields applied perpendicular to a surface of a topological insulator.

## 1.2 Topological insulators

In this section, I will present a short historical introduction of topological insulators. The details of theoretical developments in the field will not be treated in depth. A comprehensive introduction to the important theoretical concepts of topological insulators can be found in the book by Bernevig and Hughes [42]. In particular, the Berry curvature, the Chern number and the  $\mathbb{Z}_2$  index will be introduced only very rapidly. It shall be mentioned that topological phases can be classified into a “topological periodic table” [43, 44]. Details on these classifications are omitted. I will rather point out the

relevant properties of topological surface states for the understanding of this thesis in section 1.2.2 and invite the interested reader to consult – besides Ref. [42] – the reviews by Kane and Hasan [45], Qi and Zhang [46], but also my previous work [47] as well as the PhD thesis by Veyrat [48] and some of the original work [43, 44, 49–54] for details on theoretical aspects. For a popular scientific introduction in French, I recommend the article by Carpentier and Lévy [55].

### 1.2.1 A historical approach

As explained in the beginning of this chapter, shortly after the foundations of quantum mechanics were laid, the band theory of solids predicted with good reliability the electronic properties of most materials. In 1979 however, Su, Schrieffer and Heeger [56] found that although the one-dimensional chain of polyacetylene generally has a band-gap, some *soliton* electronic states exist within the band-gap at the domain-boundary between “A”- and “B”-type chains<sup>1</sup>. The topological origin of this soliton solution remained obscure at the time. A first interpretation of these solitons in terms of topology was developed by Ryu and Hatsugai [54].

The Quantum Hall Effect (QHE) [57] is probably the best-known example of a system where standard band theory was shown to be misleading. Indeed, the electronic band structure of a 2DEG under the influence of a strong external magnetic fields is determined by the formation of Landau levels. If the Fermi level is tuned to lie in between two such Landau levels, band-theory predicts that no current can flow in the system. However, (dissipationless) conduction through edge states on the sample boundaries is observed [58]. These edge states are *chiral*, i.e. depending on the direction of the magnetic field, the electrons propagate clock or anti-clockwise. Thouless *et al.* (TKNN) [53] were the first to reveal a link between the observed quantization of transverse (Hall) conductivity and a topological index, the *Chern* number  $c$ . They realized that the Bloch wave-functions  $|u_n(\mathbf{k})\rangle$  describing the *bulk* electrons in the Quantum Hall regime acquire a phase when the wave-vector  $\mathbf{k}$  varies around the boundary of the Brillouin zone<sup>2</sup>:

$$\Phi_B = \oint_C \langle u_n(\mathbf{k}) | \nabla_{\mathbf{k}} u_n(\mathbf{k}) \rangle d^2\mathbf{k}. \quad (1.4)$$

This phase is called the *Berry phase* [59]. The integrand is called the *Berry connection*  $\mathcal{A}_B$ . Using Stokes’ theorem the line integral can be expressed as a surface integral of the *Berry curvature*  $\mathcal{B} = \nabla_{\mathbf{k}} \times \mathcal{A}_B$  over the Brillouin zone [45]. The Chern number

<sup>1</sup>In polyacetylene the C-C bonds are alternating single and double bonds. “A”- and “B”-type differ by the phase of this alternation.

<sup>2</sup>The path can also be deformed as long as the gap is preserved, in other words as long as the band-index  $n$  is well-defined.

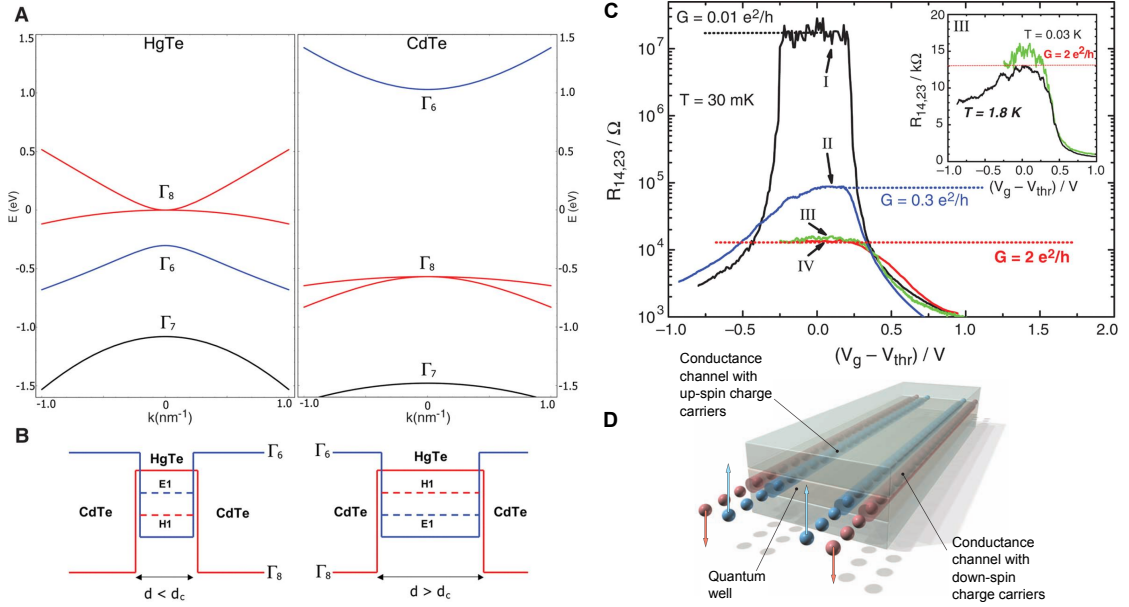


FIGURE 1.2: The quantum spin Hall effect in HgTe Quantum wells. A: Inverted band structure of HgTe and normal ordered band structure of CdTe. B: Depending on the width of the Quantum well, the bands are inverted (right) or not (left). C: Experimental realization of quantized edge state conductance (III and IV) without magnetic field. D: Schematic view of the QSHE. (A and B adapted from Ref. [62], C and D adapted from Ref. [63].)

is defined as the sum of the Berry phases (divided by  $2\pi$ ) of all occupied bands:  $c = \frac{1}{2\pi} \sum_{\text{occupied bands}} \Phi_B$ . It shall be mentioned that the calculation of the Berry phase (and consequently the Chern number) is mathematically analogous to the calculation of the genus of a Riemannian Manifold via the Gauß-Bonnet theorem [60, 61]. This connection to “pure mathematics” justifies the terminology *topological* insulator. Importantly, the number of conducting edge modes  $\nu$ , defining the Hall conductivity in the Quantum Hall regime  $\sigma_{xy} = \nu \frac{e^2}{h}$  is equal to the Chern number, calculated from *bulk* bands. This link between topological properties of bulk bands and edge-modes – also called bulk-boundary correspondence – is of great importance for the understanding of topological insulators. We highlight that a 2DEG in the integer QHE regime can thus be interpreted as the first realization of a TI. It took some time before other topological indexes were identified.

The prediction and coining of the term “topological insulator” goes probably back to two seminal papers by Kane and Mele [49, 50], in which a general scheme for identifying another topological index (the  $\mathbb{Z}_2$  index) was laid out and a “toy model” in graphene with spin-orbit interaction (actually dating back to Haldane [64]), illustrating the emergence of topologically protected edge states was presented. These edge-states are similar to the chiral edge states of the Quantum Hall effect. However, as time-reversal symmetry is preserved in this system, chiral edge states are forbidden due to symmetry. Importantly the edge states are *helical*, i.e. spin-polarized (cf. Fig. 1.2). This new type of spin-polarized quantum Hall edge states without magnetic fields is called the quantum spin

Hall effect [65]. Unfortunately, it quickly turned out that spin-orbit interactions in graphene are far too weak to observe topological effects [66–68]. An alternative approach to topological insulators was simultaneously developed by Bernevig, Hughes and Zhang (BHZ) and presented in Ref. [62]. Here, a six-band model for CdTe/HgTe was reduced to the case of a quantum well grown in [001] direction (Fig. 1.2). This led the authors to an effective 4-band Hamiltonian that is nowadays called the BHZ-Hamiltonian. Importantly, HgTe presents a large spin-orbit coupling, leading to an inversion of  $\Gamma_6$  and  $\Gamma_8$ -bands. They thus proposed the first realistic system in which non-trivial topological phases (apart from QHE) could be observed in an experiment. Shortly after, the Molenkamp group in Würzburg indeed observed quantized edge-state conduction without magnetic field in a CdTe/HgTe/CdTe quantum well [63] as predicted for a 2D TI, Fig. 1.2. In a subsequent experiment, the spin-polarization of these edge states could be measured and confirmed their topological character [69].

After these initial findings, the hunt for other topological materials started. In particular, the prediction of 3D TIs – 3D bulk insulators with conductive topological surface states (TSS) – cf. Kane, Fu and Mele, Ref. [52], led to considerable research effort in this direction, cf. Ref. [45] for a review. In this context,  $\text{Bi}_{1-x}\text{Sb}_x$ ,  $\text{Bi}_2\text{Se}_3$ ,  $\text{Bi}_2\text{Te}_3$  and  $\text{Sb}_2\text{Te}_3$  were proposed by Zhang *et al.* [70] and confirmed in several ARPES measurements [71–74]. In 2011, the Würzburg group demonstrated that thicker ( $\sim 100$  nm) layers of (strained) HgTe are also 3D TIs [75].

## 1.2.2 Properties of topological surface states

For the understanding of this thesis, some properties of topological surface states are particularly important.

First, the topological surface states are *robust*: They emerge at the interface between two materials of different topological index. To understand this point in more detail, it is insightful to stick to the edge states of the QHE in first place. As explained above, the Hall conductance of a 2DEG in the integer Quantum Hall regime is given by  $\sigma_H = \nu e^2/h$ , where  $\nu$  is equal to the sum of Chern numbers of all occupied bands (calculated for an infinite system). Importantly, as  $\nu$  is a (topological) integer, it cannot vary under smooth transformations of the Hamiltonian (as for example due to weak disorder). This “topological robustness” can be illustrated by the topological distinction of a ball and a donut, where smooth transformations (mathematically homeomorphisms) cannot pierce a hole into a ball, cf. Fig. 1.3. As stated above, the calculation of the topological indexes is analogous to the calculation of the genus of a manifold, i.e. the number of holes in a structure.



FIGURE 1.3: Topologically a football and a calabash gourd – a traditional gourd for drinking *mate*, the argentinian national drink – are identical, with genus  $g = 0$  (no holes, they can smoothly be transformed into each other). Similarly a donut and a *Maßkrug* – the traditional mug for drinking beer, the bavarian national drink – are also identical with genus  $g = 1$ .

Following the argumentation in Ref. [42, Chapter 6], it is now interesting to investigate the phenomenology at the boundary between two systems with different Chern number, i.e. different Hall conductance. The integer Chern number is unambiguously defined on both sides of the boundary and cannot be changed as long as the system remains gapped. Thus, when approaching the boundary region from one side, the gap must close and re-open with a different Chern number on the other side in order to explain the change in Hall conductivity between the two systems. This implies that at the boundary between two materials with different Chern number (Hall conductivity) electronic states are *always* available in the boundary regions at in-gap energies. It is important to highlight that it is a *bulk* property that determines the existence of *boundary* states. Therefore, disorder in the boundary region cannot gap out these edge-modes. This phenomenology is often called *bulk-boundary* or *bulk-edge correspondence*. In a topological insulator it is not necessarily the Chern number that takes non-zero values, resulting in edge/surface states, but it can be another invariant as the  $\mathbb{Z}_2$ -index [43, 50]. Importantly the bulk-edge correspondence, if extended to a 3D system, results in topological surface states whose existence is ensured by the same topology based arguments as described for 2D systems above.

Second, the TSS are spinors, i.e. (at least) two-component wave-functions. This is a clear difference to (spinless) quantum well states that can be described by a scalar wave-function. In particular the TSS (in a time-reversal invariant system) are spin-polarized<sup>3</sup>, i.e. the vector product  $\mathbf{k}_\perp \times \mathbf{s}$  – also called the *helicity* – is a constant for all in-plane momenta  $\mathbf{k}_\perp$ . This phenomenon is very similar to the *pseudo-spin* polarization of electrons in graphene where the pseudo-spin is associated to the sub-lattice index,

<sup>3</sup>This terminology has to be handled with care: Indeed, it is not necessarily the real electron spin  $\mathbf{s}$ , but rather the total angular momentum  $\mathbf{j}$  that is polarized. More precisely, in a time-reversal invariant system of spin-1/2 particles, all energies are (at least) doubly degenerate due to Kramer's theorem. The two states corresponding to the same energy are called Kramers partners that have opposite total angular momentum. To simplify the notation, the term spin will however be used.

cf. e.g. [76]. An important consequence of this spin polarization is that direct back-scattering is forbidden [77–80]. This results generally in a high mobility of topological surface states, e.g. on the order of  $\sim 100.000 - 600.000 \text{ cm}^2/(\text{Vs})$  for HgTe TSS [81, 82].

Third, related to the first and second point, the TSS Fermi surface encloses an odd number of Dirac points [52, 83] – usually a single one. A Dirac point is characterized by a linear band-crossing, such that the small-energy spectrum can be approximated as  $E = \hbar v_F k$  with the Fermi velocity  $v_F$ . The consequence of such a linear band dispersion – yet another similarity to graphene, is a linear density of states

$$\text{DoS}(E) = \frac{gE}{2\pi(\hbar v_F)^2}, \quad (1.5)$$

where  $g$  is a degeneracy factor. In contrast to graphene ( $g = 4$  due to spin and valley degeneracy) for TSS  $g = 1$ . In the context of quantum capacitance, this linear relation is particularly important. It shows that when the charge carrier density is lowered, e.g. by application of a gate voltage, the quantum capacitance varies linearly with the chemical potential. This is in strong contrast to a massive 2DEG, e.g. emerging at the interface between two semi-conductors [84, 85], where the density of states is constant and given by

$$\text{DoS}_{2\text{DEG}} = \frac{gm^*}{2\pi\hbar^2}. \quad (1.6)$$

### 1.3 Other topological phenomena in physics

Topological phenomena in physics are not limited to topological insulators. Indeed, presumably the first link between this field of mathematics and the physical world was established by Berezinskii [86, 87] and Kosterlitz and Thouless [88] in order to describe a *topological* phase transition in a 2D spin system. Kosterlitz and Thouless received the 2016 Nobel prize in Physics for this discovery, together with Haldane who, besides his contributions to the “quantum Hall effect without Landau levels” [64], revealed the importance of topological solitons in 1D spin-chains [89, 90].

Over the last decade, a true hunt for new topological phenomena in solid state physics started. One of the most prominent is the so-called Majorana zero mode. E. Majorana predicted the existence of zero-energy particles, described by a real-valued wave-function, based on the Dirac equation [91, 92]. Importantly, these “Majorana” quasi-particles are their own anti-particles. Several candidates for these exotic particles have been proposed over the last decades, including the photino – the supersymmetric partner of the photon – or the neutrino [93] and excitations within vortex cores of p- or f-wave superconductors [94, 95]. Possible experimental realizations are  $\text{Sr}_2\text{RuO}_4$  [96] and  $\text{UPt}_3$  [97–99],

respectively as well as p-wave superfluids such as Helium 3 [100]. Combining s-wave superconductivity (NbTiN) with strong spin-orbit-coupled semiconductors (InSb) in a Zeeman-field [101], first (controversial) signatures of Majorana bound states were detected in Kouwenhoven’s group in Delft [102]. Since then, important theoretical and experimental effort has been made on these Majorana bound states, due to their potential applications for fault-tolerant quantum computing, cf. Refs. [103–107, and references therein]. As an alternative platform for the observation of Majorana end modes, chains of ferromagnetic atoms on the surface of superconductors have been proposed [108, 109]. A real space mapping of such Majorana states using Fe on Pb has been performed via scanning tunneling microscopy in Yazdani’s group at Princeton [110, 111] and recently confirmed and complemented in Basel and Berlin [112, 113]. From the topological perspective, Majorana zero-modes occur at the boundary of topological superconductors [43, 114]. If a topological insulator is rendered superconducting, e.g. by proximity coupling to a (standard) s-wave superconductor, such Majorana modes are predicted to occur. Besides the above, further experimental signatures for Majorana zero modes were predicted, such as a splitting of the zero-bias peak [115] or a  $4\pi$ -periodic AC Josephson effect [116, 117]. Such a  $4\pi$ -periodic Josephson effect (and the corresponding vanishing of odd Shapiro steps) was reported by the Würzburg group on Josephson junctions made out of HgTe in 2D [118, 119] and 3D [120].

The existence of topological surface states in topological insulators is ensured by time-reversal symmetry. This concept can be extended to crystal symmetries leading to so-called topological crystalline insulators [121, 122]. The  $\text{Pb}_{1-x}\text{Sn}_x(\text{Se},\text{Te})$  material class has been identified as a realization of this topological platform [123], observed in ARPES [124, 125] and magneto-optics [126]. Importantly a topological phase transition can be driven by changing the Sn content [127]. Yet another topological class are the topological Kondo insulators [128] realized e.g. in  $\text{SmB}_6$  [129]. Recently, a systematic numerical approach to identify topological non-trivial band-structures was developed and published as a software package allowing to screen material databases [130].

Another fundamental aspect of topological physics and topological insulators is the close link to axion electrodynamics. Wilczek pointed out that an additional term  $\theta \mathbf{E} \cdot \mathbf{B}$  in the electromagnetic Lagrangian – initially introduced in particle physics to resolve a problem related to CP-violation – leads to modifications of Maxwell’s equations [131]. Here  $\theta$  is the so-called *axion* field. When Qi, Hughes and Zhang developed a field-theoretical approach to topological insulators in Ref. [132], they noted that the electromagnetic action of a topological insulators includes such an axionic term, where the topological insulators “magnetoelectric polarization”  $P_3$  plays the role of the axion field  $\theta$ . A direct consequence of this magnetoelectric polarization are crossed terms in the constituent equations between  $\mathbf{D}$  ( $\mathbf{H}$ ) and  $\mathbf{E}$  ( $\mathbf{B}$ ). Furthermore, they lead to surprising physical

phenomena, such as magnetic monopoles [133] and (recently observed) quantized Kerr and Faraday rotations [82, 134].

Although some experimental techniques developed during this PhD might be adapted to the study of the above-mentioned new topological phenomena, they do not lie in the focus of this work.

## 1.4 Scope and outline of this thesis

It is the goal of the present thesis to investigate the dynamical electron compressibility of 3D TIs. In particular, the role of strong electric fields applied perpendicular to the surface of 3D TI systems will be investigated in a radio-frequency metal-insulator-topological insulator (MITI) capacitor geometry.

The thesis is organized as follows:

The investigated materials are strained layers of three-dimensional HgTe thin films grown on CdTe substrates and Bi<sub>2</sub>Se<sub>3</sub>-flakes grown by solid vapor deposition (SVD). It is the topic of chapter 2, to introduce the main properties and to provide a short overview of the experimental and theoretical state of the art for those two representatives of 3D TIs.

When probing the capacitance of a 3D TI system, depending on the carrier concentration, the corrections to the geometrical capacitance can be dominated by the quantum capacitance of a TSS, or feature a combined response of TSS and bulk states, similar to the Debye capacitance of a doped semi-conductor. In the degenerate limit, i.e. if the doping concentration of the bulk is sufficiently high to lift the Fermi level into a bulk band, the standard formulae for semi-conductor capacitance (accumulation, depletion, inversion) do not hold any more [2]. In chapter 3, I will formally introduce the concept of quantum capacitance and derive useful formulae for the response of a bulk system, possibly coexisting with the TSS.

Chapter 4 is divided into two parts. First, I will present the fabrication techniques of the studied MITI-capacitor devices. Afterwards, I will present the measurement setup used for DC biasing, lock-in capacitance measurement and radio-frequency (RF) admittance measurements. To conclude this chapter, the RF de-embedding procedure will be explained in some detail.

In Chapter 5, I present the main results of this work that have been obtained on strained HgTe MITI capacitors. I will discuss experimental results on two different batches of samples, corresponding to an intrinsic, i.e. almost bulk-carrier free, and

an unintentionally  $n$ -type doped sample. By comparing these two samples, we conclude on the high quality of the intrinsic sample by investigating the energy dependence of the electronic diffusion constant, finding a constant charge carrier mobility of  $\mu_e = 120.000 \text{ cm}^2/(\text{Vs})$ . We observe a drastically increased scattering rate for this sample at large electric fields. Combining this observation with magneto-transport data, obtained by our collaborators in Würzburg, our RF admittance measurements and the appearance of meta-stability above a certain threshold voltage in low-frequency quantum capacitance measurements, we present four-fold evidence of massive surface sub-bands at high electric fields ( $\sim 10^8 \text{ V/m}$ ). Furthermore, the capacitance measurements confirm the intriguing screening properties of TSS, coined “Dirac screening” in Ref. [135]. For the  $n$ -type sample, we present oscillations in the electrical resistivity as a function of applied gate voltage, i.e. electric field and charge carrier density. A simple model, developed by Serguei Tchoumakov, Mark Oliver Görbig (Université Paris Sud) and David Carpentier (ENS Lyon), depending on very few adjustable parameters, will be presented. It explains most of the observed phenomenology. In particular, we show that the electronic spectrum for the interface region between an inverted gap and a normal gap insulator has a richer structure than naively expected. Indeed, if a finite width  $\xi$  of the interface region is assumed, massive *surface states* coexist with the massless Dirac TSS. Interestingly the properties of the interface region are determined by only a few parameters that are the Fermi velocity  $v_F$ , the gap of the topological insulator  $\Delta$  and the width  $\xi$ . In particular natural scales for electric fields  $\mathcal{E}_T \sim \Delta/\xi$  and “topological confinement energies”  $\varepsilon = \hbar v_F/\xi$  emerge. Our thin gate design for the quantum capacitance studies enables us to investigate the high-electric field limit  $\mathcal{E} \rightarrow \mathcal{E}_T$ . The observed sub-band population as well as the resistance oscillations can be explained through a gap reduction of massive surface states and a renormalization of the Fermi velocity in this high field limit.

Chapter 6 contains recently realized measurements of  $\text{Bi}_2\text{Se}_3$ -based MITI capacitors. In particular, we report on the observation of a capacitance minimum associated to a TSS Dirac point in a hBN-encapsulated  $\text{Bi}_2\text{Se}_3$ -flake. Interestingly, on this alternative 3D TI platform, similar features as for the HgTe samples can be observed in the resistance data at high electron concentration. At low TSS carrier concentration, the resistance data suggests however the coexistence of other conducting channels in the system that are attributed either to bulk or bottom-surface carriers. From the temperature dependence of capacitance and resistance, we identify the role of electron-acoustic phonon scattering and find a value of the deformation potential  $D = 17 \text{ eV}$ . To conclude the chapter, we show indications for TSS Dirac physics at room temperature. Furthermore, we assess a sixfold mobility difference between the top- and the bottom surface of the investigated sample, with a very high carrier mobility of the bottom TSS on the order of  $\mu_e \approx 4000 \text{ cm}^2/(\text{Vs})$ .

This observation highlights the importance of protecting the surface of  $\text{Bi}_2\text{Se}_3$  during device fabrication in order to maintain high electron mobilities of the TSS.

To conclude, I will summarize the main findings of this thesis in chapter 7 and provide an outlook of future experiments on strained (3D) HgTe and encapsulated  $\text{Bi}_2\text{Se}_3$ -samples as well as on more exotic emergent systems such as Weyl semi-metals. I will also shortly comment on how capacitance measurements might be used to investigate axion physics in topological matter.

## Chapter 2

# A short review of the three-dimensional topological insulators HgTe and Bi<sub>2</sub>Se<sub>3</sub>

This chapter provides an overview of the theoretical and experimental studies on topological insulators. The following does not pretend to be a complete review of a field with over 1.600 publications in 2015 [136], but it will focus on the two main materials studied in this thesis, Bi<sub>2</sub>Se<sub>3</sub> and HgTe. To start, I will quickly present four approaches to investigate topological insulators in general, pointing out their advantages and drawbacks. This will be followed by a presentation of HgTe and Bi<sub>2</sub>Se<sub>3</sub>. In these sections, the focus lies on relevant findings for the understanding of the subsequent chapters of the present thesis and aims at placing my work in the context of current research. In the last section, I will summarize the main similarities and differences of these two materials.

### 2.1 Methods for characterizing topological insulators

There are four main approaches for the characterization of topological insulators. These are a) theoretical band-structure calculations, b) angle-resolved photoemission spectroscopy (ARPES), c) classical and quantum magneto-transport and d) Capacitance spectroscopy. All the presented methods are in fact not limited to TIs and date back to the early or mid 20th century. I will therefore not explain them in detail but rather point out their advantages and limitations when employed on topological insulators.

### 2.1.1 Theoretical band-structure calculations

Generally, the investigated materials are present as solids and usually form a crystalline structure. Once the crystal structure is determined, several methods can be employed to calculate the band-structure of the material, i.e. the energy quasi-momentum relation within one Brillouin zone. Commonly used (textbook) methods are quasi-free electrons in a weak periodic potential or tight binding calculations, along with several other methods cf. Ref. [2, Chapter 11: “Other methods for calculating band structure”]. A prominent example is given by the  $\mathbf{k} \cdot \mathbf{p}$ -method: If the band structure for a given pseudo-momentum  $\hbar\mathbf{k}_0$  is known (typically a high-symmetry point), the band structure around this  $\mathbf{k}$ -vector can be found using perturbation theory. Most of these methods work well in the limit of an infinite crystal. Thus bulk bands can theoretically be calculated with relatively good precision. For the case of TIs, where surfaces play a crucial role, these methods have their limitations. This issue can be circumvented using the so-called envelope function method developed by Bastard [137, 138]. This method treats generally the case of an abrupt (step-like) change in some parameters of the Hamiltonians “left” and “right” of the barrier. We will discuss an alternative approach in chapter 5, where a finite width  $\xi$  for this region is assumed. Furthermore, almost all methods mentioned so far describe single-electron motion. Including electron-electron interactions requires other (numerically expensive) methods like density functional theory, see e.g. Ref. [70, 139]. Note that most of these methods are valid for infinite crystals at zero applied electric fields. Most technologically relevant devices are however based on gate-tunable electron transport. Quite often, a classical description using Maxwell’s equations and (very few) material-specific parameters is sufficient to catch the experimentally observable phenomenology. Such an approach will be explained in detail in chapter 3. However, there are also quantum mechanical methods to treat this kind of situation, like for example Schrödinger-Poisson calculations: There, the electron density is calculated self-consistently from a Schrödinger equation including an (electrostatic) potential created by this electron density in the original Hamiltonian [41].

### 2.1.2 ARPES

The concept of angle-resolved photo-emission spectroscopy (ARPES) goes back to the beginning of the 20th century and the photo-electric effect: The investigated material is exposed to high energy photons  $E_\gamma$  in order to overcome the electronic work function (typically on the order of  $\gtrsim 5$  eV). If an initially bound electron of the material absorbs such a photon, it is released into free space. By measuring the energy and momentum of the photo-emitted electrons, using an angle resolved setup, one can access the initial

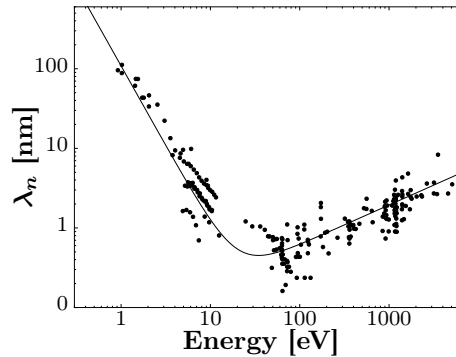


FIGURE 2.1: The inelastic mean free path of electrons as a function of energy above the Fermi level follows a universal law [140]. We observe that ARPES probes mainly the surface band structures of materials. Adapted from Ref. [140].

state of the electron and reconstruct the dispersion relation (i.e. the band-structure)  $E(\mathbf{k})$  of the investigated material.

However, the concept of ARPES leads to an important drawback of this method: Only occupied electronic states, i.e. the valence band can be observed by this technique. In the case of p-doped samples, or intrinsically undoped topological insulators, no information about the dispersion at energies above the Fermi level can be gained by standard ARPES.

Furthermore, due to the finite (and energy dependent) inelastic mean free path of photons and photo-electrons, ARPES probes the electron structure typically only in the surface layers ( $\sim 1\text{-}10$  nm) of the investigated material [140], cf. Fig. 2.1.

### 2.1.3 Magneto-transport

#### 2.1.3.1 Classical

When a conducting sample is placed in orthogonal electric and magnetic fields, a voltage develops along the axis orthogonal to the axes of the fields. This effect was first investigated by Hall [141] and carries his name nowadays. It is a standard exercise for undergraduate students to show that the Hall resistance is given by

$$R_H = \frac{V_y}{I_x} = \frac{B}{ne}, \quad (2.1)$$

where  $B$  and  $I$  designate magnetic field and current respectively whereas  $e$  is the electronic charge and  $n$  the 2D carrier density. In eq. (2.1), a current is driven along the  $x$ -axis,  $V_y$  is the voltage along the direction orthogonal to the current and the magnetic field (oriented along the  $z$ -axis). This relation can therefore be used to extract the carrier density in a system of one type of charge carriers. The temperature dependence of charge carrier density can in principle be used to determine the type of conductor: For a metallic

system this quantity should not depend on temperature whereas it decreases exponentially for a semi-conductor. This argumentation was used also for topological systems (e.g. Ref. [142]), in order to identify the contributions of topological (metallic) surface states vs (semi-conductor like) bulk states. A problem with classical magneto-transport arises naturally when dealing with topological insulators. As typically the two surface states and often the bulk states contribute to transport, the linear relation between Hall resistance and magnetic field breaks down and one typically observes S-shaped features. This situation is treated, e.g. in Ref. [2]. In this case, correct identification of the different parameters becomes cumbersome and requires several *a priori*-assumptions. Eguchi *et al.* addressed this issue for the particular case of topological insulators [143].

### 2.1.3.2 Quantum Hall effect and Shubnikov-de Haas oscillations

Under strong magnetic fields, Landau levels develop, causing oscillations in the longitudinal resistance (Shubnikov-de Haas effect) and plateaus in the Hall resistance (Quantum Hall effect), cf. Ref. [144] for an introduction to both effects.

Especially the analysis of SdH oscillations is a common tool for Fermi-surface determination [2, p. 263 ff.]. For Dirac fermions with non-vanishing Berry phase (i.e. the TSS, cf. chapter 1), the Landau level index and magnetic field are related via

$$N = 2\pi \frac{B_F}{B} + \beta, \quad (2.2)$$

where  $N$  is the LL index,  $B_F$  is the frequency of the oscillations, and  $\beta$  the Berry phase. In principle, the phase of a topological surface state differs by  $\pi$  with respect to a non-topological state (chapter 1). As pointed out by Görbig *et al.*, this phase yields the *Diracness* of the states, but need not necessarily be equal to  $\pi$  for topological states [145].

Further information can be obtained from the frequency of oscillations. For spin-degenerate (2D) carriers, it is given by<sup>1</sup>  $B_F = n\hbar/(2e)$ . The frequency of SdH oscillations thus yields the charge carrier density. In the presence of multiple carrier types, several frequencies can be involved giving rise to beating in the SdH oscillations. In this case, a Fast Fourier Transform (FFT) can be used to identify the corresponding charge carrier densities. This was done e.g. in Ref. [146] as illustrated in Fig. 2.2 (g).

In order to distinguish between bulk and surface carriers, it is common to change the angle between magnetic field and sample surface. A detailed analysis of the electron motion under strong magnetic fields shows indeed that the frequency of oscillations is

<sup>1</sup>remove the factor 2 in case of lifted spin degeneracy.

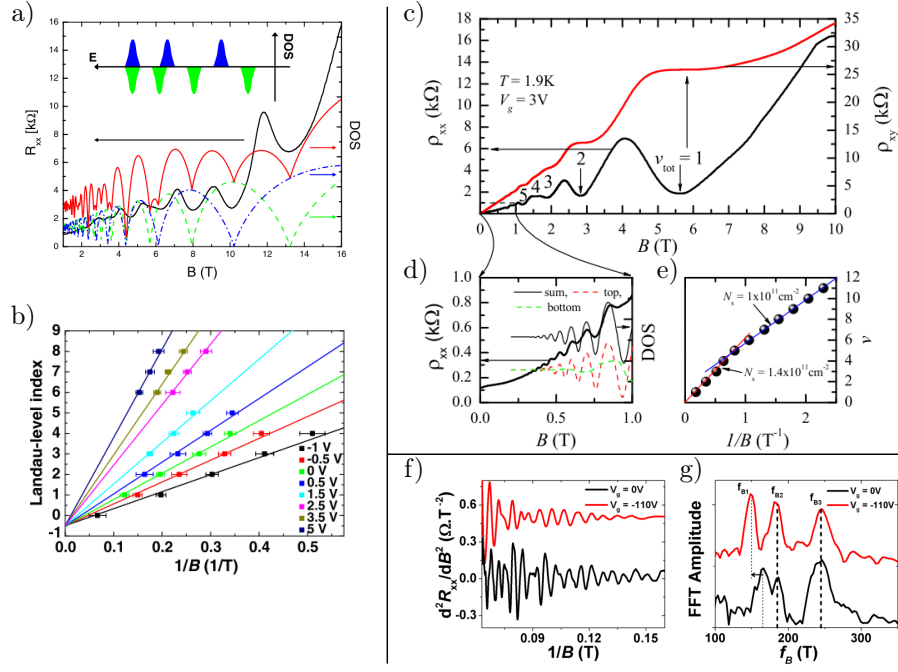


FIGURE 2.2: Typical examples of magneto-transport on topological insulators. a) SdH oscillations in strained HgTe revealing two carrier type transport, b) Landau-level index as function of inverse magnetic field reveals  $\pi$  Berry phase. Adapted from Refs. [75, 135]. c)-d) Quantum Hall effect and SdH from strained HgTe with e) Landau level index vs inverse magnetic field used to extract charge carrier densities. Adapted from Ref. [81]. f) Multi-frequency SdH from Bi $_2$ Se $_3$ -flakes. The FFT in g) reveals three different carrier types. Adapted from Ref. [146].

actually related to the cross section of the Fermi surface orthogonal to the magnetic field direction  $A_{\perp}$  via [2, 146, 147]

$$A_{\perp} = \frac{2\pi e B_F}{\hbar}. \quad (2.3)$$

Thus, by changing the angle of magnetic field, one can reconstruct the Fermi surface and identify its two- or three-dimensional character.

#### 2.1.4 Quantum transport

Due to the spin-orbit-locking of topological surface states, electron back-scattering off non-magnetic impurities is suppressed, a phenomenon known as weak anti-localization (WAL) [148–150] as long as time-reversal symmetry is preserved. It originates from the destructive interference of a scattering path with its own time-reversed path. Experimentally this effect manifests itself as an increased conductivity at zero magnetic field. Hikami, Larkin and Nagaoka derived an analytical formula for this correction in Ref. [149]:

$$\Delta\sigma = \sigma(H) - \sigma(0) = -\frac{\alpha e^2}{2\pi^2 \hbar} \left[ \ln \frac{1}{\tau a} - \psi \left( \frac{1}{2} + \frac{1}{\tau a} \right) \right], \quad (2.4)$$

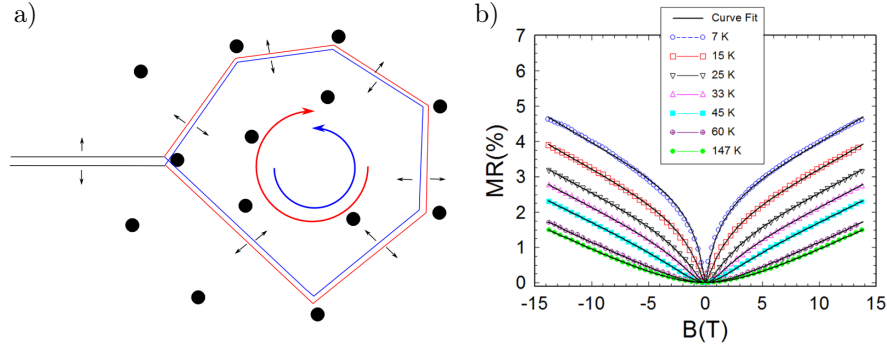


FIGURE 2.3: a) Principle of weak antilocalization: clock-wise and anti-clockwise spin-polarized closed loops interfere destructively, leading to an enhanced conductivity at zero magnetic field  $B = 0$ . b) Weak-anti-localization data. Adapted from Ref. [153].

where  $\alpha = -1/2$  per channel, cf. Ref. [151],  $a = 4DeH/(\hbar c)$  with the diffusion constant  $D$  and the relaxation time  $\tau$ . Fitting the conductance data at low magnetic fields is often used to extract the  $\alpha$ -“amplitude” of the WAL and thus the number of channels presenting weak anti-localization, i.e. TSS [150–153]. It must however be noted that there is controversy about this equation, and a modification for the analysis of topological surface states was pointed out e.g. by Assaf *et al.* [153] and Adroguer *et al.* [154], the latter suggesting a reinterpretation of existing WAL-data.

Another interesting effect of quantum transport in topological insulators can be observed in small-radius nano-wires. The surface states form a cylindrical conducting layer. If a magnetic flux threads the cylinder, as long as the phase coherence length exceeds the circumference of the wire, Aharonov-Bohm oscillations appear in the longitudinal resistance along the wire [155, 156]. As quantum transport experiments are based on a phase-coherence length larger than (at least one) other typical length-scale of the physical problem, they require generally ultra-low temperatures (typically in the mK range) in order to manifest themselves.

### 2.1.5 (Quantum) Capacitance

Measurements of capacitance as a function of DC-gate voltage constitute a standard characterization tool for semi-conductors [18]. To my knowledge, only three studies employed capacitance measurements on topological insulators [16, 19, 157]. We will discuss these experiments in some detail in the following sections.

## 2.2 Materials

As pointed out in the introduction, chapter 1, topological phenomena extend nowadays from Quantum Hall effects over two- and three-dimensional TIs to Weyl semi-metals. Focusing on 3D TIs, the list of materials is still rather long:  $\text{Bi}_{1-x}\text{Sb}_x$ ,  $\text{Bi}_2\text{Se}_3$ ,  $\text{Bi}_2\text{Te}_3$  and  $\text{Sb}_2\text{Te}_3$  were the first proposed systems [70] and confirmed by ARPES [71–74] shortly after. However, strained HgTe, first identified as 2D TI, turns out to be a 3D TI as long as the sample is thick enough in order to avoid opening of a confinement gap due to hybridization of top and bottom surface states [41, 75, 81]. The issue of unintentional bulk doping in the Bismuth based binary compounds quickly lead to a search for ternary or even quaternary compounds with non-trivial topology. Thus, some non-stoichiometric compounds of  $(\text{Bi}_{1-x}\text{Sb}_{1-x})_2\text{Te}_3$  were identified as ternary 3D TIs [158]. The Ando group explored different compounds of Bi, Sb, Se and Te and identified  $\text{Bi}_{1.5}\text{Sb}_{0.5}\text{Se}_{1.3}\text{Te}_{1.7}$  to be an “ideal” TI [159, 160]. Moreover, a large number of TIs are predicted in more exotic systems, such as half-Heusler alloys [161, 162] or topological crystalline insulators like PbSnSe [125], PbSnTe [163].

The materials studied in this thesis are strained HgTe and  $\text{Bi}_2\text{Se}_3$ . This choice is mainly motivated by the following: First,  $\text{Bi}_2\text{Se}_3$  can be easily obtained by several methods. For this thesis mechanical exfoliation and catalyst free chemical vapor transport (CVT) was used. For HgTe, we had access to thin films grown by molecular beam epitaxy (MBE) via a collaboration with the Molenkamp group in Würzburg. MBE-growth is a highly controlled fabrication process which brings the advantage of yielding large sample numbers and therefore makes it possible to check the reproducibility of experimental results. Second,  $\text{Bi}_2\text{Se}_3$  has a band-gap of  $\sim 300$  meV rendering the investigation of TSS transport *a priori* possible even at room temperature. It might thus be a good candidate for future TI applications. However, as-cleaved (or as-grown) crystals are most often heavily n-type doped due to the formation of Se vacancies [164, 165]. HgTe on the other hand requires low temperature due to its small band gap on the order of 25 meV. For the investigation of basic physics issues it is however probably the best 3D TI available today due to its very low intrinsic doping concentration.

In the following, I will thus focus on these two materials and present their most important properties.

### 2.2.1 Mercury telluride

Mercury telluride (HgTe) and cadmium telluride (CdTe), both of the II-VI class of semiconductors, grow in a zinc-blende structure. As explained for example in Ref. [168] the

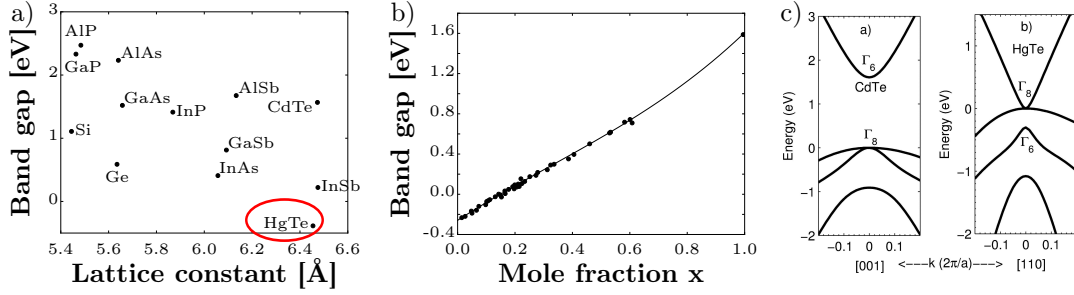


FIGURE 2.4: a) Gap of different semi-conducting compounds (Adapted from Ref. [166]) b) Evolution of the band gap of  $\text{Cd}_x\text{Hg}_{1-x}\text{Te}$  as a function of Cd mole fraction  $x$ . (Adapted from Ref. [167]). Bulk band structures of HgTe and CdTe, revealing the “inverted” character of  $\Gamma_6$  and  $\Gamma_8$  in HgTe. (Adapted from Ref. [33]).

crystal lattice can be seen as two intercalated face-centered cubic lattices, with either Hg or Cd on sub-lattice “A” and Te on sub-lattice “B”. Thanks to a relatively small (0.3%) lattice mismatch between stoichiometric HgTe and CdTe, non-stoichiometric compounds  $\text{Hg}_{1-x}\text{Cd}_x\text{Te}$  are stable and available at “all desired” cadmium contents  $x$  [169]. First band-structure calculations of InSb as a typical II-VI compounds date back to Kane [170] and were applied to  $\text{Hg}_{1-x}\text{Cd}_x\text{Te}$  compounds in Ref. [171]. Already in these “historical” papers, the existence of a “negative” gap in HgTe was highlighted. The evolution of the band-gap with respect to cadmium content and temperature was then investigated by Wiley and Dexter [172], Scott [173], Guldner *et al.* [174] and Berroir *et al.* [175]. Hansen *et al.* [167] collected data of 22 studies and found a nowadays accepted formula for the band gap as a function of temperature and chemical composition. This is illustrated in Fig. 2.4 (b). It shall be pointed out that the gap as defined by Ref. [167] is measured between extrema of the  $\Gamma_6$  and the  $\Gamma_8$  bands. The symmetries of the  $\Gamma_6$ -band is of atomic “s-type”, whereas the symmetry of the  $\Gamma_8$ -band is of “p-type”. The origin of the observed band inversion in HgTe lies in the relativistic effects due to the large atomic mass of Hg ( $M=200.6$  u) as compared to Cd ( $M=112.4$  u). It is the light hole part of the  $\Gamma_8$  band that turns into a conduction band by increasing the mercury content. Based on topological arguments, surface states are predicted to span between the inverted bands, i.e.  $\Gamma_8$  electrons and  $\Gamma_6$  light holes. However, it is important to note that bulk HgTe has no band gap, i.e. it is a semi-metal. Indeed, the  $\Gamma_8$  heavy holes and  $\Gamma_8$  electrons touch at the Fermi level, cf. Fig. 2.4 (c). Even in this situation, topological surface states have been observed by ARPES buried within the  $\Gamma_8$  heavy hole band [75, 176]. At first sight, it seems thus difficult to observe topological *insulator* behavior in HgTe samples. A way to overcome this problem is to apply strain on the system which lifts the light electron - heavy hole degeneracy and leads to a finite (inverted) gap [177].

Not only the negative gap of HgTe was readily discovered long before the link to topology was identified: Even the emergence of interface states was already mentioned in a study from the late 1980’s by Volkov and Pankratov [178] and Berroir *et al.* [177, 179] where

a well of HgTe sandwiched between CdTe layers was studied theoretically and using magneto-optics. This study highlighted also two effects of strain on HgTe: increasing the gap between heavy-holes and light electrons as well as the emergence of interface states whose energy levels lie within this bulk band-gap. Unfortunately, this study concluded that strain effects could be neglected and no special attention was paid to these interface states. Furthermore, even their spin-polarization was highlighted already in 1990 by Pankratov [180].

The identification of the topological non-trivial character of the inverted gap in strained HgTe was discovered by Bernevig, Hughes and Zhang [62]<sup>2</sup>. These findings were also supported by Fu and Kane [51] who developed a recipe for identifying  $\mathbb{Z}_2$  TIs based on a simplified criterion, valid in the case of time-reversal and inversion symmetry of the system. Even though the zinc-blende structure of HgTe does not present inversion symmetry, they claim that HgTe should fall into the 3D TI class according to an argument based on adiabatic continuity between an inversion symmetric model and the HgTe model.

First experimental hints of transport by surface states (although their topological character remained completely obscure) go back to the 1980's, Ref. [181]. New band-structure calculations with special focus on band-topology was carried out by Dai *et al.* [182], where the non-trivial topological character of strained HgTe was confirmed. They calculated the local density of states for a HgTe/CdTe interface and found a (bulk) band gap on the order of 30 meV together with champagne-glass shaped topological surface states (TSS), cf. Fig. 2.5 (a). As is obvious from this study, the Fermi velocity of the TSS is almost constant over a large energy range and slightly “slows” down near the valence band edge. The asymptotic electronic Fermi velocity extracted from this paper is on the order of  $8 \cdot 10^5$  m/s.

Further information about the band-structure can be gained from a recent ARPES study, Ref. [176]. Although the authors of this paper investigated bulk, i.e. unstrained, samples of HgTe, they can clearly resolve TSS-like features buried in the heavy hole band, interconnecting the  $\Gamma_8$  heavy holes and the  $\Gamma_6$  light holes. Assuming that this sample's properties are not too different from those for thin layers of MBE-grown strained HgTe, studied in the present thesis, two main features of this study are of great importance. First, the Fermi velocity, measurable from the data on cesium doped HgTe surfaces, corresponds to a value of approximately  $1.0 \cdot 10^6$  m/s (dashed lines in Fig. 2.5 e)). However, the subjective perception of the ARPES features might also be in agreement with a slightly higher Fermi velocity on the electron side of the TSS (compare dotted green lines in Fig. 2.5 d) and black dotted lines in 2.5 e)). Furthermore, I will discuss in chapter 5

---

<sup>2</sup>See also chapter 1

that the Fermi velocity of TSS depends on the applied electric field. Doping the surface with Cs atoms might lead to relatively strong fields close to the surface. Therefore, the extracted Fermi velocities should not be over interpreted.

Second, surface doping via cesium deposition makes it possible to resolve the electron-part of the spectrum as well. Surprisingly, although unstrained HgTe is expected to have no bulk band gap, the ARPES data seems to be TSS dominated over several hundreds of meV with an increasing gap when adding surface dopants. This can be seen as hint indicating a certain robustness of TSS with respect to increasing surface carrier concentration, similar to the Dirac-screening observed in transport (see below).

A recent magneto-optics study by Teppe *et al.* [183] on bulk crystals with different compositions of  $\text{Hg}_{1-x}\text{Cd}_x\text{Te}$  sheds further light on the Fermi velocity: For compositions  $x$  close to the band inversion, they find that the Fermi velocity parameter for a simplified Kane model, i.e. a spectrum roughly given by  $E = \pm\sqrt{\Delta^2 + (\hbar v_F k)^2}$  is universal, i.e. it does neither depend on temperature nor on composition and is given by  $v_F = (1.07 \pm 0.05) \cdot 10^6$  m/s. Typically, one expects that the TSS Fermi velocity is similar to that of the light electron band.

The first electric transport experiments on (3D) strained HgTe on CdTe with focus on topology were carried out by the Würzburg group [75]. In this work, additional ARPES data, Fig. 2.5 (b), clearly shows the linearly dispersing bands within the bulk valence band that are attributed to surface states. Note that these TSS extend in energy far beyond the valence band maximum. The TSS hole Fermi velocity corresponding to the dashed white lines in Fig. 2.5 reads  $5.5 \cdot 10^5$  m/s. In the same paper, a quantized Hall effect was measured, resolving only odd steps at low fields. This is a direct hint for a parallel contribution of two distinct Dirac-like conductors. Indeed, a single Dirac cone contributes to the (quantized) Hall conductance by  $e^2/h(n + 1/2)$ , where the  $1/2$  term comes from the (non-trivial) Berry phase of TSS. The sum of two such cones, yields thus an odds series of quantum Hall plateaus as long as the filling factor of the two systems remains identical. The data presented in this work seems quite self-consistent up to one point: The extracted surface carrier densities of  $3.7$  ( $4.8$ )  $\times 10^{11}/\text{cm}^2$  for the bottom (top) surface correspond to Fermi levels on the order of  $\gtrsim 100$  meV, far beyond the expected strain-induced transport gap. This points towards an unexpected screening behavior of TSS.

This feature was further investigated in a gated sample [135]. Here, the evolution of quantized Hall plateaus with respect to an applied gate electrode was carefully analyzed. The experimental findings confirm that electric fields are screened in an unexpectedly efficient way by the TSS, leaving the bulk unpopulated over a broad range of gate voltages. These experimental findings are in contrast to a self-consistent Schrödinger-Poisson calculation,

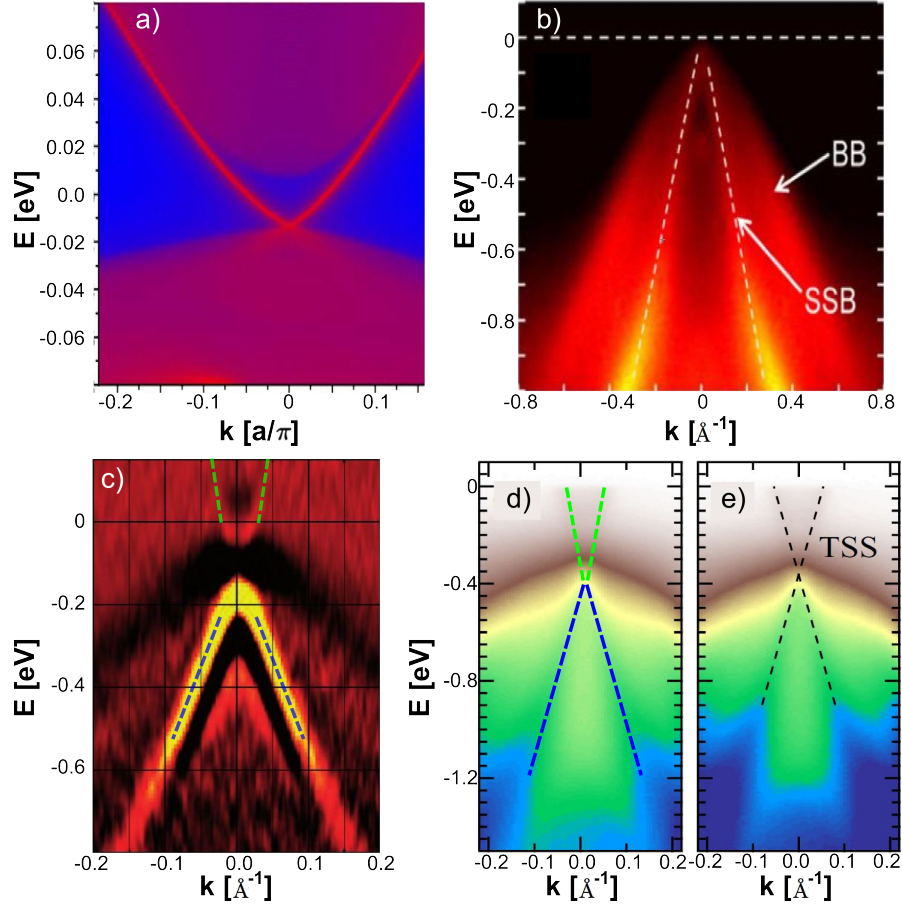


FIGURE 2.5: HgTe band structures obtained from theory and ARPES. a) Interface density of states as a function of energy and in-plane momentum calculated using Green's functions on a tight-binding description. Figure adapted from Ref. [182]. b) ARPES data on a fully relaxed  $1\mu\text{m}$  thick film of HgTe. Figure adapted from Ref. [75]. c) ARPES data on strained HgTe. The blue (green) dashed lines correspond to a hole (electron) Fermi velocity of  $0.6\cdot 10^6\text{ m/s}$  ( $1.6\cdot 10^6\text{ m/s}$ ). Figure adapted from Ref. [184]. d) and e) ARPES data on bulk HgTe cleaved *in-situ*. The surface is doped with Cs in order to resolve the electronic part. The dotted blue line in d) and the dotted black lines in e) correspond to a Fermi velocity of  $1.0\cdot 10^6\text{ m/s}$ . As for c), a Fermi velocity of  $1.6\cdot 10^6\text{ m/s}$ , dotted green line in d) is not incompatible with the ARPES spectrum. Images d) and e) adapted from Ref. [176].

carried out for the same system, in which bulk bands are expected to be populated at moderate electric fields [41]. In Ref. [135] an ad-hoc model of sharply varying dielectric constants yields a suitable potential landscape and explains the observed only-TSS behavior.

It is one of the main goals of the present thesis to investigate these unusual screening properties of TSS in HgTe by means of quantum capacitance spectroscopy. The exact procedure will be explained in the following chapters and the results of chapter 5 indeed support the so-called Dirac-screening in the case of low bulk doping of the sample.

In order to give an approximately complete overview of the bibliography on (3D) HgTe

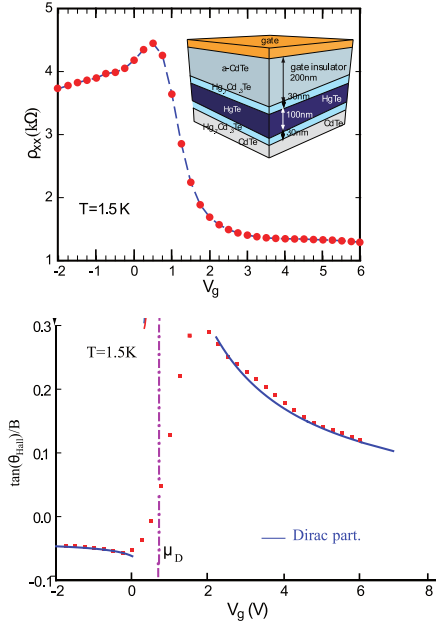
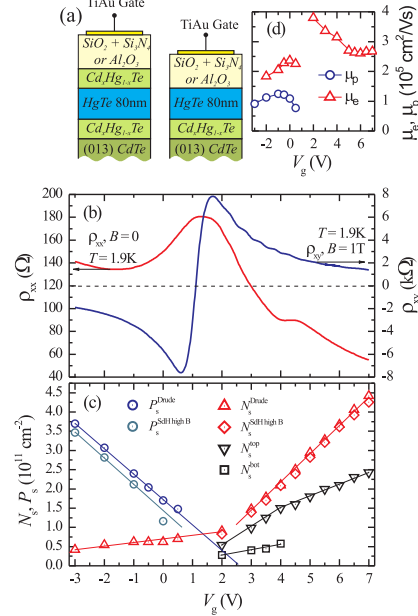
Bouvier *et al.* [186]Kozlov *et al.* [81]

FIGURE 2.6: Left: Longitudinal resistance (top) and Hall angle  $\Theta_{Hall}$  (bottom) as a function of gate voltage on strained HgTe. Image adapted from Ref. [186]. Right: Longitudinal resistance (blue) and Hall resistance red as a function of gate voltage (b). In (c) the authors show the calculated charge carrier densities as a function of gate voltage. Adapted from Ref. [81].

since its identification as a TI, I want to quickly review further results, not linked to the Würzburg group. To my knowledge, there are currently only three research groups worldwide able to grow strained HgTe films in MBE for fundamental research purposes: Würzburg, Grenoble and Novosibirsk [185].

There are two preprints from the Grenoble group on strained HgTe on CdTe in the [001] orientation, thus similar to the Würzburg samples, showing two carrier magneto-transport features and weak-anti-localization at low fields, characteristic for TSS [186]. It is however unclear in the paper why the bulk contribution to the Hall conductivity can be completely neglected. Generally, multi-carrier fits to magneto-transport data are always subject to some uncertainty as one of the variables has to be chosen a little arbitrarily (e.g. neglecting  $\sigma_{xy}^{bulk}$  but including an offset on  $\sigma_{xx}$  [186]). However, this work observes a n- to p- crossover in the carrier type as a function of gate, pointing towards a strongly gate tunable TSS in which p-like conduction can be observed. In particular they interpret the diverging Hall angle, cf. Fig. 2.6, as a clear signature of Dirac fermions. This interpretation is based on an energy independent scattering time, cf. Ref. [186]. In chapter 5 of this thesis we show that this assumption must be revisited for our samples.

For band-structure information, an ARPES study on strained *in-situ* etched films of

(strained) HgTe can provide valuable information [184]. As in Ref. [75], extraction of features related to the electron side, i.e. above the Fermi level, are poorly resolved. However, some spectral features can be observed up to  $\sim 100$  meV above the valence band edge. It is of course difficult to attribute these faint features to TSS or bulk states, i.e. one cannot extract a bulk gap. However, it seems like the Fermi velocity on the electron side is larger than for the TSS hole states. The green dotted line in Fig. 2.5 (d) corresponds to a Fermi velocity of  $1.6 \cdot 10^6$  m/s, compatible with the ARPES data<sup>3</sup>.

In 2014 the Novosibirsk group and Regensburg presented magneto transport results on HgTe films as well in the (classical) low field limit as in the (quantum) Shubnikov-de Haas and IQHE regime. Their treatment of the bulk's contribution seems to rely on a rather simplified "two-dimensional description". Even though not stated explicitly, the bulk's properties are treated as an effective 2D system with a density of states given by  $d \cdot DoS_{3D}$ , where  $d$  is the thickness of the sample and  $DoS_{3D}$  is the three dimensional density of states evaluated at the surface chemical potential. We point out that this interpretation contradicts the Dirac screening observed by the Würzburg group and furthermore completely neglects any screening properties of the bulk. A detailed analysis in chapter 3 of this thesis shows that screening leads to an inhomogeneous chemical potential along the vertical (i.e. the growth-)axis. This effect can generally not be neglected. A detailed analysis of this is one of the aims of the present thesis. The reported SdH oscillations in this paper show the ambiguity of magneto-transport data (even in the quantum transport case): Whereas they attribute the observed minima to a single series of SdH oscillations with changing frequency as a function of magnetic field, Brüne *et al.* [75] interpret the oscillations rather as two series with different frequencies. The goal of this thesis consists however not in a reinterpretation of these measurements but in the presentation of an alternative experimental approach as laid out in the following chapters.

Finally, and closing this section about the existing literature on (3D topological) HgTe, the Novosibirsk/Regensburg collaboration published recently a paper about quantum capacitance in HgTe [16] which is of great relevance for the present thesis. One of the conclusions of this paper is that quantum capacitance is a particularly surface sensitive tool. This point will be further discussed in chapter 3. This conclusion is based on a comparison between the quantum corrections to the capacitance and the resistance oscillations at high magnetic fields. As I will explain in chapter 4, the extremely thick gate stack (over 300 nm between gate electrode and HgTe) used in this study leads to a very small geometrical capacitance, rendering the detection of any quantum correction extremely difficult. This explains why the actual value of the quantum capacitance is not discussed in Ref. [16], but only its variations that are on the order of 5%. The main

<sup>3</sup>As will be shown in chapter 5, this value can be extracted from our capacitance measurements.

conclusions of this work are based on similar arguments as those in [81] and therefore subject to the same problem when it comes to labeling of minima. In this thesis I will take a complementary approach and analyze the “bare” quantum capacitance at zero magnetic field quantitatively.

### 2.2.2 Bismuth selenide

Bi<sub>2</sub>Se<sub>3</sub> together with Sb<sub>2</sub>Te<sub>3</sub> and Bi<sub>2</sub>T<sub>3</sub> were among the first proposed candidates for 3D topological insulators. Zhang *et al.* [70] performed first-principles calculations for these materials and predicted their topological character. The crystal structure of Bi<sub>2</sub>Se<sub>3</sub> is “*rhombohedral [...] with the space group  $D_{3d}^5$  ( $R\bar{3}m$ ) with five atoms in the unit cell*” [70, 187]. For details on the crystallography, the interested reader might refer to Ref.[70]. As compared to HgTe, Bi<sub>2</sub>Se<sub>3</sub> has the advantage to form a layered structure, shown in Fig. 2.7 (a,c), similar to graphite and can thus be – just like graphene – reduced to very thin flakes using mechanical exfoliation following the original Scotch-tape technique [188]. In contrast to graphene, the Bi<sub>2</sub>Se<sub>3</sub>-layers are not mono-atomically thin. Instead, five covalently bound atomic layers form a so-called quintuple layer (QL) of thickness  $t_{QL} \approx 1$  nm. The possibility to fabricate samples via mechanical exfoliation renders this system more cost-efficient than the expensive MBE setups required for HgTe studies. This might partly explain, why up to date, the literature on Bi<sub>2</sub>Se<sub>3</sub> is far more extensive than on HgTe.

Using this scotch tape method for obtaining freshly cleaved Bi<sub>2</sub>Se<sub>3</sub>-surfaces, already in 2004, Urazhdin *et al.* [187] found in a scanning tunneling spectroscopy (STS) study that Bi<sub>2</sub>Se<sub>3</sub> and Bi<sub>2</sub>Te<sub>3</sub> present in-gap states localized close to the sample surface. Their results of DoS mapping excluded these surface states to be due to surface impurities. Similar to HgTe, the topological character of these surface states remained obscure until these two materials were proposed as TIs in 2009.

#### 2.2.2.1 ARPES

Indeed, surface states of Bi<sub>2</sub>Se<sub>3</sub> were revealed by ARPES shortly after [72, 74]. These studies reveal a band gap on the order of 300 meV, much larger than for HgTe, rendering the study of topological surface transport *a priori* accessible at room temperature, Fig. 2.7 (b,d). Already these first experimental observations of the surface states via ARPES revealed the main problem of this material. The clear visibility of the TSS dispersing over the bulk band gap implies a Fermi level high above the conduction band edge. This implies that bulk carrier density in Bi<sub>2</sub>Se<sub>3</sub> samples is generally high due to

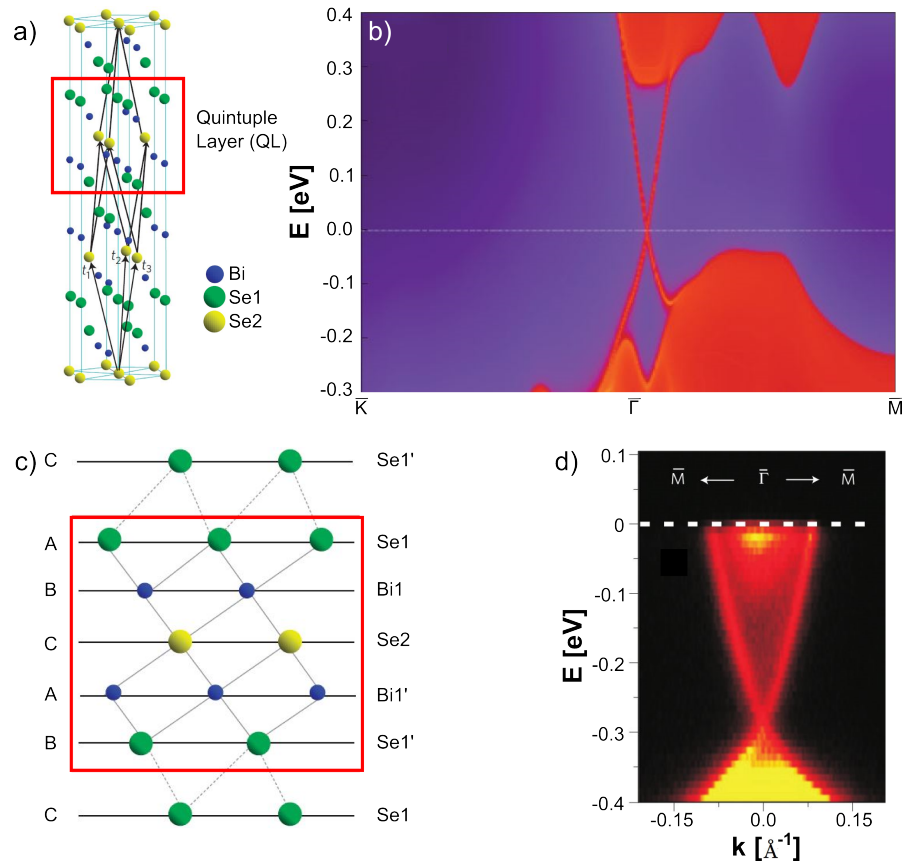


FIGURE 2.7: Crystallographic structure and band structure of  $\text{Bi}_2\text{Se}_3$ . a) The layered structure of  $\text{Bi}_2\text{Se}_3$ . b) *Ab-initio* band-structure calculation along high symmetry axis. c) Side view of the crystal structure revealing the quintuple layers (QLs). d) ARPES data around the  $\Gamma$ -point of  $\text{Bi}_2\text{Se}_3$ , revealing the TSS. Images a), b) and c) adapted from Ref. [70]. Image d) adapted from Ref. [72].

unintentional doping. Commonly, the high doping concentrations are attributed to Se-vacancies [164, 165]. Such a high Fermi level explains why  $\text{Bi}_2\text{Se}_3$  was discovered so early in ARPES: As discussed in the beginning of this chapter, levels need to be filled in order to be visible in ARPES. At the same time, this is a drawback for transport studies as most electrical phenomena are dominated by a large (trivial) bulk contribution. It was shown in ARPES [74] that admixing of Ca can reduce the Fermi level and NO<sub>2</sub>-surface doping of  $\text{Bi}_2\text{Se}_3$  leads to an upwards shift of the Dirac point with respect to the bulk bands. ARPES can also yield an estimate of the Fermi velocity. Thus, for  $\text{Bi}_2\text{Se}_3$ , Xia *et al.* found a Fermi velocity on the order of  $5\text{-}8 \cdot 10^5$  m/s for the electronic part of the TSS [72].

Concerning the electronic surface structure, calculations and ARPES data, presented by Bahrami *et al.* [189], reveal that the electronic surface spectrum of  $\text{Bi}_2\text{Se}_3$  does not only present the topological surface states, but excited massive states that shift to lower energies at finite (built-in) electric fields. A similar evidence for the coexistence of TSS and (trivial, massive) 2DEG states has been reported by Bianchi *et al.* [190].

It is a central part of this thesis to show the importance of electron scattering between topological surface states and massive surface states for electron transport.

### 2.2.2.2 (Magneto)-transport

The first “direct” signatures of topological surface conduction in Bi<sub>2</sub>Se<sub>3</sub> were reported in 2010 [191, 192]. The experimental method that led to the observation of surface state signatures was in both cases compensation doping in order to decrease bulk contributions.

Analytis *et al.* [191] performed magneto-transport studies on Sb compensated Bi<sub>2</sub>Se<sub>3</sub>, substituting Bi by Sb, leading to bulk carrier densities on the order of several 10<sup>16</sup>/cm<sup>3</sup>. From the angle dependence of the SdH oscillations, they conclude that in one of their samples the bulk is in the extreme quantum limit (i.e. only the lowest LL is filled), and that the TSS quantum limit can also be reached for sufficiently high fields. However, plotting the LL index against inverse magnetic field leads to an interception at 0, in contradiction to the expected Berry phase (1/2) for TSS. The authors argue that this is due to Zeeman-splitting. Without entering into the details of their analysis, the mere fact that the labeling is discussed in much detail reveals the ambiguity of correctly assigning LL-labels to resistance oscillations (see also the discussion in Ref. [193]).

As an alternative to (quantum) magneto-transport, the temperature and thickness dependent resistance of Bi<sub>2</sub>Se<sub>3</sub>-flakes was investigated by Steinberg *et al.* [192]. They used As-doping to compensate the natural *n*-doping of Bi<sub>2</sub>Se<sub>3</sub>. A main result, indicating the existence of TSS was obtained by tracing the total conductivity as a function of sample thickness. This leads to a linear relation with a non-zero intercept, attributed to the (thickness-independent) surface states. From the thickness dependence of low field Hall resistivity, they conclude on a combined 2D and 3D conduction. Using a combined back- and top-gate design, the authors were able to individually tune the carrier densities of top TSS (<sup>*t*</sup>TSS) and bottom TSS (<sup>*b*</sup>TSS). Sweeping the top-gate, they observed a conduction minimum around  $V_g = 0$  independent of the backgate. This shows that <sup>*t*</sup>TSS and <sup>*b*</sup>TSS can be treated independently (at least on bulk doped samples) due to efficient screening via bulk states. A similar approach was used by Checkelsky *et al.* [194]. Instead of As, they used Ca doping to reduce bulk contributions. A gate voltage allowed them to observe ambipolar conduction on thin flakes at low temperatures. They also observed a dramatic decrease of mobility between bulk samples ( $\mu=7000$  cm<sup>2</sup>/Vs) and thin flakes ( $\mu=1000$  cm<sup>2</sup>/Vs). From the temperature dependence of the sample’s resistance, they conclude coexistence of bulk and surface conduction. These authors might be the first to specifically address the issue of bulk screening in the case of a doped TI. They adapt

a text-book analysis of semi-conductor screening [18]. In chapter 3 I extend this kind of analysis to degenerate bulk-doping.

Several studies [150–152, 194] reported on weak-antilocalization in  $\text{Bi}_2\text{Se}_3$ . Due to the spin-momentum locking of the TSS, these observations are also strong indications for the existence of TSS in  $\text{Bi}_2\text{Se}_3$ .

The (trivial) 2DEG-like surface states, coexisting with the TSS, identified by ARPES (cf. above) were also investigated in electronic transport studies. Brahlek *et al.* calculated these in the context of band-bending. Experimentally, this issue was addressed in some detail by Veyrat *et al.* [146] to identify up to five oscillations with different frequencies on  $\text{Bi}_2\text{Se}_3$  flakes grown via solid-vapor-deposition (SVD, cf. chapter 4 for more details). From the gate dependence of these oscillations, the contributions of bulk, the two (topological) surfaces and additional massive surface bands attributed to surface-band bending could be identified. In chapter 5 of the present thesis, an explanation for the emergence of massive surface states, based on topological confinement and (surface) electric fields, will be presented.

Similar to the work by Veyrat *et al.*, Sacépé *et al.* [193] analyzed quantitatively the bulk and surface contribution to conduction based on a comparative analysis of SdH oscillations and gate-induced charge carrier density variations. Particularly, they pointed out an interesting interpretation of observed SdH oscillations: As the total conduction is dominated by bulk (according to the authors presumably through an impurity band), the observed oscillations are not attributed to an enhanced scattering within the TSS when the surface Fermi level crosses a LL but are due to enhanced scattering between bulk and surface states: The augmented DoS when the Fermi level crosses a surface LL, leads to enhanced bulk scattering as the number of available final states for scattering is increased. Investigating this kind of TSS-to-bulk / TSS-to-massive surface state scattering is also part of the present thesis.

### 2.2.2.3 Other characterization methods

Scanning tunneling spectroscopy (STS) can also yield valuable information, such as an estimate of the band-gap and the Fermi velocity. Hor *et al.* [165] found a band gap on the order of 150 meV for  $\text{Bi}_2\text{Se}_3$  and thus a value somehow smaller than earlier ARPES studies. STM setups are also used for quasi particle interference measurements. Beidenkopf *et al.* [195] found a Fermi velocity in Mn-doped  $\text{Bi}_2\text{Se}_3$  on the order of  $2 \cdot 10^5$  m/s using this method.

Xiu *et al.* [19] investigated the quantum capacitance of thin flakes of  $\text{Bi}_2\text{Se}_3$ . As for Ref. [16], the actual quantum capacitance is never evaluated but the authors focus rather

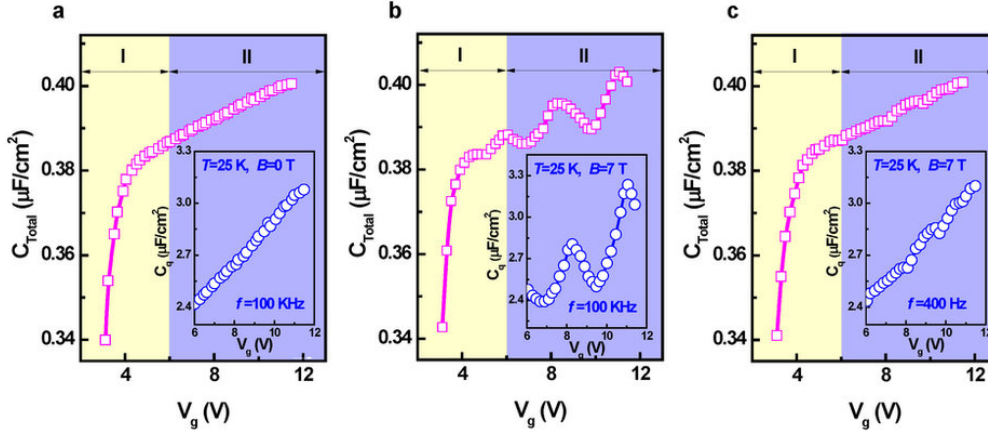


FIGURE 2.8: Total capacitance in the accumulation regime shows (quantum) oscillations at large magnetic fields ( $B=7$  T) and only at “high” frequencies. Image adapted from Ref. [19].

on magneto-capacitance oscillations, presumably due to Landau quantization of TSS, cf. Fig. 2.8. Although the experimental findings are very interesting in many aspects such as the frequency dependence of the observed oscillations, a relatively large tunability (15%) of the total capacitance and the angle dependence, the interpretation of the data is however questionable in many aspects: The authors of Ref. [19] introduce a model for the total capacitance, effectively placing all involved capacitances in series. As I will develop in chapter 3, this is generally not valid. It is particularly interesting for the present thesis that the amplitude of the oscillations depends on the measurement frequency. Their claim that the bulk cannot follow the excitations at frequencies above 4 kHz and hence does not contribute to the total capacitance, seems inconsistent to me: If this were true, the total value of capacitance should decrease<sup>4</sup> at higher frequencies. Such a global variation as a function of frequency is however not observed. Only the amplitude of the oscillation changes in their data. It is unclear up to which point the authors ensured the correct phase of the measurement signal. This is important as at high frequencies, the phase of AC-signals depends on the actual measurement setup (stray-capacitances, cable inductances, wave propagation, etc.). If the phase reference is ill-defined, the measured signal is not necessarily the capacitance but a combination of capacitance and resistance. It might therefore be that the observed oscillations are actually originating from the sample’s resistance. The correct phase calibration of high-frequency measurements constitutes a section in chapter 4.

A new route to overcome the issue of (extreme) bulk doping of as-grown Bi<sub>2</sub>Se<sub>3</sub> was demonstrated by Xu *et al.* [157]. They succeeded in growing ultra-thin ( $< 6$  nm) to thin flakes of Bi<sub>2</sub>Se<sub>3</sub> directly on exfoliated high-quality hexagonal boron nitride (hBN).

<sup>4</sup>If the bulk capacitance does not follow at high frequencies, its capacitance should go towards zero for increasing frequency. Within their model of series contributions, this would lead to a total capacitance going to zero at high frequency as well.

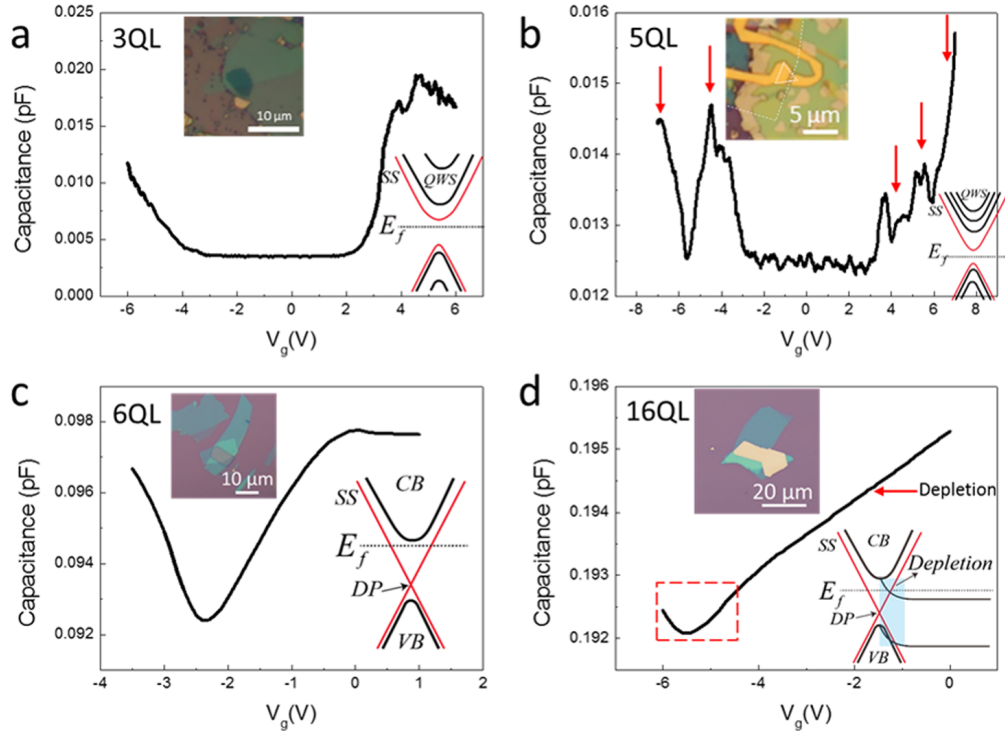


FIGURE 2.9: Total sample capacitance as a function of gate voltage for  $\text{Bi}_2\text{Se}_3$ -flakes epitaxially grown on hBN. The capacitance data illustrates qualitatively the flake-thickness dependent electronic transport regimes. Reproduced with permission from Ref. [19]. Copyright 2015 American Chemical Society.

Recently, we established the same growth technique at the LPA, cf. chapter 4. The techniques employed in Ref. [157] to characterize the grown flakes include optical microscopy, high-resolution transmission electron microscopy, selected-area electron diffraction, Raman spectroscopy and capacitance-voltage characterization, cf. Fig. 2.9. Even though the authors do not attempt a quantitative analysis of the C-V data, the qualitative observations are interesting and extremely relevant for this thesis: In the ultra-thin limit of 5 QL or less, The capacitance shows a large region of gate voltage with low capacitance, corresponding presumably to a true gap region of a genuine two-dimensional system. Indeed, it was theoretically predicted that ultra-thin samples of 3D TIs can undergo a topological crossover to either a trivial or a 2D TI phase [196, 197]. Generally this phenomenon is explained by a model involving a hybridization gap when the two TSS wave-functions start to overlap. At higher gate voltages, 2D sub-bands contribute to the capacitance. For thicker flakes, the authors claim to observe the quantum capacitance of a TSS (for a 6nm thin flake) and combined quantum capacitance of a TSS and a bulk contribution manifest as a depletion capacitance (for a 16 nm flake). From this study, we can conclude that for quantum capacitance studies a  $\text{Bi}_2\text{Se}_3$ -flake thickness on the order of 10 nm is advantageous for the investigation of TSS.

## 2.3 Summary of HgTe and Bi<sub>2</sub>Se<sub>3</sub> properties and conclusion

In this chapter a non-exhaustive overview on the state of the art in the research on topological insulators was given with focus on the two relevant materials for this thesis: 3D (strained) HgTe and Bi<sub>2</sub>Se<sub>3</sub>. In order to provide an easy-to-use overview of the most relevant properties of the two investigated materials, I present these in table 2.1. These values will be particularly useful for the interpretation of my measurements, presented in chapters 5 and 6.

It is striking that some values vary strongly depending on the reference. This is especially true for the position of the Dirac point with respect to the valence band maximum. These discrepancies can however easily be understood: For example ARPES probes typically features around a well-defined  $k$ -vector and therefore the Dirac point position can only be measured with respect to a local valence band maximum in the Brillouin zone. A theoretical simulation however extends over a larger range of  $k$  vectors (ideally over the full Brillouin zone). Therefore, the relative position of the Dirac point and the global valence band maximum is given in Table 2.1. Furthermore, a large discrepancy for the Fermi velocities can be found for HgTe. The value of  $1.6 \times 10^6$  m/s is estimated from faint

TABLE 2.1: Some important parameters for HgTe and Bi<sub>2</sub>Se<sub>3</sub>. The provided quantities are extracted from different types of theoretical or experimental papers, including *ab-initio* calculations, ARPES, magneto-optics and magneto-transport.

Property	(strained) HgTe [Ref]	Bi <sub>2</sub> Se <sub>3</sub> [Ref]
Band gap [meV]	15 [81], 23 [41], 35 [184], -302.5 [174] <sup>5</sup>	350 [190]
Dirac point with respect to valence band maximum (at zero electric field) [meV]	-22 [198], -65 [184, Fig. 2], -30 [184, Text]	+130 [190], +21 [70]
Typical (bulk) doping [cm <sup>-3</sup> ]	$\lesssim 10^{17}$ [135], $10^{16}$ [81]	$>10^{16}$ (rare) [199–201], $10^{18} - 10^{19}$ [201]
effective mass [% $m_e$ ] (at conduction band edge)	0.03 [177], 0.07 [198]	$\sim 0.11$ [190], $0.140 \pm 0.005$ [202]
Fermi velocity [ $10^5$ m/s]	$\sim 5.5$ [75], 10.5 [176, 183] $\sim 16$ [184]	5–8 [72], 3.6 [203]
Typical mobility [cm <sup>2</sup> /(Vs)]	$10^4 - 10^5$ [75, 81, 82]	100 – 20.000 [201]

features, shown in Fig. 2.5 (c). It corresponds to an estimate of the TSS Fermi velocity on the electron side. Depending on the reference, it is assumed or not that the Fermi velocity of TSS is constant over the full electron-to-hole range. It must be pointed out that the values of Fermi velocity from ARPES can fluctuate according to the subjective interpretation of the image, cf. figures 2.5 (d, e). As I will show in chapter 5, the Fermi velocity of topological surface states depends on the applied perpendicular electric field. It might be that the observed discrepancies between different studies are due to the fact that the sample surface's were subject to built-in fields.

The main difference between the materials – as presented in table 2.1 – can be summarized in a single sentence: Strained (3D) HgTe has a smaller gap and generally lower bulk doping concentration than Bi<sub>2</sub>Se<sub>3</sub>.

---

<sup>5</sup>In contrast to the other numbers, describing the strain-induced transport gap, this is the “inverted” gap between  $\Gamma_6$  and  $\Gamma_8$  band.



## Chapter 3

# The metal-insulator-topological insulator capacitor - Understanding the compressibility

Generally, a capacitor is a device consisting of two electrodes separated by an insulating region. The main physical quantity that characterizes a (linear) capacitor is its capacitance  $C$ , defined via the relation between the accumulated charge  $Q$  on one of the electrodes and the applied voltage  $V$

$$Q = C \cdot V. \quad (3.1)$$

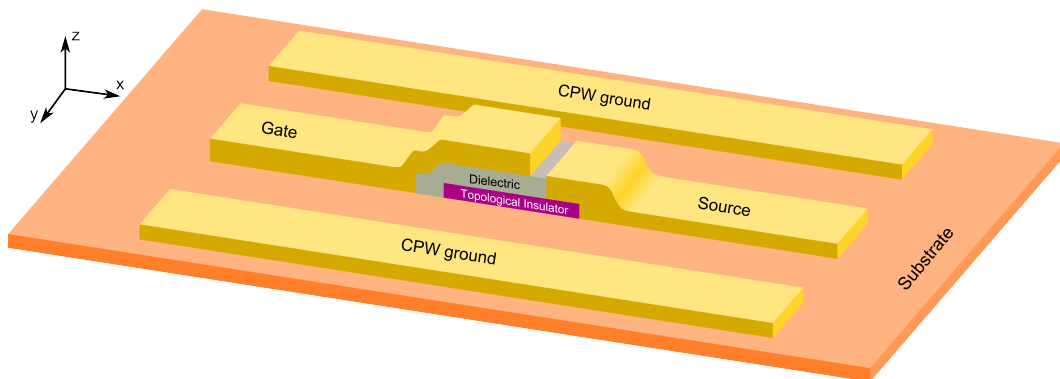


FIGURE 3.1: An artist view of a typical device structure: A rectangular slab of a topological insulator (HgTe or Bi<sub>2</sub>Se<sub>3</sub>, purple) is contacted on one side by an ohmic contact, whereas the other end of the slab is covered with an insulating layer (typically HfO<sub>2</sub>) and a gate electrode, thus forming a capacitor. The capacitor structure is embedded in a coplanar waveguide (CPW).

However, in general, the charge-voltage characteristic needs not be linear, and – as will be seen later – it is useful to define the differential capacitance as

$$C = \frac{\partial Q}{\partial V}. \quad (3.2)$$

In order to simplify the notations and if not stated otherwise, the word capacitance designates the differential capacitance *per unit surface* in the following. More specifically, non-linear charge-voltage relations arise typically in metal-insulator-semiconductor (MIS) structures. Technologically, a non-constant capacitance can be extremely useful. As an example, it can be used to tune the resonance frequency of an L-C circuit by applying a voltage on the capacitor plates. This feature can for example be exploited in radio receivers. According to Ref. [18], the first proposal of a voltage controlled capacitor goes back to 1959 [204, 205], named “varistor” at the time - for “variable” and “capacitor”. Nowadays, this term is rather used for variable resistors and the (commercial) term “varicap” is more widely used [206]. Furthermore, measurements of the capacitance-voltage characteristics of MIS-, or – technologically even more relevant – MOS- (metal-oxide-semiconductor) structures, yield valuable information on the interface of such structures. They can provide “[...]gate oxide thickness, oxide charges and interface state density, flat band voltage, doping concentration etc. [...]” [207]. These results are often used prior to transistor design.

It is one of the main goals of the present thesis to show that capacitance measurements are an alternative, powerful tool of probing electronic properties of topological insulators. In this chapter I will derive several theoretical formulae and concepts relevant for TI capacitance. This will constitute a theoretical background for understanding the capacitance-voltage (C-V) characteristics presented in chapters 5 and 6. The results of this chapter apply generally to C-V curves and are independent of the exact sample geometry and the chosen measurement setup. For the moment, I will therefore not focus on the choice of geometrical parameters, like width, thickness, etc. These experimentally highly relevant aspects will be treated in some detail in chapter 4. However, to illustrate the following discussion, a sketch of a typical device structure is shown in Fig. 3.1.

This chapter is organized as follows: I will first comment on the limits of thermodynamic equilibrium and show that the device geometries chosen in this thesis remain within these limits. This significantly simplifies the discussion in the subsequent sections.

Second, the electronic *surface* compressibility will be formally introduced and its close relation to the *surface chemical potential* will be pointed out. We show that in the presence of bulk carriers, the measurable quantity is not directly related to the local (three-dimensional) density of states.

Third, I will discuss some examples of 2D conductors in order to illustrate capacitance

measurements and derive analytical formulae for the expected behavior of 3D systems. To conclude the chapter, I will comment on the issue of “Dirac screening” and its signatures in capacitance.

By analogy to the acronyms MOS and MIS, we introduce “MITP” to designate a metal-insulator-topological insulator heterostructure.

### 3.1 Equilibrium

In order to measure capacitance, the simplest experiment consists in the measurement of an AC-current resulting as response to a small AC-voltage applied onto the two electrodes forming the capacitor. It is easy to show (cf. chapter 4) that the measurement signal increases with increasing frequency. Thus, it is *a priori* advisable to measure at high frequencies. We shall now address the question whether there is an upper frequency limit for the electrons to follow the excitation while remaining in thermodynamic equilibrium. Equilibrium along the  $y$ -direction in Fig. 3.1 follows from geometry: all excitations are invariant along this direction (at least if boundary effects are negligible). However for the  $x$  and  $z$  directions, this must be checked more carefully. As shown e.g. in Ref. [15] and recalled in Appendix C, the characteristic length-scale for variations of the electric potential along the  $x$ -direction is governed by the electrostatics of a distributed  $R-C$  line, given by (see also eq. (4.2) below in chapter 4):

$$\lambda \approx \frac{2\pi}{\sqrt{rc\omega}}, \quad (3.3)$$

where  $\omega$  is the frequency and  $r$  ( $c$ ) are infinitesimal resistance (capacitance) elements of the distributed line. With typical parameters of our experiment, i.e. capacitances on the order of millifarad per square meter, square resistances on the order of a few hundreds of Ohm and a measurement setup-limited maximum frequency of 40 GHz, this length scale is in the range of several hundreds of microns to millimeters. This must be compared to the length of our devices  $L = 4 - 80 \mu\text{m}$ . Therefore, the variation of the potential along the  $x$  direction is negligible. In other words, the gate excites the full channel homogeneously.

In general, for non-degenerate MOS-Caps, the measured admittance  $Y$  depends on frequency not only via  $\text{Im}\{Y\} \propto \omega C$  (at relatively low frequencies<sup>1</sup>), but the capacitance itself might depend on it. This is particularly true in the so-called *inversion regime* as discussed for example in Ref. [18]. The inversion regime corresponds to a situation in which minority carriers accumulate close to the gate oxide. When exciting the sample

<sup>1</sup>This is textbook knowledge, but will be shown to hold also in a lossy RC-line in chapter 4.

with the gate electrode at high frequencies, the charge transfer mechanisms through the depletion zone between the region of majority carriers (far away from the oxide) and the inversion layer are slow. Therefore, the accumulation layer cannot be charged at high frequencies. In this case, one measures a total capacitance that is simply given by the series contribution of the oxide and the depletion zone capacitance. In contrast, at low frequencies, the charge transfer between bulk and inversion layer is fast enough and the total capacitance is given by the oxide capacitance only. However, in our sample, there are two reasons why we always measure low-frequency-like behavior: First, both  $\text{Bi}_2\text{Se}_3$  and  $\text{HgTe}$  have small gaps as compared to silicon or most other semiconductors. Correspondingly, the depletion zone separating the inversion layer and the bulk material is rather thin, i.e. tunneling rates are much higher. Second – and more interesting – topology dictates the (gap-less) surface state to wrap completely around all surfaces. Hence, even if there is a finite barrier between bulky inversion layers and the bulk, these regions are always shorted via the topological surface states on the side surfaces. This further ensures an equilibrating charge transfer between bulk and surface states.

To sum up, the capacitor samples studied in this thesis are always in thermodynamic equilibrium. We can therefore define an electrochemical potential  $\mu^*$  that is constant all over the TI. This also means that there is a one-to-one relation between chemical and electrostatic potential (noted  $\mu$  and  $V$ , respectively) given by

$$\mu^* = \mu + qV = \text{const.} \quad (3.4)$$

With this at hand, we will now develop some formulae that allow us to predict the capacitive responses of a MITI-Cap and illustrate which quantities can be extracted from it.

## 3.2 Electron compressibility and the surface potential

In the device geometry given by Fig. 3.1, the gate voltage applied between the gate and the drain contact does not entirely drop within the oxide layer. A finite potential drop occurs in the TI material between sample surface and contact. Indeed, the applied *voltage* corresponds to a difference in *electrochemical potential* between gate and drain electrodes. The drain electrode and the TI can freely exchange carriers. Therefore, they are in thermodynamic equilibrium, i.e. at the same electrochemical potential. However,  $\mu$  (the chemical potential) and  $V$  (the electrostatic potential) can vary independently unlike in metals where independently  $\mu = \text{const.}$  We note  $V_0$  the electrostatic potential at the surface. In equilibrium the sample's area under the gate electrode is homogeneous:  $\partial_x V_0 = \partial_y V_0 \approx 0$ , cf. section 3.1. According to Gauß' law, the drop of electrostatic

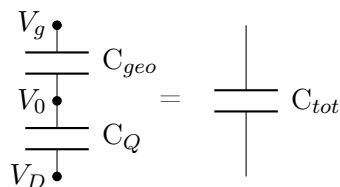


FIGURE 3.2: The voltage between the gate and metal electrodes does not drop in the oxide only. Indeed, there can be a small voltage difference between the surface of the TI and its backside and accordingly the contact electrode. The surface's electrostatic potential is called  $V_0$ . The measured capacitive response is a series contribution of the oxide's capacitance and a second "capacitive" term that turns out to be the electron compressibility.

potential between the gate electrode and the sample's surface is given by

$$c_{\text{geo}}(V_g - V_0) = q_{\text{gate}} = -q_{\text{sample}}. \quad (3.5)$$

Note that  $c_{\text{geo}} = \varepsilon_0 \varepsilon_{\text{r,ox}}/d_{\text{ox}}$  does not depend on gate voltage whereas  $V_0$  does. The second equality in (3.5) stems from overall charge neutrality of the system. In principle, the relation between the total charge within the sample  $q_{\text{sample}}$  and the surface potential can be non-linear and rather complex. In any case, we can define the *quantum capacitance* here as

$$c_Q := -\frac{\partial q_{\text{sample}}}{\partial V_0}. \quad (3.6)$$

**Is the quantum capacitance a capacitance?** At first sight, definition (3.6) seems motivated only by dimensional arguments. However, this quantity is useful for two reasons: First, it is experimentally accessible and second, it yields information about the electron *surface compressibility*. This thermodynamic quantity is directly related to the density of states for low-dimensional systems and yields valuable information about screening in a three-dimensional conductor. These features shall be explained below. Let us first show that it is indeed a capacitance. Therefore, rewrite (3.5):

$$c_{\text{geo}}(V_g - V_0) = \int_{V_0(V_g=0)}^{V_0(V_g \neq 0)} c_Q dV. \quad (3.7)$$

After taking the derivative<sup>2</sup> with respect to  $V_0$  and rearranging the terms, we find the following relation

$$c = \left( \frac{1}{c_{\text{geo}}} + \frac{1}{c_Q} \right)^{-1}, \quad (3.8)$$

where  $c = -\partial q_{\text{sample}}/\partial V_g$  is the total capacitance which is measured by the small signal admittance, cf. chapter 4. Thus, the total capacitance is a series contribution of geometrical and quantum capacitance as depicted in Fig. 3.2.

<sup>2</sup>Note:  $\partial V_g/\partial V_0 = (\partial V_g/\partial q_{\text{sample}}) \cdot (\partial q_{\text{sample}}/\partial V_0)$

**Relation to surface compressibility** The *electronic surface compressibility* is defined as

$$\kappa = \frac{\partial n}{\partial \mu_{\text{surface}}} \quad (3.9)$$

with the integrated 2D electron density of the sample

$$n := - \int_0^{d_{\text{sample}}} \frac{\rho(z)}{e} dz \quad (3.10)$$

and the chemical potential at the sample's surface  $\mu_{\text{surface}} =: \mu_s$ . Using the equilibrium condition (3.4), it is straightforward to show

$$c_Q = e^2 \kappa. \quad (3.11)$$

This surface compressibility describes the rate of change in carrier density with respect to a change of chemical potential which justifies the terminology. At first sight, it seems somewhat disappointing that the measurable quantum capacitance is a non-local quantity, as it relates the *total (i.e. integrated) charge* to the sample's *surface chemical potential*. However, especially for topological insulators, this chemical potential is particularly interesting as it corresponds to that of the surface state.

From the formulae above, it follows immediately that in general the investigated samples will exhibit a *non-linear* charge-voltage relation. We emphasize that in order to accurately measure the quantum capacitance, eq. (3.8) shows that the geometrical capacitance should be chosen as large as possible (as compared to the quantum capacitance). Before I discuss the expected capacitance-voltage characteristics for a topological insulator system, I want to give some additional very useful formulae that follow directly from the above definitions: The measurement of capacitance gives directly – without need for any kind of modeling – access to the total charge variation within the TI and to the surface (electrostatic) potential  $V_0$ , or equivalently via eq. (3.4) to the chemical potential *at the sample's surface*. Indeed, the variation of total charge within the TI is simply given by

$$\Delta n(V_g) = \frac{1}{e} \int_0^{V_g} C(V) dV. \quad (3.12)$$

This formula is the natural generalization of the usual charge-voltage relation for a capacitor to the case of a non-constant capacitance. Furthermore, from definition eq. (3.6), the variation of surface chemical potential is given by [208]:

$$\Delta \mu_s = \int_0^{V_g} \frac{1}{c_Q} c(V) dV = \int_0^{V_g} \left( 1 - \frac{c(V)}{c_{\text{geo}}} \right) dV. \quad (3.13)$$

With this at hand, it is possible to trace the variation of the *surface* chemical potential versus the applied gate voltage. By fixing an origin for the energy scale, the applied gate voltage can thus be converted to the absolute chemical potential at the surface. It will turn out in the following that a minimum in the C-V-characteristic sets a natural origin for this voltage-to-energy conversion.

Let us now turn towards the electron compressibility in a TI sample. From the definition, eq. (3.6), it is obvious that surface and bulk contribute in parallel to the (surface) electron compressibility<sup>3</sup> as  $n = n_{\text{surf}} + n_{\text{bulk}}$ .

The total quantum capacitance is therefore a sum of the two-dimensional topological surface states and a bulk background. We can therefore – in a first step – decouple the response of the two systems. Let us start with a 2D system.

### 3.3 Electron compressibility in 2D systems and its relation to the density of states

As 3D TIs exhibit topological two-dimensional surface states, it is important to understand the electron compressibility of a 2D system. For a 2D conductor, the *surface* chemical potential is – obviously – equal to the chemical potential, i.e. one has simply

$$c_Q = e^2 \frac{\partial n}{\partial \mu}. \quad (3.14)$$

At zero temperature, this derivative is exactly the density of states for the 2D conductor. For finite temperatures please refer to Appendix. A. Let us focus on the density of states for a moment. As explained above, we can not only measure the density of states as a function of gate voltage but can actually convert the applied gate voltage to the (surface) chemical potential or the charge on the sample. With these quantities at hand, it becomes clear that electron compressibility measurements are a powerful spectroscopic tool that makes even a band-structure reconstruction possible. Indeed, one can invert the  $\mu(V_g)$ -relation, eq. (3.13) and use eq. (3.12) in order to obtain

$$k_F = \sqrt{\frac{4\pi n[V_g(\mu)]}{g}}, \quad (3.15)$$

where  $g$  is a degeneracy factor. This relation can of course be inverted and one obtains the band-diagram  $\mu(k_F)$  purely based on the capacitance measurement. This justifies

---

<sup>3</sup>Here and in the following  $n_{\text{bulk}}$  designates a two-dimensional charge density if not otherwise stated. It is obtained by integrating the (non-uniform) three-dimensional charge density along  $z$  over the thickness of the sample.

TABLE 3.1: Several models of two-dimensional band dispersions and their corresponding quantum capacitances at zero temperature. The finite temperature expressions can be found in Appendix A.  $g$  is a degeneracy factor.

Type	Example	Band dispersion	Quantum capacitance
Schrödinger	2D electron gas	$E = \frac{\hbar^2 k^2}{2m^*}$	$c_Q = e^2 \frac{gm^*}{2\pi\hbar^2} \Theta(\varepsilon_F - \varepsilon_{BE})$
Dirac	Graphene	$E = \hbar v_F k$	$c_Q = e^2 \frac{g \varepsilon_F }{2\pi(\hbar v_F)^2}$
massive Dirac	TSS of Fe-doped Bi <sub>2</sub> Se <sub>3</sub> [209]	$E = \pm \sqrt{\Delta^2 + (\hbar v_F k)^2}$	$c_Q = e^2 \frac{g\varepsilon}{2\pi(\hbar v_F)^2} \Theta(\varepsilon_F - \Delta)$

the name of “capacitance spectroscopy”<sup>4</sup>. In order to get an understanding for electron compressibilities of topological surface states, let us first concentrate on the expected results for given band-structures.

Even though topological surface states are often assumed to follow a perfectly linear dispersion relation (like graphene at low energies), angle-resolved photo emission (ARPES) studies suggest for Bi<sub>2</sub>Se<sub>3</sub> and HgTe rather champagne-flute shaped dispersions, Ref. [72, 75, 190] and Fig. 2.5. The energy-dependent quantum capacitances for different types of 2D conductors are illustrated in Table 3.1 and Fig. 3.3. We highlight the explicit energy dependence of a TSS’ quantum capacitance in contrast to a trivial 2DEG.

Although for 2D systems capacitance spectroscopy is a powerful tool and was used e.g. on graphene [14, 15, 72], some caution is appropriate when it comes to the interpretation of surface compressibility in a TI.

First, a rather strong (*a priori* unknown) background signal from the bulk renders reliable spectroscopy a difficult task. This issue can partly be solved by relying on a model band-structure for the bulk as will be shown in the following section.

Second, charge inhomogeneities (also referred to as *puddles*) on the surface state tend to blur all features in a very similar way as temperature does [195, 210]. In particular, Beidenkopf *et al.* reported on spatial fluctuations of chemical potentials of  $\sim 50$  meV over typical length-scales on the order of 10-20 nm. This observation illustrates the importance of clean and homogeneous TI-oxide surfaces. More specifically, these can be achieved using capped MBE-grown TIs (cf. chapter 5) or epitaxial growth of Bi<sub>2</sub>Se<sub>3</sub> on hexagonal Boron Nitride (cf. chapter 6).

Third, as capacitance spectroscopy relies on the use of a gate electrode exerting strong electric fields to the surface, one has to consider the electrostatics of the problem. In any electrostatic calculation, it is helpful to assume the topological surface state to be truly 2D, i.e. described by a  $\delta$ -peak at  $z = 0$ , where the origin of the  $z$  axis is chosen

<sup>4</sup>The term *spectroscopy* is used here to describe an experimental tool yielding the energy dispersion  $E(k)$ .

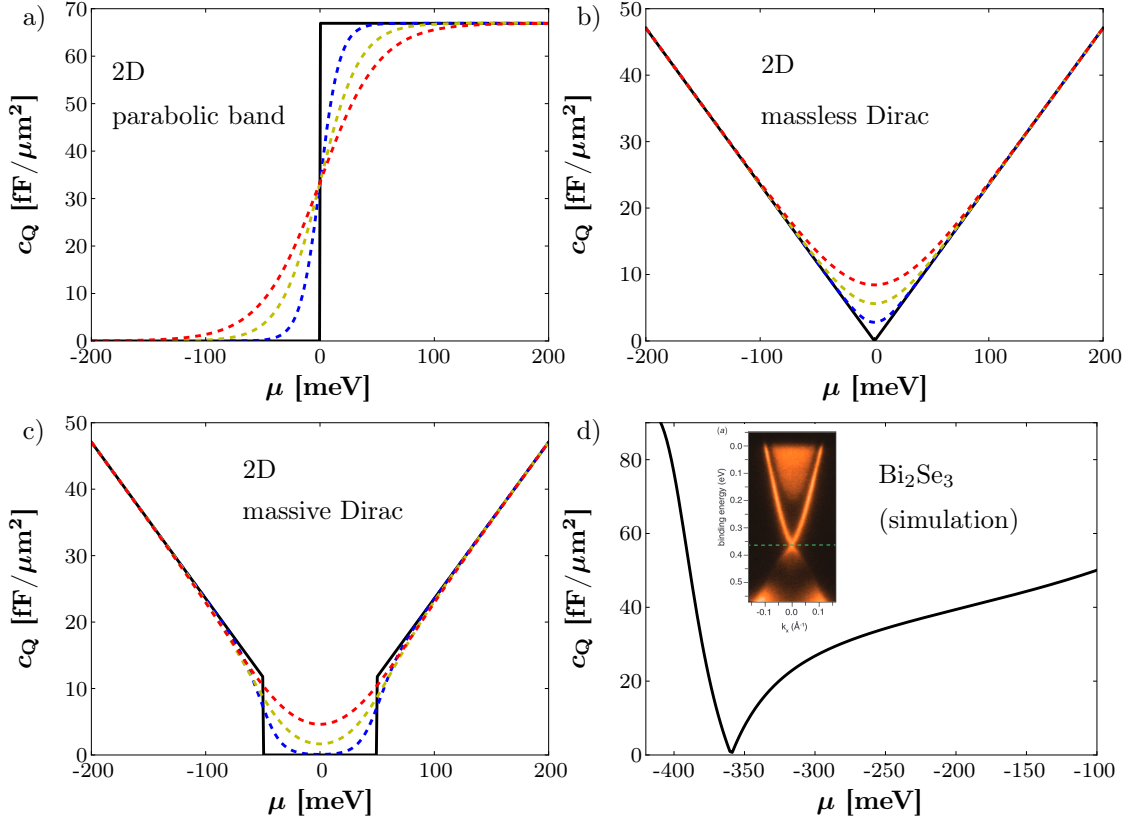


FIGURE 3.3: Calculated quantum capacitances for varying temperatures: 0 K (black), 100 K (blue), 200 K (yellow), 300 K (red) and different types of 2D band structures: a) Massive (Schrödinger like) band, b) Dirac and c) massive Dirac. d) corresponds to the expected quantum capacitance of the TSS for the TSS band-structure of Bi<sub>2</sub>Se<sub>3</sub> as obtained from high-resolution ARPES, represented in the inset. Inset image adapted from Ref.[190]. The parameters are a degeneracy factor  $g=2$  for the Schrödinger band,  $g=4$  (inspired from graphene) for the two Dirac bands. Further parameters (cf. Table 3.1) are  $m^* = 0.1 m_e$ ,  $\Delta = 50$  meV,  $v_F = 10^6$  m/s.

at the sample surface. In this case, according to Gauß' law the electrical field acquires a sharp discontinuity at  $z = 0$  and the surface chemical potential is uniquely defined for the surface state. In reality however, the surface-state's (envelope) wave-function has a certain width  $\xi$  along the  $z$ -axis, estimated to range from a few to a few tens of nanometers [41, 211, 212]. Therefore, the surface states' chemical potential is not uniquely defined: The surface states live on a potential gradient and thus average over the relevant energies. Furthermore, the width might depend on the position of the Fermi level. The main effect of this finite width are a decrease in the apparent geometrical capacitance and an additional smearing out of the features in the  $c_Q$  vs  $V_g$  curves. Therefore, the spectroscopic results obtained from capacitance measurements must not be overestimated. Specifically, they should not be used solely to determine physical parameters such as the Fermi velocity.

Furthermore, the capacitance is probed by applying a small but finite AC-field. In this case, the capacitance is averaged over the amplitude of the probing field. In practice,

resolution in energy can be improved by decreasing the excitation amplitude. However, this increases the noise level and thus decreases the resolution on the capacitance. I will comment on these experimental issues in more detail in chapter 4.

### 3.4 Surface compressibility for 3D conductors.

Most TI samples (especially the Bismuth based) are heavily  $n$ -type doped. To be specific, I therefore discuss generally the case of bulk  $n$ -type doping here. The case of  $p$ -doping is analogous. Due to heavy doping, the bulk is generally not insulating in most TIs as suggested by the term topological *insulator* but rather metallic as the Fermi level tends to lie in the bulk conduction band. These bulk electrons must therefore be considered when calculating the electric field response of the total TI device. In other words, the bulk screening properties cannot be neglected. As was pointed out in the beginning of this chapter, the measured total electronic *surface* compressibility is given by the sum of surface state and bulk contributions. In the following, I will develop an analytical expression for the bulk's capacitive response.

Depending on the doping concentration, the bulk capacitance can be divided into two categories, corresponding either to the non-degenerate or the degenerate case. Most studies focus on the case of a non-degenerate semiconductor, i.e. the doping level is such that the Fermi level lies within the band gap  $\mu_\infty < E_{\text{CBE}}$ , with the Fermi level deep in the bulk  $\mu_\infty$  and the conduction band edge  $E_{\text{CBE}}$ . In this situation, the capacitance shows a rather strong temperature dependence. Generally, when a gate voltage is applied to the MIS-structure, three regimes can be identified depending on the value of the surface chemical potential:

1.  $\mu_s > \mu_\infty$  (corresponding to  $V_g > 0$ ): This situation is called the *accumulation* regime in which the bulk electron concentration close to the surface exceeds that of the bulk far from the surface, where the Fermi level is unaffected by surface effects and remains at  $\mu_\infty$ .
2.  $E_i < \mu_s < \mu_\infty$ : This situation is called the *depletion* regime. The surface electron density is smaller than the bulk's density, but the nature of charge carriers close to the surface remains electron-like ( $E_i$  designates the mid-gap here).
3.  $\mu_s < E_i$ : This regime is referred to as the *inversion* regime in which a p-n junction forms between a p-type surface layer and the n-type bulk.

After introducing these terms, I will not comment much further on the non-degenerate case and refer to the book by Sze [18] where it is discussed in much detail. However,

the description of the non-degenerate case is often limited to surface chemical potentials remaining in the bulk band-gap<sup>5</sup>:  $E_{\text{VBE}} < \mu_s < E_{\text{CBE}}$ . More precisely, the results presented in Ref. [18] rely on a Boltzmann approximation of the electron occupation factor valid only as long as the Fermi level (in all points of space) lies at least  $k_{\text{B}}T$  away from a band-edge. Thus, these formulae are inadequate for small gap systems like HgTe (gap  $\sim 25$  meV), where the Fermi level lies always close to the band edges. Also for larger-gap TIs like Bi<sub>2</sub>Se<sub>3</sub>, this image breaks down as in the degenerate case, the Fermi level (at low temperature) lies within the conduction band<sup>6</sup>. The goal of the following discussion is to provide analytic expressions for this “metallic bulk” regime.

In order to simplify the discussion, I will adopt the local density approximation. This corresponds to a classical treatment of the electrostatics. It consists in the assumption that the electron density and the chemical potential can be defined *locally*. Furthermore, it is assumed that the (local) electron density depends on the (local) chemical potential only. It also means that the electrons are described as a continuum of negative charge, i.e. the granularity of charge is neglected. Strictly speaking, this assumption holds only if the length-scale of potential variations is larger than the typical size of an electronic wave-packet. Even though I will show that the variations of the potential are typically on the order of a few nm and the volume per electron is on the order of  $10^4$  nm<sup>3</sup> for a typical density of  $10^{17}$  cm<sup>-3</sup>, this approximation seems to hold beyond its strict domain of validity. More precisely, I do not follow a Schrödinger-Poisson approach, where the coupled quantum mechanical Schrödinger and the classical Poisson equation are solved iteratively. Such an approach would require very precise knowledge of the  $k \cdot p$ -parameters of the investigated system and was already shown to fail in the description of gated HgTe, cf. the discussion in Refs. [41] and [135].

In the following, dopants are assumed to be distributed in a homogeneous way throughout the TI and for the sake of clarity I assume the low temperature limit. This is justified as most measurements presented in this thesis were carried out at 10 K. As was shown in Fig. 3.3, finite temperature effects tend mainly to blur the features of capacitance.

### 3.4.1 A first rough estimate for the bulk response

For small electric fields, i.e. around  $V_g = 0$ , all density variations are very small and as a first approach, we can linearize the  $\mu - n$  relation:  $n = N_0\mu$ , where  $N_0 = \partial n / \partial \mu$  designates the (constant) density of states and  $n$  is the total charge variation with respect to the zero-field case. For simplicity of notation, we fix the zero of chemical potential to

<sup>5</sup>CBE stands for “conduction band edge” and VBE for “valence band edge”.

<sup>6</sup>for most *as-grown* Bi<sub>2</sub>Se<sub>3</sub> samples.

the Fermi-level in the following discussion. In this case, the equilibrium condition (3.4) leads (after derivation) to

$$\frac{\partial}{\partial z} \left( \frac{n}{N_0} \right) = q \mathbf{E}_z, \quad (3.16)$$

with the  $z$ -component of the electric field  $\mathbf{E}_z$ . A second derivative along the  $z$ -axis introduces a Gauß' law expression on the right-hand side whereas on the left-hand side we make explicit use of the constant DoS assumption and find a second order differential equation for the charge density:

$$\frac{1}{N_0} \frac{\partial^2 n}{\partial z^2} = q^2 \frac{n}{\varepsilon} \quad (3.17)$$

where  $\varepsilon = \varepsilon_0 \varepsilon_{\text{TI}}$  with the topological insulator's dielectric constant  $\varepsilon_{\text{TI}}$ .

The density profile follows an exponential law given by

$$n(z) = n_0 e^{-z/\lambda_{TF}} \quad (3.18)$$

with the electron density at the surface  $n_0$  and the Thomas-Fermi screening length [3, p. 324]:

$$\lambda_{TF} = \sqrt{\frac{\varepsilon}{q^2 N_0}}. \quad (3.19)$$

It is straightforward to calculate the total charge on the capacitor plate, given by  $Q_{\text{tot}} = e \lambda n_0 = e \lambda N_0 \mu_s$ , where I used the (local) relation between chemical potential and the charge density. According to the definition of the quantum capacitance given in the beginning of this chapter, one finds

$$c_Q = \frac{\varepsilon}{\lambda_{TF}}, \quad (3.20)$$

the so-called ‘‘Thomas-Fermi’’ capacitance that remains constant as a function of gate voltage<sup>7</sup>.

Note the importance of a constant DoS in the derivation of this formula. This situation occurs in true metals: The Fermi level lies deep in a band, where the DoS is large and therefore remains fairly constant over the small variations of surface Fermi level when a gate voltage is applied. Furthermore, a large DoS leads to a very short screening length, i.e. a large quantum capacitance. This is the reason why for a metal-insulator-metal capacitor, the total capacitance is entirely dominated by the geometric capacitance.

What about a degenerate semi-conductor or – in our case – a topological insulator? The small masses and gaps encountered in TIs cause the bulk density of states to be rather small close to the band edge as compared to real metals and hence the assumption of

<sup>7</sup>In Ref.[201] it is stated that the Thomas-Fermi wavelength is below 1nm and therefore gating a doped TI is generally impossible. However, in the expression there, the rather large dielectric constant of TI materials is neglected and rather heavy bulk carriers were considered.

a constant DoS becomes questionable. For small gate voltages however, the shift in the Fermi level is always small and therefore a linearization of the  $n - \mu$  relation holds for small gate voltages. Experimentally, the small bias capacitive response allows us therefore to assess semi-quantitatively the 3D-DoS at the bulk's Fermi level. For a given model, this is a quick way of assessing the bulk's Fermi level.

### 3.4.2 Dimensional analysis

A numeric estimate for the screening length can readily be obtained from dimensional analysis. The quantities entering the screening problem are the 2D donor density  $N_D$ , the elementary charge  $e$ , the permittivity of the material  $\varepsilon = \varepsilon_0 \cdot \varepsilon_r$  and the chemical potential (in the unperturbed system). With these quantities, one can define a typical length given by<sup>8</sup>:

$$\lambda_{\text{dim}} = \sqrt{\frac{\mu\varepsilon}{e^2 N_D}}. \quad (3.21)$$

In order to get a feeling for the order of magnitude of this screening length, let's measure  $\mu$  in meV, and  $N_D$  in  $\text{cm}^{-3}$ . Then one has

$$\lambda_{\text{dim}} = \sqrt{\frac{\varepsilon_r \mu / (\text{meV})}{N_D / (10^{17} \text{cm}^{-3})}} \cdot 7.43 \text{ \AA}. \quad (3.22)$$

### 3.4.3 Exact calculation of the bulk's surface compressibility for a degenerate semi-conductor

The Thomas-Fermi formula gives only an estimate of the bulk's contribution to the total capacitance of the studied MITI-Caps valid in the low bias regime. Here, I will develop exact expressions for this quantity in a very general way, i.e. band-structure independent. For simplicity, I restrict the discussion to the (degenerately) n-doped case, the p-doped case is completely analogous.

From the definition of the quantum capacitance, and Gauß' law, it follows immediately that<sup>9</sup>

$$c_Q = -\varepsilon \frac{\partial}{\partial V_0} \int_0^\infty \frac{\partial}{\partial z} E_z(z') dz'. \quad (3.23)$$

As the total capacitor remains charge neutral – the amount of charge on the metallic plate is compensated by the total charge in the studied material – the electric field has to drop to zero for large  $z$ . In a (thin) TI device, this might happen at the backside of the sample. However, we shall assume here that the screening happens entirely in the

<sup>8</sup>Corresponding to the Thomas-Fermi length at  $V = 0$  if the density of states is energy independent  
<sup>9</sup> $z = 0$  corresponds to the TI-insulator boundary and the  $z$ -axis points towards the TI.

bulk, i.e. the screening length is shorter than the sample's thickness. The validity of this assumption will be confirmed *a posteriori*. In this case, the electric field at infinity drops to zero and together with the definition of the electrostatic potential  $V$ , we find

$$c_Q = -\varepsilon \frac{\partial}{\partial V_0} V'(0). \quad (3.24)$$

Here,  $V'$  designates the  $z$ -derivative of  $V$ . Hence, the surface compressibility describes how the surface electric field varies with respect to a change of the surface potential. For an exponential decay (in the case of Thomas-Fermi screening) this relation is obviously trivial and explains the expression from the last paragraph. The goal is now to calculate this derivative. From Poisson's equation we know

$$V''(z) = -\frac{\rho(z)}{\varepsilon}. \quad (3.25)$$

In the local density approximation, the charge density  $\rho$  depends on position via the local potential:  $\rho(V(z))$ . This greatly helps to simplify further. Indeed, multiplying eq. (3.25) with  $V'$  and integrating once between  $z' = 0$  and  $z' = z$  and changing integration variables, one finds

$$\frac{1}{2}(V'(z)^2 - V'(0)^2) = -\frac{1}{\varepsilon} \int_{V(0)}^{V(z)} \rho(\tilde{V}) d\tilde{V}. \quad (3.26)$$

It is remarkable that now, the integral does not depend on the exact spatial shape of the potential landscape but only on its endpoints. As explained above, we assume “total screening” within the bulk, i.e. the electric field (and the potential) to drop to zero for large enough  $z$  (with  $z < t$ , where  $t$  is the sample's thickness). Under these assumptions, we find the following expression:

$$V'(0)^2 = \frac{2}{\varepsilon} \int_{V_0}^0 \rho(\tilde{V}) d\tilde{V}. \quad (3.27)$$

Equation (3.24) can now be rewritten using this result:

$$c_Q = -\frac{\varepsilon}{2V'(0)} \frac{\partial}{\partial V_0} V'(0)^2 = \frac{\rho(V_0)}{V'(0)}. \quad (3.28)$$

Note that this equation relates the following quantities: The (measurable) quantum capacitance, the electric field at the sample's surface and the (local) charge density at the sample's surface. From the form of this equation it is obvious that even though the exact shape of the potential landscape within the bulk depends strongly on the band structure of the investigated material, the measurable quantity simply relates surface quantities. This also means that there is no need to calculate this profile for a given

scenario in order to get a prediction for  $c_Q$ . For completeness, (3.28) can be written as

$$c_Q = \frac{\rho(\mu_S)}{\sqrt{\frac{2}{e\varepsilon} \int_{\mu_S}^{\mu_\infty} \rho(\mu) d\mu}}. \quad (3.29)$$

Before I provide some formulae for different regimes of gate voltage, I want to highlight the link between this precise formula and the simplified (Thomas-Fermi) result. According to Gauß' law,

$$\varepsilon \cdot \operatorname{div} \mathbf{E} = \rho. \quad (3.30)$$

In the case of Thomas-Fermi screening, this relation (integration between 0 and  $\infty$ ) turns into

$$\frac{\varepsilon}{\lambda} E(0) = -en_0. \quad (3.31)$$

This corresponds to the exact result with  $c_Q = \varepsilon/\lambda$ . Hence, there will be a correction to the Thomas-Fermi result only if the assumption  $n = N_0\mu$  is invalid. Generally, the electron concentration does not decay exponentially in this case, eq. (3.18). However, it is tempting to write

$$c_Q = \varepsilon/\tilde{\lambda} \quad (3.32)$$

with an *effective* screening length that – in contrast to Thomas-Fermi screening – depends on the applied voltage

$$\tilde{\lambda} = \frac{\varepsilon V'(0)}{\rho(V_0)}. \quad (3.33)$$

This quantity is still an estimate of a length-scale over which most of the electric field becomes screened. The bulk's quantum capacitance can now be calculated in three different regimes, depending on the Fermi level at the sample's surface: It can lie in the conduction band, in the gap or in the valence band.

**Surface Fermi level in the conduction band** As long as the chemical potential at the samples surface lies within the conduction band, formula (3.28) directly applies and yields

$$c_Q = \sqrt{\frac{\varepsilon e}{2}} \frac{(N_D - N(V_0))}{\sqrt{\int_{V_0}^0 [N_D - N(\tilde{V})] d\tilde{V}}} \quad (3.34)$$

where  $N_D$  designates the (uniform) donor density in the material and  $N(V)$  the bulk's electron density at an electrochemical potential of  $\mu_\infty + eV$ , with the boundary condition  $N(0) = N_D$ . In order to be quantitative, a material-specific 3D density of states needs to be inserted into the given formula.

**Surface Fermi level in the band gap** The situation changes once the Fermi level at the surface reaches the conduction band minimum<sup>10</sup>. At this point, a depletion region of width  $\delta$  starts to form where no free charges are present, i.e.  $\rho(z) = N_D$  for  $0 < z < \delta$ . A direct way of calculating the bulk's quantum capacitance is again given by (3.28). However, as there are no free charges within the depletion region we can simplify the result by splitting the integral into two parts: The first running from  $V_0$  to  $V_{CBE}$ , the second running from  $V_{CBE}$  to zero. Mathematically, the calculations are very easy to carry out in this case. However, not much physical insight can be gained. Physically, one can show that the depletion zone acts simply as a geometrical capacitance of value

$$c_Q^{\text{depl.}} = \frac{\varepsilon}{\delta} \quad (3.35)$$

and that the total (quantum) capacitance is given by the series contribution of the (minimal) capacitance  $c_Q^0 = c_Q(V_0 = V_{CBE})$  from the situation when the surface potential lies in the band gap and this geometrical capacitance:

$$\frac{1}{c_Q} = \frac{1}{c_Q^{\text{depl.}}} + \frac{1}{c_Q^0}. \quad (3.36)$$

The derivation of this result is a little lengthy and subject of appendix B, where I also derive the formula for the depletion length

$$\delta = -\frac{\varepsilon}{C_Q^0} + \sqrt{\left(\frac{\varepsilon}{C_Q^0}\right)^2 - \frac{2\varepsilon}{e^2 N_D} \mu_{\text{surface}}}. \quad (3.37)$$

At some point, the surface Fermi level enters the bulk valence band. In this situation, the depletion width reaches its maximum given by

$$\delta_{\text{max}} = \frac{\varepsilon}{C_Q^0} \left( \sqrt{1 + 2 \frac{\Delta_{\text{Gap}} C_Q^0{}^2}{e^2 N_D \varepsilon}} - 1 \right). \quad (3.38)$$

The scaling of the maximum depletion width with respect to the dopant concentration scales thus like  $\delta_{\text{max}} \propto \sqrt{\Delta_{\text{Gap}}/N_D}$  for small gaps and not too low dopant concentrations. This estimate allows us to confirm a) the equilibrium hypothesis. Indeed, for realistic estimates of the doping concentration, the depletion width for HgTe samples is on the order of a few nanometers ( $\sim 5$  nm), i.e. electrons can actually tunnel through the depletion area. b) The electrostatic screening properties happen entirely within the bulk. The depletion width and the effective screening length remain much smaller than the sample thickness. To be more specific, let us consider a realistic HgTe sample used in this thesis: The thickness of HgTe is 67 nm. With a dielectric constant  $\varepsilon_r \approx 21$  and

<sup>10</sup>This case is also discussed in Ref.[213]

a gap on the order of 30 meV, the dopant concentration would need to be homogeneous and below  $\sim 5 \cdot 10^{15}/\text{cm}^3$  to obtain  $\delta_{\text{max}} > d_{\text{sample}}$ . Such a small carrier concentration is difficult to obtain and the precision of our measurements is not good enough to resolve features in this regime.

**Surface Fermi level in the valence band** Once the surface Fermi level lies in the valence band, a procedure exactly analogous to the previous situation can be applied. In the end, the total quantum capacitance of the bulk is given by the series contribution of three capacitances: The (minimal) value of the capacitance in situation (A), the minimal depletion capacitance, i.e.  $\varepsilon/\delta_{\text{max}}$  and a contribution from the surface hole layer. However, the model prediction for this range of  $\mu_s$  must be treated with more caution: Indeed, it corresponds to a situation in which a p-n barrier forms between the sample surface and the deep bulk. The strong confinement of holes close to the surface might lead to quantization of hole energy-levels in the surface inversion layer. In this case, the classical electrostatics used in the derivation above breaks down. It shall therefore be kept in mind that theoretical modeling of quantum capacitance on the *p*-side remains rather qualitative in this thesis.

To summarize the model calculations, Fig. 3.4 shows the evolution of the bulk's quantum capacitance over an experimentally relevant domain of surface chemical potential for a (doped) HgTe sample. Note the very low bulk doping concentration required to resolve gap-features in the C-V characteristics.

#### 3.4.4 Comment on finite temperature effects

The formulae derived above rely on the classical Poisson equation. The evaluation of the charge carrier densities is however model dependent and can be easily carried out at zero-temperature. It is also possible to tackle the finite temperature situation numerically. The details for this calculation along with a python code for the finite temperature calculations is provided in Appendix B. Taking thermal excitations into account, the model can be extended to a situation in which the Fermi level deep in the bulk lies within the band gap. Indeed, this situation cannot be described by a zero temperature model, as strictly no carriers are available for screening if the Fermi level lies in the band gap. Qualitatively, this situation is far more difficult to describe as surface band-bending will lead to an effective confinement potential close to the surface leading to quantized levels. To be fully quantitative, a self-consistent treatment of the emerging surface subbands and their back-action on the confinement potential would be necessary. This goes beyond the scope of this work.

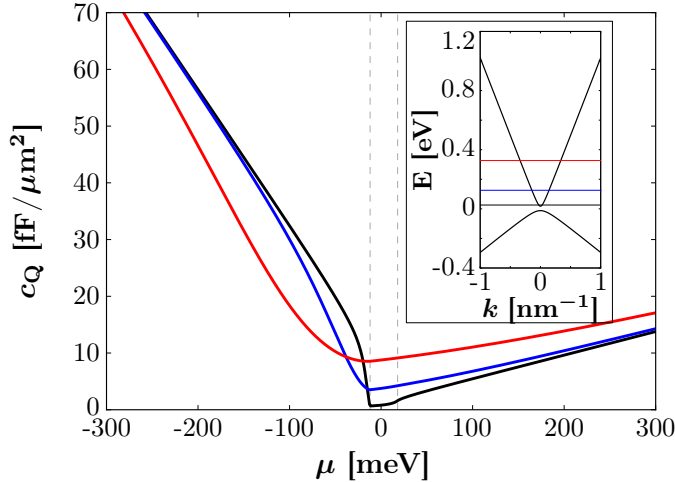


FIGURE 3.4: Calculated quantum capacitance for the bulk of HgTe for three different bulk Fermi levels (with respect to the conduction band minimum): 10 meV (black,  $\sim 0.3 \cdot 10^{16}/\text{cm}^3$ ), 100 meV (blue,  $\sim 8.1 \cdot 10^{16}/\text{cm}^3$ ), 300 meV (red,  $\sim 1.2 \cdot 10^{18}/\text{cm}^3$ ). The dashed lines correspond to valence band maximum and conduction band minimum. A three-dimensional massive Dirac dispersion was assumed for electrons and holes. The parameters for the calculations are:  $v_F^e = 1.6 \cdot 10^6$  m/s,  $v_F^h = 0.5 \cdot 10^6$  m/s,  $\Delta = 50$  meV. The band extrema are shifted to reproduce the gap of  $\sim 30$  meV. The inset shows the corresponding model 3D band-structure.

### 3.5 Dirac screening and its signatures in capacitance

The idea behind “Dirac screening” as introduced in Ref. [135] is an enhanced screening of electric field by the TSS. This causes the bulk to remain carrier-free even when the surface Fermi level rises above (falls below) the (bulk) conduction band minimum (valence band maximum). We developed a toy model for Dirac screening together with S. Tchoumakov, M.-O. Goerbig and D. Carpentier, inspired by the work of some of our collaborators on Weyl semi-metals [214]. This model will be presented in some detail in chapter 5. Within the Dirac-screening paradigm, the total quantum capacitance is equal to the surface compressibility.

### 3.6 Conclusion

As several main results of this thesis rely on the measurement of capacitances, the above considerations are of great importance for the understanding of the experimental results. Since topological insulators generally present topological surface states and bulk carriers, it is particularly important to develop a feeling for their respective contributions to the total quantum capacitance. As TSS are Dirac Fermions, it was shown in this chapter that their signature in quantum capacitance resembles that of graphene, in contrast to other (non-topological) surface states encountered in semi-conductor hetrostructures. In order

---

to assess the bulk quantum capacitance, a simple calculation for small gap (light mass) semi-conductors (like e.g. HgTe or InAs) was presented. This model complements the usual models for semiconductor capacitances that are often limited to non-degenerate semi-conductors [18]. It is therefore particularly useful for the description of heavily doped samples, i.e. HgTe films without capping layer that tend to develop n-type doping during the fabrication process or Bi<sub>2</sub>Se<sub>3</sub> flakes obtained by exfoliation or CVD-growth.

Although the model relies on a classical treatment of the electrostatics and is expected to be less adequate in the so-called inversion regime, i.e. when the surface chemical potential reaches the valence band-gap for an n-type sample, it will be seen in chapter 5 that the presented results are quantitatively adequate for the comparison between two different batches of HgTe samples: One with vanishingly small bulk doping for which the results of this chapter on 2D compressibility can be used to obtain an estimate for the TSS Fermi velocity and another batch where bulk doping leads to an additional contribution to the quantum capacitance.



## Chapter 4

# Sample fabrication and experimental techniques

A considerable amount of research on topological insulators over the last years consisted in increasing material quality in order to reduce the bulk carrier concentration and enhance the mobility of topological surface states. For the bismuth-based compounds, several routes can be followed for the material synthesis, ranging from exfoliation, over methods similar to chemical vapor deposition (CVD), i.e. solid-vapor transport or deposition (SVT/SVD) to molecular beam epitaxy (MBE). For (electronic) transport studies on mercury telluride, due to the necessary strain in order to open a transport gap, only MBE can be considered so far. These different methods will be shortly explained in the beginning of this chapter, section [4.1.1](#).

A good material quality however does not guarantee a good device performance. For electric measurements, contacts must be attached to small pieces of the material. This typically involves several steps of lithography and thus exposure to chemicals. In section [4.1.2](#), I will explain the different clean-room techniques employed in this work that allowed us to observe the results presented in chapters [5](#) and [6](#). This section is particularly useful for future studies on the investigated materials.

This thesis focuses on compressibility measurements on TI samples, carried out at finite frequency and under strong external electric fields. In order to obtain insight in the physics of the electronic motion in topological insulators under these conditions, the microscopic samples need to be connected to a measurement setup. It will be shown that low frequency measurements provide information about the equilibrium properties, i.e. the compressibility, whereas dynamical effects manifest at higher frequencies, ranging up to the GHz range. Measurements at these frequencies require a precise understanding of losses, phase shifts and parasitic contributions. All details concerning the experimental

setup, as well in the low frequency AC setup as in the microwave range are addressed in section 4.2.

## 4.1 Sample fabrication

### 4.1.1 Topological insulator synthesis

Before I explain the clean-room fabrication processes, I briefly review the main syntheses of the investigated bismuth-based and mercury telluride (HgTe) materials. It shall be pointed out that these steps of device fabrication were mostly not carried out at the LPA but by our collaborators in Würzburg, Dresden, Grenoble and at the Université Pierre et Marie Curie (Paris).

#### 4.1.1.1 Bismuth based materials

The main issue with  $\text{Bi}_2\text{Se}_3$  is a generally high bulk doping concentration, transforming the topological *insulator* to a topological *metal*, cf. chapter 2. One way of circumventing this issue consists in improving the growth conditions of  $\text{Bi}_2\text{Se}_3$  thin flakes, e.g. via SVT or SVD in a bottom-up synthesis. Another approach is to change the stoichiometry of bulk crystals in a top-down process, effectively reducing the bulk carrier concentration. Subsequently, it is advisable to thin down the crystals, e.g. via mechanical exfoliation, in order to further reduce bulk contributions. These two methods are interesting for fundamental research, as they aim at obtaining an intrinsic TI. Unfortunately, both methods yield a rather low number of samples, require time-consuming preparation and are not reproducible. This is particularly regrettable as  $\text{Bi}_2\text{Se}_3$  presents a gap of  $\sim 300$  meV, thus being in principle highly interesting for (room temperature) applications. A scalable, reliable synthesis, like MBE would therefore be of great importance. Unfortunately, we were not able to unify large scale production and reliability of the process during the preparation of this thesis, but investigated both paths. I will now present the employed methods, pointing out the “pros and cons” concerning these two requirements.

**Solid-vapor-transport and -deposition** Some results, however not presented in this thesis were obtained on thin flakes of  $\text{Bi}_2\text{Se}_3$  synthesized via SVT. These samples were grown by our collaborators from the Leibniz Institut für Festkörper- und Werkstoff-forschung in Dresden (Germany). The basic idea behind this growth technique consists in evaporation and subsequent recrystallization of  $\text{Bi}_2\text{Se}_3$  in a catalyst-free environment. Therefore, a cleaned target Si/SiO<sub>2</sub> wafer and purified  $\text{Bi}_2\text{Se}_3$  powder are placed in a

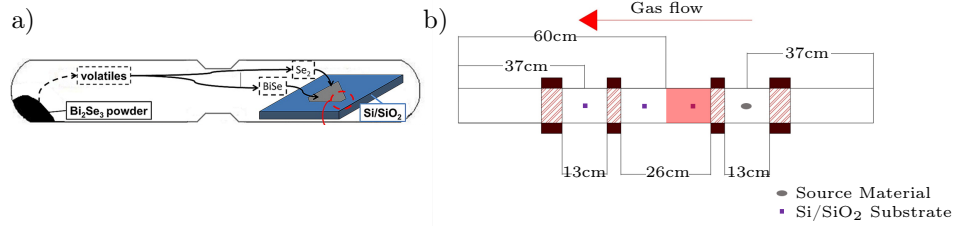


FIGURE 4.1: a) Principle of Solid-vapor transport growth in a sealed Quartz tube as carried out by our collaborators in Dresden. Adapted from Ref. [215]. b) Solid-vapor deposition growth in a tubular furnace. The Bi<sub>2</sub>Se<sub>3</sub> is transported in an Argon gas flow. Adapted from [216].

silica ampule, sealed under vacuum conditions. For practical reasons, i.e. unwanted sliding of wafer or powder within the ampule, and in order to reduce the growth rate by limiting the gas flow, the ampule is thinned between the source material and the target. Subsequently, the ampule is placed in a temperature gradient such that the source material lies in a region of high temperature exceeding the sublimation temperature, i.e. 500-600°C, whereas the target chip is maintained at 350-400°C [48] leading to deposition in mono-crystalline form. The transport of gas between the two regions follows the thermal expansion of the gaseous phase. The details of this method are explained in Ref. [215]. Interestingly, the deposited crystals form different types of structures, presumably depending on the seed defect on the SiO<sub>2</sub> and the local surface temperature. As can be seen in Fig. 4.2, the flakes are of high crystalline quality as evident from the clear 60° or 120° angles at the sample boundaries. Typical thicknesses of these flakes are comprised between 16 and 110 nm.

Inspired by a technique developed at the Hong-Kong University for Science and Technology, proving the feasibility of direct Bi<sub>2</sub>Se<sub>3</sub>-growth on exfoliated thin flakes of hBN [157], we developed a similar SVD growth technique of Bi<sub>2</sub>Se<sub>3</sub> at the Ecole Normale Supérieure (Paris) and LPA. The main effort in developing this technique was made by Jack Duffy during an internship in our laboratory. The detailed results and recipes can be found in Ref. [216]. The main difference as compared to Dresden's SVT technique consists in the growth environment. Instead of placing the source and target materials in a sealed tube, they are placed in an open tube connected to an Argon source and a filtered exhaust. The whole tube is installed in a three-zone furnace that allows us to precisely control temperature and source-target distance. It was further shown that the angle of the target substrate with respect to the gas flow, plays a crucial role [216]. Typical flake thicknesses are between 3 nm and 40 nm with lateral dimensions on the order of a few to tens of microns. However, as revealed by AFM scans, shown in the box p. 63, the top surfaces of so-obtained thin flakes are typically not atomically flat. First experimental results, presented in chapter 6 encourage however this technique to be further developed.

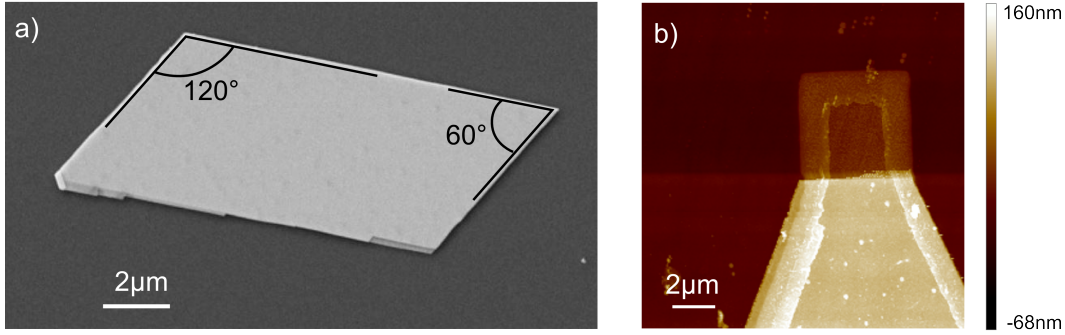


FIGURE 4.2: a) SEM image of an SVT grown  $\text{Bi}_2\text{Se}_3$  flake on  $\text{SiO}_2$  (growth in Dresden). b) AFM image of a contacted MBE  $\text{Bi}_2\text{Se}_3$ -mesa structure after defining a rectangular shape (darker part on top) via Ar-etch. The issue of cross-linked PMMA on the etch boundaries (see main text) is clearly visible.

For the analysis of our measurement, see below in section 4.2, it would be convenient to work with regularly shaped and ideally rectangular flakes. Due to the crystal structure of  $\text{Bi}_2\text{Se}_3$ , as-grown flakes tend however to be diamond shaped (Fig. 4.2). As explained in Appendix C, we can analyze the spectra of trapezoidal flakes anyway. The measurement interpretation is simplified when the width of the TI channel is constant under the gate. Therefore, we align the edge under the gate with the edge of the contact whenever possible.

**Exfoliation** Due to the layered structure of  $\text{Bi}_2\text{Se}_3$  (Fig. 2.7), this material can be exfoliated in the same way as graphene [188] in order to obtain small (ideally monocrystalline) flakes of well-defined thickness. An advantage of this top-down technique is the possibility to intentionally introduce compensating bulk dopants (i.e. electron acceptors) during the growth of bismuth-based materials in order to reduce the overall bulk doping concentration. All bulk materials used for exfoliation during the preparation of this thesis were obtained by the Bridgman growth method. For  $\text{Bi}_2\text{Se}_3$ -flakes, we exfoliated crystals obtained either by a collaboration with Ning Wang’s group at the Hong Kong University for Science and Technology or commercially acquired from HQ graphene. These samples showed no gating effect over the full range of gate voltages up to dielectric breakdown. We assume that the carrier concentrations in these samples were too high to be significantly reduced by gating. Therefore, these results will not be presented in this thesis. In order to reduce bulk conduction, the admixing of antimony and tellurium to the  $\text{Bi}_2\text{Se}_3$ -structure was shown to be successful [142]. Following this technology,  $\text{BiSbTeSe}_2$  crystals are grown by Benjamin Sacépé’s group at the Institut Néel in Grenoble (France) from whom we obtained bulk materials for exfoliation. However, in contrast to graphene or hBN (that we obtained from a collaboration with Kenji Watanabe, National Institute for Materials Science, Tsukuba, Japan), bismuth-based bulk materials tend to break into extremely small flakes ( $\lesssim 2 - 5 \mu\text{m}^2$ ) with varying thickness. A slight improvement of

TABLE 4.1: Recipe for exfoliation

step	description	tool	notes
1	substrate cleaning	acetone + isopropanol	5 min, sonicate
2	substrate cleaning	<i>Corial 200R</i> RIE O <sub>2</sub> plasma	2 min. Perform step 3 simultaneously
3	exfoliation	<i>Semiconductor Equipment Corp</i> “Blue Low Tack”	Fold adhesive tape with small bulk crystal $\sim 20$ times until a homogeneous film covers the tape.

the flake yield was obtained using an aggressive oxygen plasma-based surface cleaning prior to exfoliation. The recipe for exfoliation is found in Table 4.1. However, scotch tape cleaving was shown to increase the surface defect density, resulting for example in half-quintuple layers (QL<sup>1</sup>) steps [187, 217]. Such surface defects are proven to be particularly harmful for the surface properties, as the Bismuth atoms tend to oxidize stronger than the (intrinsic) Se-terminated surfaces [187, 218]. Transferring the exfoliation and first processing steps to a glove box with controlled inert atmosphere might lead to an improved Bi<sub>2</sub>Se<sub>3</sub>-sample performance in the future. As I show in chapter 6, the direct growth on hBN leads to a significantly improved surface quality.

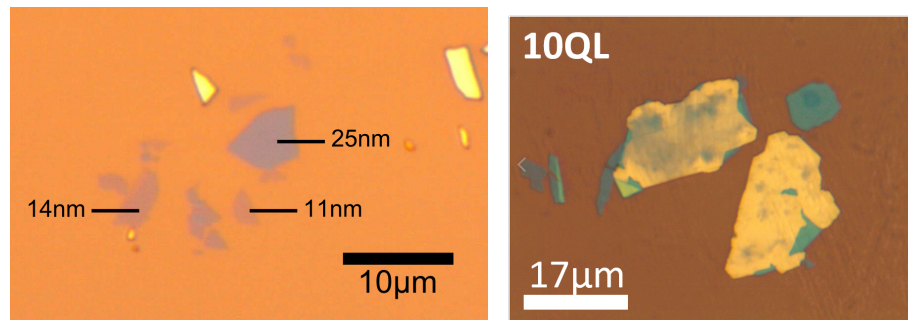
**Molecular beam epitaxy** For the scalability of bismuth based TI devices, a large scale production of thin films is required in the future. Our collaborators from the Institut des Nanosciences de Paris, Mahmoud Eddrief and Paola Atkinson, grow these films on (111) oriented GaAs substrates. As shown by Raman spectroscopy, the growth conditions are sufficiently controlled to obtain a precise number of QLs [219]. The details of MBE growth can be found in the same reference. In a magneto-optics study at LPA, T. Phuphachong, Y. Guldner and L.-A. de Vaulchier showed that the intrinsic carrier concentration of these MBE grown films can be minimized by post-annealing under Se flux for one hour at the growth temperature and maintaining the Se flux during cool-down [220]. Although several devices were fabricated from these thin MBE films, their performance in the electrical measurements remained poor. The main reason for this lies presumably in an etch-related problem that will be addressed below in section 4.1.2. The regime of 3D TI is expected to persist only for films with a thickness exceeding  $\sim 6$  QLs, on the other hand thin films are required in order to limit the total contribution of bulk carriers to electric conduction. In the beginning phase of MBE growth, the thin film

<sup>1</sup>As explained in chapter 2, 1QL  $\approx 1$  nm.

begins to grow at different sites forming triangular terraces, reminiscent of the underlying crystal structure. These islands connect at some points, forming the different QLs of the final sample. However, the initial growth morphology tends to propagate through the full thickness of the sample, forming triangular shaped pyramidal structures [197, 221]. The terraces of these pyramids are typically one QL high, confirming the QL per QL growth of the crystal. However, these defects show that even if the growth yields in principle a QL-per-QL growth, the total thickness corresponds only to an average. Moreover, these defects might lead to oxidization issues like described for the exfoliation and enhanced electron scattering for the TSS.

### Characterization methods:

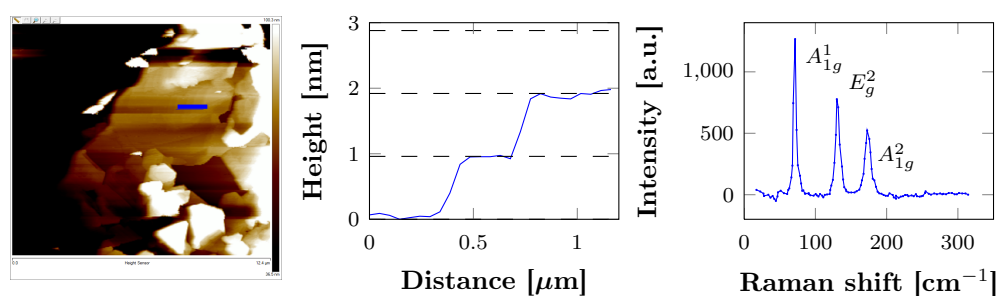
**Optical microscopy:** After exfoliation or crystal growth, flakes of thin layers of  $\text{Bi}_2\text{Se}_3$  are identified and localized with respect to the reference grid (see main text, p. 67) using an *Olympus BX51* microscope with a mounted *ALTRA20* CCD camera. Thin flakes, up to roughly 10-25 nm show a rather blueish color, whereas thicker flakes become more reflective and their color turns to orange, yellow and golden for samples thicker than 100 nm.



Left: Exfoliated flakes of different thickness. Right: 6 QL  $\text{Bi}_2\text{Se}_3$  grown on hBN.

**Atomic force microscopy:** In order to identify the exact thickness of thin flakes, area scans are performed using a commercial *Veeco Dimension edge* AFM. The QL growth can be checked by measuring a step height.

**Raman spectroscopy:** The LPA recently acquired a commercial microraman spectroscopy tool (*Renishaw inVia*). The in-plane ( $E_g^2$ ,  $\sim 131 \text{ cm}^{-1}$ ) and out-of-plane vibrational modes ( $A_{1g}^2$ ,  $\sim 173 \text{ cm}^{-1}$ ) are characteristic of  $\text{Bi}_2\text{Se}_3$ , Ref. [157].



Left: AFM height mapping of  $\text{Bi}_2\text{Se}_3$  grown on hBN. Middle: Height profile along the blue line in the left figure (dashed lines correspond to 0.96 nm, i.e. 1 QL). Right: Raman spectrum of a similar sample.

#### 4.1.1.2 Strained three-dimensional mercury telluride

As explained in chapter 2, bulk HgTe is a semi-metal. Even though the band-inversion between  $\Gamma_6$  and  $\Gamma_8$  bands is sufficient for the emergence of surface states, they are energetically buried within bulk bands and thus hardly visible in transport. In order to obtain a topological insulator, a gap between  $\Gamma_8$  heavy hole and electron band must be opened. This is achieved by growing strained HgTe films on CdTe. The growth of strained HgTe layers was carried out by Christopher Ames, Raimund Schlereth supervised by Christoph Brüne and Hartmut Buhmann, our collaborators from the Molenkamp-group at the Julius-Maximilians-Universität, Würzburg, Germany. Details on growth conditions, strain-engineering etc. are far beyond the scope of the present thesis. I will therefore only present the main features of the growth techniques and invite the interested reader to find further details in Ref. [222].

Commercial CdTe (*JX Nippon*, 800  $\mu\text{m}$  thickness, surface roughness  $\sim 0.3\text{ nm}$  [222]) is used as a substrate material and cleaned in HCl, prior to mounting on a molybdenum block with liquid Ge [222]. The whole system is transferred in an ultra-high vacuum (UHV) chamber (base pressure  $\sim 10^{-10}$  Torr). In order to further flatten the CdTe surface, a 40 nm MBE buffer layer is grown ( $T = 315^\circ\text{C}$  [222, p.61]). In principle, tensile strained HgTe layers are obtained by growing directly on CdTe up to thicknesses on the order of 155 nm [222]. However, our collaborators observed that the intrinsic carrier density can be reduced and the mobility significantly enhanced by growing on a cadmium mercury telluride (CMT,  $\text{Hg}_{0.3}\text{Cd}_{0.7}\text{Te}$ ) buffer layer. In our case, this layer is 43 nm thick. Subsequently 67 nm of HgTe were grown (at  $T = 180^\circ\text{C}$  [222]). Within this work, two types of samples were studied. Sample “A” was removed from the UHV conditions immediately after HgTe growth. For sample “B” a capping layer of CMT (5nm) was grown afterwards. This layer protects the sample surface from a) diffusion of Hg out of the material, b) surface oxidation, c) surface contamination during lithography steps for sample fabrication. The thickness is controlled via  $\omega - 2\Theta$  high resolution x-ray diffraction scans [222].

#### 4.1.2 Device fabrication of radio-frequency metal-insulator-topological insulator capacitors

For compressibility measurements, the capacitance of a metal-insulator-topological insulator structure has to be measured. We are particularly interested in the high frequency response of the material, in order to simultaneously measure conductance and capacitance in a quasi-equilibrium situation. This leads to two very important considerations for the general sample design: First, it should be as simple as possible in order to limit

parasitic contributions, e.g. from stray capacitances. Second the capacitance structure should be embedded in a coplanar waveguide (CPW) in order to ensure a good coupling of the probing microwave (MW) field between cables and embedded device. In the following, I will first explain the implications of these two requirements, before I provide the “recipes” for the sample fabrication of HgTe, Bi<sub>2</sub>Se<sub>3</sub> and BiSbTeSe<sub>2</sub> MITI capacitors.

#### 4.1.2.1 Choice of substrate

TABLE 4.2: Different substrates and their characteristics

Purpose	Material	Thickness [ $\mu\text{m}$ ]	Resistivity [ $\Omega\cdot\text{cm}$ ]	Dielectric constant
Exfoliation, SVT, SVD (bismuth based samples)	Si/SiO <sub>2</sub> ( <i>Applications couches minces</i> )	500/0.280	>3000	11.8/3.8
MBE growth of strained HgTe	CdTe ( <i>JX Nippon</i> )	800	20 <sup>2</sup>	10.2 [223]
MBE growth of Bi <sub>2</sub> Se <sub>3</sub>	GaAs single crystal ( <i>AXT, Inc.</i> )	350	> $8.5 \cdot 10^7$	13

The objective of high frequency measurements restricts the choice of the substrate: As the measurement setup is suited for measurements up to 40 GHz, a conductive substrate would strongly decrease the upper frequency bound due to parasitic coupling between CPW and conducting substrate layer. This rules out most back-gating experiments where a conducting substrate is used as a global gate electrode. Fortunately the CdTe substrates (gap = 1.56 eV) required for the synthesis of strained HgTe meet this requirement. For the bismuth-based materials obtained by either SVT-, SVD-growth or exfoliation, we used a highly resistive Si wafer with thermally grown 280 nm thick, polished SiO<sub>2</sub> surfaces. For MBE growth of Bi<sub>2</sub>Se<sub>3</sub>, single crystals of GaAs cut into polished wafers were used. The physical properties of the involved substrates are summarized in table 4.2. For exfoliation or non-MBE growth, the sample positions on the substrate are non-reproducible and therefore require a grid, typically defined by optical lithography, see Ref. [224] for details. This grid facilitates navigation on the sample surface. However, the arbitrary shape of flakes obtained by these methods requires adapting the contact geometry to each flake. Hence, e-beam lithography is used as a convenient tool, see p. 72 for details.

<sup>2</sup>Data from substrate provider only available at room temperature. At low temperature, the resistivity is likely to be much higher.

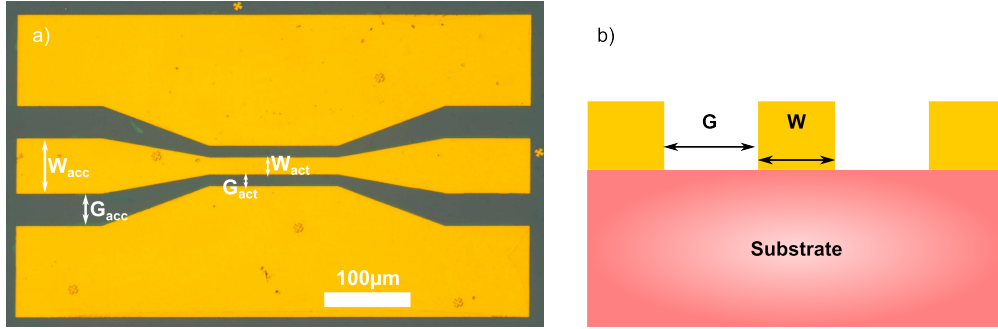


FIGURE 4.3: a) Optical microscope image of a CPW through-line on Si/SiO<sub>2</sub> substrate. Also seen are the alignment marks for e-beam lithography (small crosses on top and to the right of the CPW). b) Schematic side view of a CPW.

As e-beam lithography relies on the emission of high-energy electrons onto the sample, (very) high resistive substrates cause surface charging that deviates the electrons and results in extremely poor resolution. The substrates cited in table. 4.2 were sufficiently conductive for 20 keV electrons to be e-beam lithography compatible. However, several lithography tests on sapphire substrates failed due to this problem. Furthermore, the standard procedure of covering an insulating substrate with a thin layer of Al on top of the PMMA during lithography and subsequently removing it in a KOH-solution is incompatible with Bi<sub>2</sub>Se<sub>3</sub>, as I will explain below.

#### 4.1.2.2 Coplanar wave-guide designs

The electrical measurements require a connection between the microscopic sample and the macroscopic measurement setup, described in sec. 4.2. In order to probe the physical properties of the material at radio frequencies, the sample is embedded in a coplanar wave-guide (CPW), optimized to match the 50 Ω impedance of our high frequency setup. A side-cut and a top-view of such a structure is shown in Fig. 4.3. The optimization of the CPW is subject to some boundary conditions that are defined by the inter-tip distance of the RF-probes (pitch) and the actual width of the investigated sample structure. The pitch of 100 μm and the typical sample width of 20 μm leave therefore the gap/width ratio as free parameter to optimize the transmission through the CPW. We optimize independently the impedance-match of the access area and the active region and design a linear interpolation between these two regions in order to avoid microwave reflections from abrupt geometry changes. The characteristic impedance of the CPW does however also depend on the dielectric constant of the underlying substrate. The CPW dimensions on the Si/SiO<sub>2</sub> substrates were optimized by former students in the laboratory [224, 225]. It turns out that the same geometry works well on GaAs (transmissions  $\gtrsim 97\%$  over 0-40 GHz). For the design on CdTe, we first calculated geometrical parameters using HP's *AppCAD* software before we fabricated nine different CPW with varying

TABLE 4.3: Dimensions for optimized CPWs.

Substrate	$W_{\text{acc}}$ [ $\mu\text{m}$ ]	$G_{\text{acc}}$ [ $\mu\text{m}$ ]	$W_{\text{act}}$ [ $\mu\text{m}$ ]	$G_{\text{act}}$ [ $\mu\text{m}$ ]
GaAs, Si/SiO <sub>2</sub>	70	40	21	10
CdTe	72.5	35	23	9.15

central conductor width while keeping the total width of the central region (gap+width) constant. S-parameter measurements, revealed that a central conductor of 23  $\mu\text{m}$  width yields the best transmission ( $96.1 \pm 1.5\%$ ) averaged over the full 40 GHz broadband range, cf. Fig. 4.11 below. The optimized CPW-dimensions are found in Table 4.3. The phase velocity on these CPW is  $\sim 0.37 \cdot c$ .

#### 4.1.2.3 Fabrication of Bismuth-based devices

**A coordinate system** Exfoliated or SVD/SVT synthesized Bismuth-based flakes need to be identified and thickness-characterized using an optical microscope and AFM (see the box, p. 63). Therefore a grid of gold crosses is defined by optical lithography and Joule evaporation of Cr/Au. These serve as a coordinate system for the localization of flakes and the alignment of e-beam lithography masks in the subsequent contact patterning.

**Localization** If these gold crosses are added to the substrate prior to the SVD process, Bi<sub>2</sub>Se<sub>3</sub> crystals grow abundantly on these Au crosses. However, the crystal growth initiated on these surface “defects” is rather multi-crystalline and unsuitable for further processing. Depending on the local surface temperature, some crosses also tend to melt and be removed during growth. One route to overcome these issues consists in adding the alignment marks after growth, which might however lead to surface contamination of the Bi<sub>2</sub>Se<sub>3</sub> flakes.

**To etch or not to etch?** Designing the sample geometry as simple as possible simplifies the analysis of measurement data, especially in the high-frequency limit. Therefore, it is *a priori* preferable to define a rectangular TI channel under the gate electrode, requiring an etching step. This is particularly true for MBE grown thin films where the film must be patterned in order to avoid short circuits. However, the etch rate of Bi<sub>2</sub>Se<sub>3</sub> under Ar plasma in our *Corial* RIE system is only on the order of  $\sim 6$  nm/min, leading to rather long etch times even for thin samples. Furthermore, the PMMA resist cross-links during exposure to the high-energetic Ar ions, presumably due to over-heating. This typically leads to a very rough sample surface especially along mask edges, cf. Fig. 4.2

b). The lift-off of these cross-linked zones rapidly becomes impossible. A way to improve the lift-off was to perform a buffered etch, alternating etch phases (10 s) with cool-down phases (30 s), during which the plasma was switched off. Further ideas to overcome this “etch-issue” consisted in a) using multi-layer resist stacks, b) using trichloroethylene as an aggressive solvent, c) “brushing” the sample with a cotton swab, etc. Seemingly violent, the “brushing method” turned out to work best, although such mechanical methods risk to lead to a surface degradation or – worse – a complete detach of flakes. Another route was to use an Aluminum hard mask (defined by lithography and Joule evaporation), removed in KOH after the etch. We observed however a drop in Bi<sub>2</sub>Se<sub>3</sub> resistance by a factor 100 after short exposure to KOH, indicating an unwanted chemical reaction. As all these techniques did not lead to convincing results, we decided to investigate grown and exfoliated flakes *as-synthesized*.

### Reactive Ion Etch

In order to define mesa structures on MBE-grown Bi<sub>2</sub>Se<sub>3</sub> films or to define a rectangular channel on flakes, we employed a physical etch in Ar plasma. For the removal of HfO<sub>2</sub> in the contact and CPW areas, we used a SF<sub>6</sub> etch. Both etch methods were carried out in a *Corial 200R* reactive ion etch (RIE) system. The parameters are listed in the following table.

Material	gas	pressure	gas flow	RF Fwd Power
Bi <sub>2</sub> Se <sub>3</sub>	Ar	50 mTorr	40 sccm	85 W
HfO <sub>2</sub>	SF <sub>6</sub>	7.0 mTorr	25 sccm	70 W

### Dielectric

**hexagonal Boron Nitride** Due to its atomical flatness exfoliated hexagonal Boron Nitride (hBN), is a good material not only as a “substrate” for van-der-Waals epitaxy as described in section 4.1.1.1, see also Ref. [157], but also as a gate dielectric. Furthermore, transfer techniques for hBN have been previously developed, adapted and optimized at the LPA [224–228] making it possible to place thin layers of hBN with 1-2 μm precision on flakes of Bi<sub>2</sub>Se<sub>3</sub>. The dielectric constant of hBN deposited by dry-transfer, measured in a metal-hBN-metal capacitor geometry in our laboratory was on the order of  $\epsilon_r \approx 2.7$ –3.2 on several samples. The discrepancy with the value found in literature ( $\epsilon_r \approx 4$  [229]) might be explained by the inclusion of small vacuum/air layers due to surface roughness or a size effect. Indeed, for several dielectric materials, a decrease of the dielectric constant in the thin-film limit has been reported [230, 231]. We used exfoliated hBN

flakes obtained from high-quality hBN-crystals grown in Watanabe and Taniguchi [232]. The dielectric strength was reported to lie in the range of 1-2 V/nm [229].

**Hafnium oxide** For some Bi<sub>2</sub>Se<sub>3</sub>-samples<sup>3</sup> and the HgTe samples (see below), we chose atomic layer deposition (ALD)-grown Hafniumdioxide (HfO<sub>2</sub>) as gate dielectric due to its reported high breakdown fields ( $\sim 0.6$  V/nm [233]) and its large dielectric constant ( $\epsilon_r \approx 23$ , [234, 235]). It was shown in Ref. [236] that depending on the preparation of the HfO<sub>2</sub> layer, this dielectric constant varies between 26 and 16 as a function of frequency between quasi-DC and 1 MHz. Neumaier *et al.* at AMO GmbH (Germany) measured a dielectric constant  $\epsilon_r = 11.7$  [237].

After contacting Bi<sub>2</sub>Se<sub>3</sub>-flakes, such a HfO<sub>2</sub> was grown at the Laboratoire de Photonique et de Nanostructures (LPN) at Marcoussis, France. We measured the dielectric constant for this growth method of HfO<sub>2</sub> in a metal-oxide-metal structure and found  $\epsilon_r = 12$ . For these samples, the contact electrode was added to the flake prior to thin oxide growth as explained in the next paragraph.

For ALD growth, the growth chamber is pumped below 0.1 Torr and then purged with Ar. Throughout the following steps, the Ar flow is fixed at 230 sccm and the pump rate is adjusted in order to keep the growth chamber at 0.1 Torr. As a first precursor, H<sub>2</sub>O gas is introduced into the chamber forming a thin water film on the sample surface with a hydroxide termination. The (gaseous) water molecules are pumped out of the chamber and the chamber is flushed with Ar. Then, Tetrakis(dimethylamido)hafnium(IV) (TDMAH) is introduced into the chamber, reacting with the hydroxinated termination, forming Hf-O bounds and liberating ethylamine as a byproduct. The NC<sub>2</sub>H<sub>6</sub> terminated surface self-limits this layer's growth. Again, the chamber is purged with Ar gas before a second cycle is started. The exact time constants of the different steps are summarized in table 4.1.2.3

---

<sup>3</sup>Experimental results not presented in this thesis

Thin HfO<sub>2</sub> layers are grown using Atomic layer deposition as well for the Bi<sub>2</sub>Se<sub>3</sub> as for the HgTe samples. However, the growth techniques vary slightly for the two types of samples. For Bi<sub>2</sub>Se<sub>3</sub> samples, the growth was carried out at the LPN in a commercial Cambridge NanoTech - Fiji system. Growth temperature was 150°C. 85 cycles were used in order to obtain a total film thickness of about 10 nm.

The ALD chamber in Würzburg is relatively large, which requires longer purging times. In order to reduce the Hg-diffusion, c.f. main text, the temperature is kept at 35°C. Only 45 cycles are used, resulting in an oxide thickness on the order of 7-10 nm.

#### Parameters for ALD growth of HfO<sub>2</sub>

Step	Molecule	Bi <sub>2</sub> Se <sub>3</sub> -samples	HgTe-samples
1	TDMAH	0.25"	0.2"
2	Purge with Ar gas	30"	200"
3	H <sub>2</sub> O	0.06"	10"
4	Purge with Ar gas	30"	200"

One important advantage of ALD with respect to other thin dielectric layers is its isotropic growth (*conformity*), Ref. [238], i.e. also the side edges of the flakes are covered by the dielectric. However, the conformity renders a lift-off procedure rather difficult: The acetone does not enter in contact with the resist. Furthermore, due to the relatively high temperature and the need of keeping the growth chamber as clean as possible, we ruled out the idea of using lithography for the Bi<sub>2</sub>Se<sub>3</sub>-samples in order to define the growth area of HfO<sub>2</sub>, but proceeded to a “global” growth instead. Thus, after the HfO<sub>2</sub> growth, the area of the CPW where the probe tips are going to be placed is also covered with an insulating layer. We solve this issue as explained in the following.

**Defining the gate electrodes and coplanar waveguides** For the hBN technology, gate, contact and CPW electrodes are defined within a single e-beam lithography step. Prior to Ti/Au contact deposition in the Plassys evaporator at the Université Paris-Diderot, a short Ar plasma is applied *in-situ* to improve access resistance. If this short plasma thins the hBN layer, the etch rate is too slow to be detectable by our AFM setup.

For the HfO<sub>2</sub> samples, prior to oxide growth, the contact electrode is defined via e-beam lithography and the aforementioned short-etch metal deposition. After oxide growth, we use MAN2405 as a *negative* photoresist in our e-beam lithography in order to define a mask for the etching of HfO<sub>2</sub> in the CPW areas (away from the flakes). The details for using this resist are given in table 4.4. After lithography and development, the resist

TABLE 4.4: Recipe for the negative photoresist MAN2405 used for the definition of an etching mask for the HfO<sub>2</sub> etch.

Step	Description	Tool	Notes
1	Sample cleaning	Acetone + IPA	~ 1'00" each.
2	Spin coating	Spin coater and MAN2405	30", 4k rpm, 4k rpm/s → ~500 nm.
3	Baking	Heating plate	1'00" @ 90°C
4	e-beam lithography	<i>Raith e-Line</i>	7.5 μm aperture, 20 kV, Dose: 300 μC/cm <sup>2</sup>
5	Developing	AZ-726 MIF & H <sub>2</sub> O	Develop 1'00" in AZ-726 MIF. Rinse in H <sub>2</sub> O.

covers the active zone of the device, i.e. the region with Bi<sub>2</sub>Se<sub>3</sub>. The HfO<sub>2</sub> is etched following the protocol described on p. 68. We achieve an etch rate of ~10 nm/min. The sample is over-etched for about 10 seconds in order to ensure a good contact between the following layers and the existing contact structure. Afterwards, as a last fabrication step, we use again e-beam lithography in order to define the gate electrode and the CPW. For this last step, we evaporate Cr(~1.5 nm)/Au(~200 nm) using either a custom-made evaporator or a commercial *Edwards* Joule evaporator at the LPA.

### e-beam lithography

Patterning of contacts and gate on thin flakes was performed by e-beam lithography in a *Raith e-line* scanning electron microscope at the LPA. For precise alignment of the contacts with the micron-sized crystals, we developed a *one-lithography* precision alignment protocol. Instead of placing small alignment crosses via coarse alignment using the reference grid with subsequent metalization (cf. Ref. [224] for this technique), we pattern small crosses in the PMMA resist, develop according to the protocol defined in the following table, and then *reload* the sample into the SEM. The lithography defined crosses are sufficiently precise to obtain alignment on the order of  $<200$  nm.

### e-beam lithography with alignment

step	description	tool	notes
1	localization of flakes	optical microscope	Save coordinates, align mask with optical image in $100\times$ magnification
2	characterization	AFM (+ Raman)	Identify exact layer thickness
3	surface cleaning	acetone and IPA	no ultrasound cleaning in order to avoid flake detach
4	spin coating	<i>Süss</i> spin coater and 950 PMMA AZ6 ( <i>MicroTech</i> )	30 s, 4k rpm, 4k rpm/s
5	baking	heater plate	8 min, $160^\circ\text{C}$
6	e-beam lithography	<i>Raith e-line</i>	20 kV, $280 \mu\text{C}/\text{cm}^2$ , Aperture: $7.5 \mu\text{m}$ , define crosses spaced by $80\times 80 \mu\text{m}^2$ around the flake
7	develop	MIBK + IPA	90 s MIBK:IPA(1:3)+90 s IPA
8	align image	optical microscope	align optical image in $500\times$ magnification with <i>e-line</i> mask.
9	e-beam lithography	<i>Raith e-line</i>	20 kV, $280 \mu\text{C}/\text{cm}^2$ , Aperture $7.5 \mu\text{m}$ : define fine contacts; $120 \mu\text{m}$ : CPW
10	develop	MIBK + IPA	90 s MIBK:IPA(1:3)+90 s IPA

### Metalization of bismuth based devices

For the contacts on the bismuth-based samples, a short etch *in-situ* using an Ar plasma in a commercial *Plassys MEB 550S* e-gun evaporator turned out to improve contact resistance. Good results ( $R_{\text{access}} \approx 500 \Omega \cdot \mu\text{m}$ ) were obtained with an 8 second etch using the following parameters:  $I_{em} = 80 \text{ mA}$ ,  $V_{ann} = 350 \text{ V}$ ,  $V_{acc} = -50 \text{ V}$ , Ar flow: 5 sccm.

#### Parameters for e-gun (contact) metalizations:

step	metal	pressure	current	rate	thickness
1	Ti	$3.2 \cdot 10^{-7} \text{ mbar}$	40 mA	0.05 nm/s	4 nm
2	Au	$5.0 \cdot 10^{-7} \text{ mbar}$	220 mA	0.2 nm/s	$\sim 200 \text{ nm}$

#### Parameters for Joule (gate + CPW) metalizations:

step	metal	pressure	current	rate	thickness
1	Cr	$10^{-5} \text{ mbar}$	$\sim 90 \text{ A}$	0.01 nm/s	2.5 nm
2	Au	$10^{-5} \text{ mbar}$	120 A	0.2 nm/s	$\sim 200 \text{ nm}$

#### 4.1.2.4 Fabrication of HgTe devices

As Hg tends to diffuse out of the HgTe crystal structures for temperatures exceeding  $\sim 100^\circ\text{C}$  [222], all fabrication steps need to keep the sample below this temperature. Our collaborators in Würzburg have several years of experience in sample fabrication and continue to improve these procedures. I designed the masks for optical lithography, but the sample fabrication was mainly carried out by Kalle Bendias in Würzburg whose thesis is to appear next year and will contain further information about the exact protocols. For completeness, I describe his recipe for the fabrication of HgTe-based MITI Caps in the following.

**Sample preparation** Before each fabrication step, the sample is cleaned in Acetone (with ultrasonic treatment), IPA and deionized water (DIW).

**Mesa etching** As for MBE-grown  $\text{Bi}_2\text{Se}_3$  samples, the first fabrication step is the definition of the 3D TI channel. Two procedures of mesa etching were developed, based on a) ion milling and b) chemical etching. The former is an anisotropic etch, therefore defines steep edges and the etching can be controlled by reflectance of light on the sample

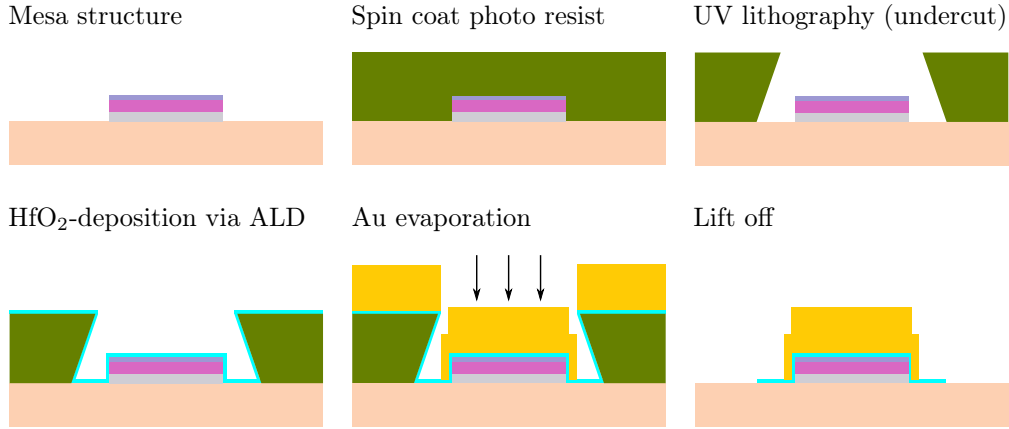


FIGURE 4.4: Fabrication steps of self-aligned gates (not to scale). The photoresist presents a strong undercut. The conformal ALD growth results in an  $\text{HfO}_2$  layer covering the undercut area. The evaporation of Au (gate electrode) is anisotropic which ensures the  $\text{HfO}_2$  to cover a larger area than the electrode (thus avoiding shorts). As the ALD layer is much thinner than the photoresist layer, a lift-off is possible.

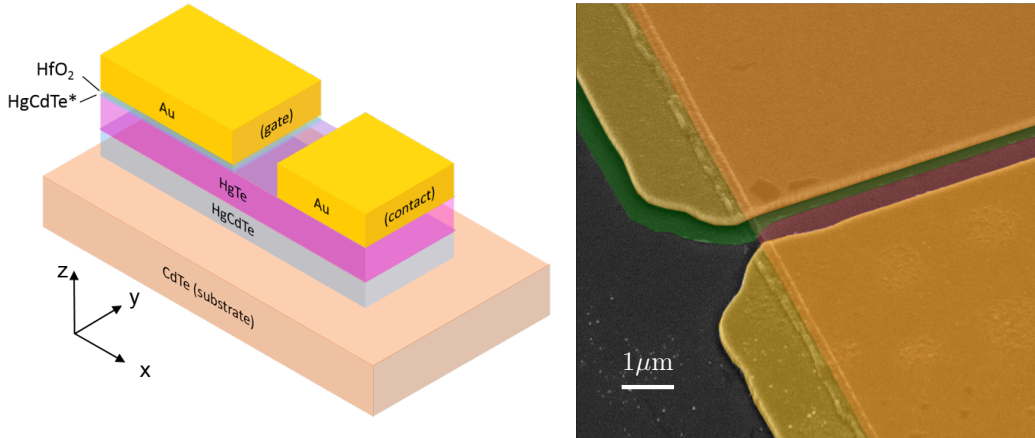


FIGURE 4.5: Left: Artist view of a HgTe-based metal-oxide-TI capacitor. The HgCdTe capping layer is not present for the uncapped sample. Right: False color SEM image of the capacitor structure, showing the HgTe layer (purple), the contact electrode (bottom, orange) and the self aligned gate stack with the  $\text{HfO}_2$  layer (green) and the electrode (top, orange).

surface. However, the same problem as for  $\text{Bi}_2\text{Se}_3$ -etching described above occurs: The photo-resist tend to cross-link. In Würzburg, this problem could be resolved by an additional cleaning step, cf. the box on p. 77. The second method does not lead to cross-linking of the photo-resist, but the isotropy of the etch leads to formation of a trench close to mask-edges. Furthermore, the etch rate has to be determined by trial-and-error. In both cases, the mask is defined using a *positive* photo-resist, cf. p. 77 for details.

**Contacting** The next fabrication step is the definition of the contact at one end of the channel. To improve the contact resistance, the metal composition is Ge/Au, renowned to yield ohmic contacts. Prior to metal deposition a short ion milling (same parameters as for mesa etching, cf. p. 77 and reduced 8 sec. etch-time) cleaning of the contact area

is performed. The sample is transferred under vacuum conditions (*in-situ*) to the e-gun evaporation chamber.

**Gate definition** The gate is formed by stacking of a thin insulating layer ( $\text{HfO}_2$ ) and a gate electrode over the remaining HgTe channel. For subsequent contacting of the CPW on the predefined contact electrode, the ALD growth is limited here to the channel area via photo-lithography. The gate electrode and the  $\text{HfO}_2$  layer are self-aligned as follows: The negative photo-resist shows an undercut of  $\sim 400$  nm after exposure. As the ALD-growth (cf. the table p. 70 for details) is conformal, it covers the HgTe in this undercut region, cf. Fig. 4.4. After ALD growth, the same mask is used for the evaporation of the gate electrode. As the evaporation is highly anisotropic (the evaporated atoms are vertically incident on the sample surface), the gate electrode does not form in the undercut region. Although the ALD is conformal, due to the very small thickness of the  $\text{HfO}_2$  layer, a lift-off in acetone is possible. A false-color scanning electron microscope image of the self-aligned gate on top of the HgTe mesa is shown in Fig. 4.5.

**CPW** The lithography and metalization of the CPW is analogous to the contact fabrication, leaving out the etch step.

**Photoresists**

For etching purposes a positive resist is used, for metal deposition and ALD, a negative resist. The recipes for both resists are summarized below.

**Positive photo-resist**

step	description	tool	time	details
1	Spin coating	<i>MicroChemicals ECI 3012</i>	20 s	6k rpm
2	Baking	heating plate	2 min	80°C
3	Exposure	Hg-steam lamp	5-6 s	
4	Develop	<i>AZ 726 MIF</i>	22 s	rinse in DIW

**Negative photo-resist**

step	description	tool	time	details
1	Spin coating	<i>AllResist ARN4340</i>	20 s	6k rpm
2	Baking	heating plate	2 min	80°C
3	Exposure	Hg-steam lamp	20 s	
4	Re-Bake (resist reversal)	heating plate	6 min	80°C
5	Develop	AR 300-47	45 s	Rinse in DIW

### Etching of HgTe Mesa-structures

For both etch procedures, the mask is defined using positive photo-resist, cf. the table on p. 76.

#### Ion milling

step	description	tool	time	details
1	Etching	Ar plasma	2-3 min	$V = 1\text{ V}$ , $V_{grid} = 1\text{ kV}$ , $I = 8\text{ mA}$
2	Lift off	Acetone	5 min	50°C, Ultrasonic treatment, then IPA rinse
3	Lift off	<i>Technistrip</i> <i>P1316</i>	2 min	50°C, DIW rinse

#### Wet etch

step	description	tool	time	details
1	Etching	$\text{K}_{4.15\text{ g}}:\text{I}_{0.1\text{ g}}:\text{HBr}_{4.15\text{ g}}$ in 50 ml DIW. Dilute in 1:8 with DIW.	35 s	under constant flow using a tube pump
2	Lift off	Acetone	5min	room temperature, IPA+DIW rinse

### Metalizations of HgTe-devices

After metal deposition a lift-off in acetone at 50°C with subsequent IPA and DIW rinsing is performed.

#### Parameters for contact and CPW metalizations:

step	metal	current	velocity	thickness
1	Ge/Au	400-600 mA	0.7 nm/s	50 nm (contact); 200 nm (CPW)
2	Au	500-700 mA	0.7 nm/s	50 nm (contact); 200 nm (CPW)

#### Parameters for gate metalizations:

step	metal	current	velocity	thickness
1	Ti	~200 mA	0.8nm/s	10 nm
2	Au	500-700 mA	0.7 nm/s	90 nm

## 4.2 Experimental techniques

In the following section, I will present the small signal equivalent circuit of the investigated MITI capacitors and the experimental setup used for their characterization.

### 4.2.1 Small signal response of a metal-insulator-TI Capacitor

The basic design of the studied MITI-Cap structures is represented in Fig 4.5. One plate of the capacitor is formed of a metallic gate electrode, the other by the material under investigation, i.e. the TI. The two capacitor plates are separated by a thin dielectric layer and the TI is contacted on one side with a metallic contact. If the height and width of the TI conductor under the gate electrode is constant, the charge dynamics can be described by a simple 1D model. In this case, the small signal equivalent circuit is given by a distributed RC-line represented in Fig. 4.6. Note that our small-signal model accounts also for a finite access resistance that describes the (resistive) charge transfer between metal and TI. In the following, lower case  $r = R/L$  and  $c = C/L$  stand for resistance and (total) capacitance per unit length, respectively. The quantum corrections to  $c$  have been discussed in chapter 3. The admittance  $Y(\omega)$  (i.e. the complex conductance as a function of frequency) of such a distributed RC line (without the access resistance) can be calculated analytically, cf. Ref. [224] and appendix C:

$$Y(\omega) = \frac{ik}{r} \tanh(ikL), \quad (4.1)$$

where

$$k = \sqrt{-irc\omega} \quad (4.2)$$

is a complex wave vector taking into account the propagation (real part) and the damping (imaginary part) due to dissipation in the resistive elements.

To gain insight in this expression, let us study the low frequency behavior:

$$\begin{aligned} Y(\omega \approx 0) &\approx i\omega cL + \frac{1}{3}L^3 r (c\omega)^2 + \mathcal{O}(\omega^3) \\ &= i\omega C + \frac{1}{3}R(C\omega)^2 + \mathcal{O}(\omega^3). \end{aligned} \quad (4.3)$$

The imaginary part (out-of-phase component) of the low frequency admittance is therefore used to extract the total capacitance. The real part (in-phase component) contains a mixed information about the capacitance and the resistance. The capacitance per unit area and sheet resistivity of the sample can be calculated according to  $c_{\square} = C/(L \cdot W)$  and  $r_{\square} = R \cdot W/L$ . From this we can deduce the (sheet) conductivity  $\sigma = 1/r_{\square}$ . For

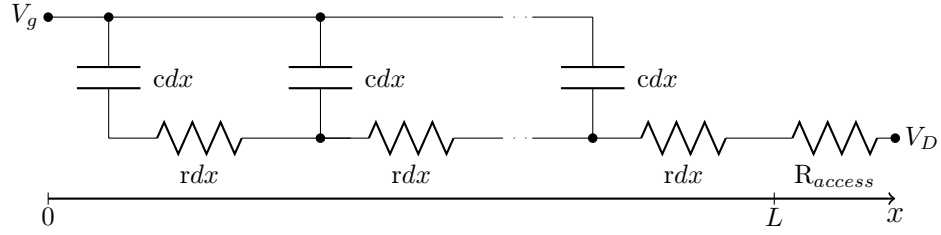


FIGURE 4.6: Small signal equivalent circuit of a metal-insulator-TI capacitor.

(very) low frequency Lock-in measurements (typically in the kHz range), the signal is dominated by the imaginary part, i.e. it yields only information about the capacitance.

From the perspective of electromagnetic fields, the RC line damps an incident wave, i.e. the wave is evanescent within the line. At high frequencies, this regime is characterized by an asymptotic  $\sqrt{\omega}$  law for both, real and imaginary part. More precisely

$$Y(\omega) \sim (1 + i)\sqrt{\frac{c\omega}{2r}}. \quad (4.4)$$

Note that – reminiscent of the evanescent wave character – this asymptotic behavior is independent of the sample length.

Further information can be extracted from the frequencies for which the imaginary part and the real part are equal. They are given by:

$$\omega_n = \frac{\pi^2}{2crL^2}n^2, \quad (4.5)$$

where  $n$  is a natural. The lowest (non-zero) frequency ( $\omega_1 \propto 1/(RC)$ ) is also called the cut-off frequency [224]. Experimentally, besides the asymptotic behavior at large frequencies, the ratio of  $\omega_2/\omega_1 = 4$  can be used as a clear confirmation of the 1D line model.

**Effect of the finite access resistance** Due to work-function mismatch and microscopic details of the contact-TI junction, the charge transfer between electrode and TI is dissipative, taken into account as a finite (lumped) resistance  $R_{\text{access}}$  shown in Fig. 4.6. This leads to a correction of the total admittance

$$Y_{\text{tot}}(\omega) = \left( \frac{1}{Y(\omega)} + R_{\text{access}} \right)^{-1}. \quad (4.6)$$

A low frequency measurement can only identify the sum of TI resistance (under the gate electrode) and access resistance  $R_{\text{access}}$  as is obvious from the low frequency development,

if  $R_{\text{access}}$  is taken into account:

$$Y_{\text{tot}}(\omega) = i\omega C + \left(\frac{1}{3}R + R_{\text{access}}\right) (C\omega)^2 + \mathcal{O}(\omega^3). \quad (4.7)$$

Note that the access resistance does not affect the imaginary part at low frequencies. Thus, the capacitance measurement is not affected by this element. However, at relatively low frequencies a (phase-sensitive) measurement can give access only to the so called low frequency resistance

$$R_{\text{lo}} = \frac{1}{3}R + R_{\text{access}}. \quad (4.8)$$

Our broadband setup allow us to determine the high frequency admittance, where channel and access resistance can be disentangled. The main effect of  $R_{\text{access}}$  manifests at high frequency, where the asymptotic behavior of the admittance spectrum is changed. A lengthy calculation shows that the real and imaginary part of the admittance tend to “open” up at high frequencies. This can be best seen by considering the impedance, i.e. inverse admittance at high frequencies given by

$$Z_{\text{tot}} = R_{\text{access}} + 1/Y(\omega) \stackrel{\omega \rightarrow \infty}{\sim} R_{\text{access}} + (1 - i)\sqrt{\frac{r}{2c\omega}}. \quad (4.9)$$

Thus the calculation of  $\Re(Z_{\text{tot}}) + \Im(Z_{\text{tot}})$  yields the access resistance  $R_{\text{access}}$ . Note that this method relies only on experimentally accessible quantities and does not require any *a priori* knowledge of the access resistance. Therefore the broadband, full frequency spectrum allows us to robustly disentangle the access resistance from channel impedance in a “one-contact design”. For RF-applications it is always desirable to keep the sample design as simple as possible in order to minimize stray capacitances between the metallic leads. This requirement actually hinders four-or-more-point measurements on RF-devices. With this in mind, our method is particularly interesting as it demonstrates the feasibility of measuring the access resistance with one single contact.

### 4.2.2 The cryogenic probe station and measurement equipment

All measurements presented in this thesis were carried out in a *Janis ST-500* cryogenic probe station, designed for variable temperature (5 – 450 K) and broadband (0 – 40 GHz) operation, Fig. 4.7. The sample is glued with silver paste on a metallic chuck, mounted on a cold finger in the probe station’s vacuum chamber ( $P \approx 10^{-6}$  mbar). The temperature is controlled by adjusting the flow of liquid Helium and the Joule power dissipated by a resistor integrated in the cold finger using a *Scientific Instruments Model 9700* temperature controller. Although the Janis setup can be operated at 5 K, for the sake of temperature stability and lower LHe consumption, all measurements, if not stated

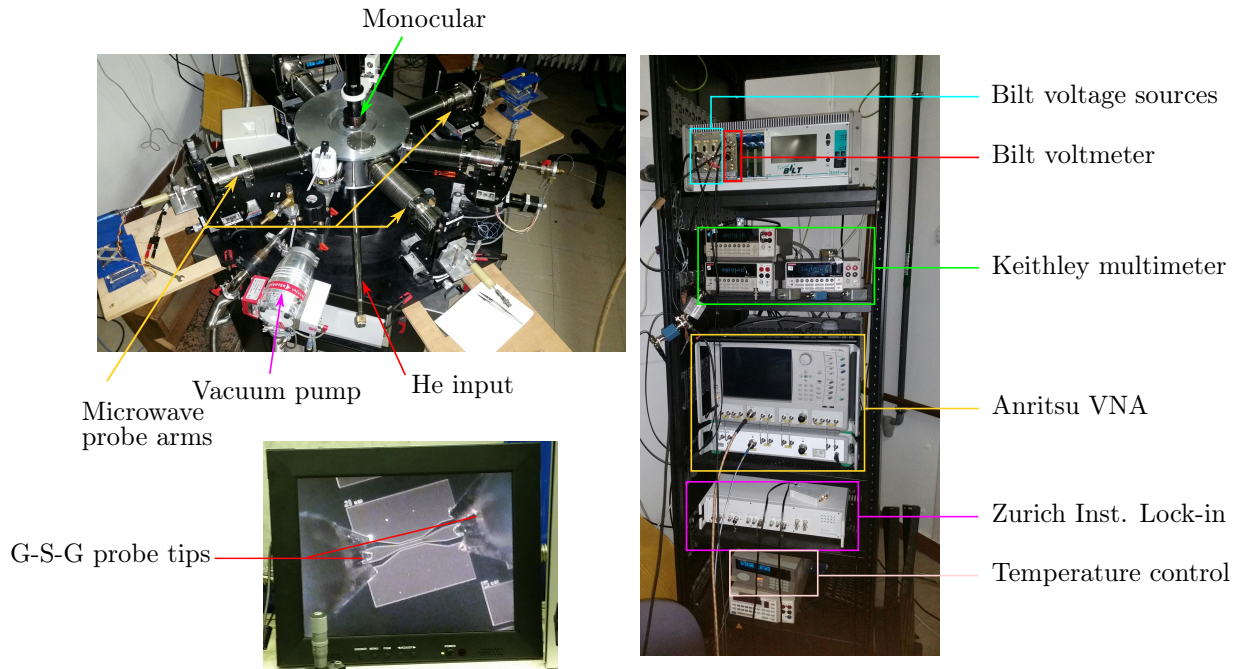


FIGURE 4.7: The experimental setup. Top left: Janis probe station. Bottom left: A CPW being measured with two RF probe tips. Right: RF and DC measurement equipment.

explicitly otherwise, were carried out at 10 K. The probe station is equipped with four arms consisting of RF lines and RF probe tips (*GGB industries*) with a  $100\ \mu\text{m}$  pitch in a ground-signal-ground (GSG) design. An optical window together with a *Edmund Optics* monocular ( $4.5\times$  magnification) and a *Hitachi* CCD camera enable to see sample and probe tips simultaneously. The probe tips are placed with almost micron precision via XYZ manual linear stages. A custom-made tilt fixture, makes it possible to adjust the angle of the probe tips in order to ensure planarity of the tips relative to the CPW. In order to avoid photo-voltaic or -conductive effects, the optical window is blinded during measurements.

**Lock-in measurements** For low frequency measurements (kHz-range) Lock-in measurements are carried out using a *Zurich instruments HF2LI* 0-50 MHz lock-in amplifier together with the corresponding *HF2TA* current pre-amplifier. The output of the Lock-in is directly connected to the gate electrode of the sample, whereas the drain electrode is connected to the input of the *HF2TA*'s operational amplifier in current amplification (i.e. negative feedback) mode (feedback resistance  $R = 1\ \text{M}\Omega$ ). For a given amplitude of a voltage excitation  $V$ , the AC-current through the capacitor device is given by  $I = iC\omega V$ . In order to obtain a signal-to-noise ratio on the order of 1000 for capacitances on the order of several pF (for the HgTe samples) and given the input current noise of  $150\ \text{fA}/\sqrt{\text{Hz}}$ , we chose the excitation voltage for lock-in measurements to be  $V_{\text{rms}} = 50\ \text{mV}$ . DC biasing is achieved via the “Add”-port of the *HF2LI*. In order to obtain fast sweeps of the quasi

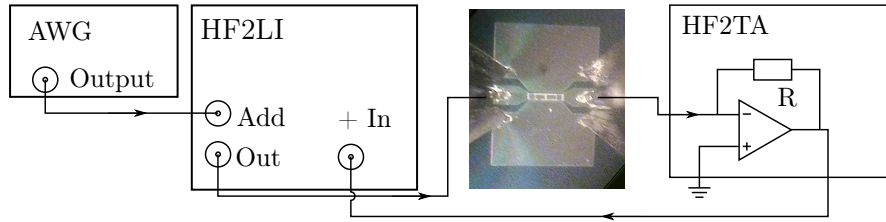


FIGURE 4.8: Wiring scheme for Lock-In measurements.

static gate voltage, we used an *Agilent* arbitrary wave generator (AWG), performing repeated triangular sweeps between a maximum and a minimum gate voltage at typically 0.1 Hz. The Lock-in time constant is chosen to be  $\tau = 1.6$  ms. Then a pseudo-continuous measurement of the demodulated signal at a sampling rate of 112 S/s is performed while simultaneously tracking the actual gate voltage on the device. In this way, three to seven repeated gate voltage oscillations are recorded. Forward (i.e. from  $V_{\min}$  to  $V_{\max}$ ) and backward sweeps are identified in the data *a posteriori*. Subsequently, the data of both sweep types is binned to gate voltage steps of  $\sim 30$  mV, yielding an average value and an error estimate for the corresponding signal.

**Radio-frequency measurements** For RF measurements, we use an *Anritsu VectorStar* Vector Network Analyser (VNA) with a low frequency extension, enabling measurements over a very broad band between 70 kHz and 40 GHz. For DC biasing we use either *iTest BILT 2101* or *Yokogawa 7651* as voltage sources and *iTest BE4082* or *Keithley 2000* as voltmeters. In the case of RF measurements, DC gate biasing is achieved using *Marki* 20 kHz-40 GHz bias-Tees. The leakage current is calculated using a voltage divider configuration, cf. Fig. 4.9. The (source) excitation of the VNA is chosen to lie below the estimated thermal broadening, typically at  $-50$  dBm<sup>4</sup> at low temperatures ( $\sim 10$  K). The linearity of the capacitor's response with respect to the excitation amplitude was controlled explicitly on some devices.

### 4.2.3 RF measurements, scattering and admittance parameters

The working principle of a VNA consists in sending radio-frequency waves from one port towards the sample and measuring the amplitude and phase of the reflected and transmitted signal.

<sup>4</sup>Assuming a  $50\ \Omega$  impedance matching of the device, this power corresponds to  $V_{AC} = \sqrt{50\ \Omega \cdot 10^{-8}\ \text{W}} \approx 0.7\ \text{mV}$ .

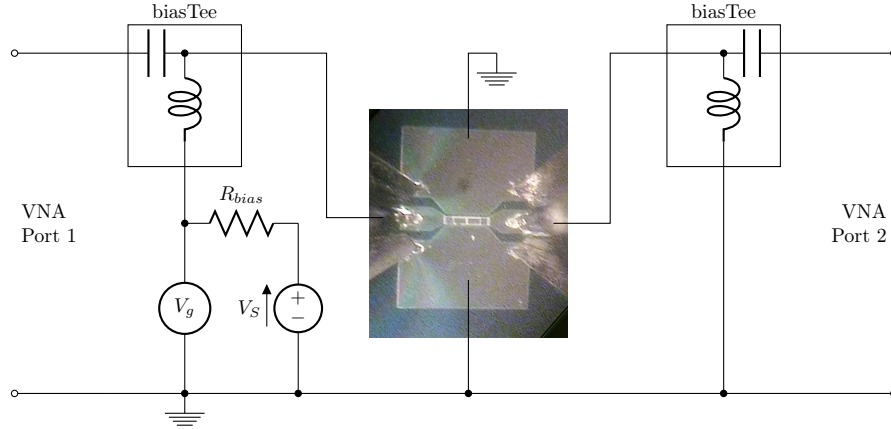


FIGURE 4.9: The sample is connected to the VNA via RF-cables and biasTees. On the gate side of the sample, the DC part of the biasTee is connected to a voltage source in voltage divider configuration. The DC part on the drain side is connected to ground in order to enable charge transfer to the channel.

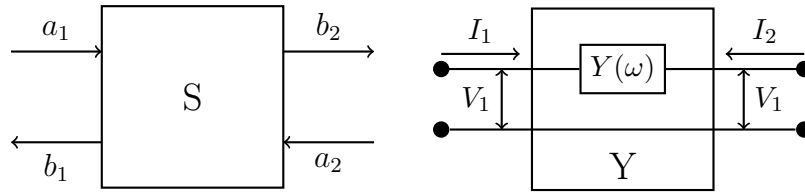


FIGURE 4.10: Left: The scattering parameters (S-matrix) relate reflected and transmitted ( $b_{1,2}$ ) to incident ( $a_{1,2}$ ) waves' amplitudes. Right: The admittance parameters (Y matrix) relates the currents flowing towards the device to the voltages at its ports. In our sample design the admittance  $Y(\omega)$  of the lossy capacitor (Fig. 4.6) is placed along the central conductor of a CPW.

**S-parameters** From the viewpoint of RF-networks, the MITI-capacitors are two-port networks (represented in Fig. 4.10). The measured quantities are the scattering parameters of this two-port (as a function of frequency and gate voltage). The scattering matrix  $S$  relates the (complex) amplitudes of reflected and transmitted waves ( $b_i$ ,  $i \in \{1, 2\}$ ) to the incoming amplitude ( $a_i$ ,  $i \in \{1, 2\}$ ) via

$$\begin{pmatrix} b_1 \\ b_2 \end{pmatrix} = S \cdot \begin{pmatrix} a_1 \\ a_2 \end{pmatrix} \quad (4.10)$$

or element-wise

$$S_{ij} = \left. \frac{b_i}{a_j} \right|_{a_k=0|k \neq j}, \quad \text{with } \{i, j\} \in \{1, 2\}. \quad (4.11)$$

**Y-parameters** As shown above, the admittance is directly related to physical quantities of interest like the resistance and capacitance. It is therefore suitable to transform the measured S-parameters to admittance parameters. This transformation can be found

e.g. in Ref. [239, p. 187]. We recall it here for completeness:

$$Y_{11} = Y_0 \frac{(1 - S_{11})(1 + S_{22}) + S_{12}S_{21}}{(1 + S_{11})(1 + S_{22}) - S_{12}S_{21}}, \quad Y_{12} = Y_0 \frac{-2S_{12}}{(1 + S_{11})(1 + S_{22}) - S_{12}S_{21}},$$

$$Y_{21} = Y_0 \frac{-2S_{21}}{(1 + S_{11})(1 + S_{22}) - S_{12}S_{21}}, \quad Y_{22} = Y_0 \frac{(1 + S_{11})(1 - S_{22}) + S_{12}S_{21}}{(1 + S_{11})(1 + S_{22}) - S_{12}S_{21}},$$

where  $Y_0 = 1/Z_0 = 20 \text{ mS}$  is the reference admittance of our measurement setup. The parameter  $Y_{ij}$  for a two-port network is defined as the ratio of current  $I_i$  over voltage  $V_j$  at one port when the other port is virtually shorted:

$$Y_{ij} = \left. \frac{I_i}{V_j} \right|_{V_k=0|k \neq j} \quad \text{with } \{i, j\} \in \{1, 2\}. \quad (4.12)$$

Note that, in this definition, currents are always defined positive when they *enter* a port. In the present case of a capacitor placed along the line of the central conductor in a coplanar waveguide, cf. Fig. 4.10, the Y-parameters are simply given by

$$Y_{11} = Y_{22} = -Y_{12} = -Y_{21} = Y_{\text{tot}}(\omega), \quad (4.13)$$

as is obvious from eq. (4.12). Note the high symmetry of this matrix. Comparing the four elements of the Y-matrix constitutes thus a first check whether or not contributions of the access area (not shown in Fig. 4.10) are negligible or not<sup>5</sup>.

**Calibration** As the microscopic sample is connected through cables, bias-Tees and probe tips to the macroscopic VNA, the raw signal at the VNA inputs includes spurious information on the transfer functions of these elements (Fig. 4.9). In order to remove these contributions, an *in-situ Short-Open-Load-Thru* (SOLT) calibration is performed. These four standard impedances are defined on a commercial calibration substrate. The possibility of such an *in-situ* calibration is the main advantage of our probe station as compared to traditional cryostats, where impedance standard and sample cannot be measured during the same cooldown. Furthermore, the impedance of wire-bondings would in general differ between sample and impedance standard, ruling out the possibility of a phase-sensitive calibration.

Our calibration procedure shifts the RF reference plane (phase offset) from the output ports of the VNA to the end of the probe tips. As the length of the wires varies during cool-down or heating, the calibration is repeated at each temperature after thermalization (typically  $\sim 20 - 30 \text{ min}$ ).

<sup>5</sup>This issue will be explained in more detail below and in Appendix D.

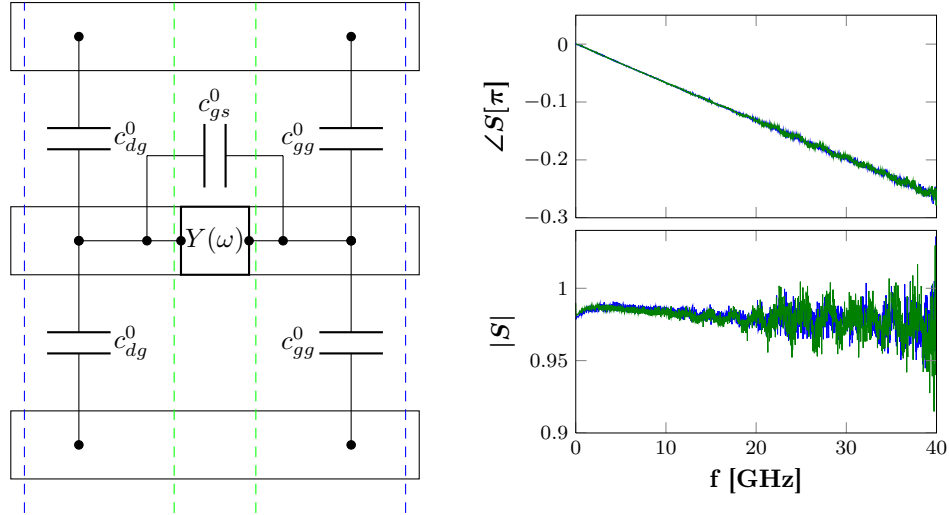


FIGURE 4.11: Left: Parasitic couplings (“cross-talk” capacitances marked by a superscript “0”) are in parallel to the DuT’s admittance  $Y(\omega)$  on the CPW. The RF reference plane after calibration is shown by the dotted blue lines. After correcting for the propagation (see main text), the reference plane is moved towards the active part of the device (dotted green lines). Right: Phase (top) and magnitude (bottom) of CPW THRU S-parameters  $S_{12}$  (blue) and  $S_{21}$  (green).

#### 4.2.4 Deembedding

Even though the probe station makes *in-situ* calibration possible, there are two unavoidable issues in the interpretation of our RF-spectra. The first is the stray (capacitive) coupling between the gate and drain electrodes (“cross-talk”),  $c_{gs}^0$  in Fig. 4.11. In order to correct for this issues, an additional “Dummy” device is systematically fabricated on the same chip next to the capacitor device under test. It has the exact same geometry as the tested capacitor, but the topological insulator is absent. An artist view of the Dummy device is shown in Fig. D.3 in Appendix D. As can be seen from the small signal equivalent circuit of a realistic device, Fig. 4.11, the parasitic couplings are in parallel to the capacitor’s (complex) admittance. In other words, the Y-matrix of the dummy contains all information about these parasitic couplings. The net capacitor’s Y-matrix is obtained by subtracting the dummy’s Y-matrix from the measured Y-matrix (see also [224]):

$$Y_{\text{MITI-Cap}} = Y_{\text{measured}} - Y_{\text{dummy}}. \quad (4.14)$$

The second issue is the propagation along the CPW between probe tips and the actual capacitor device, i.e. a change of the reference plane. As can be seen in Fig. 4.11, the finite length of the CPW causes a phase shift at high frequencies, eventually causing modifications in the admittance spectrum, see also Appendix D. Precise correction of this contribution, requires a through-line (THRU) that is also systematically added *on-chip* during fabrication. The so-called ABCD-parameters (closely related to the transfer

matrices, up to a sign) are suited to describe a series connection of elementary two-ports: The equivalent ABCD matrix of a series of elementary two-ports is simply the matrix product of the ABCD-matrices of its elements [239]. Thus, the ABCD-matrix of the device under test (DuT), i.e. either the dummy or the capacitor,  $ABCD_{\text{DuT}}$  is related to the measurable quantity  $ABCD_{\text{meas}}$  via

$$ABCD_{\text{meas}} = ABCD_{1/2\text{Thru}} \cdot ABCD_{\text{DuT}} \cdot ABCD_{1/2\text{Thru}}. \quad (4.15)$$

Here we assume the length of the active area (the MITI Cap) to be small as compared to the total CPW length and the CPW to be left-right symmetric. Equivalently, the ABCD matrix of the THRU is given by

$$ABCD_{\text{Thru}} = ABCD_{1/2\text{Thru}} \cdot ABCD_{1/2\text{Thru}}. \quad (4.16)$$

Therefore,  $ABCD_{1/2\text{Thru}}$  corresponds to the (matrix) square root of the measured  $ABCD_{\text{Thru}}$ . To summarize, the following algorithm is used for (full) deembedding:

1. Calculate  $ABCD$ -parameters from the measured  $S$ -parameters for DuT.
2. Remove phase-shift due to propagation by multiplying the (matrix) inverse of  $ABCD_{1/2\text{Thru}}$ :

$$ABCD_{\text{DuT}} = ABCD_{1/2\text{Thru}}^{-1} \cdot ABCD_{\text{meas}} \cdot ABCD_{1/2\text{Thru}}^{-1}. \quad (4.17)$$

3. Transform the resulting DuT's  $ABCD$ -matrix back to  $S$ - or  $Y$ -parameters.
4. Subtract the admittance matrix  $Y_{\text{dummy}}$  of the dummy structure from the corrected sample's  $Y$ -matrix. Here, the dummy structure is also de-embedded using the THRU measurement.
5. Check that the final  $Y$  matrix obeys the symmetries required by eq. (4.13).

In Appendix D, these steps are further detailed and illustrated on an exemplary 70 kHz-40 GHz broadband admittance spectrum of a HgTe MITI-Capacitor.

Measurements of THRU and dummy are always performed immediately after or before measuring the DuT, i.e. at the same temperature, for the same cool-down and with the same VNA calibration.

In Fig. 4.12 (a) I show the typical admittance of a (strained) mercury telluride MITI-cap over the full band-width of the measurement setup after de-embedding. Also shown is a fit of eq. (4.6) to the data. When the data is corrected for the finite access resistance,

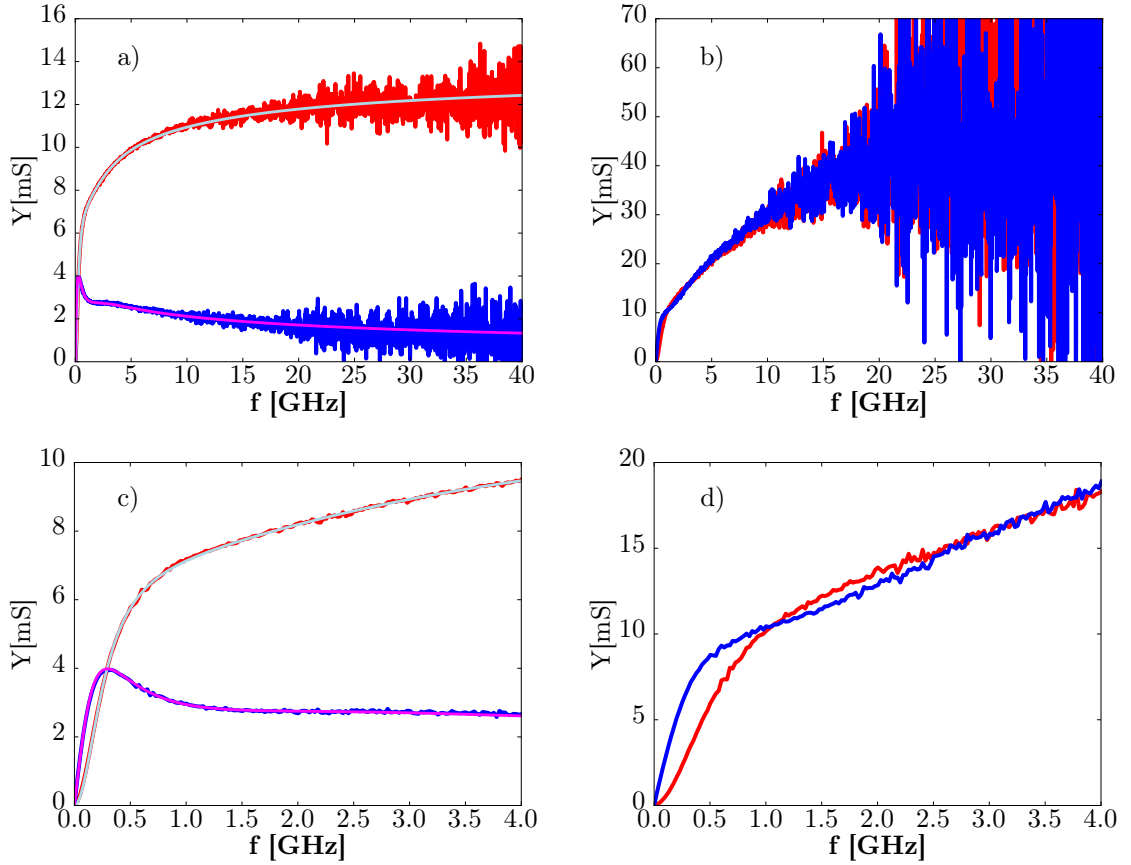


FIGURE 4.12: Full bandwidth de-embedded admittance spectrum at  $T = 10$  K of a (strained) HgTe MITI-Capacitor. RF excitation:  $-45$  dBm. Real parts are represented in blue, imaginary parts in red. a) The de-embedded spectrum. b) The same spectrum after correcting for the finite access resistance. c) Zoom in on the low frequency (0-4 GHz) range of (a). d) Zoom-in on the low frequency (0-4 GHz) range of (b). In a) and c), the result of fitting eq. (4.6) to the data is also shown: real part in light blue, imaginary part in magenta.

real and imaginary part feature an asymptotic  $\sim \sqrt{\omega}$  behavior at high frequencies, a typical signature of the evanescent wave regime. This is shown in Fig. 4.12 (b). Above  $\sim 20$  GHz, losses in the cables cause the measurement signal to be smaller. This manifests itself in increased noise. Figs. 4.12 (c) and (d) show the low frequency part of (a) and (b) respectively. There, the linear (quadratic) frequency dependencies of the imaginary (real) part of the admittance is evident. We highlight that the fit describes the data well over the full band-width. For extraction of physical parameters, it is sufficient to limit the analysis on lower frequencies (up to typically  $\sim 4$  GHz). Therefore, most measurements are limited to this smaller bandwidth.



## Chapter 5

# Topological confinement of surface states in three-dimensional strained HgTe and its evolution under strong electric fields

This chapter constitutes the main body of my thesis. In the previous chapters, I have argued that there exist several distinct paradigms for the electric screening behavior of a 3D topological insulator. First, if the bulk is doped, the electric field is expected to be screened partly by the topological surface states and partly (like in a conventional semi-conductor) by bulk carriers. For the case of an intrinsic topological insulator (i.e. with negligible bulk contribution), the TSS are expected to screen electric fields. This is achieved by changing the 2D charge carrier concentration as a response to an external electric field. Due to the finite density of states, this additional charge in the TSS leads to a change of the surface chemical potential, eventually falling above or below bulk band edges. At this point, one expects the bulk to be populated. However, as shown by Brüne *et al.* [135], the range of surface charge carrier density over which pure TSS-screening persists extends far beyond the bulk band gap, a phenomenon labeled “Dirac screening”. In section 5.1, I will shortly present two different types of samples studied in this thesis. I will show that they fall into two distinct categories of screening by investigating the different screening regimes.

In particular, in section 5.2, I highlight the differences between a bulk-doped and a TSS-dominated sample. In this part, my capacitance spectroscopy measurements confirm the Dirac screening on the TSS-dominated sample.

Due to the helical nature of the surface states, TSS conduction is robust against backscattering as long as time-reversal symmetry is conserved. This generally leads to high electron mobilities for TSS conduction. In section 5.3, I present high frequency measurements providing information about the charge dynamics, i.e. the dissipation or equivalently the conductivity of the samples. These not only illustrate large TSS mobilities on the order of  $100.000 \text{ cm}^2/(\text{Vs})$ , but reveal the onset of a new scattering channel for high-mobility TSS electrons at high energies. I will motivate that this new scattering channel corresponds to a (massive) surface sub-band.

This idea is endorsed by supplementary DC magneto-transport data (section 5.4) and by the appearance of metastability in the sample above a certain threshold voltage (section 5.5).

These observations are confirmed and enriched on the bulk-doped sample in section 5.7. Here, several scattering peaks are resolved in the resistance data, pointing to the existence of several sub-bands, influencing the conductivity of the topological surface state and consequently the total resistance of the sample.

In order to describe the observed phenomenology, we collaborated with Serguei Tchoumakov, Mark Oliver Görbig and David Carpentier for the elaboration of a heuristic theory. Albeit the model over-simplifies several aspects of the measurement, it has the great advantage of explicitly including electric fields into the calculations and relies only on two adjustable parameters: The Fermi velocity  $v_F$  and a critical electric field  $\mathcal{E}_T$ . It describes Dirac screening and predicts the existence of additional gapped electron bands coexisting with the TSS at the sample surface. The model highlights the role of external electric fields having a twofold effect on the surface state properties: First, the Fermi velocity of the TSS is renormalized by electric fields leading to a higher surface density of states (DoS). Second, the gap of the excited surface states decreases as a function of applied field. The model is compared qualitatively and quantitatively to the experimental data, allowing us to identify a critical electric field for the topological insulator HgTe.

## 5.1 Introduction: Two samples and focus of this work

The main fabrication steps of metal-oxide HgTe capacitors have been described in chapter 4. It is crucial for the understanding of this chapter to recall that two types of (strained) HgTe samples were studied: A so-called *capped* sample (5 nm of  $\text{Hg}_{0.3}\text{Cd}_{0.7}\text{Te}$  between HgTe and  $\text{HfO}_2$ ) and an *uncapped* sample ( $\text{HfO}_2$  in contact with HgTe). Although this nomenclature is unambiguous from the sample fabrication point of view, it gives no physical insight. Anticipating the results of this chapter, the *capped* sample will be labeled *intrinsic* and the *uncapped* will be called *n-type*. Furthermore, on each *sample*,

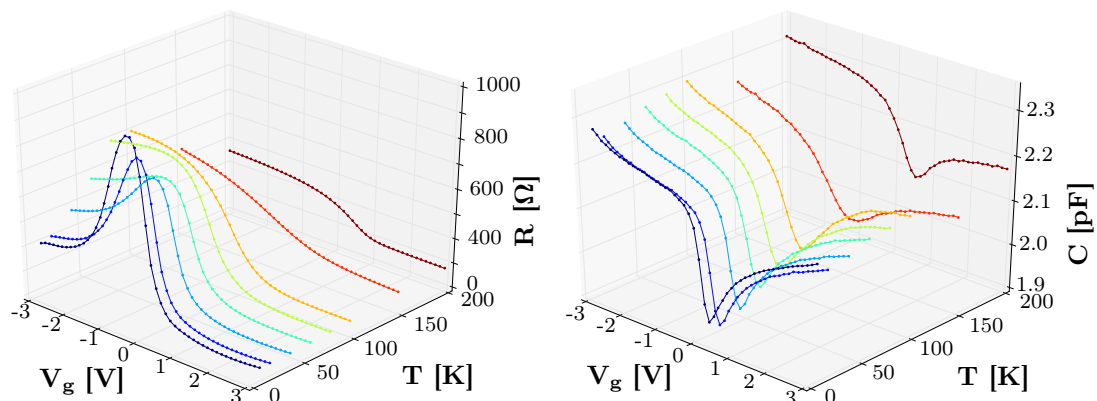


FIGURE 5.1: Temperature and gate voltage dependence of the resistance and the capacitance for the intrinsic sample.

five *devices* with slightly varying geometries were fabricated. The devices vary in the length of the channel. The main findings of this chapter are quite generally independent of the length. Therefore, I focus on the measurements of devices with a channel length  $L = 44 \mu\text{m}$  and a width  $W = 20 \mu\text{m}$  for a HgTe slab thickness of  $t = 67 \text{nm}$ .

We are interested in the thermodynamic surface compressibility of topological surface states defined as (cf. chapter 1):

$$\chi(n, T, \mathcal{E}, B, \dots) = \left( \frac{\partial n}{\partial \mu} \right)_{T, \mathcal{E}, B, \dots}. \quad (5.1)$$

The compressibility thus depends not only on  $n$  but also on temperature  $T$  and the electromagnetic fields  $\mathcal{E}$  and  $B$ . Furthermore in our experiment – as will be explained in detail below – the electron number and the electric field are not independent quantities. Without entering into the experimental details here, I show in Fig. 5.1 the resistance and the capacitance as a function of gate voltage and temperature for the intrinsic sample. The resistance data shows the emergence of a clear peak feature around  $V_g = 0 \text{V}$ , indicating the typical Dirac-point features expected for surface states. In the context of topological insulators (and especially for the small gap system HgTe), finite temperature effects lead typically to enhanced bulk contributions, rendering the quantitative analysis more cumbersome and the physical messages more obscure. I will therefore restrict the discussions in this chapter to low temperatures (10 K). However, these plots show that the experimentally accessible phase space is rather large. In the future, further studies and a detailed analysis of the temperature behavior could (and should) be considered. However, this goes beyond the scope of this work.

In order to further restrict the scope of this work to the influence of strong electric fields on compressibility and conductivity we concentrate on the case of zero magnetic field. This is partly due to the limitations of the measurement setup (rendering magnetic field

sweeps extremely complicated) but also to the fact that topological surface states are protected in the presence of time-reversal symmetry which is broken by application of a magnetic field. Thus, our results are complementary to the work by Kozlov et al.[16].

## 5.2 Low frequency capacitance spectroscopy

As was shown in the previous chapter, the low frequency admittance of a MITI-Capacitor is dominated by an out-of-phase signal proportional to the frequency and the capacitance of the device. Therefore, low frequency measurements are in principle sufficient for the extraction of the device's capacitance. We performed lock-in measurements at 10 kHz in order to get a relatively fast tracking of the capacitance. As the excitation voltage and the frequency are known, the measurement of the AC-current directly yields the capacitance. The geometry of the TI channel under the gate (forming the capacitor plate) is known from sample fabrication. Hence, we focus on capacitance per surface areas, measured in  $\text{fF}/\mu\text{m}^2$ . This procedure simplifies comparison of different devices. We checked that the phase of the AC-current remains fairly constant as a function of gate voltage, cf. Appendix E.

### 5.2.1 Capacitance-voltage characteristic

Figure 5.2 shows the capacitance-voltage characteristics of the intrinsic and the n-type samples. The total capacitance variations are on the order of 20% much larger than those reported in Refs. [16, 19, 157]. This is due to the choice of a thin gate dielectric, resulting in a large geometrical capacitance. Both samples present a clear minimum in the C-V characteristic associated with a minimum of quantum capacitance.

**Comment on metastability** Both samples show qualitative differences between small ( $\pm 3\text{ V}$ ) and large ( $\pm 7/\pm 10\text{ V}$ ) amplitude sweeps. Whereas for small voltage ranges the C-V characteristic is reversible, i.e. independent of sweep-direction, forward and backward sweeps for large gate voltages are clearly different. This hysteresis is associated to some metastability in the sample. We will comment further on this in section 5.5. For now we shall focus on the reversible regime, i.e. gate voltage sweeps limited to  $-3\text{ V} < V_g < 3\text{ V}$ . As the n-type sample shows a slight hysteresis already in this restricted voltage range, for definiteness, the forward sweep ( $-3\text{ V} \rightarrow 3\text{ V}$ ) will be analyzed below.

**The geometrical capacitance** Besides metastability, the large gate voltage range sweeps on both samples show clear trends towards a saturation of the total capacitance.

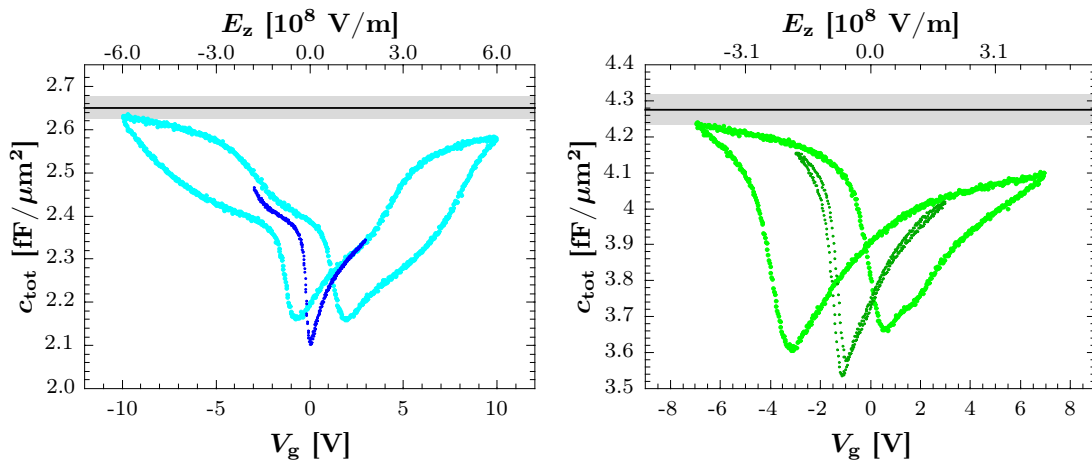


FIGURE 5.2: Capacitance vs voltage characteristic of the intrinsic (left) and the n-type (right) sample. For the intrinsic (n-type) sample, the dark blue (green) lines correspond to sweeps within a reversible range ( $|V_g| < 3\text{ V}$ ), the light blue (green) lines correspond to a larger gate range in which hysteresis effects become prominent. The black line illustrates the value of the geometrical capacitance. The gray area corresponds to a 1% uncertainty of this value.

According to eq. (3.8) the value of the saturation capacitance corresponds to the geometrical capacitance. From Fig. 5.2, we extract  $c_{\text{geo}} = 2.65\text{ fF}/\mu\text{m}^2$  and  $c_{\text{geo}} = 4.27\text{ fF}/\mu\text{m}^2$  for the intrinsic and the n-type sample, respectively. As expected, the geometrical capacitance for the capped (i.e. intrinsic) sample is smaller. Indeed, due to the additional  $\text{Hg}_{0.3}\text{Cd}_{0.7}\text{Te}$ -layer, the total insulating layer thickness is increased resulting in a lower capacitance. Note that we have fabricated metal-oxide-metal (M-O-M) capacitors *on-chip* yielding the (pure) oxide capacitance. A schematic view of such a M-O-M structure is shown in Fig. D.3 in Appendix D.

For the intrinsic sample the oxide capacitance determined from this control structure is on the order of  $3.22\text{ fF}/\mu\text{m}^2$  and depends very weakly on gate voltage ( $\sim 0.6\%$  for  $V_g$  within  $\pm 9.5\text{ V}$ ), cf. Appendix E. This corresponds to a gate oxide effective dielectric constant of  $\varepsilon_{\text{HfO}_2} = 3.6$ . The  $5\text{ nm}$   $\text{Hg}_{0.3}\text{Cd}_{0.7}\text{Te}$  capping layer corresponds to a series contribution to the total geometrical capacitance. Assuming a dielectric constant of  $\varepsilon_r = 8.5$  [240] for this capping layer we find a total capacitance of  $2.65\text{ fF}/\mu\text{m}^2$  in perfect agreement with the value obtained from the asymptotic behavior of the total capacitance in the left panel of Fig. 5.2.

For the n-type sample the situation is different. In principle, the capacitance of the M-O-M is expected to be equal to the saturation capacitance of the devices. However, the M-O-M structure on this sample yields an oxide capacitance of  $6.9\text{ fF}/\mu\text{m}^2$ , in contrast to the value obtained from extrapolation. Furthermore, it is different from the oxide capacitance of the intrinsic sample. We do not have a microscopic explanation for this observation. It is however likely that for the n-type sample, due to the missing capping layer, a

thin insulating film of oxidized HgTe, formed at the HgTe/HfO<sub>2</sub> interface, explains the observed discrepancy.

**Estimation of carrier concentration** Besides the different absolute values of capacitance, the striking difference between the intrinsic and the n-type sample lies in the position of the capacitance minimum. As the capacitance minimum corresponds to a minimum in the electron compressibility, it must be associated to the Dirac point of the surface state or the bulk band gap (at the surface), cf. chapter 3. For simplicity, this point will be called “Dirac point” in the following.

As explained in chapter 3, the C-V characteristic provides the relation between total charge density  $n$  and gate voltage  $V_g$ , via  $en = \int c(V)dV_g$ . We can thus calculate how many charge has to be transferred to the TI such that the electrostatic doping compensates the residual chemical doping. We use the Dirac point as a reference point. For the intrinsic sample this charge is zero as the Dirac point lies at  $V_g = 0$ . For the n-type sample, we find  $n_0 = 2.56 \times 10^{12}/\text{cm}^2$ . We conclude that the capped sample is intrinsic, in the sense that chemical doping is negligible, whereas the un-capped sample is – presumably due to the creation of defects such as Te vacancies during the fabrication process –  $n$ -doped. This justifies the earlier introduced terminology (“intrinsic” and “n-type”). Furthermore, these observations suggest that the effect of bulk carriers in capacitance and in total conductivity will be more important in the n-type sample.

### 5.2.2 Surface chemical potential and electric fields

Using formulae (3.12) and (3.13), we can easily calculate the electron density  $n$ , chemical potential at the sample surface<sup>1</sup>  $\mu$  and the electric field  $\mathcal{E}$  in the capacitor from our C-V characteristics. These quantities are shown as a function of gate voltage in Fig. 5.3.

As the DoS is smallest around the Dirac point, the chemical potential varies most rapidly in this region. Indeed, adding or removing charges cannot happen at constant energy due to Pauli’s exclusion principle. The electric field between the plates is given by

$$|\mathcal{E}| = \left| \frac{V_g - V_{\text{surface}}}{d_{\text{ins}}} \right|, \quad (5.2)$$

where  $V_{\text{surface}}$  can be calculated using equations (3.13) and (3.4). Note that the electric field and the total number of charges on the plates of the capacitor are related via Gauss’

<sup>1</sup>Here and in the following, the *surface* chemical potential  $\mu_s$  will be labeled  $\mu$  if not otherwise stated.

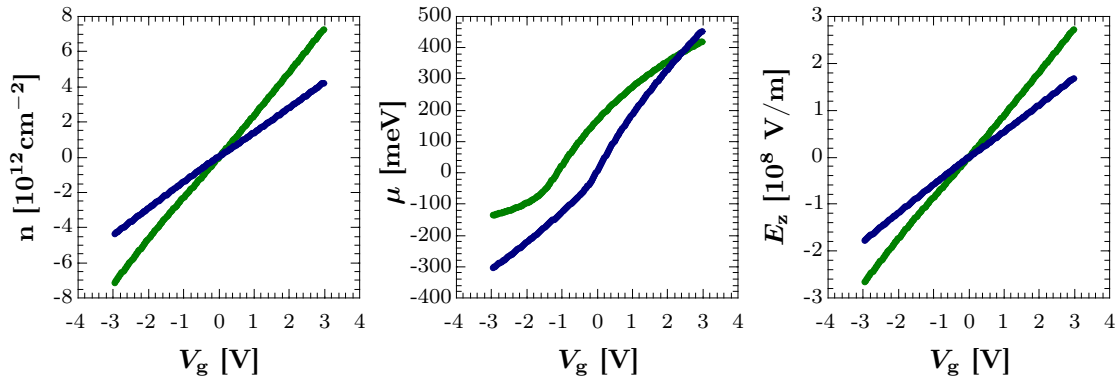


FIGURE 5.3: Total charge carrier variation in the TI electrode (left), surface chemical potential with respect to the Dirac point (middle) and electric field (right) as a function of gate voltage for the intrinsic (blue) and the n-type (green) sample, measured at  $T = 10$  K. The effect of quantum capacitance leads to an S-shape of the  $\mu - V_g$  relation.

law. Indeed, it is straightforward to show that the definition, eq. (5.2), is equivalent to

$$|\mathcal{E}| = \frac{en_{tot}}{c_{geo} \cdot d_{ins}} = \frac{en_{tot}}{\varepsilon_0 \tilde{\varepsilon}_{ins}}, \quad (5.3)$$

where I introduced the effective insulator dielectric constant  $\tilde{\varepsilon}_{ins}$ . In the right panel of Fig. 5.3 we observe that electric field and gate voltage are fairly proportional. For the calculation of  $\mathcal{E}$  quantum capacitance effects are therefore negligible.

The large variations of  $\mu$ ,  $n$  and  $\mathcal{E}$  are all due to the very thin oxide layer design. We can thus probe the electro-dynamic properties of the topological insulator over a broad range of thermodynamic parameters.

Consistent with the observation of a shifted Dirac point is the qualitative comparison of the intrinsic and the n-type sample: Whereas the electric field (or equivalently the number of charges) of the n-type sample varies more rapidly with the gate voltage due to the increased total capacitance, the variation of chemical potential is significantly smaller. The reason lies in the fact that for the n-type sample, the charge does not only populate the surface states (changing the surface chemical potential), but some of the charges are transferred to the bulk of the material.

These simple observations point towards an important experimental fact: Although for a given sample, electric field and surface chemical potential cannot be varied independently, comparison of the two samples yields valuable information for the *independent* variation of these two quantities. This will be particularly important for the understanding of further data and the theory presented below.

### 5.2.3 Interpretation and discussion

We choose the minimum in capacitance as a natural origin of surface chemical potential. Using eqs. (3.8) and (3.13) we calculate  $c_Q$  as a function of  $\mu$  for both samples as represented in Fig. 5.2.

Assuming a 1% uncertainty on  $c_{geo}$  (from the saturation behavior represented by the shaded areas in Fig. 5.2), we obtain rather large uncertainties on  $\mu$  and  $c_Q$  for large gate voltages represented by error bars in Fig. 5.2. However, close to the Dirac point, variations of the geometrical capacitance cause negligible uncertainties making a quantitative analysis possible.

**Quantitative analysis of the intrinsic sample** Besides the position of the Dirac point in Fig. 5.2 the two samples differ in the value of the measured minimal quantum capacitance.

As was shown in chapter 3, quantum capacitances add up. Therefore, the lower quantum capacitance of the intrinsic sample supports the idea that it is surface dominated. Furthermore, the clear linear relation between quantum capacitance and surface chemical potential observed for the intrinsic sample corresponds to Dirac fermions with linear dispersion  $E(k) = \hbar v_F k$ , cf. chapter 3.

For negative energies, i.e. on the hole side, a hybridization of TSS and bulk  $\Gamma_8$  heavy holes is likely to occur rendering the analysis here more difficult. However, even on the hole side we observe a small energy range in which  $c_Q$  varies linearly with  $\mu$ .

For a TSS, the quantum capacitance is related to the chemical potential via  $c_Q = \frac{e^2}{2\pi(\hbar v_F)^2} \mu$  (Tab. 3.1). Hence, the analysis of the linear regions allows us to give an estimate for the corresponding Fermi velocities. We find  $5 \cdot 10^5$  m/s and  $1.6 \cdot 10^6$  m/s for holes and electrons, respectively. These values correspond to the black dashed lines in Fig. 5.4. Note that our value of Fermi velocity on the electron side is higher than the values reported from ARPES or magneto-transport and -optics typically around  $0.5 - 1.0 \cdot 10^6$  m/s, cf. chapter 2. We note that on the hole side our result agrees with existing ARPES studies most often limited to the hole side.

**Comment on (quantum) capacitance background** For Dirac fermions the quantum capacitance is expected to vanish at the Dirac point. However, such a behavior is not observed in Figs. 5.2 and 5.4. A similar background capacitance at the Dirac point was reported for graphene in Refs. [11, 15, 224]. There are several explanations for this observation. Generally, the dispersion relation of a TSS can deviate from linearity close

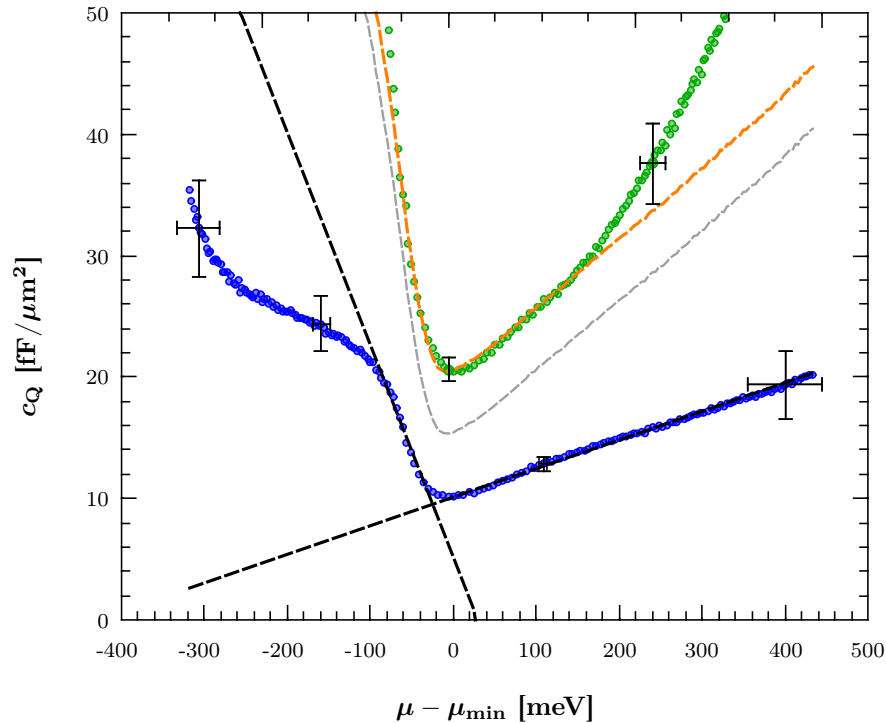


FIGURE 5.4: Quantum capacitance vs surface chemical potential for the intrinsic (blue) and the n-type sample (green). Some representative error bars reflect the (dominating) uncertainty on the value of the geometrical capacitance  $\delta c_{geo} = 1\%$ , cf. Fig. 5.2. The dashed black lines correspond to TSS Fermi velocities of  $5 \cdot 10^5$  m/s and  $1.6 \cdot 10^6$  m/s for holes and electrons, respectively. The dashed orange (the light gray) line corresponds to an estimate of combined bulk and TSS response, cf. main text.

to the Dirac point (see also Fig. 3.3). In such a situation, any blur of either the energy or the capacitance resolution causes a non-vanishing capacitance close to the Dirac point. Such a blurring is likely to occur for several reasons:

First, the rather large excitation voltage of  $50 \text{ mV}_{rms}$  causes an averaging in  $c_Q$  and consequently in  $\mu$ . From Fig. 5.3, we conclude that such an averaging reduces the resolution on  $\mu$  down to at least 10 meV. For the RF measurements presented below, a comparison of results obtained from excitations with different amplitudes (-35 dBm and -50 dBm, corresponding to  $V_{rms}$  on the order of 4 mV and 0.7 mV, respectively) did however not reveal any excitation dependence.

Second, inhomogeneities in either chemical doping or oxide thickness over the  $44 \times 20 \mu\text{m}^2$  channel are known to occur in gated TI structures, forming so called “puddles”, cf. chapter 2. These are likely to explain the finite quantum capacitance close to the Dirac point. Third, all analysis of our experiments is based on a 1D model for the capacitor’s response to an external excitation (chapter 4). However, our capacitor structures have a finite width of  $20 \mu\text{m}$  and are thus 2D objects. Therefore, edge effects might also affect the measurement.

A fourth explanation lies in the relative position of the TSS Dirac point with respect to the bulk band structure. TSS screening close to the Dirac point is likely to be reduced

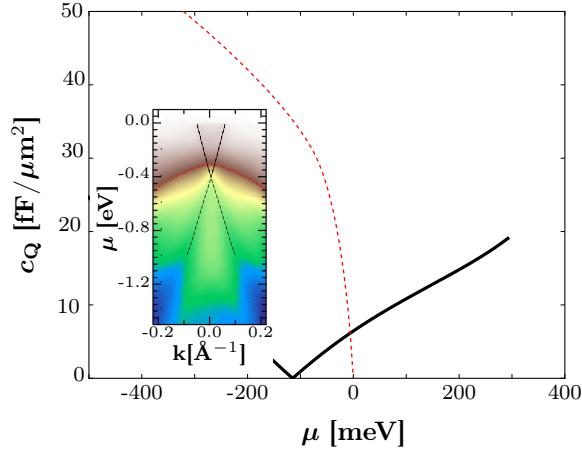


FIGURE 5.5: The quantum capacitance as calculated from the ARPES spectrum in Ref. [176] (shown in the inset) along the dashed black line. Note that the ARPES reveals a band (illustrated as a dotted red line in the inset). A sketch of the contribution of this band to the quantum capacitance is shown as a red dotted line. Note that the intersection of the two contributions to the quantum capacitance leads to a quantum capacitance minimum on the order of  $10 \text{ fF}/\mu\text{m}^2$ .

due to low surface carrier densities. The physical situation is similar to a gated graphene contact as studied by Wilmart *et al.* [241]. As revealed by ARPES on *unstrained* samples [75, 176], the TSS Dirac point might be nested (also in a strained sample) within a hole band [242, 243]. In Fig. 5.5 I show the expected surface quantum capacitance for the ARPES spectrum from Ref. [176] shown in the inset. The nature of this hole band (surface or bulk) is unclear, therefore it is difficult to numerically evaluate its contributions to electron compressibility. The red dotted line represents thus only a sketch of the expected compressibility when the surface Fermi level crosses this hole band. It is remarkable in Fig. 5.5 that the crossing of quantum capacitances for the sketched hole band and the TSS occurs at a quantum capacitance close to  $10 \text{ fF}/\mu\text{m}^2$ . In this interpretation of the capacitance minimum, it does not correspond to the “true” TSS Dirac point. For simplicity, we will however stick to this nomenclature.

The contribution of heavy-hole states for surface chemical potentials below the Dirac point is thus likely to be two-fold: It might lead to a bulk-like contribution to the measured electronic surface compressibility but also lead to hybridization with the TSS, eventually affecting its properties. A detailed description of these phenomena goes beyond the scope of this work. We shall therefore restrict the discussion to the electron side in the following.

However, several explanations for the apparent lack of a vanishing capacitance at the Dirac point can safely be ruled out. These include a background signal due to electron-band bulk carriers. Indeed, following the calculations presented in chapter 3, assuming a vanishing TSS contribution to the quantum capacitance at the Dirac point, the bulk’s

DoS (at  $V_g = 0$ , assumed corresponding to flat band) is given by eq. (3.20) as

$$DoS_{3D,bulk} = \frac{C_{Q,min}^2}{e^2 \epsilon_0 \epsilon_r}, \quad (5.4)$$

i.e.  $DoS_{3D,bulk} \approx 3.35 \cdot 10^{18}/(\text{eV cm}^3)$ , corresponding to a dopant density on the order of  $\sim 10^{18}/\text{cm}^3$  or equivalently  $\mu \approx 300 \text{ meV}$ . This is incompatible with the observation that the Dirac point lies at  $V_g = 0$ . Another candidate for the measured capacitance background is the bottom surface. However, its contribution is limited to the geometrical capacitance due to the finite width of the HgTe layer given by  $c_{top-bottom} = \epsilon_0 \epsilon_r / d \approx 2.7 \text{ fF}/\mu\text{m}^2$ , where a bulk HgTe dielectric constant of  $\epsilon_r = 21$  was assumed<sup>2</sup> [135, 244]. This rules out the idea of the bottom TSS to cause the observed minimal capacitance.

At last, parasitic capacitances between gate and drain electrode can be ruled out as an explanation of the measured background capacitance. The on-chip fabricated dummy structures (cf. chapter 4) show that these parasitic contributions are roughly three orders of magnitude smaller than the measured capacitances on actual devices, see also Appendix D.

**Combined bulk- and TSS response for the n-type sample** For the n-type sample, the shift of the Dirac point towards negative gate voltages suggests a non-negligible residual bulk doping. The formalism developed in chapter 3 allows us to assess the expected contribution of bulk carriers to the quantum capacitance, given a chemical potential  $\mu_\infty$  deep in the bulk<sup>3</sup>, corresponding to the global chemical potential at  $V_g = 0$ . Using these results, we can calculate the bulk's depletion/inversion capacitance as a function of surface chemical potential for  $\mu_\infty = 170 \text{ meV}$ . This value corresponds to a 3D charge carrier density of  $2.1 \cdot 10^{17}/\text{cm}^3$ . This quantum capacitance adds to the response of the topological surface state. We can thus calculate the sum of this modeled quantum capacitance and the measured quantum capacitance of the intrinsic sample. The resulting quantum capacitance is represented in light gray in Fig. 5.4. Although the general behavior and the slopes of the resulting line correspond to the measured data (in green), there is a constant offset of  $\sim 5.1 \text{ fF}/\mu\text{m}^2$ . Adding this constant offset to the so-calculated curve yields the orange line, in good agreement with the measurement. Although we lack a precise understanding concerning the origin of this (constant) offset, similar arguments as for the  $\sim 10 \text{ fF}/\mu\text{m}^2$ -offset on the intrinsic sample could be considered.

<sup>2</sup>We highlight that this value for the dielectric constant is associated to the bulk. As observed in [135] and as I will show in section 5.9 a smaller dielectric constant must be considered for the HgTe surface region.

<sup>3</sup>As shown in chapter 3, for doped samples, screening occurs on length scales on the order of several nanometers. This ensures the chemical potential deep in the bulk (and at bottom surface) to be gate-voltage independent.

The analysis of the bulk response relies on the models presented in chapter 3. For the predictions of the model, it is crucial to assume that the bulk carriers indeed screen the electric field over a width shorter than the sample thickness. We can estimate this screening length to be

$$\lambda \sim \frac{\varepsilon_0 \varepsilon_r}{c_{Q,bulk}}. \quad (5.5)$$

This leads to screening lengths on the order of 10-30 nm, indeed much smaller than the sample thickness (67 nm).

**Dirac screening** Now that we have established a combined bulk and TSS response for the n-type sample and an “ideal TI” response for the intrinsic sample, we shall address the following question: In which ranges of chemical potential do these observations hold? As can be seen in Fig. 5.4, the experimental data for the n-type sample deviates from the model calculation for chemical potentials larger than  $\sim 150 - 200$  meV. As will be explained below, this observation is likely due to the formation of massive surface states.

However, the linear relation between electron compressibility and chemical potential, characteristic for Dirac fermions of a TSS extends beyond  $\sim 300$  meV for the intrinsic sample. This is surprising, as band-calculations (cf. chapter 2) predict a transport band gap on the order of 25 meV. In other words, our measurements reveal a pure TSS response over an energy range that exceeds the transport band gap by more than one order of magnitude. This observation can be interpreted by an anomalously strong screening of electric fields via the TSS: Indeed, if the surface Dirac fermions screen the electric field completely, no field penetrates into the bulk and the bulk’s charge state remains unchanged. A very similar effect was observed and reported by our collaborators in Würzburg in (quantum) magneto-transport [135] and named “Dirac-screening”. It is striking that the intrinsic sample’s surface states screen electric fields up to  $2 \cdot 10^8$  V/m (cf. Fig. 5.3). It will be shown below that this screening breaks down for higher fields.

In order to further investigate the Dirac-screening regime and its limitations, in the following sections, we concentrate first on the intrinsic sample.

### 5.3 Scattering process revealed by high frequency capacitor admittance

So far, we have focused on the low frequency capacitance data. We have revealed a TSS-dominated response for the intrinsic sample and confirmed the Dirac screening [69] using complementary experimental tools.

We shall now turn towards the charge dynamics in the HgTe-based radio-frequency MITI-Capacitors. As explained in chapter 4, high frequency measurements simultaneously provide conductivity and compressibility. Before presenting the experimental results and their interpretation, I will introduce some important concepts. In particular, I show that RF measurements directly probe the diffusion constant of electrons.

### 5.3.1 Einstein-Boltzmann relation, diffusion constant, Thouless time

It can easily be shown, e.g. [2, 15, 224] that the DoS  $\partial n/\partial\mu$  is related to the conductivity  $\sigma$  via the diffusion constant  $D$ . For completeness a short proof of this relation shall be presented here. An electric current (density)  $\mathbf{j}$  is the response of a (conducting) system to an inhomogeneous *electrochemical* potential  $\mu^* = \mu + qV$ . In linear response, the current is thus proportional to the gradient of  $\mu^*$ . Furthermore, it is proportional to the available charge carrier density  $n$ . For definiteness, I describe the case of electrons with elementary charge  $q = -e$ . Labeling the proportionality constant  $\mu_e$  (as will turn out, the electron mobility), one finds<sup>4</sup>

$$\mathbf{j} = n\mu_e \nabla(\mu - eV). \quad (5.6)$$

Now, using  $E = -\nabla V$ , we find

$$\mathbf{j} = \sigma \mathbf{E} + n\mu_e \frac{\partial\mu}{\partial n} \nabla n, \quad (5.7)$$

with the Drude conductivity  $\sigma = ne\mu_e$ . The electron compressibility being defined as  $\kappa = \partial n/\partial\mu$ , one finds

$$\mathbf{j} = \sigma \mathbf{E} + \frac{\sigma}{e^2 \cdot \kappa} \nabla(en). \quad (5.8)$$

This last expression can be understood as follows: The first term describes the system's response to an external electric field via Ohm's law. The second term accounts for diffusion of charges. Indeed, it implies that (electronic) currents flow from regions of large electron concentrations (i.e. strong negative space charge regions  $-en$ ) towards regions of lower concentration<sup>5</sup>. In analogy to Fick's law, the proportionality factor between current density and concentration gradient is called the diffusion constant  $D$ . According to eq. (5.8), one has thus

$$D = \frac{\sigma}{e^2 \kappa}. \quad (5.9)$$

<sup>4</sup>This relation can be rigorously derived from a semi-classical Boltzmann equation for transport. This is shown for example in references [2, 224].

<sup>5</sup>Note the sign convention for charge currents, being opposite to the flow of electrons.

This is the (*Boltzmann-Einstein relation*). Note that for the case of 2D conductors,  $c_Q = e^2\kappa$  and thus the Einstein relation can be written as  $\sigma = c_Q D$ , relating the measurable quantities  $c_Q$  and  $\sigma$ . It can be shown, using the Boltzmann equation [144, 224, 245] that – as long as the transport scattering  $\tau$  varies slowly with energy (i.e. slow on the scale of  $k_B T$ ) – the Einstein relation holds for arbitrary disorder, and finite temperature. Furthermore, in dimension  $d$ , the (energy dependent) diffusion constant is given by

$$D(E) = \frac{1}{d} v_F(E)^2 \tau(E). \quad (5.10)$$

Note that for Dirac Fermions, the Fermi velocity is constant. Thus, measuring the energy dependence of the diffusion constant, directly yields the energy dependence of the scattering time  $\tau$ .

As shown in chapter 4, RF measurements provide  $\sigma$  and  $c_Q$ . Furthermore, the frequency at which real and imaginary part of the admittance are equal, eq. (4.5), is directly related to the *Thouless time* of electrons in the conductor (for a 2D conductor like the TSS). Indeed, rewriting of eq. (4.5) yields [15]

$$\omega_1 = \frac{\pi^2 \sigma}{2c_{\text{geo}} L^2} + \frac{\pi^2}{2\tau_{Th}}. \quad (5.11)$$

The Thouless time  $\tau_{Th} = L^2/D$  corresponds to the time an electron takes to diffuse from one end of the conductor to the other. Thus, an idealized RF capacitor, with a geometrical capacitance going to infinity constitutes a direct measurement of electronic diffusion through the system. RF capacitors are therefore a formidable tool to investigate mesoscopic conductors.

In the context of semi-conductors, the diffusion constant is rarely considered, as most literature investigates rather the electron mobility, measurable e.g. in a Hall bar. However, Hall measurements can only provide the density dependence of mobility  $\mu_e(n)$  and not its energy dependence. The conversion  $n \rightarrow \mu$  requires knowledge of the underlying band structure. It is easy to show that the diffusion constant and the mobility of Dirac fermions (in 2D) are related by<sup>6</sup>

$$D = \frac{\mu \cdot \mu_e}{2e}. \quad (5.12)$$

Note that this relation only requires a linear band structure, but is independent of the Fermi velocity.

In the following, I will investigate the scattering properties of electrons in the MITI-Capacitors via the RF-admittance spectra.

---

<sup>6</sup>As a reminder:  $\mu_e$  designates electron mobility, whereas  $\mu$  designates chemical potential.

### 5.3.2 Radio-frequency spectra and extracted parameters

For the moment, we shall focus on the intrinsic sample, where surface conduction is dominating over the full explored energy range discussed so far. We also restrict the RF investigation to the reversible range for the moment ( $|V_g| < 3\text{ V}$ ).

A typical RF admittance spectrum at  $V_g = 0$  is shown in Fig. 5.6. As expected for a 1D-cavity formed by the RF-capacitor, the low frequency behavior (shown in the inset) reveals the linear relation between (imaginary part of) admittance and frequency. This allows us to extract the capacitance. The inset also shows a real part quadratic in frequency related to the losses due to the finite resistivity of the HgTe. As explained in chapter 4, the spectral footprint of a finite access resistance is the opening of real and imaginary part at frequencies beyond the crossover frequency  $\omega_1$ . The Figure also shows a three-parameter fit using the total capacitance  $C$ , the total resistance  $R$  and the contact resistance  $R_c$  as parameters. We highlight that the fit describes the full complex spectrum over a broad frequency range. Thus, the extracted parameters can be determined with high accuracy. Specifically, we can subtract the contact resistance contribution from the spectrum and trace only the response of the channel under the gate electrode. The resulting spectrum is represented in the right panel of Fig. 5.6. Note in particular that real and imaginary part are equal and proportional to  $\sqrt{\omega}$  at high frequencies, a clear confirmation of the accuracy of the simple 1D model. Furthermore, the excellent agreement of fit and data shows that the fitting parameters can be chosen

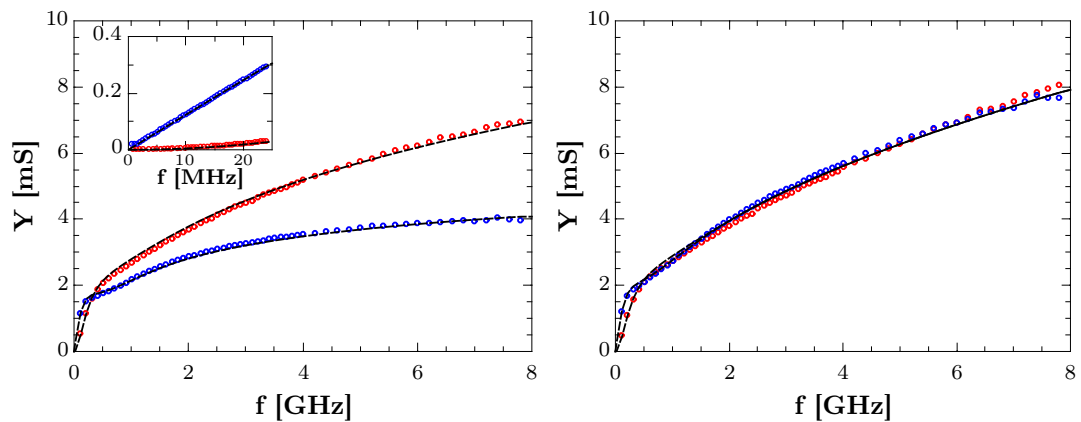


FIGURE 5.6: Admittance spectra at  $V_g = 0$  for the intrinsic sample. Out-of-phase component (imaginary part) represented in blue, in-phase component (real part) in red. The black dashed lines correspond to a three-parameter fit on the complex spectrum. Left:  $Y = -Y_{21}$  after de-embedding of thru-line and dummy (cf. chapter 4 for details). The opening of real and imaginary part at high frequencies is due to a finite access resistance on the order of  $50\ \Omega$ . Inset: Zoom on the low frequency part of the spectrum, revealing the linear (quadratic) low frequency behavior of the imaginary (real) part. Right: After subtraction of the access resistance, the spectrum corresponds to the spectrum of a one-dimensional distributed RC-line, cf. chapter 4. For clarity of the plot, only one point in ten is shown.

*frequency-independent*. This is particularly important as for the C-V characteristics of MIS structures, strong frequency dependencies especially in the inversion regime are likely to occur, cf. Ref. [18] for a short discussion. This observation thus confirms the equilibrium condition, introduced in chapter 3, eq. (3.4). Furthermore, it contradicts the findings of Kozlov *et al.* [16, suppl. mat.], where an increased access resistance in high magnetic fields renders capacitance extraction at higher frequencies unreliable.

In Fig. 5.7 (left panel), the admittance spectra for three representative gate voltages are presented. Fitting was carried out over the full spectrum and the contact resistance was removed from every spectrum. The fitting parameters are represented in the right panel of Fig. 5.7.

**Capacitance** The RF  $C$ - $V$ -characteristic shows the same qualitative features as the low-frequency measurement (shown in gray, see also the left panel of Fig. 5.2). However, the absolute value of capacitances are shifted. This difference between low and high frequency characterization was similar on all measured structures and is likely to be due to an offset either in the calibration of the vector-network analyzer or a systematic offset in the Lock-in measurement, e.g. in the amplification chain. In order to take the global shift into account, for further interpretation of the measurement a geometrical capacitance of  $c_{\text{geo}} = 2.76 \text{ fF}/\mu\text{m}^2$  is assumed for the RF measurements. Conversion to surface chemical potential and quantum capacitance, shown in the right panel of Fig. 5.8

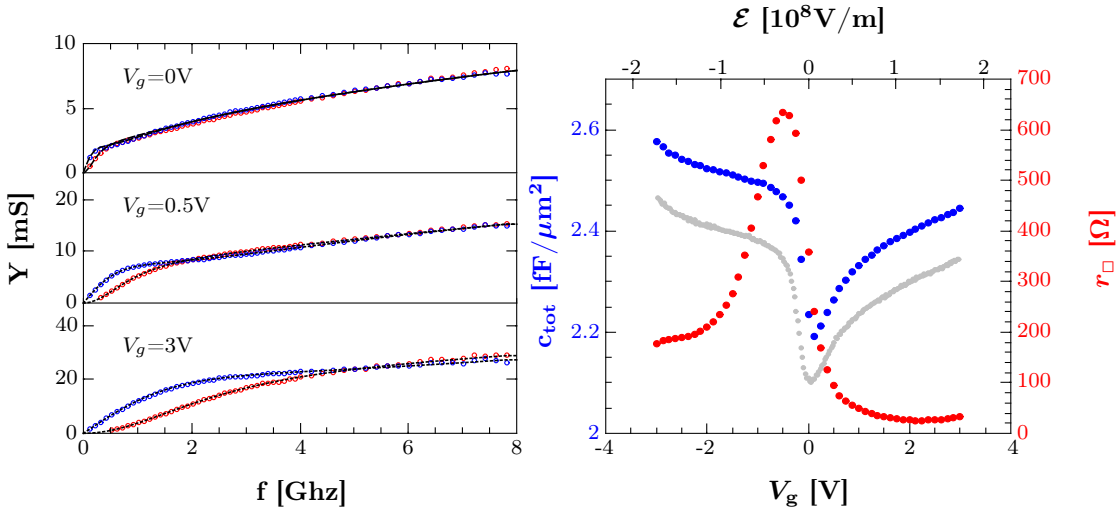


FIGURE 5.7: Left: Admittance spectra at different gate voltages (imaginary part in blue, real part in red), corrected for the access resistance and the corresponding best fit (black lines). Note the changes of the scale on the y-axis. Right: Total capacitance (blue) and resistivity (red) extracted from RF spectra as a function of gate voltage. The gray line corresponds to the capacitance extracted from the low frequency Lock-in measurements.

does not provide further information than the low frequency measurements discussed above. The interpretation of the data below does not depend on this subtlety.

**The sheet resistance** Similar to the capacitance showing a clear minimum associated with the Dirac point and thus a minimum in the DoS, the sheet resistivity features a strong maximum in close vicinity to this gate voltage. This is consistent with the conclusions drawn from the low frequency measurements: Transport in the intrinsic sample is TSS dominated, leading to a strong top-gate sensitivity of the total sample conductance. As expected for Dirac fermions, the resistance peaks at the Dirac point and is scattering limited at higher charge carrier concentrations. Negative (positive) gate voltages correspond to an electrostatic  $p$  ( $n$ )-doping of the HgTe channel. As the resistance saturates on a lower level on the electron side, we conclude that TSS electrons are more mobile than TSS holes. This is consistent with the lower Fermi velocity of holes observed above.

The slight horizontal offset between resistance maximum and capacitance minimum remains slightly obscure. However, similar shifts were observed between the crossover from  $2\pi$  to  $4\pi$  Shapiro steps and the  $2\Phi_0$  to  $\Phi_0$  SQUID response in topological superconducting junctions [118]. A possible explanation in the context of this work might be given as follows: Although “Dirac-screening” is observed on the electron side, from  $k \cdot p$ -calculations, the TSS-Dirac point is expected to be buried in the bulk’s heavy hole band [41, 184]. In case a bulk-like  $p$ -type quantum well state forms close to the interface at  $V_g \approx 0$  V, the quantum capacitance is expected to rise. However, such states are mainly formed from bulk heavy hole states with a large effective mass and typically a low mobility (there is no topological protection from back-scattering). Thus, their contribution to the total conductivity remains negligible. The resistance maximum is reached only once the TSS changes from  $n$ - to  $p$ -type conduction. If the same sheet resistivity data is traced as a function of surface chemical potential, Fig. 5.8, the maximum is shifted by  $\sim 80$  meV with respect to the capacitance minimum. Within such a “buried Dirac-point” scenario, this value is not inconsistent with  $k \cdot p$ -calculations by Baum *et al.* [41].

**Contact resistance** The contact resistance varies between  $43 \Omega$  and  $56 \Omega$  with gate voltage. It is shown in the left panel of Fig. 5.8. It shall be pointed out that the extraction of this quantity is limited by the chosen band-width (and the phase precision at high frequencies). The quality of the fit does not crucially depend on this access resistance. It is however likely that the small observed variations are associated with the formation of  $p$ - $n$  barriers in the small gap (on the order of  $\sim 2 \mu\text{m}$ ) between gate end drain electrode. The general trend towards a lower access resistance for electrostatic  $n$ -doping suggests

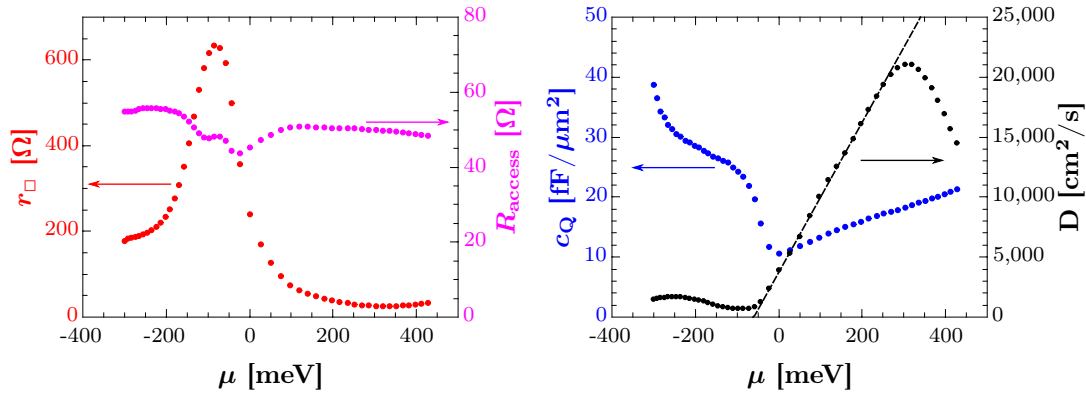


FIGURE 5.8: Left: Sheet resistivity (red) and contact resistance (pink) as a function of surface chemical potential  $\mu$ . Right: The quantum capacitance (blue) and the diffusion constant (black) as a function of surface chemical potential. The dashed black line corresponds to a constant TSS-mobility of  $120.000 \text{ cm}^2/(\text{Vs})$ .

an n-type doping of the HgTe in the vicinity of the contact electrode (cf. Ref. [241] as an example of similar effects in graphene).

**Electron diffusion** Using the results of section 5.3.1, we proceed now to the calculation and interpretation of the energy dependent diffusion constant  $D$ . It is represented in the right panel of Fig. 5.8. Reminiscent of the shifted resistance maximum, the diffusion constant minimum is shifted by the same amount. Over a very broad range of chemical potential, the diffusion constants varies linearly with chemical potential. For Dirac fermions, eq. (5.12), this corresponds to a constant electron mobility. We extract  $\mu_e = 120.000 \text{ cm}^2/(\text{Vs})$  from the slope of the linear region (shown as a dashed dotted line). This high electron mobility is typical of TSS in (capped) strained HgTe 3D TIs [81, 82]. Obviously the mobility is harder to extract on the hole side. In view of the above discussion, it is likely to observe a mixed TSS electron and bulk-like hole conduction in this energy range. The coexistence of several types of conducting channels renders the evaluation of the Einstein relation impossible. There is a drastic drop in the diffusion constant (and thus in the mobility) for chemical potentials above  $\sim 300 \text{ meV}$ . Before we turn to investigate this feature in more detail, let us focus on the “Dirac-screening” regime in which the mobility is constant.

**Dominant scattering mechanisms** Despite forbidden back-scattering for helical TSS, multiple scattering events can lead to back-scattering and thus render the investigated system diffusive. This is the situation studied in this thesis. Transport signatures of several TSS electron scattering mechanisms have been theoretically investigated. These include short-range scattering, scattering off screened charge impurities [246], electron-phonon scattering [247] and TSS-to-bulk [212] scattering. Without entering into details

TABLE 5.1: Overview on predicted energy dependence of scattering times (note that  $k_F \propto \mu$  for Dirac fermions). Also shown is the expected dependence of conductivity as a function of charge carrier density. Here  $\rho$  designates the charge carrier density and the limit between “high” and “low”  $\rho$  corresponds to  $\sim 10^{13}/\text{cm}^2$  [246]. \*For surface-to-bulk scattering, the original paper does not provide these dependencies. (See main text for further explanations.)

Mechanism	Scattering time	Conductivity	Author [Ref.]
screened charges (low $\rho$ )	$\sim k_F$	$\sim n$	D. Culcer <i>et al.</i> [246]
screened charges (high $\rho$ )	$\sim k_F + k_F^2$	$\sim n + n^{3/2}$	—”—
Short range (low $\rho$ )	$\sim 1/k_F$	$\sim \text{Const}$	—”—
Short range (high $\rho$ )	$\sim \text{Const} + 1/k_F$	$\text{Const} + n^{1/2}$	—”—
Acoustic phonons	$\sim k_F^2$	$\sim n^{(3/2)}$	S. Giraud, R. Egger [247]
Surface-bulk scattering	$\sim 1/\sqrt{k_F}$	$\sim n^{1/4}$	K. Saha, I. Garate* [212]

of these theory papers, they predict clear signatures of these different scattering mechanisms in the energy dependence of the scattering time. These dependencies are summarized in table 5.1. Note that Saha and Garate [212] do not provide any power-law expression for surface-to-bulk scattering. Their numerical results feature several peaks in the scattering rate due to van-Hove singularities each time the chemical potential crosses a bulk sub-band. As we treat bulk conduction in the continuum limit (justified for thick enough samples), these divergences are expected to be washed out. An attempt to smooth their numerical data yields roughly the energy dependence of surface-to-bulk scattering provided in the table. It must be kept in mind that these calculations express the scattering rate as a function of the *global* chemical potential. As explained in chapter 3, in our experiment, only the surface chemical potential is varied.

The linear energy dependence of  $D$  corresponds to a linear increase of  $\tau$  for Dirac Fermions. Our experimental observations support thus electron scattering off screened charges to be the dominant TSS scattering mechanism in our sample. As the total charge carrier concentration varies only within several  $10^{12}/\text{cm}^2$ , cf. Fig. 5.3, the high density corrections calculated in reference [246] are negligible. This observation is also consistent with the “puddle-scenario” introduced in the discussion of the quantum capacitance data.

**Scattering enhancement at large chemical potentials** Fig. 5.8 shows a dramatic drop in the diffusion constant above 300 meV, corresponding to a drastic drop in the scattering time. This observation indicates the opening of a new – extremely efficient – scattering path for topological surface electrons. As described by Bastard in [85], based on a theoretical description developed by Mori and Ando [248, 249], for two-dimensional conductors, inter-sub-band scattering manifests itself as a discontinuity in the mobility. The authors consider a Boltzmann-equation approach to derive expressions for the scattering times  $\tau(\mu)$  in two-dimensional electron gases. In particular, they show

that when the Fermi level crosses a sub-band, the charge carrier density of this sub-band is small and therefore it does not contribute to transport. However, the scattering time is lowered by a factor roughly proportional to the DoS of the sub-band. In these works, it is also highlighted that “in practice, the mobility drop can never be achieved in quasi bi-dimensional materials due to thermal and collisional broadenings which blur the  $E_2$  onset.” [85, p.202].

Based on the presented experimental results, the following scenario is likely to occur: At low energies, the conductivity is dominated by high-mobility TSS. Application of an electric field on the surface rises the chemical potential, i.e. the electron concentration of the TSS. We have shown experimental evidence that this holds for surface chemical potentials below 250-300 meV in the so-called “Dirac-screening” regime. Over this region, the measured mobility is constant until the diffusion constant reaches a maximum value. This maximum corresponds to an electric field of  $1.6 \cdot 10^8$  V/m. The sudden mobility drop observed above 300 meV can be associated to the crossing of the Fermi level with another surface state (in principle featuring a step in the total surface DoS). However, no clear step feature is observed in the compressibility data (blue dots in Fig. 5.8, right panel). This can be understood either as the above mentioned blurring of the sub-band onset, or a lack of experimental resolution.

I claim that the observed mobility drop is indeed due to the appearance of a surface sub-band. In contrast to the case of semi-conducting (e.g. GaAs/GaAlAs quantum wells) 2D electron gases, the topologically protected high mobility of TSS makes them particularly sensitive to a sudden increase in the scattering rate. To my knowledge, this work constitutes the first experimental observation of such a drastic drop in mobility presumably due to inter-sub-band scattering.

### 5.3.3 Larger gate range

In order to confirm these observations, larger gate sweeps were performed. Fig. 5.9, shows the capacitance and resistance data as a function of gate voltage for the intrinsic sample over a larger gate voltage range ( $\pm 5$  V). Both resistance and capacitance show slight (reproducible) hysteresis. This gate voltage range remains however in the (almost) reversible regime, such that a quantitative analysis is still reasonable.

The drop in mobility (i.e. the maximum of the diffusion constant) develops into a resistance minimum, visible in the raw resistance data: above  $\sim 2.75$  V, the resistance increases. This *negative* transconductance is a striking feature of two-dimensional sub-band scattering and could be used in electronic device applications. As an example, a small signal amplifying transistor operated in the negative transconductance range

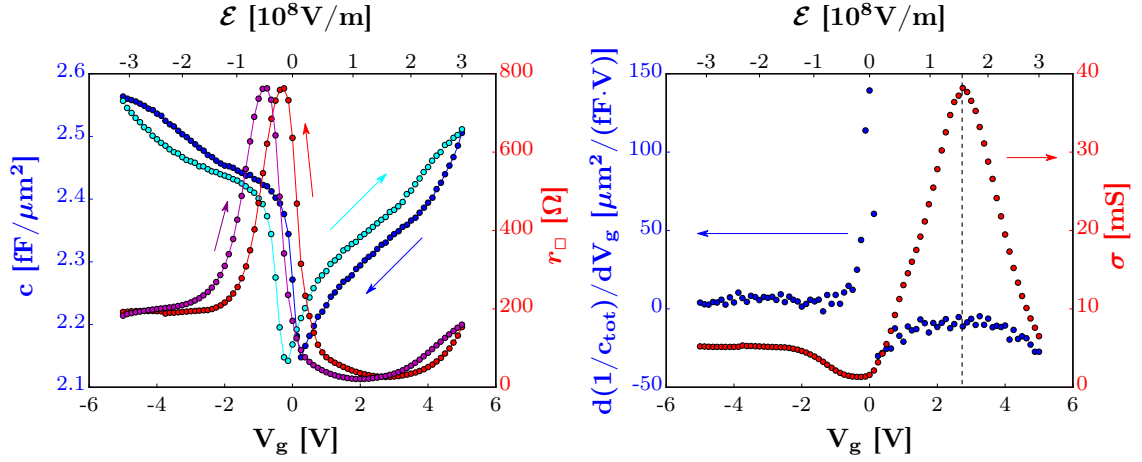


FIGURE 5.9: Left: Total capacitance per unit area and resistivity as a function of gate voltage for the intrinsic sample. The arrows indicate the direction of sweep. Right: the derivative of the inverse capacitance with respect to gate voltage (blue) reveals a change in the  $c_Q - V_g$  relation, accompanied by a conductance maximum (red) at  $V_g = 2.75$  V (indicated by the dashed line).

might show improved signal-to-noise performance, as it can be operated at high carrier densities, thus reducing shot-noise. A similar negative transconductance due to inter-sub-band scattering has recently been predicted for bilayer graphene [250], where the role of an external electric field was shown to play a crucial role.

The observed metastability in Fig. 5.9, renders the transformation to  $c_Q$  and  $\mu$  less reliable, as these transformations rely on equilibrium, whereas the hysteresis indicates the coexistence of different metastable equilibrium configurations. The data allows us however to investigate the capacitance behavior in the region of the resistance minimum in more detail. In order to overcome the issue of some uncertainty in  $c_{geo}$  we calculate the derivative of  $1/c_{tot} = 1/c_{geo} + 1/c_Q$  with respect to gate voltage in the right panel of Fig. 5.9. As ensured by the independent measurement of the M-O-M structure,  $1/c_{geo}$  is gate independent. Thus, this derivative contains only information about  $c_Q$ . The right panel of Fig. 5.9 shows also the conductivity for the same gate voltage range. We observe that conductance maximum and curvature inversion in the  $c_Q - V_g$  characteristic happen at the same critical voltage of 2.75 V. This unambiguously shows that the scattering enhancement is accompanied by a trend towards increasing quantum capacitance. This observation supports the inter-sub-band scattering hypothesis introduced above. We can identify the critical field for the appearance of this first sub-band based on this criterion to be given by  $\mathcal{E} = (V_g - V_s)/d_{ins} \approx 1.5 \cdot 10^8$  V/m.

As revealed by Fig. 5.10, very large gate voltage sweeps ( $|V_g| < 10$  V) present a more complex metastable behavior in capacitance and resistivity, presenting as a major feature a horizontal shift between forward and backwards sweep. As can be seen in the

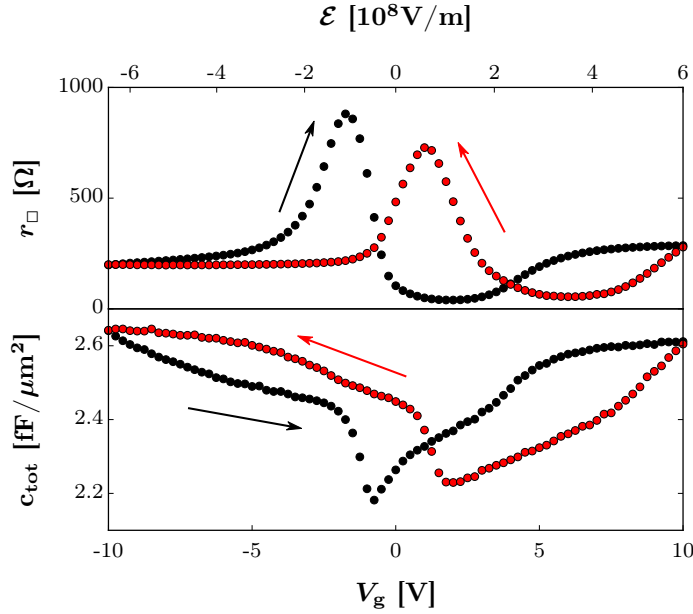


FIGURE 5.10: A gate voltage sweep over a very large range ( $|V_g| < 10$  V) reveals strong metastability and a saturating feature in the resistance data at large gate voltages. The arrows indicate the direction of sweep.

forward sweep, the observed resistance increase develops into a plateau, corresponding to a maximum in the scattering rate.

## 5.4 DC transport confirms sub-band scattering

As a crosscheck of the observed phenomenology, our collaborators in Würzburg, made Hall bars on the same material, respecting the same fabrication steps as for our RF MITI-Caps. Sample fabrication was carried out by Kalle Bendias. David Mahler carried out magneto-transport measurements at  $\sim 1.9$  K on a  $L = 600 \mu\text{m}$ ,  $W = 200 \mu\text{m}$  Hall bar.

**Longitudinal resistance** Fig. 5.11 shows the measured longitudinal resistance ( $R_{xx}$ ) at zero magnetic field as a function of gate voltage. The data shows qualitatively and quantitatively the same features as the RF measurements, cf. Fig. 5.9. As for the RF results, a large variability of the sheet resistance as a function of gate voltage can be observed with a resistance ratio  $r_{max}/r_{min} \approx 30$ , indicating that the gate mainly affects the top-surface as opposed to bottom TSS and bulk states. Furthermore, the resistance increase can also be observed in DC transport. However, the transfer curve is slightly shifted horizontally with respect to the RF data. Whereas the “resistive Dirac-point” in the RF measurement, Fig. 5.7, lies at  $V_g = -0.5$  V, it lies at  $-1.1$  V for the DC measurement.

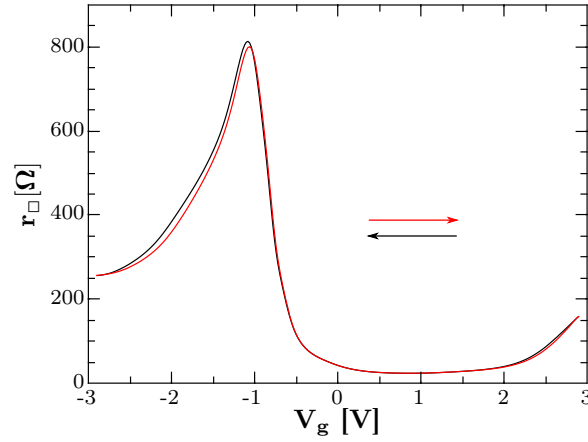


FIGURE 5.11: The longitudinal resistance of a Hall bar as a function of gate voltage. Dirac point and scattering onset are clearly visible. Measurements carried out by David Mahler in Würzburg. Note the close resemblance of this transfer curve as compared to the RF results in Fig. 5.9.

The same applies to the onset of a new scattering channel, manifest in the resistance minimum occurring at  $V_g \approx 0.9\text{ V}$  in DC ( $\sim 2\text{ V}$  in RF). The resistance minima being broad in both – RF and DC – measurements, the difference in gate voltage between Dirac point and onset of the new scattering channel  $\Delta V$  is subject to a rather high uncertainty. It lies in the 2 to 3 V range, whereas the DC measurements has a trend to show a smaller gate voltage distance. It can however not be excluded that capping layer and gate oxide slightly differ between the two samples.

**Small field Hall measurements** To support the sub-band hypothesis, magnetic field sweeps were carried out for different gate voltages by David Mahler in Würzburg. While the magnetic field  $B$  was swept, the Hall voltage  $V_H$ , was monitored, yielding  $R_{xy} = V_H/I$ . These measurements are shown for a selected range in Fig. 5.12 (a, b). For a single carrier type system, the Hall voltage is given by [141]:

$$R_{xy} = \frac{1}{en}B, \quad (5.13)$$

whereas the relation is largely enriched when two types of carriers coexist in the sample, Ref. [2, p. 240]:

$$R_{xy} = \frac{R_1\rho_2^2 + R_2\rho_1^2 + R_1R_2(R_1 + R_2)B^2}{(\rho_1 + \rho_2)^2 + (R_1 + R_2)^2B^2}B, \quad (5.14)$$

where

$$R_{1,2} = \frac{1}{en_{1,2}}, \quad \rho_{1,2} = \frac{1}{n_{1,2}e\mu_{1,2}}. \quad (5.15)$$

The main difference between the one- and the two-carrier situation is in the B field dependence of the derivative  $\partial R_{xy}/\partial B$ . Whereas it is constant for the former, it explicitly depends on the magnetic field for the latter. An S-shape in the  $R_{xy}-B$  characteristics can

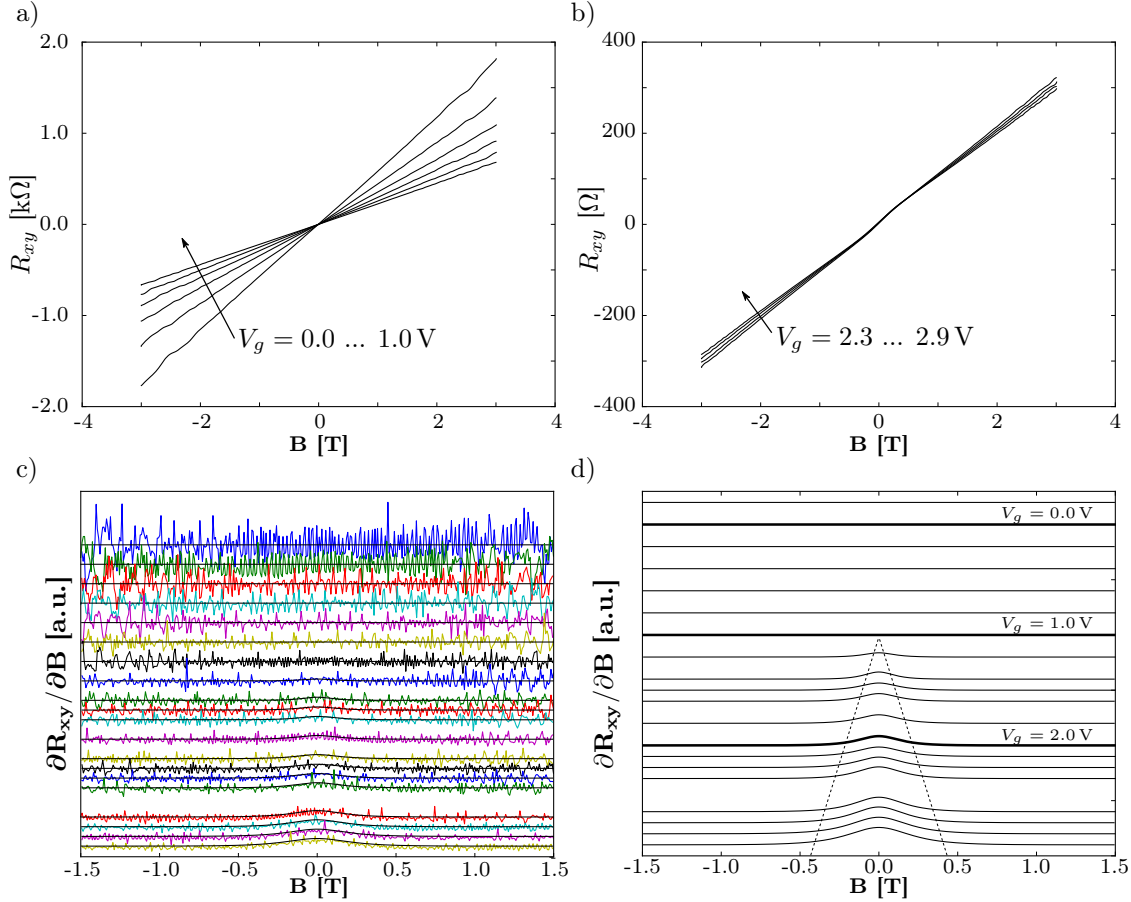


FIGURE 5.12: a)  $R_{xy}(B)$  for  $V_g = 0.0, \dots, 1.0$  V. The linearity of  $R_{xy}(B)$  is an indication of a single type of charge carriers contributing to electron transport. b)  $R_{xy}(B)$  for larger values of  $V_g$ . The curve features an S-shape at low fields. c) Numeric derivative  $\partial R_{xy}/\partial B$  and fits (black lines) to eq. (5.17). Background is subtracted and curves are shifted by an amount proportional to  $V_g$ . d) As (c). For clarity only the fitting results are shown. NB: The y-scale is stretched as compared to (c). The dashed triangle is a guide for the eye indicating the appearance of the S-shape.

thus be interpreted as a signature of two-carrier conduction. The raw data in Figs. 5.12 (a, b) indicate that for low positive gate voltages (a), only one carrier type exists, whereas the slight S-shape in (b) indicates the formation of a sub-band hosting a second type of carriers for higher gate voltages.

Here we do not aim at a quantitative analysis of the data, but focus on a qualitative understanding as follows: Instead of performing a four-parameter fit on the experimental data, subject to relative large uncertainties (cf. the discussion in chapter 2), we describe the S-shape by a generic function, based on a tanh:

$$R_{xy} \approx \alpha_1 B + \alpha_2 B_0 \tanh(B/B_0). \quad (5.16)$$

with the adjustable parameters  $\alpha_1, \alpha_2$  and  $B_0$ . Thus, the derivative of this generic S-shape function describes a peak-like curve, defined by

$$\frac{\partial R_{xy}}{\partial B} \approx \alpha_1 + \alpha_2 \frac{1}{\cosh^2(B/B_0)}. \quad (5.17)$$

In Fig. 5.12 (c), I show the numerically determined derivative of the measured Hall resistance as a function of magnetic field in the small field range ( $|B| < 1.5$  T). For clarity, the overall slope ( $\alpha_1$ ) was subtracted from all curves, and the curves were shifted by an amount proportional to  $V_g$ . Also shown in this figure are fits on the experimental data, using eq. 5.17. For clarity, only the fitting results are shown in Fig. 5.12 (d), where a smaller shift proportional to  $V_g$  was chosen in order to highlight the appearance of the peak-feature at small  $B$ -fields. Note that the peak starts to develop at gate voltages larger than 1 V. This is indicated by the dashed line in Fig. 5.12 (d), constituting a guide for the eye. Within experimental resolution, the appearance of the sub-band thus corresponds to the minimum in resistance.

We thus observe that the resistance increase is accompanied by the appearance of a sub-band. Therefore, we interpret the mobility drop (conductivity drop) as a strong inter sub-band scattering.

**Quantitative analysis** From eq. (5.14), we conclude that at high magnetic fields, the carrier type with higher concentration dominates the  $R_{xy}$  behavior:  $R_{xy} \sim 1/(n_1 e)B$ . This limit is reached for  $|B| > 0.5$  T. As the topological surface state concentration is higher than that of the sub-band, we can use the  $\alpha_1$  parameter of eq. (5.17) to obtain an estimate of the TSS filling rate. Fig. 5.13 shows the variation of the charge carrier density extracted from  $n_{\text{TSS}} = \frac{1}{\alpha_1 e}$  as a function of gate voltage. The observed linear relation corresponds to a constant filling rate  $\partial n_{\text{TSS}}/\partial V_g = 1.8/(\text{Vcm}^2)$  or equivalently to a fixed capacitance  $c_{\text{tot}} = 2.9 \text{ fF}/\mu\text{m}^2$  in good agreement with the direct capacitance measurements. The value obtained from the filling rate is roughly 10% higher than the measured capacitance values. This explains why the distance between Dirac point and the opening of the scattering channel is slightly smaller in DC: It implies that the sub-band begins to be populated at roughly the same TSS carrier concentration as was estimated from the RF measurements. The higher capacitance of the DC sample also suggests a slightly thinner gate oxide on this sample. As a consequence the electric fields applied to the top surface are also larger.

**Concluding remarks** The DC measurements support the above interpretation of the RF-capacitance data. The increase in longitudinal (sheet) resistance is caused by the

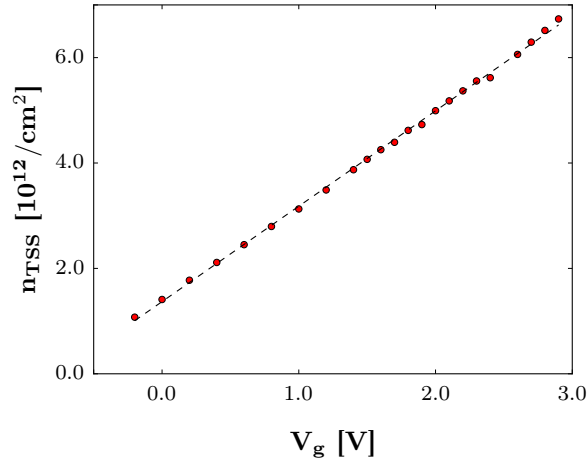


FIGURE 5.13: The electron concentration of the dominant electron-like conducting channel as extracted from  $\alpha_1 = 1/(ne)$  as a function of gate voltage. The dashed line is a linear fit to the data and indicates a filling rate  $\partial n_{TSS}/\partial V_g = 1.8/(\text{Vcm}^2)$ .

emergence of a sub-band, which has as main effect a strong increase of the TSS scattering rate, causing the overall resistance to rise. From the DC data, the electric field at which filling of a sub-band occurs can be estimated from  $\mathcal{E}_1 = V_g/d_{ins} \approx 0.7 \text{ V/m}$ . The TSS charge carrier density (as determined from magneto-transport) at which the sub-band occurs is  $n_c = 3.1 \cdot 10^{12}/\text{cm}^2$ .

## 5.5 Metastability

The capacitance measurements (section 5.2) revealed the appearance of metastability via hysteresis in the  $C(V)$  and  $R(V)$  characteristics. Note that also in DC transport such a hysteresis is visible in Fig. 5.11. We highlight that the hysteresis loops are reproducible, i.e. continuous cycling of the gate voltage produces closed loops in the capacitance data. The hysteresis is thus due to a metastable situation in the charge-voltage characteristics.

In this section we analyze the metastability in more detail and provide a physical interpretation of the phenomenology. The systematic study of hysteresis requires the acquisition of a large number of data points. The rather slow acquisition rate ( $\sim 30 \text{ s/spectrum}$ ) of the RF measurements or the magnetic field sweeps led us to focus on low-frequency Lock-in  $C(V)$  measurements in order to investigate the metastability. We shall thus focus again on the capacitor structure, presented in the first sections of this chapter.

Fig. 5.14 (a) shows the  $C(V)$  characteristics of the intrinsic sample as a function of gate voltage for different gate voltage *ranges*. The reversible  $C(V)$  characteristic  $|V_g| < 3 \text{ V}$  is highlighted in green (in the center of the figure). Experimentally, these  $C(V)$  characteristics were acquired by starting from small gate voltage sweeps ( $|V_g| \leq 0.25 \text{ V}$ )

and slowly increasing the amplitude of the gate voltage excursion up to  $\pm 10$  V by steps of 1 V.

For each choice of maximum gate range, the gate voltage was cycled 7 times between  $-V_{max}$  and  $V_{max}$  while recording the capacitance. The  $c(V)$  characteristic is reproduced over these cycles. Furthermore, we performed hysteresis loop measurements for different sweep rates (0.1-500 Hz for the gate cycling frequency) and varying probing frequency. The hysteresis was independent of these parameters. Hence, they are due to metastable equilibrium and *not* to transient charging situations.

In order to define the vocabulary of this section, a sweep from negative (positive) to positive (negative) gate voltages will be called a *forward* (*backward*) sweep. For clarity not all sweeps are shown.

The metastability presents two main features: First, the forward sweep  $C(V)$  characteristic is shifted to the left with respect to the reversible sweep, while for the backward sweep it is shifted to the right. Second, the measured minimal capacitance, i.e. the background capacitance at the Dirac point tends to *increase* when the gate voltage range is increased.

**Horizontal shift** We note that the steepest slope in  $C(V)$  is observed on the hole side in close vicinity to the Dirac point where the capacitance has a typical value of  $2.3 \text{ fF}/\mu\text{m}^2$ . In order to quantify the hysteretic horizontal shifts, we track the gate voltage corresponding to this capacitance value (on the hole side) as a function of gate voltage range.

For a given gate voltage range, defined by  $V_{max}$ , we can thus calculate the distance between forward and the backward sweeps  $\Delta V_g$ . This difference is plotted against  $V_{max}$  in Fig. 5.14 (c). As observed in the previous sections, the system remains in a reversible state as long as the gate voltage is limited to  $\pm 3$  V. For larger gate voltages, the system falls in two distinct local equilibria, depending on the sweep direction, causing the capacitance and the resistance (Fig. 5.9) to show hysteresis. We lack a microscopic understanding of the local minima, but some experimental facts give clear hints about the nature causing the hysteresis, as will be developed below.

First, we note that the appearance of metastability occurs at similar gate voltages as the resistance minimum and the change of capacitance curvature as show both panels of Fig. 5.9. The comparison of the DC and RF data have shown that this corresponds to the physical situation in which a second type of carriers contributes to the Hall resistance.

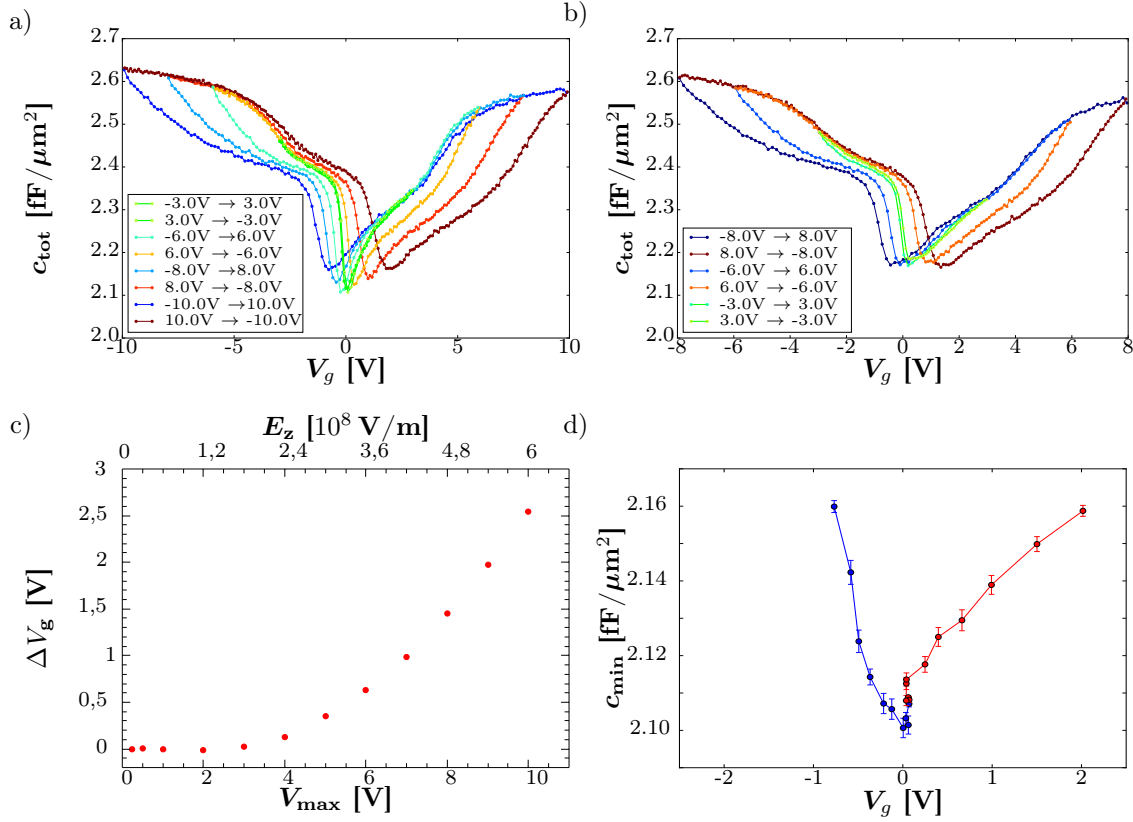


FIGURE 5.14: a) Capacitance-voltage characteristics of the intrinsic sample for different gate voltage *ranges*, when the gate voltage range is step-wise increased from  $\pm 3$  V to  $\pm 10$  V. Cold (warm) colors indicate sweeps from  $V_g < 0$  ( $V_g > 0$ ) to  $V_g > 0$  ( $V_g < 0$ ). The thick green line corresponds to the reversible sweep  $\pm 3$  V discussed in 5.2. b) Similar to (a) for stepwise decreasing gate range. c) The horizontal shift (defined by the opening of the hysteretic loop, cf. main text) as a function of maximum gate voltage range. d) Capacitance minimum and the corresponding gate voltage for the gate voltage ranges presented in (c). The blue (red) data points correspond to sweeps from  $V_g < 0$  ( $V_g > 0$ ) to  $V_g > 0$  ( $V_g < 0$ ).

These observations present evidence that the metastability is attributed to the population of a sub-band. Further information can be gained from the evolution of the minimum capacitance with increasing gate voltage range.

**Upwards shift of capacitance minimum** In Fig. 5.14 (a) we observe an increase of the minimal capacitance for increasing gate voltage range. In Panel (d) we show this minimal capacitance and the corresponding gate voltage for different gate voltage ranges. Such an increase in the background capacitance at the Dirac point is – by virtue of the discussion in section 5.2 – likely due to an increase of the bulk charge carrier density. Indeed: The Dirac point corresponds to the minimum in the TSS DoS. Thus, the background (quantum) capacitance at the capacitance minimum is due to bulk carriers.

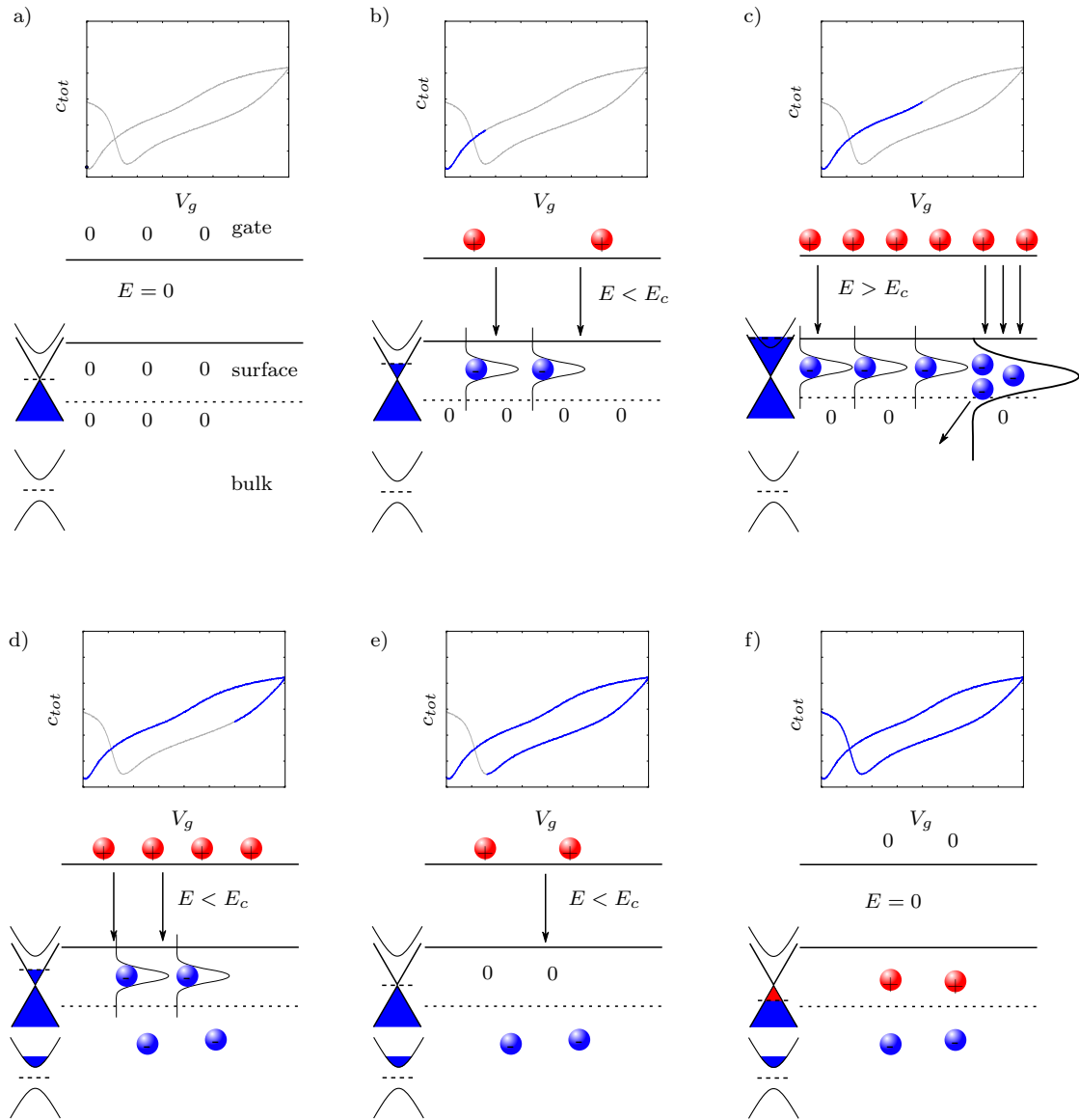


FIGURE 5.15: Sketch of the gate voltage dependent evolution of charge distribution within the sample. The shown  $C(V)$  characteristics correspond to a  $0 \rightarrow 8 \rightarrow 0V$  sweep. a) At zero gate voltage, the sample is in its intrinsic state. The bulk is charge empty, the TSS at the Dirac point (minimum in Capacitance). b) Increasing the gate voltage increases the electric field and populates the TSS. Due to Dirac-screening no charge is transferred to the bulk. c) Beyond a critical electrical field, a surface sub-band becomes populated, leading to charge transfer towards the bulk. d) When the electric field is lowered below the critical field, the system falls into a metastable configuration with charges in the TSS but also in the bulk. Due to the lack of sub-band states, Dirac screening exists again. e) At a positive gate voltage, the TSS-Dirac point is reached. The charge on the gate electrode is compensated by the (metastable) bulk carriers. f) At  $V_g = 0$ , the TSS and the bulk charges are exactly the same due to overall charge conservation. For the TSS this corresponds to  $p$ -type doping.

The observed phenomenology thus allows us to build a consistent image of the charge distribution within the sample for different situations, represented schematically in Fig. 5.15. It is based on a sub-band-induced charge pumping effect.

Starting from a situation in which the bulk charge carriers are negligible as compared to the TSS charge density and the TSS being close to the Dirac point (panel a), when small positive gate voltages are applied, the TSS becomes populated, lowering the resistance and increasing the DoS, signaled by an increasing DoS. Experimentally this corresponds to a higher capacitance (panel b). Above a threshold voltage for which a massive surface sub-band is populated, the Dirac-screening breaks down. The sub-band mediates a (metastable) charge transfer towards the bulk (panel c). Furthermore, this charge transfer tends to lower the electric field at the surface<sup>7</sup>. When the gate voltage is subsequently lowered, Dirac screening is recovered starting from the moment when the surface sub-band is emptied again. However, the electrostatic environment of the TSS is different: A negative bulk charge background exists now. Therefore, the TSS Dirac point is reached at a finite positive gate voltage (panel e). In this situation the bulk carrier density is finite. Therefore, it contributes to the overall quantum capacitance, cf. chapter 3 and section 5.2. This causes the capacitance minimum to lie at a higher level. The finite charge density in the bulk corresponds to a new (metastable) equilibrium at  $V_g = 0$ . In order to recover over-all charge neutrality, the residual negative charge in the bulk is compensated by a hole density in the TSS (panel f). The same line of thought can of course be applied to the domain of negative gate voltages. In this case, beyond the limits of Dirac screening, holes are transferred from the surface to bulk states.

When the gate voltage range is lowered after a large excursion, the capacitance minimum remains higher as compared to the initial situation. This is illustrated in Fig. 5.14 (b). We interpret this feature as a change in the sample's bulk charge properties. We highlight that the initial configuration can be recovered by warming up and subsequent cool-down.

The appearance of metastability is also observed on the n-type sample. This data is presented in Appendix E.

## 5.6 Summary and conclusions about experimental observations on an intrinsic HgTe-based MITI-Capacitor

The observations of sections 5.2-5.5 lead to the following interpretation of our experimental data on the intrinsic sample: For small gate voltage ranges, the electric field is entirely screened by topological surface states. This situation holds over a large range of

<sup>7</sup>This is important in the discussion of the simple model presented in section 5.8.

Experimental criterion	$V_{g,c}[V]$	$\mathcal{E}_1$ [ $10^8\text{V/m}$ ]	$n_1$ [ $10^{12}/\text{cm}^2$ ]	$\mu_s$ [meV]	Figure
Diffusion constant decrease	2.0	1.2	2.9	300	5.8, 5.7
Conductance maximum and Change of slope in $1/c_Q$	2.0 / 2.75	1.1 / 1.6	2.8 / 3.9	310 / 375	5.9
Onset of hysteresis	$\sim 3.0$	$\sim 1.8$	$\sim 4.2$	$\sim 450$	5.14
Non-linear $R_{xy} - B$ characteristic (DC)	1.0	$\sim 0.7$	3.2	–	5.12, 5.13
Minimum in $R_{xx}$ (DC)	0.9	$\sim 0.7$	3.0	–	5.12, 5.13

TABLE 5.2: The values of gate voltage, electric field, charge carrier density and surface chemical potential where (first) population of a sub-band occurs. For the criterion based on the conductance maximum and the change of curvature in the quantum capacitance, the first (second) value corresponds to the forward (backward) sweep. Without relying on a precise model, we cannot calculate the surface chemical potential from the DC measurements.

chemical potentials (up to  $>300$  meV) and confirms the Dirac-screening also observed by our collaborators in Würzburg, [135] in magneto-transport. Above a threshold voltage on the order of 3V (for the capacitor structures), a sub-band is populated, causing a break-down of the Dirac screening paradigm. The appearance of this sub-band has a four-fold experimental signature:

First, it causes a sudden decrease in the electronic diffusion constant, presumably due to inter-sub-band scattering. This effect is so strong that it corresponds to a minimum in the sheet resistance.

Second, it manifests itself in a smooth increase of the sample capacitance due to the enhanced surface DoS.

Third, the Hall resistance reveals the appearance of a second charge carrier type at a gate voltage coinciding with a minimum in longitudinal (i.e. sheet-) resistance.

Fourth, the sub-band states are connected to bulk-states of the HgTe TI-material, leading to a charge transfer from the topological surface states towards the bulk. This gives rise to a new (metastable) configuration of the charge distribution.

The gate voltages, charge carrier densities and electric fields at which the sub-band appearance manifests depending on the experimental criterion are summarized in Table. 5.2.

For the capacitor measurements, we have observed  $n(V_g = 0) \approx 0$ . Thus, the definition

of (total) charge carrier density and electric field (eq. (5.3)) is unambiguous. However, as revealed by Figs. 5.11 and 5.13, for the DC sample, we observe that the resistance maximum and the extrapolated minimum in charge carrier density occur at  $V_g \neq 0$ . For these measurements, it is thus natural to define the charge carrier density with respect to this minimal charge carrier density. From the analysis of the weak field Hall resistance, we extract  $n(V_g = 0) \approx 1.4 \cdot 10^{12}/\text{cm}^2$ . The electric field on the other hand as determined by Gauß' law on the other hand depends on the variation of total charge with respect to the  $V_g = 0$  situation, i.e. for the DC data, we have

$$\mathcal{E} = \frac{e[n - n(V_g = 0)]}{\epsilon_0 \tilde{\epsilon}_{ins}}. \quad (5.18)$$

The observed hysteresis can qualitatively be understood in terms of surface-to-bulk charge transfer. The hysteresis as a function of gate voltage range presents a rather smooth crossover. Hence extraction of a “critical” voltage is more difficult.

Note that the idea of the sub-band's wave-function being “connected” to the bulk states of the material, enables a charge transfer from the surface layer to the bulk. Metastability is generally associated with asymmetric barriers in the system and therefore undermines the overall electrochemical equilibrium assumption. In other words, the effective (local) electrochemical potential  $\mu^* = \mu + qV$  might be changed and become inhomogeneous once hysteresis occurs.

In section 5.8, I will present a theory that predicts the interface spectrum as a function of surface electric field and surface chemical potential. We shall point out that in the framework of this theory, the electric field has to be measured on the TI-side at the interface between gate oxide and TI. Experimentally however we determine the (effective) electric field in the insulating layer, eq. (5.2) and (5.3). This detail will be discussed in section 5.9.

Before I present this model, I will show some supplementary data on the n-type sample that supports the sub-band interpretation.

## 5.7 The n-type sample

In our experiment, it is not possible to vary electric field and surface chemical potential independently. The above (quantitative) discussion focused on the intrinsic sample. However, the n-type sample constitutes a system in which the relation between  $\mu_s$  and  $\mathcal{E}$  is different than for the intrinsic sample, cf. fig. 5.3.

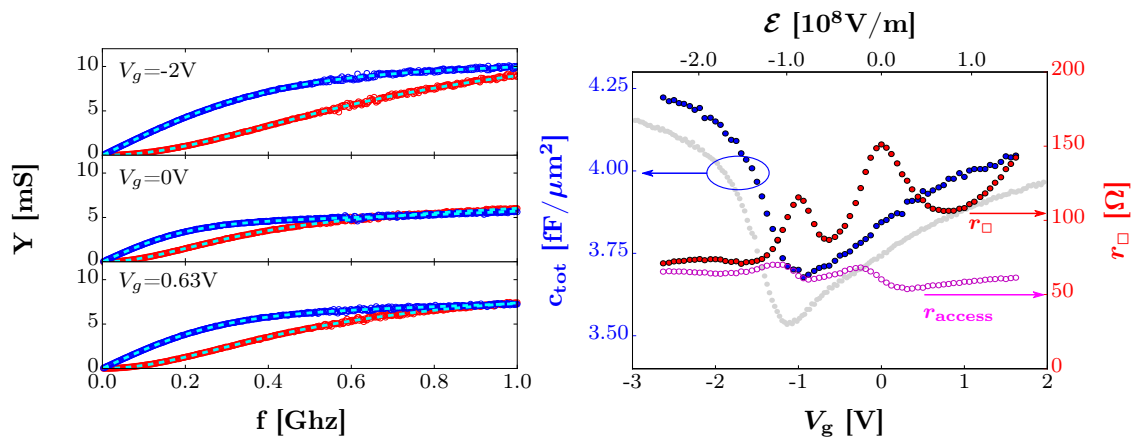


FIGURE 5.16: Left: The gate dependent admittance spectra (real part in red, imaginary part in blue) for three representative gate voltages on the *n*-type sample. The dashed light blue lines are fits using the 1D model. Spectra are corrected for the access resistance. Right: the capacitance (blue) and the sheet resistance (red) extracted from the RF admittance spectra. For comparison, the capacitance as extracted from the low frequency measurements is shown in gray. Also shown is the access resistance (pink) as extracted from the RF admittance. Note that the finite bandwidth (0-1 GHz) of this measurement renders the extraction of  $r_{access}$  less reliable.

We therefore also performed RF admittance measurements on this sample. Fig. 5.16 shows the RF spectra and the extracted capacitance and resistivity for the *n*-type sample. We note that the fitting with a 1D distributed RC-line model works equally well on this sample. Thus we can precisely extract the capacitance, resistance and access resistance, shown in the right panel of Fig. 5.16 for a  $V_g = -2.65 \text{ V} \dots 1.65 \text{ V}$  sweep.

### 5.7.1 Capacitance

Similar to the intrinsic sample the shift between RF and quasi-DC is due to a systematic offset in the amplifiers. We shall therefore not focus much on a quantitative analysis of this data. In contrast to the resistance data, the capacitance shows however a “well-behaved” gate dependence: It varies monotonically on the *p* and on the *n* side, left and right of a capacitance minimum, respectively. This observation allows us – in analogy to the intrinsic sample – to fix the following notation: We continue to call Dirac point the capacitance minimum at  $V_g \sim -1 \text{ V}$  as it corresponds to a minimum of the DoS.

### 5.7.2 Resistance

The resistance data reveals a rich phenomenology, including a global trend towards increasing resistance when the gate is varied from negative to positive values and several peaks, featuring varying widths and amplitudes.

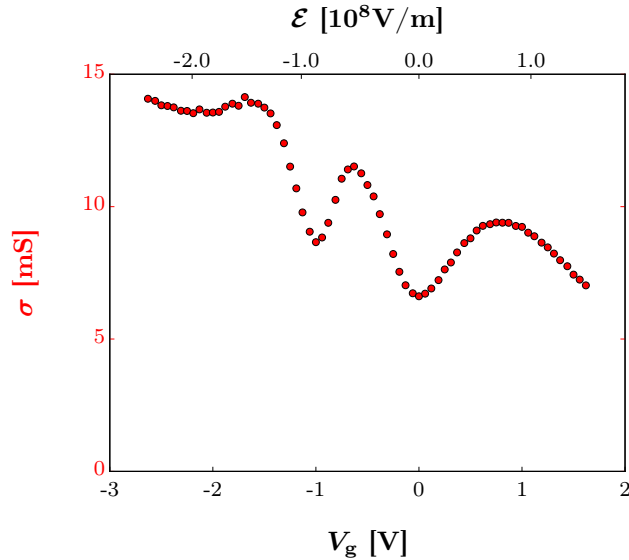


FIGURE 5.17: The conductivity as a function of gate voltage for the n-type sample. As discussed in the main text, the general downwards shift of the curve might be due to an improper assessment of the access resistance.

There seems to be a general upwards trend in the total resistance with varying gate voltage. This feature might however be an artifact of the fitting procedure: For these measurements, we limited the bandwidth to 1 GHz, rendering the extraction of  $R_{access}$  less reliable. The fitted access resistance is shown in light red in Fig. 5.16. We note that while  $r_{\square}$  shows an upwards trend,  $R_{access}$  shows the opposite trend. As the admittance's real part at low frequencies is governed by  $(1/3R + r_{access})$  (cf. Chapter 4), the orthogonality of both fitting parameters is less ensured. This could explain the apparent trends. We shall therefore not focus on this feature further.

The most striking observation are the multiple peaks in resistance, when the gate voltage is varied. Before investigating these more closely, let us highlight the differences in the resistance data between the intrinsic and the n-type sample. One main difference lies in the explored resistance range: Whereas for the intrinsic sample, it varies by roughly one order of magnitude (between  $\sim 50 \Omega$  at  $V_g \sim 2.5 \text{ V}$  and  $\sim 700 \Omega$  at  $V_g \sim -0.5 \text{ V}$ , Figs. 5.7, 5.9), the variation for the n-type sample is much weaker. This is consistent with the assumption of an (n-type) bulk background on the n-type sample. Indeed, the gate mainly varies the charge carrier density of the TSS, whereas the bulk carrier density is only affected in a thin layer corresponding to an effective depletion width on the order of  $\lambda \sim 10 - 20 \text{ nm}$ . Thus, the bulk resistivity can only vary by a factor of  $\lambda/d_{sample} \sim 20\%$ . For simplicity, we assume that the variation is completely carried by the topological surface state, whereas bulk (and bottom TSS) cause a constant conductivity background.

Within this assumption the total conductivity is given by

$$\sigma(V_g) = \frac{1}{r_{\square}(V_g)} = \sigma_{bulk} + \sigma_{TSS}^{bottom} + \sigma_{TSS}^{top}(V_g). \quad (5.19)$$

We can thus estimate  $\sigma_{bulk} + \sigma_{TSS}^{bottom}$ . In order to simplify the discussion, Fig. 5.17 shows the conductivity as a function of gate voltage as extracted from the RF resistivity, Fig. 5.16. In the following, we ignore the general downwards trend and identify a residual conductivity at the DP of 7.3 mS.

Our experiment is not able to resolve quantitatively how this residual conductivity is distributed between bulk and bottom surface. If we assume  $\sigma_{bulk} \gg \sigma_{TSS}^{bottom}$  and use the estimate of bulk carrier density from section 5.2,  $n_0 = 2.1 \cdot 10^{17}/\text{cm}^3$ , we can calculate a bulk mobility using Drude's formula  $\sigma = ne\mu_e$ . This allows us to give an upper bound for the bulk's electron mobility  $\mu_e < 32.000 \text{ cm}^2/(\text{Vs})$ . As we entirely neglected the bottom surface conduction, this is of course an overestimate. We have thus shown that the n-type sample presents the coexistence of several electronic fluids, contributing to conductivity and quantum capacitance. In this situation a naive application of the Einstein formula must be ruled out.

Let us now turn the discussion towards the multiple peaks observed in the resistance data. As seen for the intrinsic sample, one of the resistance peaks coincides roughly with the minimum of capacitance, indicating its association to the TSS Dirac point. As is expected, the resistance drops when the TSS carrier concentration is increased in the range  $V_g = -1 \text{ V}$  to  $V_g = -0.5 \text{ V}$ . The subsequent increase in resistance resembles strongly that of the intrinsic sample (around  $V_g \approx 2.5 \text{ V}$  in Fig. 5.9). It corresponds thus to a dramatic drop in mobility causing an increase in the resistance away from the Dirac point. As for the intrinsic sample, this drop in conductivity is interpreted as the appearance of a surface sub-band. This feature thus confirms our observations on the intrinsic sample. In contrast to the intrinsic sample however, the resistance increase saturates around  $V_g = 0 \text{ V}$  before it drops again at positive gate voltages (in the range  $V_g = 0 \rightarrow 1 \text{ V}$ ). This observation suggests that for the n-type sample a first sub-band augments the scattering rate before it contributes itself to the conductance, yielding the second drop in resistance between 0 and  $\sim 1 \text{ V}$ . In contrast to the intrinsic sample, going to even higher gate voltages allows us to observe the appearance of a second sub-band, eventually causing the next resistance increase (above  $\sim 1 \text{ V}$ ).

We lack an exact theory for inter-sub-band scattering in the present setting but point out that theoretical predictions on multi-layer graphene [250], point towards physical systems in which the main effect of a (massive) sub-band coexisting with an extremely mobile Dirac-like band is to cause an increase of the Dirac states scattering rate. The

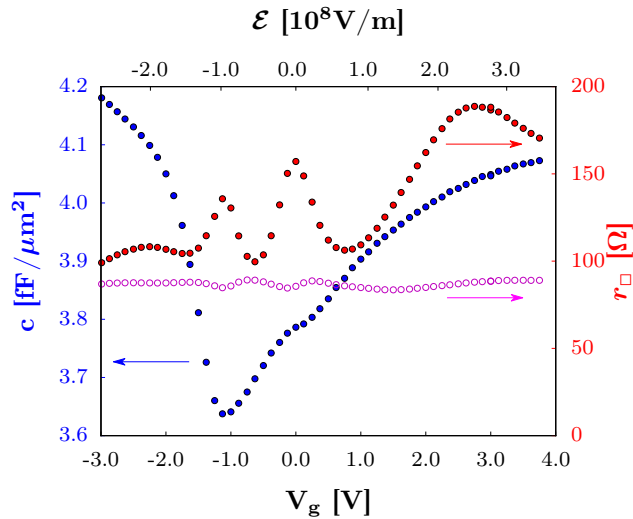


FIGURE 5.18: The capacitance (blue) and the sheet resistance (red) extracted from the RF admittance spectra for a device from the n-type batch with a longer contact area (cf. Chapter 4). Also shown is the access resistance (pink) as extracted from the RF admittance. We explored a larger gate range on this sample. The features observed in Fig. 5.16 are shown to be robust. The larger gate range reveals the peak-structure of the second resistance increase.

multiple peak features observed on the n-type sample suggest thus that in these samples, the surface Fermi level crosses not only one but several of these sub-bands.

### 5.7.3 Robustness of the phenomenology

**A second device** In order to test the robustness of these features, the same type of RF measurements was carried out on a slightly larger gate voltage range on a second device from the n-type batch. For this sample, the contact covered a longer portion of the channel (cf. Chapter 4). Fig. 5.18 shows the capacitance and resistivity data for this second device from the n-type batch over a larger gate voltage range. The Dirac point and the first sub-band-scattering peak are thus shown to be device independent features. This confirms the existence of underlying physical effects causing the observed phenomenology. The extended gate voltage range, explored on this sample reveals further that the second resistance increase observed for  $V_g > 1$  V attains also a maximum around  $V_g = 3$  V, resulting in a third resistance peak. This suggests that pushing the gate voltage to even higher values might lead to the observation of an even larger number of scattering peaks. Unfortunately this is not possible in our experiments, as at some point dielectric breakdown occurs.

For this second device, we also performed a comprehensive temperature dependence study. The resistance data as a function of gate voltage for different temperatures are shown in Fig. 5.19. As for the intrinsic sample, it goes beyond the scope of the present

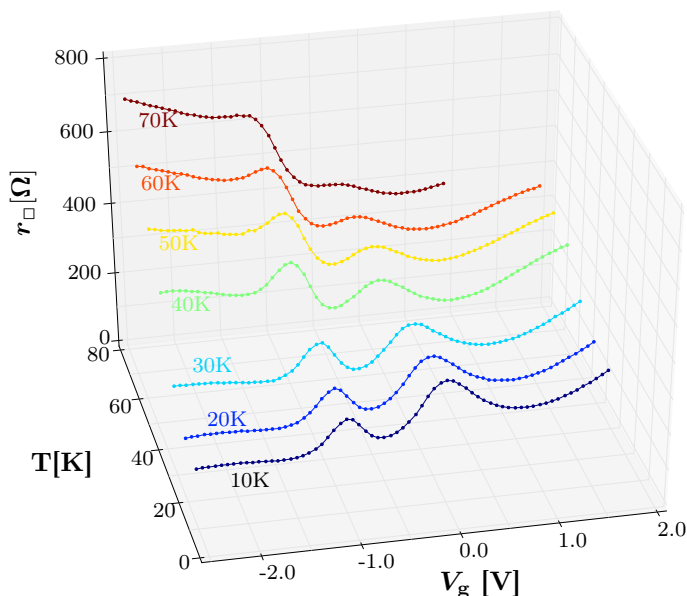


FIGURE 5.19: Resistance as a function of gate voltage for different temperatures. Note the changing relative height of the Dirac peak and the sub-band scattering peaks.

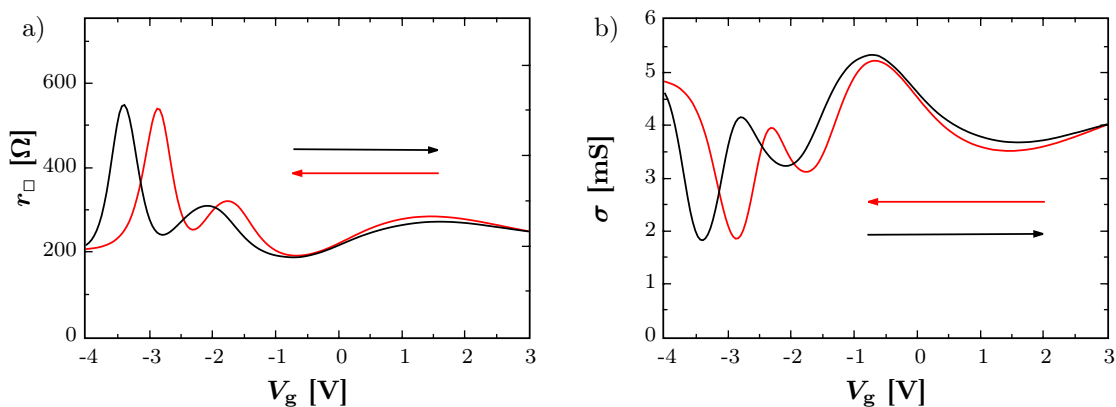


FIGURE 5.20: Sheet resistance (a) and conductivity (b) as a function of gate voltage measured in Würzburg on a Hall bar at zero magnetic field. The arrows and the colors indicate the direction of sweep.

work to understand the full image of this temperature dependence. For increasing temperatures we identify however two main features:

First, the resistance globally increases and second, the relative height of the scattering peaks with respect to the Dirac point resistance maximum decreases. We attribute these two observations to phonon scattering. It is known (e.g. Ref. [247]) that phonon scattering is enhanced at higher temperatures. This explains the general increase in resistivity and the reduced weight of inter sub-band scattering to the total scattering rate.

### 5.7.4 DC measurements

As a second double check of our experimental findings, our collaborators in Würzburg measured (similar to the intrinsic sample) the gate voltage dependent longitudinal resistance of a Hall bar ( $W = 10 \mu\text{m}$ ,  $L = 30 \mu\text{m}$ ). The sheet resistance and the conductivity are represented in Fig. 5.20. Albeit all qualitative features are reproduced, the DC data differs from the RF results in some aspects:

First, the range of resistances is higher by roughly a factor of two. This might be due to a reduced background conductivity.

Second, the general upwards trend in resistance for increasing gate voltage, observed in the RF resistance data, is not present in the DC measurements.

Third, all features in the DC data are shifted to even larger negative gate values as compared to the RF results indicating a slightly larger doping of this sample.

Fourth, the relative height of the peaks changed. The Dirac point features the highest resistance  $r_{\square} = 550 \Omega$ , whereas the first and the second scattering peaks show a decreasing amplitude. We note that it is mainly the height of the Dirac peak that increases in DC as compared to the RF measurement. However, it is interesting to highlight that the relative height of the peaks is inverted as compared to the RF measurements.

### 5.7.5 Conclusions

The experimental signatures of sub-band occupation and inter sub-band scattering at high energies in the intrinsic sample, presented in the first part of this chapter, were four fold, cf. section 5.6. Notably, we have observed the population of a first sub-band energetically above the topological surface state. The n-type sample reveals the existence of several of these sub-bands.

There are two main differences between the n-type and the intrinsic sample: The first lies in the residual charge carrier density. The second lies in the explored range of electric fields. As the insulating layer for the n-type is smaller than for the intrinsic sample, the electric fields (at same gate voltage) on the n-type sample are larger.

We search therefore for a model that describes the phenomenology of both samples, taking electric fields and carrier densities explicitly into account. In the next section I will present a heuristic model that predicts the existence of massive sub-bands. In particular, they will be shown to be of topological origin.

## 5.8 A relativistic model

As our experiments might be the first observation of sub-bands causing a mobility drop so strong that the resistance presents a minimum and the second study to report on Dirac screening, the natural question is in which detail our experiments differ from previous studies. A main difference of our experimental setup as compared to previous studies (cf. chapter 2) lies in the very thin gate insulator layer and the associated very large electric fields on the order of  $10^8$  V/m. To our knowledge, little attention has been paid to the role of strong (external) electric fields on the behavior of topological surface states. Wray *et al.* presented ARPES data, revealing a renormalization of the TSS Fermi velocity under surface dopant induced surface electric fields [251]. Baum *et al.* performed self-consistent  $\mathbf{k} \cdot \mathbf{p}$ -calculations, predicting a shift of the Dirac point position with respect to the bulk bands and the population of bulk bands [41]. This last prediction is however incompatible with experimental findings at strong magnetic fields [135] due to Dirac screening.

Here, a very simplified theoretical description of surface phenomena in TI systems with strong electric fields will be presented that was developed by our collaborators from the Université d’Orsay. The details of this work constitute a part of the PhD thesis of Serguei Tchoumakov to appear next year. I will therefore only present the main lines and the results of the calculation. Due to the relativistic character of Dirac fermions, the theory is inspired by a pseudo-relativistic treatment of Landau levels in graphene in crossed electric and magnetic fields [252]. A similar theory was developed in the context of Majorana physics [253] and Weyl semi-metals [214, 254]. The theory makes several rather rough assumptions, commented in section 5.8.2, however it has the advantage to yield analytic results and involves *in fine* only two adjustable parameters: A bulk Fermi velocity  $v_F$  and a *topological confinement field*  $\mathcal{E}_T$ .

### 5.8.1 Presentation of the model

In order to avoid confusion, electric fields are denoted  $\mathcal{E}$  and energies  $E$  in this section.

**The basic Hamiltonian of a TI-I interface** The starting point of the theory is a minimal Hamiltonian describing the bulk bands of a “massive Dirac” system. It is based on a simplified BHZ Hamiltonian initially introduced in order to describe Bismuth-based

TIs, expressed in the basis of  $(|P1_z^+, \uparrow\rangle, |P2_z^-, \uparrow\rangle, |P1_z^+, \downarrow\rangle, |P2_z^-, \downarrow\rangle)$ , Refs. [62, 70]:

$$\hat{H} = \begin{pmatrix} \Delta & \hbar v_F k_z & 0 & \hbar v_F k_- \\ \hbar v_F k_z & -\Delta & \hbar v_F k_- & 0 \\ 0 & \hbar v_F k_+ & \Delta & -\hbar v_F k_z \\ \hbar v_F k_+ & 0 & -\hbar v_F k_z & -\Delta \end{pmatrix}. \quad (5.20)$$

where  $k_{\pm} = k_x \pm i k_y$ . A more realistic treatment of HgTe / CdTe requires solving a  $6 \times 6$  Kane-Hamiltonian, what is numerically more challenging. However, the main findings presented in the following are based on the existence of an inverted gap and we postulate that they therefore extend to the case of HgTe or other TI materials.

The spectrum of eq. (5.20) corresponds to massive Dirac particles

$$E^{\pm}(\mathbf{k}) = \pm \sqrt{\Delta^2 + (\hbar v_F k)^2}. \quad (5.21)$$

Obviously, the spectrum has a gap of  $2\Delta$  and is independent of the sign of  $\Delta$ . However, a topological classification can be performed by considering this sign [51, 70], with  $\Delta < 0$  corresponding to a topological insulator.

A standard approach for treating semi-conductor interface consists in the envelope function method [137]. In this case, the boundary is modeled as an abrupt change in band-parameters at a given position. In contrast to this step-like description, the following treatment explicitly assumes a boundary of finite width  $\xi$ . It is established that at the TI-normal insulator interface TSS appear. Considering a boundary orthogonal to the  $z$ -axis, a simplified description of such a boundary consists in making  $\Delta$  space dependent over the interface region of width  $\xi$ , cf. Fig. 5.21:

$$\Delta(z) = \begin{cases} \Delta_1 & z < 0 \\ \Delta_1(1 - z/\xi) + \Delta_2 \cdot z/\xi & 0 \leq z \leq \xi \\ \Delta_2 & z > \xi \end{cases}. \quad (5.22)$$

For definiteness and inspired by our sample geometry, we assume the lower half space to be a topological insulator ( $\Delta_1 < 0$ ) and the upper half a trivial insulator ( $\Delta_2 > 0$ ). As we are interested in the surface/interface spectrum, we shall restrict the discussion to this region. Note that the assumed linear evolution of the gap parameter constitutes a simplification for the sake of analytical solvability of the model. It is likely that this parameter varies rather similarly to the interface potential in semi-conduction  $p - n$  junctions, i.e. the evolution is linear only in the middle of the interface region (e.g. Ref. [2, p.88]). It is known however that for the existence of topological surface states, the exact shape of the interface region is of little importance.

From dimensional analysis, we can introduce a natural scale for the (topological) interface electric field

$$\mathcal{E}_T = \frac{\Delta_2 - \Delta_1}{e\xi} \quad (5.23)$$

along with an energy scale

$$E_{TIC} = \frac{\hbar v_F}{\xi}. \quad (5.24)$$

This energy corresponds to the confinement of the topological surface states to the interface region. Due to the topological origin of this confinement, we shall call it the *topological confinement energy*. Note that the width  $\xi$  is left as a free parameter in this description. Physically, we argue that  $\xi$  is related to the width of the topological surface states (in the zero-field limit). According to Linder *et al.* [211],  $E_{TIC}$  is then simply given by the ‘‘charge excitation gap’’. In this case,  $\xi = \hbar v_F / \Delta_{\text{strain}} \approx 20$  nm. This claim seems inconsistent with the discussion of ARPES data in chapter 2 and as discussed for the low frequency quantum capacitance spectroscopy in section 5.2. It is likely that for the case of HgTe,  $E_{TIC}$  is determined by the inverted  $\Gamma_6 - \Gamma_8$  gap on the order of  $\sim -0.3$  eV rather than by the strain gap on the order of 30 meV. This is endorsed by  $\mathbf{k} \cdot \mathbf{p}$  calculations by Baum *et al.*, Ref. [41]: From this work, one can extract a Fermi velocity on the order of  $0.7 \cdot 10^6$  m/s and a TSS width on the order of  $\xi \approx 2$  nm. The corresponding energy scale lies thus at  $E_{TIC} \approx 230$  meV, i.e. on the energy scale of the spin-orbit induced  $\Gamma_6 - \Gamma_8$  gap (and *not* the strain-induced transport gap). Comparison between our experimental results and these estimations, presented in section 5.9 will shed further light on this question.

Calculations show that the spectrum in the interface region takes the form

$$E_l^\pm(\mathbf{k}_\perp) = \pm \sqrt{(\hbar v_F k_\perp)^2 + 2le\mathcal{E}_T \hbar v_F}, \quad (5.25)$$

with an integer  $l$ . These bands are represented in the interface region in Fig. 5.21. The  $l = 0$  state is non-degenerate and corresponds to the well-known spin-helical topological surface state. All other states are doubly degenerate, massive and consequently have a gap. We will refer to these states as *massive surface states* (MSS).

**On the topological origin of the massive surface states** It can be shown that the TSS and the MSS are all centered within the interface region. This observation checks in some sense the consistency of the solution. More specifically one has

$$\langle z \rangle = -\frac{\Delta_1}{e\mathcal{E}_T} = -\frac{\Delta_1}{\Delta_2 - \Delta_1} \xi. \quad (5.26)$$

Note that  $\langle z \rangle \in [0, \xi]$  holds if  $\Delta_1$  and  $\Delta_2$  are of opposite sign, i.e. if the two materials have different topology. Therefore, these excited states should not be mistaken for

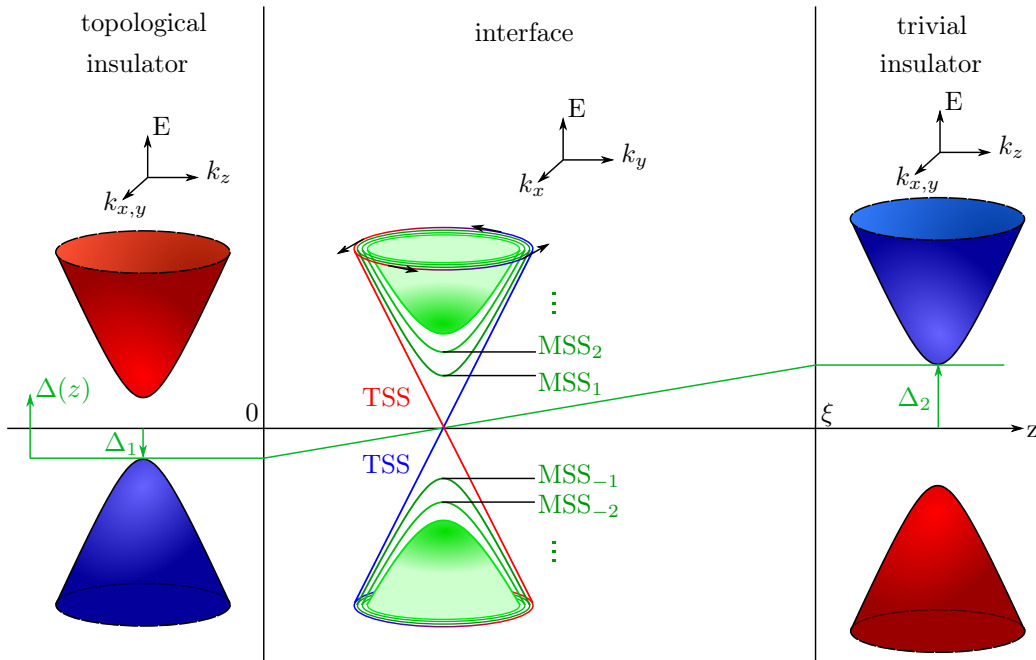


FIGURE 5.21: Schematic bulk band structure for an inverted gap insulator ( $z < 0$ ) and a normal insulator ( $z > \xi$ ). The gap parameter  $\Delta$  interpolates linearly between a negative value  $\Delta_1$  and a positive value  $\Delta_2$  over the width  $\xi$  of the interface region. Within the interface, the spectrum shows the linear dispersing spin polarized topological surface state (red and blue) together with excited *massive surface states* (green).

“trivial” (e.g. Schockley-Tamm states [255]) surface states as might occur in normal semiconductor interfaces.

**Remark about the massive surface states** The theory shows that the spread of the wave-functions  $\langle (\Delta z)^2 \rangle$  scales like  $\sqrt{l}$ . Thus, for larger  $l$ , a large proportion of the wave-function extends to a region outside of  $z \in \{0, \xi\}$ . In this case, one expects the surface states to hybridize strongly with bulk states. A detailed analysis of such a hybridization goes beyond the scope of this work. Thus, the theory shall be restricted to the lowest  $n$  modes, assuming rather a bulk-like continuum of states for larger energies. This is sketched by the shaded “continuum cone” in Fig. 5.21.

**An external electric field** An external electric field  $\mathcal{E}$  is applied to the surface at  $z = \xi$  and assumed to drop to zero at  $z = 0$  due to Dirac screening. We emphasize that this electric field (within the interface layer) might be different from the experimentally determined (insulator) field. Thus, the (electrostatic) potential within the interface region adds the term

$$H_{\text{field}} = -e\mathcal{E}z\mathbb{1} \quad (5.27)$$

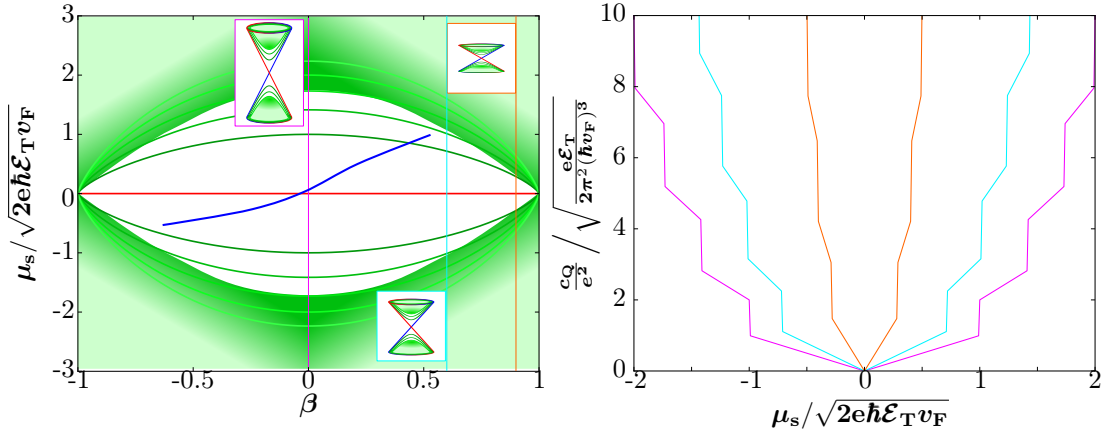


FIGURE 5.22: Left: Energy of MSS band extrema as a function of reduced electric field  $\beta = \mathcal{E}/\mathcal{E}_T$  with respect to the Dirac point. At strong electric fields the Fermi velocity and the MSS-gap decrease. The shaded areas sketch regions in which the theory might lose its accuracy due to hybridization of MSS with bulk states. Right: Quantum capacitance as a function of non dimensional energy for different cuts along constant field lines (represented as straight vertical lines in the left panel):  $\beta = 0$  (pink), 0.6 (blue), 0.9 (orange). Note that in an experiment, the chemical potential and the electric field vary simultaneously as sketched by the solid blue “charging line” in the left panel. When the charging line crosses a green line, a sub-band is populated.

to the Hamiltonian from eq. (5.20), where  $\mathbb{1}$  is the  $4 \times 4$  identity matrix. Note that for comparison with the experiment, the chosen orientation implies  $\mathcal{E} = -E_z$ , such that positive gate voltages in the experiment correspond to positive  $\mathcal{E}$ .

The problem can be simplified by a non-unitary transformation of the Schrödinger equation, corresponding to a Lorentz-boost to a reference frame in which the electric field is zero at the price of a finite magnetic field. The reduced velocity of this boost is defined via  $\beta = \mathcal{E}/\mathcal{E}_T$ . Explicitly, the transformation is written as

$$H'_{sc} = e^{\frac{\pi}{2}\sigma_y \otimes \sigma_x} (H_{\text{tot}} - E\mathbb{1}) e^{\frac{\pi}{2}\sigma_y \otimes \sigma_x}. \quad (5.28)$$

Note that this transformation is only possible in the “magnetic regime”, i.e.  $\beta < 1$ . The mathematical treatment is similar to Refs. [252, 253] and leads to a spectrum given by

$$E_l^\pm(\mathbf{k}_\perp) = -\beta\Delta_1 \pm \sqrt{(\hbar v_F \gamma k_\perp)^2 + 2le\mathcal{E}_T \hbar v_F \gamma^3}, \quad (5.29)$$

with  $\gamma = \sqrt{1 - \beta^2}$ .

The electric field has thus two main effects. First, it renormalizes the Fermi velocity according to  $v_F \rightarrow v_F \gamma$ , effectively slowing down the electrons at high fields. As the quantum capacitance of the 2D interface states depends on  $\sim 1/v_F^2$ , this leads to an increase of the slope of  $c_Q(\mu_s)$  at large electric fields. Second, the gaps of the MSS close

for  $\beta \rightarrow 1$ , i.e.  $\mathcal{E} \rightarrow \mathcal{E}_T$ . This is represented in the left panel of Fig. 5.22. Note that the gap closing does not depend on the sign of the electric field. These two observations highlight the non-trivial character of the excited states: For quantum well states, an electric field, aligned with a built-in field renders the interface potential steeper causing an energetic up-shift of the surface states. An anti-aligned electric field causes the barrier states to vanish eventually.

These two physical effects affect the DoS, yielding the 2D quantum capacitance

$$c_Q = \frac{e^2 |E + \beta \Delta_1|}{2\pi (\hbar v_F)^2 (1 - \beta^2)} \sum_l \Theta(|E + \beta \Delta_1| - G_l), \quad (5.30)$$

where  $\Theta(x)$  is the Heaviside theta function and  $G_l = \sqrt{2e\mathcal{E}_T \hbar v_F l (1 - \beta^2)^{3/2}}$ , corresponds to the band bottom of the  $l$ -th MSS for a given electric field. The jumps in quantum capacitance represented in Fig. 5.22 correspond to the band edges.

Experimentally, when varying the gate voltage, we change the electric field and the chemical potential simultaneously as sketched by the blue line in Fig. 5.22 (see also Fig. 5.3).

### 5.8.2 Summary of qualitative theoretical predictions

Before we attempt a quantitative comparison between experimental data and theory, the main predictions of the theory can be summarized as follows: In the absence of electric fields, there exist not only the linear dispersing spin-polarized topological surface states but also gapped, massive surface states. Their existence is ensured by the gap inversion. They are thus likely to be of topological origin. Similar to Landau levels, their spectrum is described by a  $\sqrt{l}$ -dependence of the band-minima. The existence and the properties of these sub-bands can explain most of the experimental observations qualitatively: We have presented experimental evidence for the appearance of an electronic sub-band at high enough surface electron concentrations on an intrinsic TI sample (section 5.6). The theoretical result, of the excited states spreading into the bulk for increasing sub-band index is in line with the surface-to-bulk charge transfer interpretation of the metastability observed in section 5.5.

Furthermore, the theory predicts the existence of *several* sub-bands. Although a precise theory of inter-sub-band scattering remains an open topic, the complex interplay of increased scattering rate and simultaneous increase of charge carrier density suggests that multiple sub-bands cause the resistance oscillations observed on the n-type sample (section 5.7).

Applying an electric field at the interface leads to a renormalization of the effective Fermi velocity by the relativistic Lorentz factor  $\gamma = 1 - \beta^2$ . This applies also to the topological surface state. Furthermore, the electric field reduces the gap of the massive surface states. The observation that the zero (electric) field gap of these states is large as compared to the bulk band gap might explain why they have not been observed in previous studies. Under the influence of large electric fields, they enter thus an experimentally available range of energies, as will be shown below in a quantitative comparison of experiment and theory.

An important feature of the model consists in the introduction of the maximal boundary field  $\mathcal{E}_T$ . The MSS gap and the Fermi velocity vanish when the electric fields approaches this “critical” electrical field.

**Limitations of the model** Obviously, the quantitative comparison between experiment and theory must be approached carefully due to several strong simplifications in the theoretical description.

First, the Hamiltonian (5.20) is electron-hole symmetric. It is known that HgTe has a strong electron-hole asymmetry. Furthermore, the hybridization between heavy-hole and topological surface states on the hole side remains unclear, as described in section 5.3. As these effects are not taken into account, we shall restrict the comparison to the electron side.

Second, the model assumes that both insulators have an aligned mid-gap. It is known however that CdTe and HgTe have a valence band offset on the order of 570 meV [256, 257].

Third, the model assumes a constant interface width  $\xi$  used simultaneously for the evolution of the gap parameter  $\Delta(z)$  and for the drop of the electric field. However, these two length scales might be different and especially the drop of the electric field might occur on a larger scale. Moreover, it seems likely that this second length-scale depends on the electric field, rendering the problem non-linear. For example, it might seem reasonable to assume that the electric field drops to zero over a length defined by analogy to the Thomas-Fermi wavelength:  $\lambda' = \sqrt{\varepsilon_0 \varepsilon_{HgTe} / (e^2 c_Q / \xi)}$ , where  $c_Q$  is field-dependent. This length corresponds to the geometrical mean of a two-dimensional screening length  $\xi' = \varepsilon_0 \varepsilon_{HgTe} / c_Q$  and the interface width  $\xi$ . In other words, it assumes the TSS to homogeneously fill (in a bulk-like manner) the interface region  $\xi$ .

Fourth, the linear evolution of the gap parameter and electrostatic potential over the interface region is unlikely to be true. Especially, assuming a constant evolution of the potential within the interface region, effectively imposing the electric field in the oxide layer to be equal to the interface field, leads to a discontinuity in the electric field at  $z = \xi$ . With Poisson’s equation, this corresponds to placing all the TSS charge in a

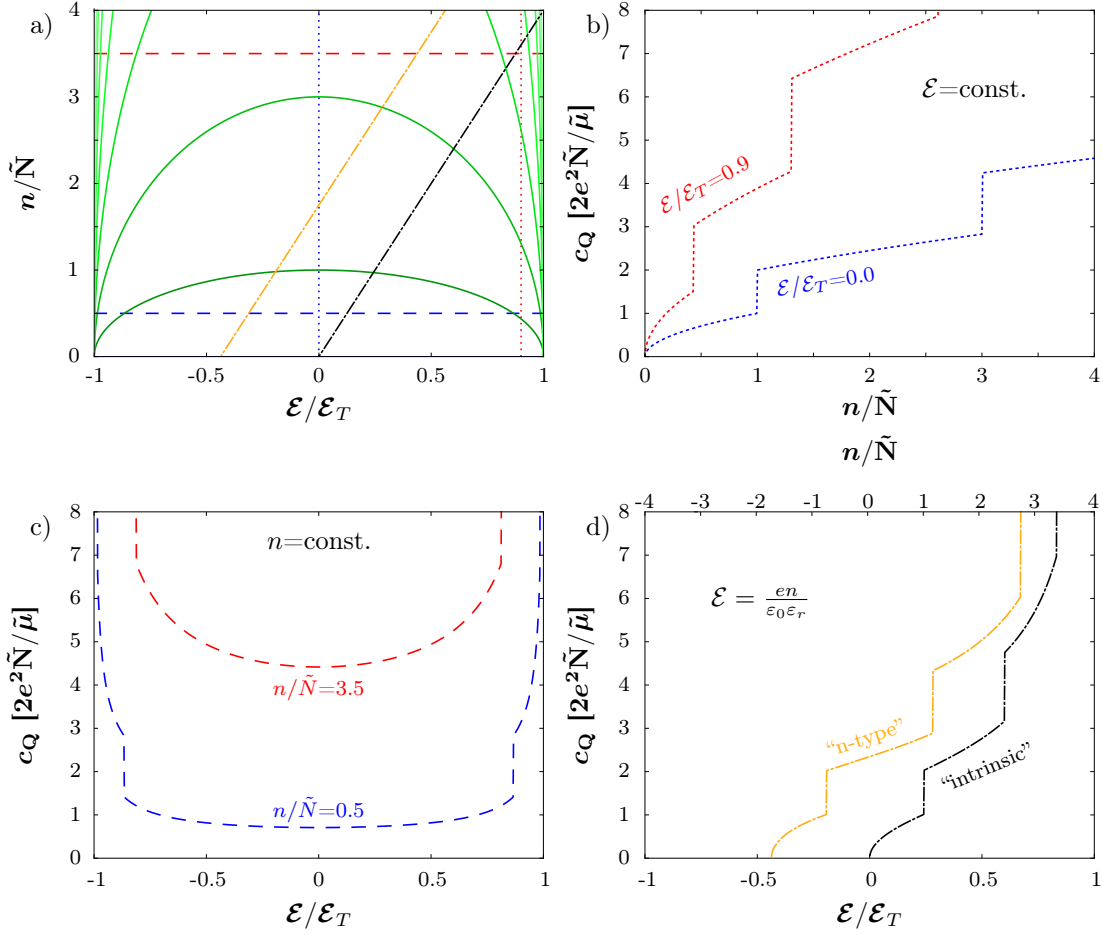


FIGURE 5.23: a) The MSS band minima as a function of  $n$  and  $\mathcal{E}/\mathcal{E}_T$  (green solid lines). b) The quantum capacitance as a function of electron density for two different fixed values of  $\beta$ , along the dotted vertical cuts in (a). c) The quantum capacitance as a function of reduced electric field  $\beta = \mathcal{E}/\mathcal{E}_T$  for two different fixed values of  $n$ , along the dashed horizontal cuts in (a). d) The quantum capacitance as a function reduced electric field  $\mathcal{E}/\mathcal{E}_T$  along two cuts corresponding to possible experimental charging lines, represented as dashed-dotted lines in (a).

charge layer at this position, whereas it is likely that the TSS have a finite width and by virtue of the definitions given in chapter 3, we measure the(ir) chemical potential at  $z = 0$ .

### 5.8.3 Relation to experiment – Choice of variables

In the single gate capacitor geometry used in this thesis, it is not possible to change  $\mu$  and  $\mathcal{E}$  independently for a given sample, cf. Fig. 5.3. Thus, the experimental *charging line* in the  $\mu - \beta$ -diagram in Fig. 5.22 is S-shaped and must be identified carefully for different samples. Moreover, the extraction of the surface chemical potential at high electric fields (large gate voltage in the experiment) becomes less reliable as in this region the uncertainty on the geometrical capacitance strongly affects the result. We shall also

note that the extraction of  $\mu_s$  relies on the equilibrium assumption, eq. (3.4). As we have noted in section 5.5, the crossing of a sub-band is accompanied by the appearance of metastability in the sample. The equilibrium assumption is therefore questionable beyond the crossing of the first sub-band. The extraction of the total charge carrier density is experimentally more reliable.

I will therefore derive some relations between electric fields, charge carrier densities and the sub-band minima that allow us to perform a more direct testing of the theoretical predictions. We can trace a  $n-\beta$  diagram analogous to Fig. 5.22 with the experimentally accessible quantities  $n$  and  $\mathcal{E}$  on the axes. Furthermore, due to Gauß' law these two quantities always follow a linear relation:  $\mathcal{E} = en/\varepsilon_{HgTe}$ . Thus the charging path follows straight lines in the corresponding diagram.

Albeit the difficulties in the description of the hole side, we will use the hole side as a counter-check of theoretical predictions also in this region. In order to take the observed electron-hole asymmetry into account, we use different values of Fermi velocity on the electron ( $v_F^e = 1.6 \cdot 10^6$  m/s) and hole ( $v_F^h = 0.5 \cdot 10^6$  m/s) sides. These are the values we obtained from our analysis of the intrinsic sample in the reversible gate voltage regime, section 5.2.

Note the  $\beta\Delta_1$  terms in eqs. 5.29, 5.30. They apply to all states, including the Dirac point. If we measure the energy not with respect to the bulk band structure but with respect to the Dirac point we can absorb this term in the energy.

We introduce the following natural scales for energy, electron number and compressibility:

$$\tilde{\mu} = \sqrt{2e\mathcal{E}_T\hbar v_F}, \quad (5.31)$$

$$\tilde{N} = \frac{e\mathcal{E}_T}{2\pi\hbar v_F}, \quad (5.32)$$

$$\tilde{C} = e^2 \sqrt{\frac{e\mathcal{E}_T}{2\pi^2(\hbar v_F)^3}} = 2e^2 \frac{\tilde{N}}{\tilde{\mu}}. \quad (5.33)$$

In order to develop a feeling for these scales, we can calculate these for a topological confinement field  $\mathcal{E}_T = 10^8$  V/m and a Fermi velocity of  $v_F = 1.6 \cdot 10^6$  m/s:

$$\tilde{\mu} = 460 \text{ meV}, \quad \tilde{N} = 1.5 \cdot 10^{12} \text{ cm}^{-2}, \quad \tilde{C} = 10.5 \text{ fF}/\mu\text{m}^2. \quad (5.34)$$

According to eq. (5.29), the band minima are given by

$$\mu_l = \tilde{\mu} \sqrt{l(1-\beta^2)^{3/2}}. \quad (5.35)$$

We can simplify the expression of the quantum capacitance (5.30), using these scales, and find for  $\mu_{l+1} > \mu > \mu_l$ :

$$c_Q = \tilde{C} \frac{\mu}{\tilde{\mu}} \frac{l+1}{1-\beta^2}. \quad (5.36)$$

For a given electric field  $\mathcal{E}$ , the band minimum of the  $l$ -th sub-band depends on the reduced electric field as follows (Appendix F):

$$n_l = \frac{l(l+1)}{2} \tilde{N} \sqrt{1-\beta^2}. \quad (5.37)$$

We can also express the quantum capacitance as a function of the experimental variables  $\mathcal{E}$  and  $n$ . For  $n_{l+1} > n > n_l$ , we find:

$$c_Q(n, \mathcal{E}) = \tilde{C} \sqrt{\frac{l+1}{1-\beta^2} \frac{(n+n_l)}{\tilde{N}}}. \quad (5.38)$$

In Fig. 5.23 (a), I show the minima of the massive surface states in the  $n - \beta$  plane. Figs. 5.23 (b-d) shows the quantum capacitance along different cuts in this diagram. Note that the electron compressibility is affected independently by the electric field and the electron number. In our experiments,  $n$  and  $\mathcal{E}$  can however not be varied independently. According to Gauß' law they obey a linear relation. Accordingly, the charging lines are represented as the diagonal cuts in Fig. 5.23 (a). The slope of this line is defined by the dielectric constants whereas the y-intercept depends on the intrinsic doping concentration.

**Comment on carrier densities and electric fields** Integration of the  $c(V_g)$  data yields information about the total charge carrier density variations in the samples, when the gate voltage is varied. This quantity can be unambiguously computed from the experimental data. The theory on the other hand describes a pure surface phenomenology, i.e. numerical predictions of the model are based on the surface states charge carrier densities  $n_{SS}$ . *A priori* we would thus need to subtract “background” and bulk contributions from the  $c(V)$  characteristics in order to obtain  $n_{SS}$ . In section 5.2, we have observed a combined bulk and TSS response for the n-type sample, but also a non-vanishing quantum capacitance for the intrinsic sample in close vicinity to the Dirac point. We have seen that a combined TSS and bulk screening model accounted semi-quantitatively well for difference between both samples. However, in both samples, an “unknown” background capacitance was observed in the  $c_Q(\mu)$  data. As discussed on p. 96, *several* physical explanations can be given for the this background. Thus a subtraction of a background capacitance seems arbitrary. We therefore decide to compare the *total* charge density to

the theoretical predictions keeping in mind that this constitutes an overestimate of the involved charge carrier densities. In any case the qualitative predictions of this work are not affected by this subtlety.

Another important difference between theory and experiment lies in the definition of the electric field. The theory describes the effect of an electric field *within* the interface region  $\mathcal{E}_{\text{HgTe}}$ , whereas the experimentally accessible electric field corresponds to the effective electric field in the insulating layer  $\mathcal{E}_{\text{ins}}$ , as defined in eq. (5.3). The model treats charge carrier density and chemical potential (i.e. electron number) as *independent* variables. In particular it does not treat the precise screening properties in a self-consistent manner. We therefore assume that the relation between the electric fields  $\mathcal{E}_{\text{HgTe}}$  and  $\mathcal{E}_{\text{ins}}$  is governed by continuity of the displacement field:

$$\tilde{\epsilon}_{\text{ins}}\mathcal{E}_{\text{ins}} = \tilde{\epsilon}_{\text{HgTe}}\mathcal{E}_{\text{HgTe}}, \quad (5.39)$$

where  $\tilde{\epsilon}_{\text{ins}} = c_{\text{geo}} \cdot d_{\text{ins}}$  is the effective dielectric constant of the insulating layer and  $\tilde{\epsilon}_{\text{HgTe}}$  is an *a priori* unknown – effective dielectric constant of the interface region (within the HgTe). The generally accepted value for bulk HgTe is  $\tilde{\epsilon}_{\text{HgTe}} = 21$ . We highlight that the dielectric constant of the interface region can be lower, as reported e.g. in Ref. [135] ( $\tilde{\epsilon}_{\text{HgTe}} = 3$ ). Due to this ambiguity we leave  $\tilde{\epsilon}_{\text{HgTe}}$  as an adjustable parameter below.

#### 5.8.4 Relation to experiment – Procedure

Comparison between experiment and theory relies on three adjustable parameters: The Fermi velocities on electron and hole side, the topological field  $\mathcal{E}_T$  and the effective dielectric constant of the HgTe interface region  $\tilde{\epsilon}_{\text{HgTe}}$ .

The Fermi velocities were determined from the quantum capacitance measurements in section 5.2, where we found  $v_F(e^-) = 1.6 \cdot 10^6$  m/s and  $v_F(h^+) = 0.5 \cdot 10^6$  m/s. We rely on these values for further analysis.

In order to interpret the experimental data in the framework of the above theory, we start by representing the charging line in the  $n - \mathcal{E}$  plane, where  $n$  is the total charge carrier density as extracted from the capacitance measurement and  $\mathcal{E}$  is the electric field in the insulating layer, defined in eq. (5.3). Depending on the sample type, this line crosses the  $n$ -axis at the origin or at a finite value, corresponding to the intrinsic doping concentration  $n_0$ , i.e. the  $y$ -intercept of the charging line in Fig. 5.24. As the n-type sample shows several maxima in conductivity, it is easier in a first step to analyze its features quantitatively. For this sample we observe that the first scattering peak occurs for negative, the second scattering peak for positive gate voltages. By comparison to

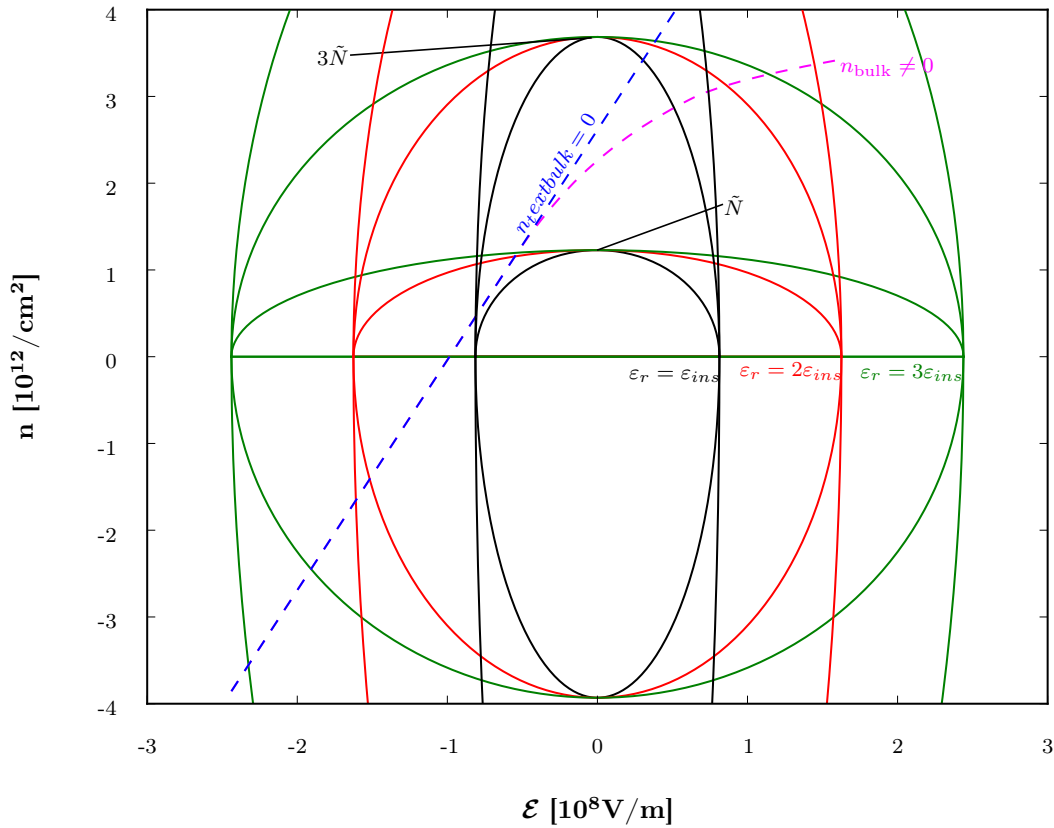


FIGURE 5.24: An  $n - \mathcal{E}$  diagram with dimensional experimental parameters. In this representation, the charging path always describes a straight line (dashed blue line). Also shown are the calculated sub-band extrema for different choices of the HgTe dielectric constant. We note that the observation of a Dirac point is incompatible with  $\varepsilon_r = \varepsilon_{ins}$ . Once the first sub-band is crossed the hysteresis reveals that not all charge is transferred to the surface states, but a part is transferred (in a metastable way) to the bulk. Thus, for comparison with the theoretical predictions,  $n_{surface} = n - n_{bulk}$  as sketched by the pink dotted line has to be taken into account.

the theory, we therefore know that  $\tilde{N} < n_0 < 3\tilde{N}$ . After fixing  $\tilde{N}$ , we note that the curvature of band minima in the  $n - \mathcal{E}$  plane is determined by  $\varepsilon_{HgTe}$ . This is illustrated in Fig. 5.24. We note that the observation of a Dirac point in our measurements implies a lower limit on  $\varepsilon_{HgTe}$ : Indeed, the black lines in Fig. 5.24, corresponding to  $\varepsilon_{HgTe} = \varepsilon_{ins}$  are incompatible with the observation of a Dirac point as the experimental line would not cross the Dirac point, represented as a red line in Fig. 5.24. We can therefore extract a lower limit of the dielectric constant. These illustrations show that we are experimentally capable of extracting  $\varepsilon_{HgTe}$  and  $\tilde{N}$ .

The observed metastability, section 5.5, led us to the conclusion that for surface charge carrier densities above the critical density for sub-band population, a certain amount of charge transferred to the sample is not occupying surface states, but is transferred to the bulk of our sample. The model does not describe these processes quantitatively. Hence

we have to keep in mind that  $n_{surface} - \mathcal{E}$  is slightly bend for  $n > n_1$  as sketched by the dashed pink line in Fig. 5.24.

More explicitly, we adjust  $\varepsilon_{HgTe}$  and  $\tilde{N}$ , using the first maximum in the conductance data (corresponding to the onset of the first sub-band) and the position of the Dirac point.

As we observe a single scattering peak for the intrinsic sample, we can assess  $\tilde{N}$  from the crossing of the charging line with the first massive surface state band minimum.

## 5.9 Quantitative comparison to experiment – estimation of topological confinement fields

### 5.9.1 The topological confinement fields

**The n-type sample** We concentrate here on the analysis of the sample with a longer access region, i.e. the data represented in Fig. 5.18. This choice is motivated by two observations: First, as explained above, the frequency range in this measurement was larger, yielding better precision on the fitting parameters than on the *short access*-sample. Second, the gate range is larger, resolving the conductance peak more clearly. Fig. 5.25 shows the measured conductivity and quantum capacitance for this sample as a function of charge carrier density. In Fig. 5.26, I show the corresponding  $n - \mathcal{E}$  diagram.

We extract  $\varepsilon_r \approx 8.9$  and  $\mathcal{E}_T \approx 0.8 \cdot 10^8$  V/m (critical HgTe surface field) from this measurement. Using eq. (5.39), this corresponds to an insulator field of  $\mathcal{E}_T^{ins} \approx 1.5 \cdot 10^8$  V/m. The corresponding path in an  $n - \mathcal{E}$  diagram is represented in Fig. 5.26.

In section 5.5, we have observed that the occupation of the sub-band gives rise to metastability in the sample via a charge transfer from the surface layer to bulk-like states. As explained in more detail below in section 5.9.2, we can estimate the amount of charge transferred to the bulk from these observations. Here, we took a finite charge transfer to bulk states into account. This causes the kink in the experimental  $n - \mathcal{E}$  path (represented in blue).

We observe that the first and second scattering peaks coincide with the theoretical appearance of sub-bands. For a more precise extraction of the two fitting parameters  $\varepsilon_r$  and  $\mathcal{E}_T$ , we took also the first scattering peak on the hole side into account. In the  $n - \mathcal{E}$  diagram we note that the charging line is expected to cross a multitude of sub-bands on the hole side at  $\mathcal{E} \approx \mathcal{E}_T$ . This situation – corresponding to the limit  $\beta \rightarrow -1$  – goes beyond the domain of validity of the model. As we have observed in the discussion of the model,

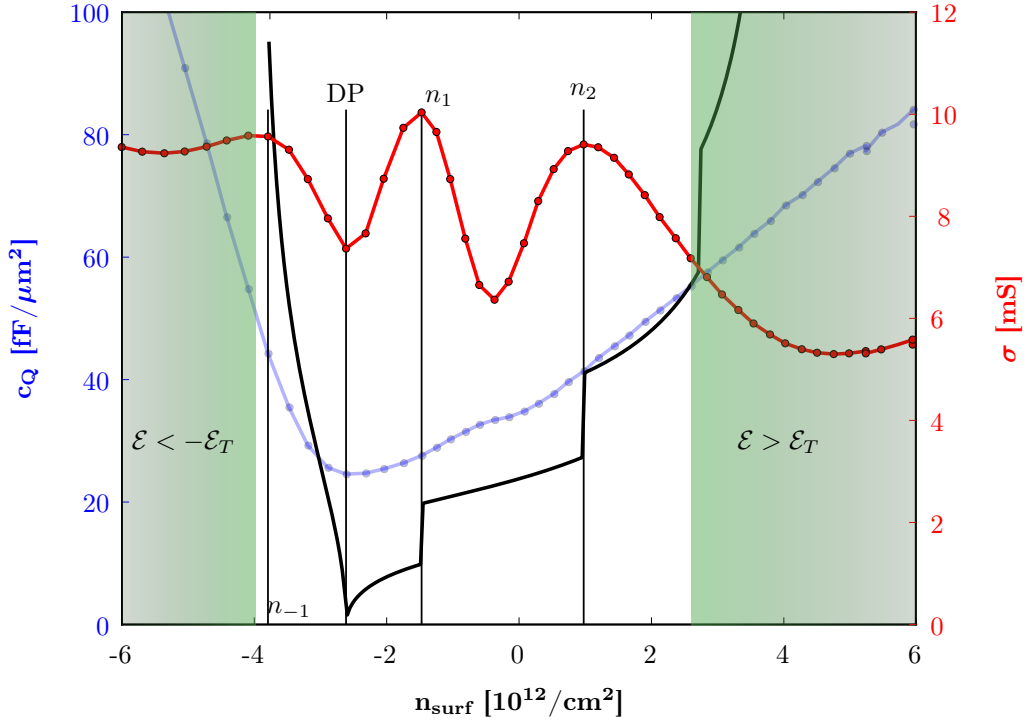


FIGURE 5.25: Quantum capacitance (blue) and conductivity (red) as a function of charge carrier density in the n-type HgTe sample. The solid black line corresponds to the theoretical prediction of quantum capacitance using the model and the parameters given in the main text. The path in  $n - \mathcal{E}$  space for this samples is depicted in Fig. 5.26. Note that here a finite charge transfer to bulk levels was explicitly taken into account.

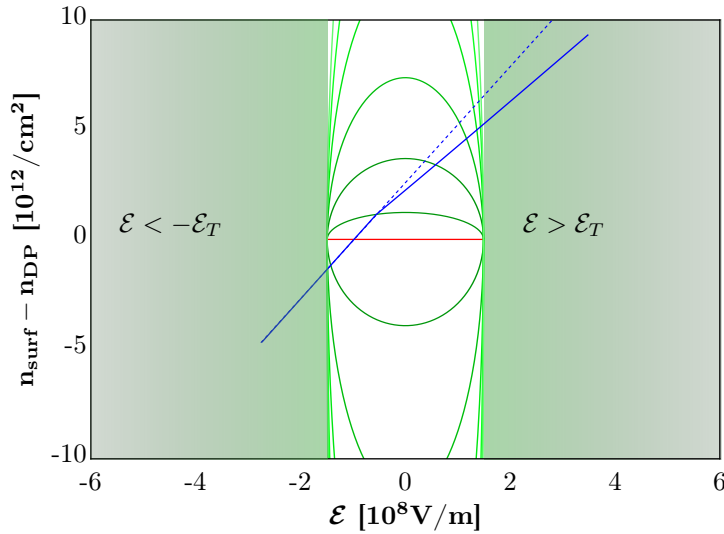


FIGURE 5.26: The band minima (green) as predicted by the model for the parameters given in the main text as a function of the effective insulator field and charge carrier density (measured with respect to the Dirac point). Note that for this sample, we explore experimentally large regions of  $\mathcal{E} > \mathcal{E}_T$ . The solid blue line corresponds to the experimental relation between *surface* charge carrier density and (external) electric field, whereas the dashed blue line corresponds to the total charge (cf. main text and section 5.9.2).

the massive surface states of higher order extend far into the bulk and are eventually indistinguishable from bulk states. The same applies to the electron side. Figs. 5.25 and 5.26 suggest a crossing with the third sub-band at  $n_{surf} - n_{DP} \approx 4.5 \cdot 10^{12}/\text{cm}^2$ . Such a third crossing is expected to result in another conductance maximum. Experimentally we observe however that the conductivity rather develops into a larger minimum. It is likely that this is due to a hybridization of higher order sub-bands (i.e.  $\geq 3$ ) into a continuum, “connected” to the bulk of HgTe. Furthermore, the conductance variations due to sub-band scattering are expected to be less important at larger sub-band index as the (TSS) mobility in these regions is already diminished due to the lower-lying sub-bands.

Further, we observe that the experimental quantum capacitance data, albeit not resolving the jumps featured in the theoretical prediction, follows qualitatively the expected behavior: The minimum capacitance occurs in vicinity to the minimum in conductivity. This identifies the Dirac point. Note that this identification is rendered possible only through the combined capacitance/conductivity measurement. We also observe a (faint) flattening in (quantum) capacitance between the onsets of first and second sub-band as predicted by the theory. Although the resolution is poor, it is remarkable that generally, the quantum capacitance shows regions with steeper variation around the expected jumps, and flattening in regions between two sub-bands. We associate the poor resolution of step features in the quantum capacitance to inhomogeneities in surface doping and bulk contribution smearing. Indeed, whereas the (local) presence of a sub-band introduces a new scattering path for surface electrons, causing the observed dramatic effects on the conductivity, the overall compressibility averages over the full sample surface: If the gate dielectric has small variations in thickness, the electric field might be slightly inhomogeneous. This will result in regions with and without sub-bands that coexist, causing the observed blurring of the experimental data.

**The intrinsic sample** As summarized in section 5.6, the appearance of a sub-band has several experimental footprints, all yielding comparable numbers for the critical charge carrier density, and consequently for the critical electric field.

We note that, as summarized in Table 5.2, the DC measurements (magneto-transport) reveal a *higher* critical charge carrier density with a *lower* critical electric field for the appearance of a sub-band as compared to the RF results. This qualitative trend is compatible with the evolution of the sub-band minima as shown in Fig. 5.23.

For a more quantitative analysis of the experimental data with respect to the theory, we focus on the RF measurement in the  $|V_g| < 5 \text{ V}$  range represented in Fig. 5.9 and Fig. 5.27 below. This experimental curve is limited to the (almost) reversible regime, i.e. metastability is kept small. Thus, the requirements for the calculation of  $\mu_s$  (eqs. (3.13),

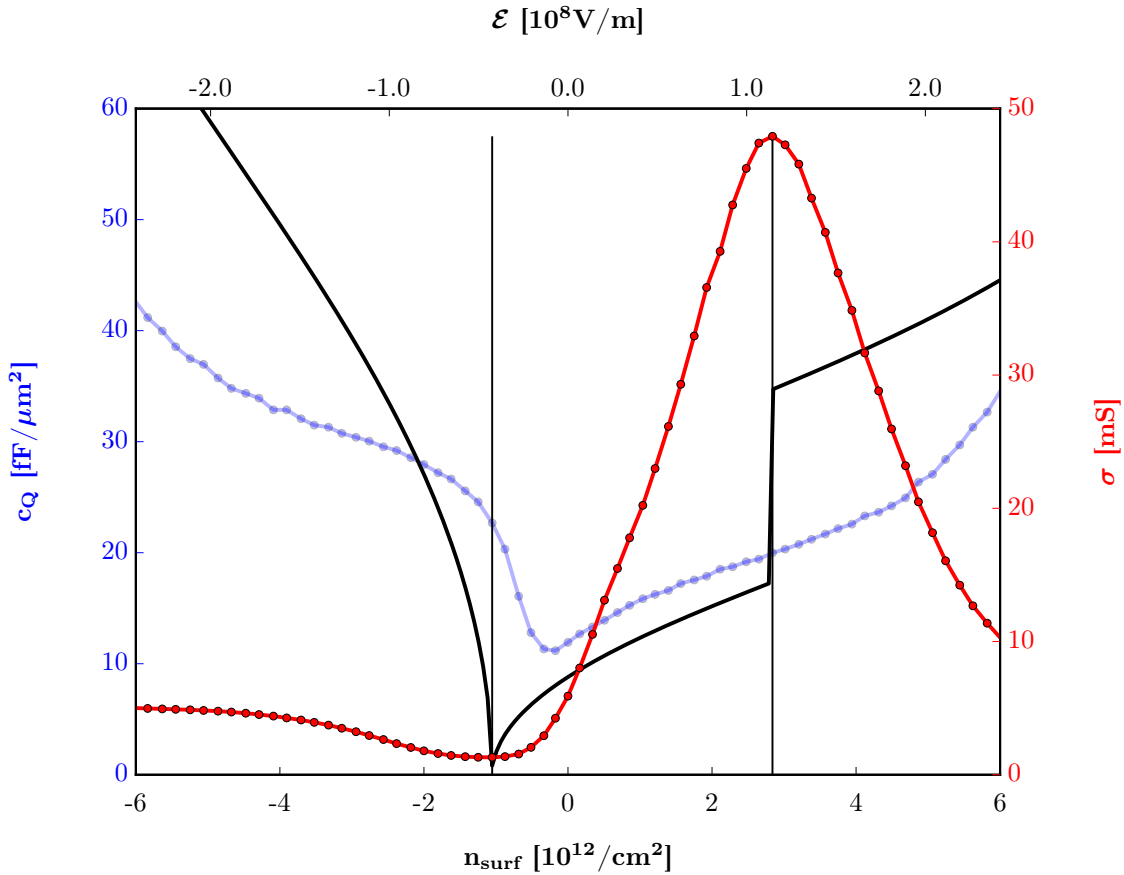


FIGURE 5.27: Quantum capacitance (blue) and conductivity (red) as a function of charge carrier density (bottom axis)/insulator electric field (top axis) in the intrinsic HgTe sample. The solid black line corresponds to the theoretical prediction of quantum capacitance using the model and the parameters given in the main text. The path in  $n - \mathcal{E}$  space for this samples is depicted in Fig. 5.28.

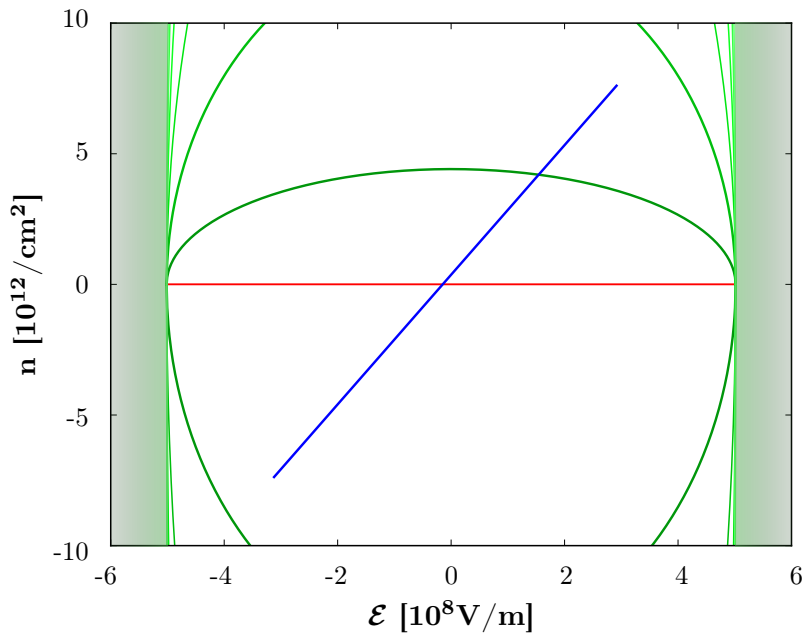


FIGURE 5.28: The band minima (green) as predicted by the model for the parameters given in the main text as a function of the effective insulator field and charge carrier density (measured with respect to the Dirac point). The blue line corresponds to the experimental path, imposed by the dielectric constants.

(3.4)) are met. We choose this gate voltage range, as the observable phenomenology is richer than for the  $\pm 3$  V sweep. For definiteness, we focus on the *forward*, i.e.  $V_g = -5 \dots 5$  V, sweep. The observation of several scattering peaks in the n-type sample allowed us to determine  $\mathcal{E}_T$  and  $\varepsilon_r(\text{HgTe})$  independently. Here, we will use the value  $\varepsilon_r = 8.9$ , obtained above in order to estimate  $\mathcal{E}_T$  for the intrinsic sample.

As shown previously for the n-type sample, I show in Fig. 5.27 conductivity and quantum capacitance as a function of charge carrier density and external electric field. From the relative position of the first scattering peak to the Dirac point, we extract  $\mathcal{E}_T = 2.6 \cdot 10^8$  V/m. With the relation between HgTe-field and effective insulator field eq. (5.39), this corresponds to a critical effective insulator field of  $5.2 \cdot 10^8$  V/m. Fig. 5.28, representing the experimental path along with the massive surface band extrema in the  $n$ - $\mathcal{E}$ -plane, reveals a clear difference between the two samples: Although the investigated gate voltage range for the intrinsic sample is larger, the explored range of charge carriers and electric fields is smaller due to the smaller gate capacitance and a larger  $\mathcal{E}_T$ . We also note that the charging line in Fig. 5.28 does not reach the second sub-band.

**Comparison between both samples** By associating the scattering peaks to the appearance of massive surface sub-bands, we found topological confinement fields of  $\mathcal{E}_T = 0.8 \cdot 10^8$  V/m and  $\mathcal{E}_T = 2.6 \cdot 10^8$  V/m for the n-type and the intrinsic samples, respectively. The theory predicts  $\mathcal{E}_T = (\Delta_2 - \Delta_1)/(e\xi)$ , cf. eq. (5.23), i.e. we might expect this quantity to be monotonically increasing with the gap of the insulators. The gap of the capping layer (intrinsic sample) being on the order of 900 meV [167], whereas the n-type sample has HfO<sub>2</sub> (gap  $\sim 5.5$  eV, [258]) in close proximity to the surface thus seems – at first sight – contradictory to the observed values. However, as we discussed in section 5.2, p. 92, the mismatch between MOM and extracted geometrical capacitance suggests the formation of an amorphous oxide layer for the n-type sample. It is difficult to evaluate an effective gap parameter for such a region, but it seems likely that it is much smaller than the pure HfO<sub>2</sub> gap.

For the intrinsic sample using eq. (5.23), with  $\Delta_2 \approx 450$  meV, we find an interface width of  $\xi \approx 2.3$  nm. Being aware of all the simplifications we made for a quantitative comparison between experiment and model, it is remarkable that the calculated widths of TSS, cf. Ref. [41], compare fairly well to this result. In particular, it illustrates the importance of the different gaps involved in the strained HgTe problem, cf. the discussion on p. 129. By relating the topological confinement energy  $E_{TIC} = \hbar v_F/\xi$  to the inverted band-gap lying at the origin of topological surface states, we find  $E_{TIC} \lesssim 0.5$  eV, rather on the order of the  $\Gamma_6 - \Gamma_8$  inverted gap of HgTe than that of the  $\sim 30$  meV strain-induced transport gap.

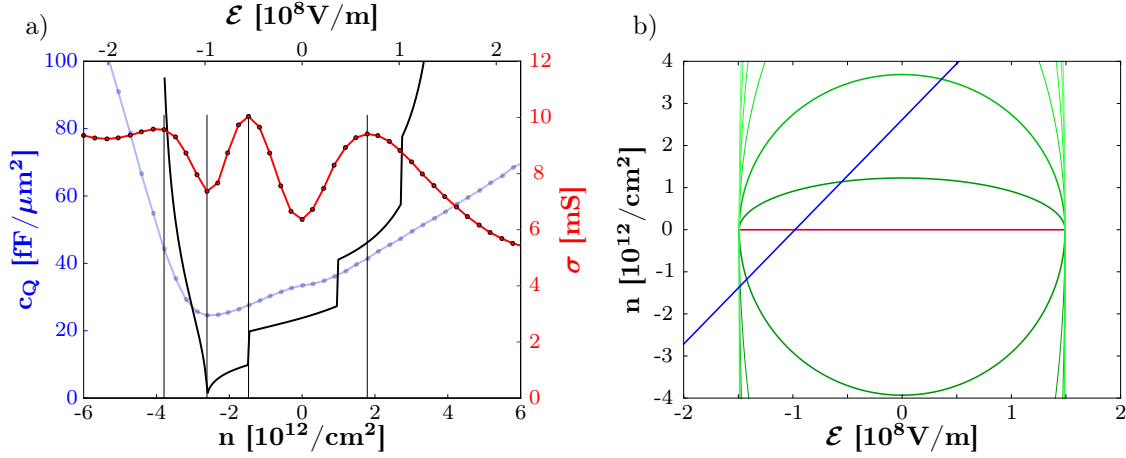


FIGURE 5.29: a) As Fig. 5.25, neglecting charge transfer to the bulk. b) As Fig. 5.26, zoomed-in on the  $\mathcal{E} < \mathcal{E}_T$  region. If charge transfer to the bulk is neglected, the relation between  $n$  and  $\mathcal{E}$  is represented as a solid blue line.

### 5.9.2 Background contributions

In the above discussion we have used the total sample charge  $n$  in order to trace the charging lines in Figs. 5.26, 5.28. As the theory treats only surface charges, we shall now shortly discuss the quantitative impact of this choice. As an example, we identified  $\Delta n = n_1 - n_{DP} \approx 4.0 \cdot 10^{12} \text{ cm}^{-2}$ . For Dirac Fermions this corresponds to  $\mu_1 = \hbar v_F \sqrt{4\pi \Delta n} \approx 0.75 \text{ eV}$  exceeding the measured value by approximately a factor of two ( $\mu_1 \sim 350 \text{ meV}$  cf. Fig. 5.8). This issue can be traced back to the (quantum) capacitance background on the order of  $c_Q \approx 10 \text{ fF}/\mu\text{m}^2$  in Fig. 5.4. As the most transparent and simple correction for the background we can assume it to be constant. In this case, the background charge between Dirac point and scattering peak for the intrinsic sample reads  $\Delta n_{bg} \approx 1.8 \cdot 10^{12} \text{ cm}^{-2}$ . Correspondingly, one finds  $\Delta n_{surf} = 2.2 \cdot 10^{12} \text{ cm}^{-2}$ , leading to  $\mathcal{E}_T \approx 1.2 \cdot 10^8 \text{ V/m}$ . In this case one obtains  $\xi \approx 5 \text{ nm}$ .

For the case of the n-type sample, the combined signatures of reversible, irreversible, TSS and bulk charges present a very rich charge-voltage diagram, where numeric evaluation of the different sub-parts based on capacitance measurements becomes somewhat arbitrary. These ambiguities concern however only the quantitative aspect of our results but do not deteriorate the qualitative observations.

We highlight that the apparent background charge is present in the reversible regime and therefore of different nature than the metastable charge causing hysteresis. A possible way of treating these “irreversible” charges on the n-type sample will now be presented.

**n-type sample** We note that the crossing with the second sub-band occurs experimentally at  $\mathcal{E}_2 = 0.67 \cdot 10^8 \text{ V/m}$  (effective insulator field) and  $n_2 = 1.8 \cdot 10^{12} / \text{cm}^2$  whereas the

bare theory predicts the crossing at  $n_2^{(t)} = 0.9 \cdot 10^{12}/\text{cm}^2$  ( $\mathcal{E}_2 = 0.36 \cdot 10^8 \text{ V/m}$ ), as represented by the dashed blue line in Fig. 5.26. This analysis relies on the assumption that all charge transferred to the HgTe slab occupies surface states only (only these are taken into account by the theory). If this charge transfer is entirely neglected, the charging path remains linear as represented in Fig. 5.29.

In the low frequency capacitance measurements, we have observed the appearance of metastability in the  $C(V)$  characteristics, section 5.5. We have argued that a possible explanation of metastability might be a MSS-mediated surface-to-bulk charge transfer. In particular, we have seen that the horizontal shift between forward and backwards sweeps is dependent on the total gate voltage range and starts opening after the gate voltage surpasses the threshold voltage beyond which the first sub-band is populated (equivalently  $\mathcal{E} > -0.55 \cdot 10^8 \text{ V/m}$ ). In low frequency capacitance measurements for a similar gate voltage range ( $\pm 4\text{V}$ ), we have observed a horizontal shift  $\Delta V_g = 0.7 \text{ V}$  between forward and backward sweep, cf. Appendix E. Attributing this shift to a surface-to-bulk charge carrier transfer, we find a bulk charge carrier density *difference* of  $1.7 \cdot 10^{12}/\text{cm}^2$ . Thus,  $\sim 0.85 \cdot 10^{12}/\text{cm}^2$  electrons are transferred during for- or backward sweep *individually*.

To take this “lost charge” quantitatively into account, we can at first order assume that (after crossing the first MSS band edge) it is proportional to the applied voltage,  $n_{bulk} = (Vg - V_{MSS1}) \cdot c_{bulk}$  where  $c_{bulk}$  describes the bulk’s filling rate. Experimentally, we find  $c_{bulk} = 0.9 \text{ fF}/\mu\text{m}^2$ . Thus within this simple approximation, we find the “lost” charge to be on the order of  $n_{lost} = 0.9 \cdot 10^{12} \text{ cm}^{-2}$  in good agreement with the “hysteretic charge”.

**The intrinsic sample** We extended the gate voltage range on the intrinsic sample to  $\pm 10 \text{ V}$  in order to investigate the high field and charge carrier density regime. In Fig. 5.30, I show conductivity and quantum capacitance together with the theoretical line using the parameters of the smaller gate voltage sweep. We note that the model predicts the population of the first massive sub-band at a lower electron concentration than observed in the experiment. Again, we can understand this apparent shift using the hysteresis data, section 5.5. For a gate voltage range of  $\pm 10 \text{ V}$ , we observe  $\Delta V_g = 2.6 \text{ V}$ , i.e.  $c_{geo} \Delta V_g / (2e) \approx 2.1 \cdot 10^{12} \text{ cm}^{-2}$  electrons are transferred to the bulk during a forward sweep. In contrast to the n-type sample, it is less clear for this measurement in which regions of gate voltage this surface-to-bulk charge transfer occurs. This  $\pm 10 \text{ V}$  sweep was recorded after cycling the gate at low temperatures in ever increasing gate voltage ranges. Therefore, the system was not in the pristine state, when the data was recorded. In particular, the finite surface-to-bulk charge transfer might also affect the effective electric interface field due to enhanced screening. Due to this rich, but complex physical

situation, we rule out a over-quantitative analysis of the data in Fig. 5.30. We shall highlight however that – as evidenced from Fig. 5.31 – this large gate voltage range explores the  $\mathcal{E} > \mathcal{E}_T$  domain. The theoretical prediction of quantum capacitance in the large electric field limit is rather correct. Taking a finite charge transfer into account, we note that the population of higher order sub-bands requires electric fields close to  $\mathcal{E}_T$ , corresponding to a situation in which single sub-bands cannot be resolved as their gap has collapsed. In this case, the massive surface states might form a continuum, connected to the bulk, i.e. the system goes over to the “normal” state of coexisting TSS and bulk states.

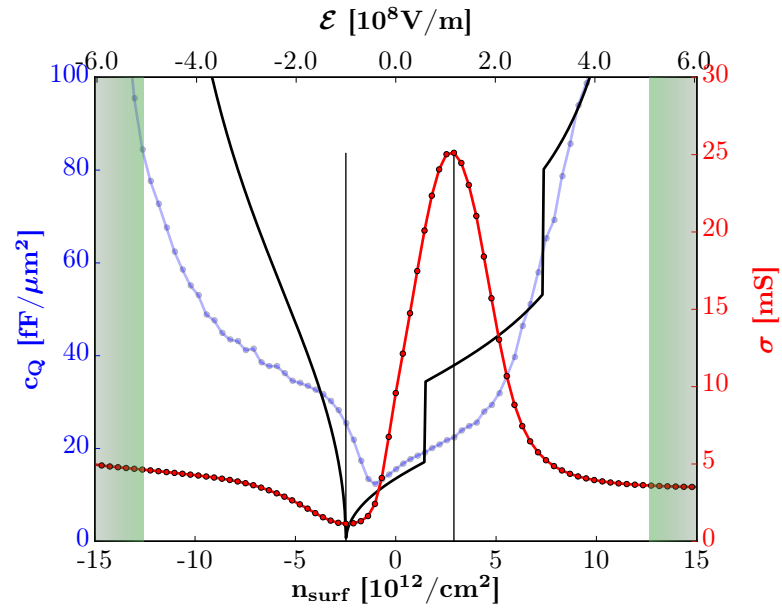


FIGURE 5.30: Quantum capacitance (blue) and conductivity (red) for the intrinsic sample measured over a much larger gate voltage range ( $\pm 10$  V) as compared to Fig. 5.27. Note that on the electron side, the predicted quantum capacitance (solid black line) describes well the experimental data for larger sub-band indexes.

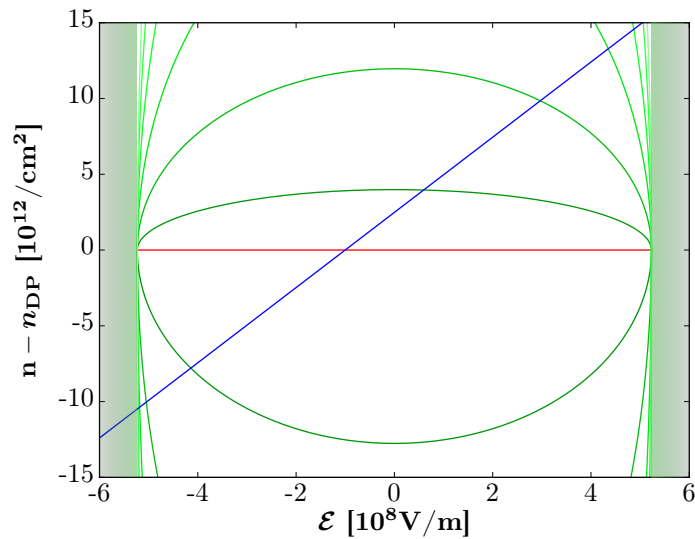


FIGURE 5.31: The band minima (green) as predicted by the model for the parameters given in the main text as a function of the effective insulator field and charge carrier density (measured with respect to the Dirac point). The blue line corresponds to the experimental path over a larger gate voltage range ( $\pm 10$  V). Note that the intersection with higher order bands ( $\geq 2$ ) occurs at large electric fields for this sample.

## 5.10 Conclusions

In this chapter, our investigations concerning the AC electron compressibility on strained HgTe 3D MITI capacitors have been presented. I have shown low frequency capacitance spectroscopy results on an unintentionally n-type doped and an intrinsic sample.

From the slope of the  $c_Q(\mu)$ -relation of the intrinsic sample, we measured a TSS Fermi velocity  $v_F = 1.6 \cdot 10^6$  m/s. Calculations based on a simple electrostatic model (cf. chapter 3) revealed combined TSS and bulk screening for the n-type sample, whereas the intrinsic sample featured Dirac screening, i.e. a TSS dominated capacitive response up to surface chemical potentials on the order of 350 meV, 10-fold higher than the expected strain-induced transport gap of HgTe.

The dynamical capacitor response to broadband radio-frequency excitations reveals a constant TSS mobility of  $\mu_e = 120.000$  cm<sup>2</sup>/(Vs) over this energy range.

At larger electric fields ( $\mathcal{E} \gtrsim 1.6 \cdot 10^8$  V/m) and carrier concentrations ( $n \gtrsim 3 \cdot 10^{12}$  cm<sup>-2</sup>), we have observed a dramatic mobility drop causing even an increase in the bare resistance data. This drop is due to inter-sub band scattering between the high-mobility TSS and (low-mobility) MSS. Further evidence for this massive sub-band was provided by complementary magneto-transport data.

We have presented hysteresis data appearing at similar critical electric fields/charge carrier densities, promoting metastability in the sample's charge distribution after a first massive sub-band population. The metastability can be semi-quantitatively understood as a surface-to-bulk charge transfer mediated by the MSS.

On the n-type sample, a similar phenomenology was presented. The large residual charge carrier density enabled us to observe several additional resistance peaks (plus the Dirac point), all associated with inter-sub band scattering physics.

We presented a model, based on the existence of a finite region of width  $\xi$  in which the gap inversion occurs. We highlight that this treatment differs from the usual envelope wave function approach, in which the interface is treated as a step-function. In other words, we assume a topological parameter (here the gap) to vary continuously in space. Introducing  $\xi$  allowed us to identify scales for electric fields  $\mathcal{E}_T$  and energies  $E_{TIC}$ , related to a topological confinement of TSS to the surface. The model lead to a qualitative understanding of all observed phenomena. In particular, it predicts the existence and the electric field dependence of excited massive surface states. A quantitative comparison between model and experimental data, revealed  $\mathcal{E}_T \approx 2.6 \cdot 10^8$  V/m for the intrinsic sample, corresponding to  $\xi \approx 2.3$  nm and a topological confinement energy on the order

---

of  $E_{TIC} \lesssim 500$  meV, exceeding by far the energy scale of the strain-induced transport gap.

It is the scope of the next chapter to counter-check the robustness of these observations on an alternative TI-platform, i.e. hBN-encapsulated  $\text{Bi}_2\text{Se}_3$ -flakes.



## Chapter 6

# Bi<sub>2</sub>Se<sub>3</sub> – Electron compressibility, scattering peak and room temperature Dirac physics

Mercury telluride (HgTe) constitutes an excellent platform for the observation of topological phenomena. This is mainly due to the fact that samples can be grown via molecular beam epitaxy (MBE), i.e. in a system where growth conditions can be tuned very precisely yielding very low intrinsic carrier densities in these thin films. This is important as the reduction of bulk-carriers is still a main issue in the field of topological insulators (TIs). However, there are two main drawbacks in using HgTe: First, the small number of research-quality MBE facilities in the world due to the elevated costs, safety constraints and required expertise, render this material accessible to a rather small community. For everyday device applications, based on topological insulators, the toxicity of Hg might eventually also constitute an issue. Second, the small (strain induced) gap, rules out the unambiguous observation of topological surface state (TSS) Dirac physics at room temperature.

It is therefore an obligatory task to search for similar physics in other topological insulator (TI) materials. In the context of this thesis, we investigate up to which point our conclusions from chapter 5 are robust and generic in TI systems. In particular, we are interested whether or not inter sub-band scattering exists in alternative TI materials. As explained in chapter 2, Bi<sub>2</sub>Se<sub>3</sub> is a prominent example for such a material.

In this chapter, I will present results obtained on a Bi<sub>2</sub>Se<sub>3</sub> sample. To proceed in analogy to HgTe, I will focus on a metal-insulator-topological insulator (MITI) device, based on Bi<sub>2</sub>Se<sub>3</sub>. This sample was fabricated entirely at the ENS (cf. chapter 4 for details).

An important step towards the realization of gate-dependent measurements on such structures lies in the encapsulation of Bi<sub>2</sub>Se<sub>3</sub> in hexagonal Boron Nitride (hBN).

At low temperature, we observe at rather high electron densities a maximum in conductivity similar to our observations on HgTe that confirm our conclusions on sub-band scattering being an important physical phenomenon in TSS conductance. However, the quantitative analysis of capacitance and conductivity will reveal that the physics is enriched with respect to HgTe: First, the thin device structure (Bi<sub>2</sub>Se<sub>3</sub> flake  $\sim$  6 nm), changes our understanding of bulk screening properties. Second, the relatively high doping concentration causes the conductivity of bulk and bottom-TSS to be far more important than on the HgTe sample. However, our measurements reveal that Dirac point features in resistance and capacitance can be observed at room temperature in Bi<sub>2</sub>Se<sub>3</sub> in a *dual-gate* geometry. The role of background carriers (either bulk or bottom surface) on resistance and capacitance is investigated combining top- and bottom gates in our measurements. These observations are particularly interesting for device applications as they demonstrate that room temperature Dirac physics based on TIs is in experimental reach.

In contrast to the results on HgTe (chapter 5), only a single Bi<sub>2</sub>Se<sub>3</sub>-device was measured. Consequently, the total set of data points is much smaller. Testing the robustness of the presented results on another sample remains to be done.

## 6.1 Sample characteristics

**Substrate for room temperature back-gating** As substrate material a high resistivity ( $\rho > 3 \text{ k}\Omega\text{-cm}$ ) Si-wafer with a 280 nm SiO<sub>2</sub> polished surface layer was used. We observed that this substrate is a bad conductor at room temperature ( $R(300 \text{ K}) \approx 100 \text{ k}\Omega$  on a typical  $1 \text{ cm}^2$ -piece of wafer connected with silver paste on top and bottom surface where the SiO<sub>2</sub> was scratched) whereas the resistance increases rapidly to over 20 M $\Omega$  at 77 K. These observations are important as they show that using the Si as a back-gate electrode is only possible at room temperature.

**Device details** The main steps of sample fabrication have been explained in chapter 4. Thin crystals of Bi<sub>2</sub>Se<sub>3</sub> were grown by SVD in a tubular furnace directly on exfoliated hBN<sup>1</sup> (“bottom-BN”) crystals (cf. Ref. [216] for details). For the investigated device (150616), the bottom-BN had a thickness of  $\sim$  30 nm. The Bi<sub>2</sub>Se<sub>3</sub> thickness as determined by AFM after growth is  $\sim$  6 nm. Subsequently, a thin layer of hBN (“top-BN”,

---

<sup>1</sup>We used high quality hBN crystals obtained from a collaboration with Kenji Watanabe and Takashi Taniguchi.

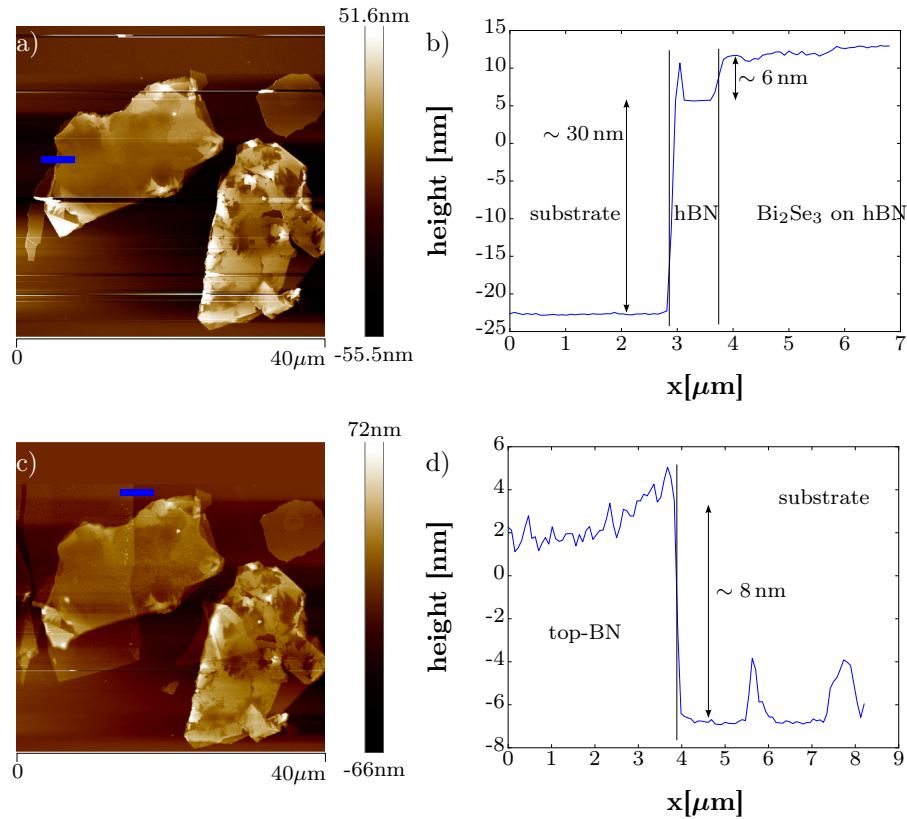


FIGURE 6.1: a) AFM scan of  $\text{Bi}_2\text{Se}_3$  grown on hBN. b) Height profile along the cut represented as a blue line in (a). c) AFM scan of  $\text{Bi}_2\text{Se}_3$  grown on hBN after deposition of the top-BN (gate) layer. d) Height profile along the cut represented as a blue line in (c)

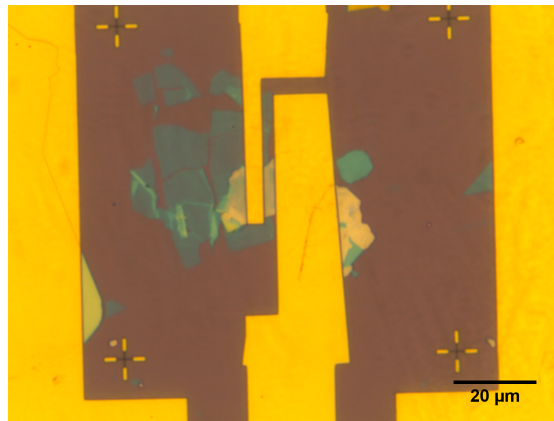


FIGURE 6.2: Optical micrograph of device 150616 after all fabrication steps. The capacitor structure is embedded in a coplanar wave guide.

$\sim 8$  nm) is deposited on *half* of the as-grown flake, cf. Fig. 6.1. In order to avoid a short on the gate side, the gate electrode covers only a strip of the sample, whereas the contact electrode covers almost entirely the top-BN free area. The resulting capacitor has a width of  $12.5 \mu\text{m}$  and a length of  $4 \mu\text{m}$ , cf. fig. 6.2

## 6.2 Low temperature radio-frequency admittance

After fabrication, the sample’s admittance was measured at 10 K in the Janis RF probe station over a broad frequency range (0→40 GHz). As described in section 4.2, we correct for thru-line propagation and dummy stray capacitances. However, the admittance spectra shown in Fig. 6.3 a) reveal a crossing of real and imaginary part in the 20-30 GHz range, a frequency range in which the spectra start to show oscillations and other noisy features. The origin of these oscillations is likely to lie in an improper calibration. It might also result from a varying inter-tip distance between the “thru” and the device measurement. Furthermore, we observe that the symmetries of the  $Y$  matrix are not entirely fulfilled after de-embedding, cf. Fig. 6.3 a). These observations suggest that the RF reference-plane is slightly shifted – an issue affecting mainly the high frequency part of the spectrum. As the contact resistance is determined from this frequency domain, its extraction is less reliable. We find a contact resistance of  $\sim 20 \Omega$ , i.e.  $250 \Omega \mu\text{m}$  and fit the spectrum only up to 10 GHz in order to obtain the sample’s resistance as a function of DC top-gate voltage. The capacitance data is obtained by fitting the imaginary part of the admittance on the low frequency part ( $f < 100 \text{ MHz}$ ).

Three representative (admittance) spectra are shown in Fig. 6.3 b). We note that these spectra show a clear gate voltage dependence. In Fig. 6.3 c), I show the corresponding fitting parameters  $C$  and  $R$  as a function of gate voltage. It shall be pointed out that before switching to an in-house hBN-Bi<sub>2</sub>Se<sub>3</sub>-hBN technique, considerable effort has been made on alternative bismuth-based TI samples, always resulting in almost gate-voltage independent spectra (spectral variations limited to 1-3%), rendering quantitative analysis and physical interpretation of these data-sets extremely cumbersome. We attribute the success on this sample to the good quality of Bi<sub>2</sub>Se<sub>3</sub> grown on hBN and the absence of chemical agents in the sample fabrication due to the dry-transfer technique of hBN as a gate dielectric.

### 6.2.1 The capacitance

We observe a slow variation of capacitance as a function of gate voltage. Note that the capacitance data presented by Xu *et al.* on similar devices [157] (shown in the inset of Fig. 6.3) shows the same features as our measurements. We observe a minimum capacitance at  $V_g \approx -4.2 \text{ V}$  while showing a trend towards saturation for positive gate voltages. From this trend in the capacitance per unit area, Fig. 6.3 d), we estimate a geometrical capacitance  $c_{geo} = 2.48 \pm 0.03 \text{ fF}/\mu\text{m}^2$ , corresponding to an effective dielectric constant of  $\epsilon_r(\text{hBN}) = 2.2$ . This small difference as compared to the reported values ( $\epsilon_r \approx 3$ ) might be due to the inclusion of small air “bubbles” between the Bi<sub>2</sub>Se<sub>3</sub> and the

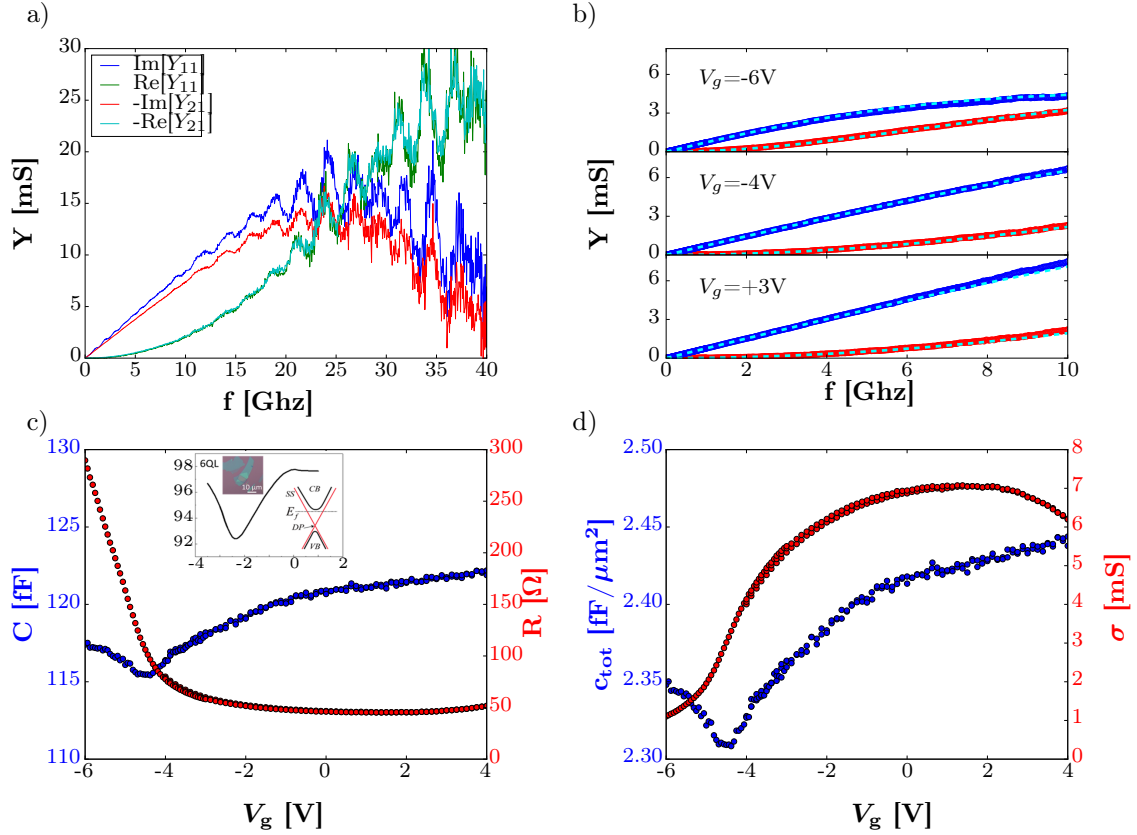


FIGURE 6.3: Broadband RF-measurements at 10 K. a) The admittance spectrum over the full bandwidth. Shown are real (green and light blue) and imaginary (blue and red) parts of two different admittance parameters  $Y_{11}$  and  $Y_{21}$ . The oscillations at higher frequency and the mismatch between  $Y_{11} = Y_{21}$  indicate a non-perfect de-embedding (cf. chapter 4). b) Admittance parameters ( $Y_{12}$ ) on a restricted frequency range for three different gate voltages. Best fits to eq. (4.1) are shown as dashed light blue lines. c) Total sample capacitance and resistance as a function of gate voltage. The inset is adapted from Xu et al. [157] and shows comparable  $C - V$  characteristic on a similar device. d) Capacitance per unit area and (sheet) conductivity as a function of gate voltage.

top-BN. The AFM scan Fig. 6.1 b) reveals a surface roughness of the  $\text{Bi}_2\text{Se}_3$ -layer on the order of 1 nm. The corresponding series geometrical capacitance  $c_{air} \approx \epsilon_0/(1\text{nm}) = 8.9 \text{ fF}/\mu\text{m}^2$  indeed yields a more consistent estimate of the geometrical capacitance (with  $\epsilon_r(\text{hBN}) = 3.1$ , one finds indeed  $c_{tot} = (1/c_{air} + 1/c_{hBN})^{-1} = 2.48 \text{ fF}/\mu\text{m}^2$ ).

Using  $c_{geo} = 2.48 \text{ fF}/\mu\text{m}^2$ , we calculate the quantum capacitance as shown in Fig 6.4. We note that the uncertainty of  $c_{geo}$ , due to the rather small overall variations of the total capacitance, results in some uncertainty on the quantum capacitance shows as shaded area. As the calculation of the surface chemical potential relies on the knowledge of  $c_Q$ , the large uncertainties render this calculation also subject to rather strong uncertainties, represented as horizontal errorbars in Fig. 6.4 b). The red dotted line corresponds to a linear fit on the  $c_Q(\mu_s)$ -relation. As explained in chapter 3, assuming the variation of capacitance to be due to the top-TSS, this slope is given by  $e^2/(2\pi(\hbar v_F)^2)$  and thus

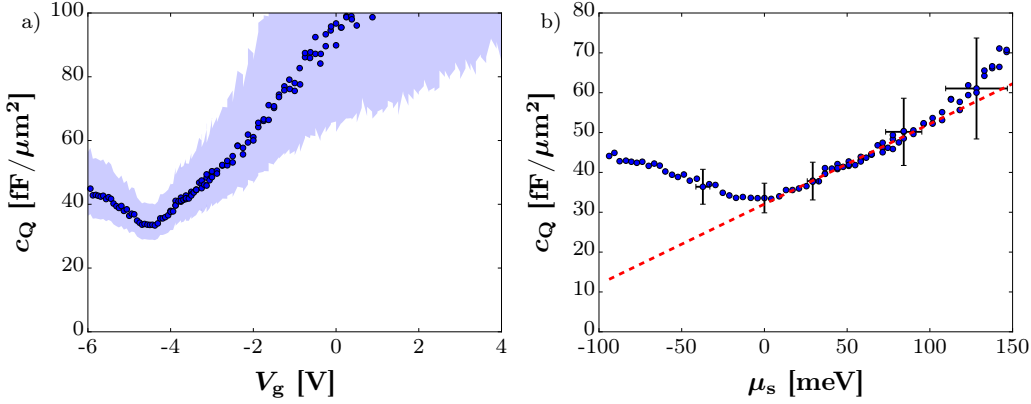


FIGURE 6.4: a) Quantum capacitance as a function of gate voltage. The shaded areas correspond to the error estimates due to the uncertainty on  $c_{geo} = 2.48 \pm 0.03 \text{ fF}/\mu\text{m}^2$  b) Quantum capacitance as a function of surface chemical potential  $\mu_s$  measured relative to the capacitance minimum. Some representative errorbars for  $c_Q$  and  $\mu$  are also shown. The dashed line corresponds to a linear fit yielding a Fermi velocity of  $v_F = 5.4 \cdot 10^5 \text{ m/s}$  (see main text).

directly related to the Fermi velocity. From the linear fit, we obtain  $v_F = 5.4 \cdot 10^5 \text{ m/s}$  in agreement (within errorbars) with earlier studies (cf. chapter 2). We point out that in contrast to HgTe, ARPES data reveals that the Dirac point of  $\text{Bi}_2\text{Se}_3$  is *not* nested in the valence band [72] (see also chapter 2). Thus, we associate the observed minimum in capacitance to a minimum in the density of states of the top-TSS.

Although the small variations of total capacitance, along with an uncertainty on  $c_{geo}$ , yield rather large errorbars in Fig. 6.4, the capacitance minimum is a robust feature. As with the HgTe n-type sample, we associate the shifted position of the capacitance minimum with respect to  $V_g = 0$  and the rather high value of the minimal quantum capacitance ( $c_{Q,min} \approx 33 \pm 5 \text{ fF}/\mu\text{m}^2$ ) to the presence of bulk-like or bottom-TSS carriers, see below. The capacitance data thus suggests that contributions other than the top-TSS need to be accounted for.

Before analyzing the capacitance data further, we turn now to the conductivity data represented in Fig. 6.3 d).

## 6.2.2 Resistance and conductivity

The resistance data in Fig. 6.3 c), shows a strong gate dependence for  $V_g < -3 \text{ V}$ . For gate voltages above  $-3 \text{ V}$ , the resistance flattens out at  $\sim 50 \Omega$ . We note that the resistance data does not reach a maximum within the investigated gate voltage range. In agreement with our interpretation of the capacitance data, this suggests that the conductivity is not carried by the TSS only. We will comment on this feature later. The resistance data shows a slight increase for large positive gate voltages ( $V_g \gtrsim 2 \text{ V}$ ). This feature is made

more visible when plotting the conductivity in Fig. 6.3 (d). We observe a conductivity drop at positive gate voltages. We shall now attempt to interpret this feature by virtue of the sub-band hypothesis, presented in chapter 5.

**Sub-band scattering as origin of scattering peak** When the gate voltage approaches 0 V, we observe a saturation of the conductivity. At positive gate voltages  $V_g > 2$  V, we observe even a *decrease* of the total conductivity. This feature is very similar to our observations on HgTe. We first investigate the explored ranges of (total) charge carrier variation and external electric field, using eq. (5.3), represented in Fig. 6.5. For definiteness, we measure the charge carrier density, the surface chemical potential and the effective insulator electric field with respect to  $V_g = 0$ . As we do not observe a maximum in resistance, we use the minimum capacitance as the definition of the Dirac point, and find  $n_{DP} = -6.5 \cdot 10^{12}/\text{cm}^2$ . Although the measured total variation of charge might be distributed over top-TSS and bulk or bottom-TSS states, an upper bound of the top-TSS mobility can be given by

$$\mu_{TSS} < \frac{1}{c} \frac{\partial \sigma_{tot}}{\partial V_g} \approx 16.000 \text{ cm}^2/(\text{Vs}) \quad (\text{at } 10 \text{ K}), \quad (6.1)$$

when we measure the slope of  $\sigma(V_g)$  close to the capacitance minimum. We highlight that this is likely to be a strong overestimation of the top-TSS mobility, see below (p. 160ff.). In any case, the top-TSS mobility is thus shown to be at least an order of magnitude smaller than those in HgTe, cf. chapter 5. As the inter sub-band scattering manifests itself in a drop in (TSS-)mobility when the Fermi level crosses a sub-band minimum, starting from a lower-mobility TSS will result in a smaller correction to the total conductivity.

However, we are able to resolve a maximum in conductivity at positive gate voltages,  $V_g = 1.4$  V. Associating this value to the appearance of a sub-band, we find a corresponding (total) charge carrier density of  $n_1 = 2 \cdot 10^{12}/\text{cm}^2$ .

In contrast to HgTe, we observe only one scattering peak, i.e. the simultaneous extraction of  $\varepsilon_r$  and  $\mathcal{E}_T$  is less straight-forward. However,  $\mathcal{E}_T$  can be determined without precise knowledge of  $\varepsilon_r$ : In chapter 5, we found that the first sub-band is expected to appear at a charge carrier density  $n_1$  and an electric field  $\mathcal{E}_1$  related via

$$(n_1 - n_{DP})^2 = \frac{e}{2\pi\hbar v_F} (\mathcal{E}_T^2 - \mathcal{E}_1^2), \quad (6.2)$$

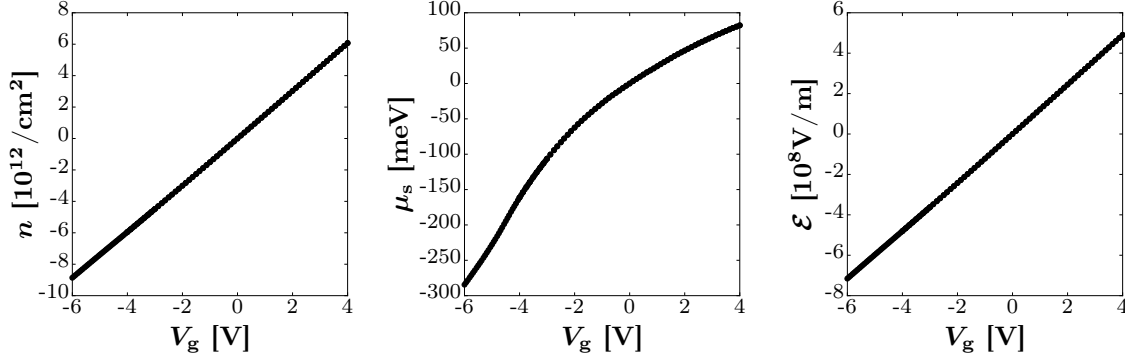


FIGURE 6.5: From left to right: total charge variation, variation of surface chemical potential and effective insulator electric field as a function of gate voltage. All three parameters presented here are measured with respect to  $V_g = 0$ .

where  $n_{DP}$  is the charge carrier density at the Dirac point. However,  $\mathcal{E}_1$  in (6.2) must be measured within the  $\text{Bi}_2\text{Se}_3$  surface layer. It is therefore given as

$$\mathcal{E}_1 = \frac{en_1}{\varepsilon_0 \varepsilon_r^{\text{Bi}_2\text{Se}_3}}. \quad (6.3)$$

Rewriting eq. (6.2), we find an expression for  $\mathcal{E}_T$ :

$$\mathcal{E}_T^2 = \underbrace{(2\pi\hbar v_F(n_1 - n_{DP})/e)^2}_{A_1} + \underbrace{(en_1/(\varepsilon_0 \varepsilon_r^{\text{Bi}_2\text{Se}_3}))^2}_{A_2}. \quad (6.4)$$

If we calculate the ratio of  $A_1$  and  $A_2$ , we find

$$\frac{A_2}{A_1} = \left( \frac{n_1}{n_1 - n_{DP}} \frac{e^2}{2\pi\hbar v_F \varepsilon_0} \frac{1}{\varepsilon_r^{\text{Bi}_2\text{Se}_3}} \right)^2 \approx \left( \frac{2}{\varepsilon_r^{\text{Bi}_2\text{Se}_3}} \right)^2. \quad (6.5)$$

For  $\text{Bi}_2\text{Se}_3$ , the lowest reported value to my knowledge is  $\varepsilon \approx 9.1$  [259], i.e. we can safely assume  $\varepsilon \gg 2$ . Hence, the  $A_2$ -term can be neglected for the determination of  $\mathcal{E}_T$ . Thus, from eq. (6.4), we calculate  $\mathcal{E}_T = 1.9 \cdot 10^8 \text{ V/m}$ . Note that this corresponds to the topological confinement field *within* the surface layer of  $\text{Bi}_2\text{Se}_3$ . The relation to the electric field imposed by the gate voltage in our experiment requires a more precise knowledge of  $\varepsilon_r^{\text{Bi}_2\text{Se}_3}$ . This value is controversial and different studies have reported on values ranging between  $\varepsilon_r^{\text{Bi}_2\text{Se}_3} = 9$  and  $\varepsilon_r^{\text{Bi}_2\text{Se}_3} = 100$  [210, 259]. As we dispose of a limited set of experimental data on  $\text{Bi}_2\text{Se}_3$ , we shall anyway not over-interpret these numbers quantitatively. To proceed and as a compromise we assume  $\varepsilon_r^{\text{Bi}_2\text{Se}_3} \approx 20$  in the following.

Using this value, we find a critical effective insulator field of  $\mathcal{E}_{ins} \sim 17 \cdot 10^8 \text{ V/m}$ . This field is larger than the dielectric strengths of most gate insulator materials. It is therefore extremely unlikely to ever observe higher order sub-bands in  $\text{Bi}_2\text{Se}_3$  if hBN is used as gate dielectric. It would require switching to high- $\kappa$  dielectrics, while preserving the low

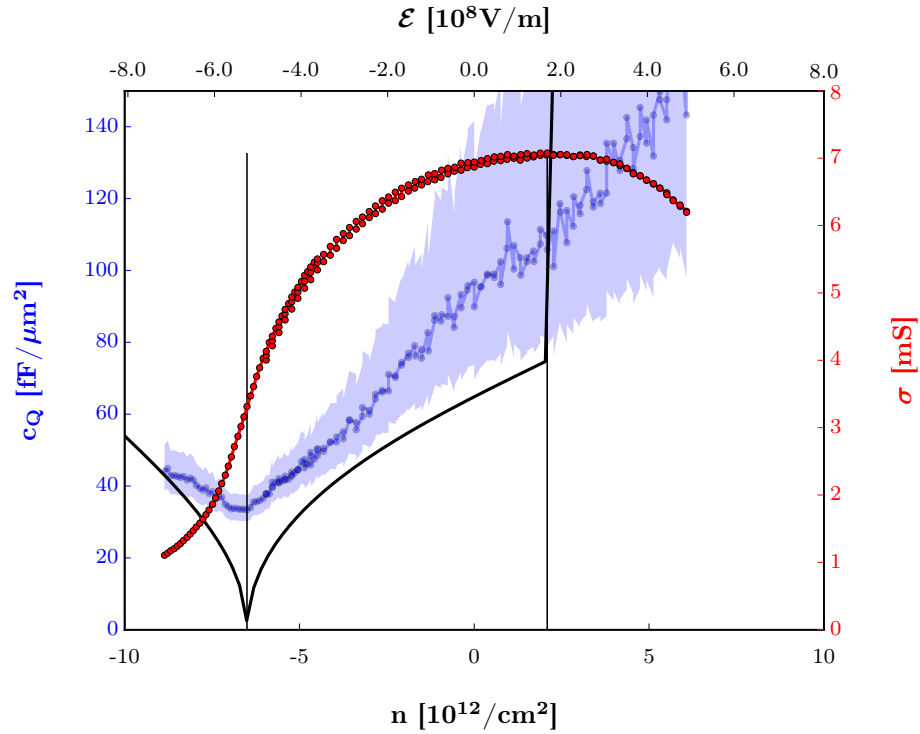


FIGURE 6.6: Quantum capacitance (blue) and conductivity (red) as a function of charge carrier density and electric (insulator) field. The shaded blue areas corresponds to the uncertainty due to uncertainties in the geometrical capacitance. The solid black line is the estimated quantum capacitance using the model, presented in chapter 5.

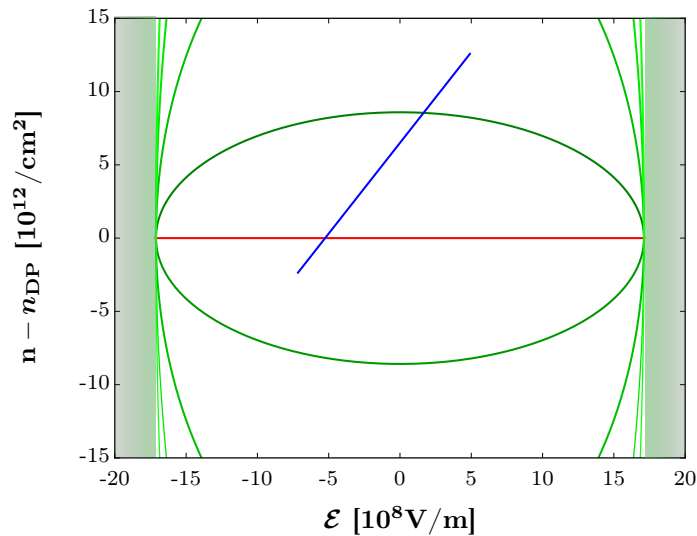


FIGURE 6.7: Massive surface states band-edges as a function of electric field and charge carrier density. The gate changes both quantities simultaneously such that in the experiment the blue line is followed.

doping concentration of  $\text{Bi}_2\text{Se}_3$  which is technologically challenging. As for  $\text{HgTe}$ , we can now trace the model predictions for sub-band calculations along with the measured conductivity and quantum capacitance in Fig. 6.6. In Fig. 6.7, I show the corresponding  $n - \mathcal{E}$  diagram for  $\text{Bi}_2\text{Se}_3$  as estimated by this experiment.

From section 5.8, we expect  $\mathcal{E}_T = (\Delta_2 - \Delta_1)/(e\xi)$ . The reported gap of hBN is 5.8 eV, i.e.  $|\Delta_2| \gg |\Delta_1|$ . We find thus experimentally a “surface width”  $\xi \approx 15$  nm. This value is obviously incompatible with the thickness of the Bi<sub>2</sub>Se<sub>3</sub>-flake of 6 nm. There are two possible explanations for this apparent contradiction: First, similar to the observations on the n-type HgTe sample, it is possible that the Bi<sub>2</sub>Se<sub>3</sub> surface is slightly oxidized, resulting in a much smaller  $\Delta_2$ . As an example, for the amorphous phase of Bismuth oxides, Leontie *et al.* found an energy gap on the order of  $\sim 2$  eV [260], yielding  $\xi \approx 5$  nm. Second, the calculations presented above assume that the total charge carrier density variation is carried by the top-TSS. This assumption seems questionable here in view of the rather weak variation of the quantum capacitance, presumably associated to a rather strong background.

In this case, the comparison to the model is by far less straight-forward as it requires a better understanding of the background capacitance. We shall attempt to understand the background capacitance below.

Anyway, we point out that the mere observation of a conductivity maximum is a strong indication that the physics described in chapter 5 also exist in Bi<sub>2</sub>Se<sub>3</sub>.

**Capacitance and conductivity in vicinity of the top-TSS Dirac point** Due to the thinness (6 nm) of the flake, treating bulk carriers within a 3D local density approximation, chapter 3, is not justified: Indeed, calculating the quantization of  $k_z$  yields confinement gaps for the bulk states. With an effective mass for bulk Bi<sub>2</sub>Se<sub>3</sub> carriers of  $m^* = 0.14 m_e$  [202], we find the (bulk’s) fundamental state to lie at  $E_0 \sim 75$  meV above the conductance band edge, and the first (excited) bulk sub-band to lie at  $E_1 \sim 670$  meV. It is thus likely that only one bulk sub-band is populated. The bulk carriers should therefore be considered as 2D carriers by themselves. Explicit treatment of the screening properties of such a two-fluid charge carrier system would require a self-consistent treatment. Furthermore, Veyrat *et al.* [146] and ViolBarbosa *et al.* [261], reported on (intrinsic) bulk band bending on length-scales on the order of 9 nm, exceeding the sample thickness. Thus, the assumption of a semi-infinite flake, chapter 3 is unjustified in the present context.

We develop a semi-quantitative understanding of the background capacitance and conductance close to the minimum in capacitance (i.e. the top-TSS Dirac point) as follows:

We note that the linear relation between  $c_Q$  and  $\mu$ , Fig. 6.4, yields a typical TSS Fermi velocity. This suggests that the observed variation of quantum capacitance is dominated by the top-TSS, over a relatively constant background capacitance. We observe

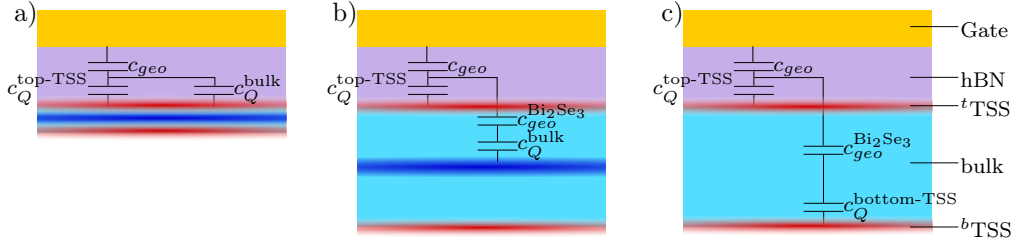


FIGURE 6.8: Possible scenarios for the background capacitance (see main text). a) The ultrathin (2D) limit. b) The bulk-carriers are described as a 2DEG centered in the flake thickness. c) Bulk carriers are negligible, the bottom-TSS causes the background capacitance.

a minimum in (quantum) capacitance of  $\sim 33 \pm 5 \text{ fF}/\mu\text{m}^2$ . There are several possible explanations for this minimum capacitance, cf. Fig. 6.8.

First, as the sample is in the thin-flake limit, i.e. bulk bending effects are expected to happen on a larger length scale than the sample thickness, we might naively treat the sample as purely 2D. In this case, a 2D bulk state can be treated as a (parabolic) band with effective mass  $m^* = 0.14 m_e$ . It has an energy independent density of states given by  $DoS = m^*/(\pi\hbar^2)$ . Thus we expect  $c_Q = 93 \text{ fF}/\mu\text{m}^2$  for a 2D bulk-like confinement band. We note that this value is incompatible with the observed background  $c_Q$ . We thus rule out this 2D-limit.

Second, in order to account for the finite thickness of the sample, as an approximation, we assume the bulk band to lie in the center of the sample, i.e. 3 nm from the surface. This implies that the bulk's capacitive response is governed by a geometrical contribution from half of the  $\text{Bi}_2\text{Se}_3$ -structure and the quantum capacitance of the bulk 2D states. In order to explain the measured minimal quantum capacitance, we find a dielectric constant for bulk  $\text{Bi}_2\text{Se}_3$  on the order of  $\epsilon_r = 20$ . We have discussed above that this value seems not incompatible with existing literature for thin flakes and at finite frequencies.

Third, we cannot rule out that the bulk band is completely empty, i.e. all observed phenomenology is carried by top and bottom-TSS: Indeed, as pointed out by Kim *et al.* [262], assuming charge carrier density independent bands, the top- and bottom-surfaces of  $\text{Bi}_2\text{Se}_3$  can carry  $\sim 5 \cdot 10^{12}/\text{cm}^2$  electrons each before the bottom of the bulk conduction band is reached. We note that the total charge carrier concentration within the  $\text{Bi}_2\text{Se}_3$ -flake varies by  $\sim 6 \cdot 10^{12}/\text{cm}^2$  between  $V_g = 0$  and the observed capacitance minimum. The observed capacitance minimum could therefore be a finite contribution from the bottom-TSS as sketched in Fig. 6.8 (c). In this case, the measured (total) quantum capacitance is given by

$$c_Q = c_{Q,top} + \left( \frac{1}{c_{\text{Bi}_2\text{Se}_3}} + \frac{1}{c_{Q,bottom}} \right)^{-1}, \quad (6.6)$$

where  $c_{\text{Bi}_2\text{Se}_3}$  is the (geometrical) capacitance between top and bottom surface. If we assume  $c_{Q,\text{top}} = 0$  at the capacitance minimum, we find a lower bound of  $\varepsilon_r = 22$ . However, our lack of an independent determination of  $\varepsilon_r$  (or  $c_Q^{\text{bottom-TSS}}$ ) rules out further quantitative analysis.

We conclude that the minimal capacitance can have different origins. However, based on the correct slope of the  $c_Q(V_g)$ -relation, we interpret the observable variations of (quantum) capacitance to be mainly due to variation of top-TSS charge carrier densities, whereas the bulk or the bottom-TSS contribute to the total capacitance as a relatively constant background with an effective (quantum) capacitance of  $33 \pm 5 \text{ fF}/\mu\text{m}^2$ . This implies that for  $V_g < -4.5 \text{ V}$ , the top-TSS shows p-type conduction, whereas a 2D bulk-like or the the bottom-TSS band remains n-type in this region.

This interpretation is consistent with the observed conductivity at large negative gate voltages: In Fig. 6.3 d), we note that the conductivity rises fastest as a function of gate voltage for  $-4.5 \text{ V} < V_g < -3 \text{ V}$ , i.e. just to the right of the capacitance minimum. From our conclusions of the capacitance data, these observations suggest that the conductivity of the background-carriers is monotonically decreasing when the gate voltage is lowered, whereas the top-TSS conductivity varies with the corresponding density of states, i.e.  $\sigma_{TSS}$  has a minimum at  $V_g \approx -4.5 \text{ V}$ , whereas  $\sigma_{\text{background}}$  varies roughly linear with  $V_g$  for  $V_g < -3 \text{ V}$ . The combined contribution of both carriers can thus qualitatively explain the conductivity variations in vicinity to the capacitance minimum.

As we have no additional knowledge of the background charge carrier's mobility or the top-TSS scattering rate, it is difficult to perform a quantitative analysis of such a (at least) two-fluid conductivity model.

In order to investigate the contributions of bulk (and eventually bottom-TSS) on capacitance and conductivity further, we performed measurements at room temperature, where the substrate can be used as a global back-gate, affecting primarily the bottom-TSS and bulk-states. These are presented in section 6.4.

### 6.3 Phonon scattering

Phonon scattering effects are generally investigated by measuring the temperature dependence of a sample's resistance.

Performing phase-sensitive RF admittance measurements at varying temperatures is challenging because the measurement setup needs to be re-calibrated *in-situ* after each change of temperature.

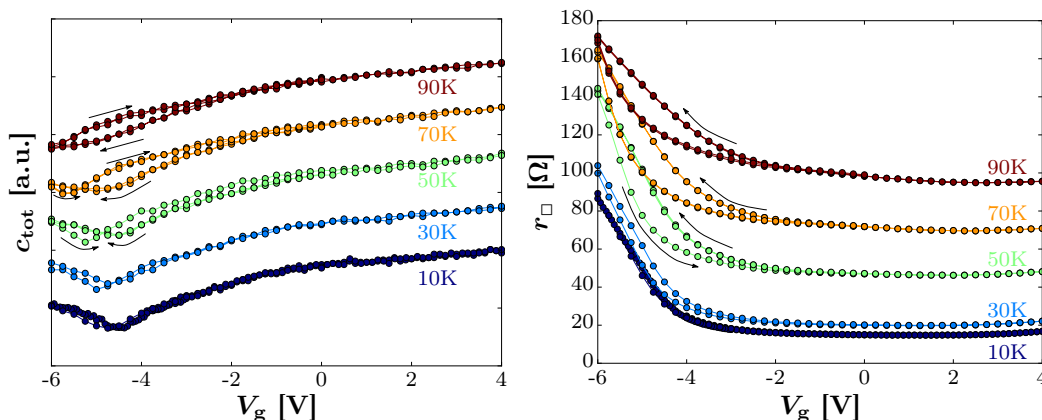


FIGURE 6.9: Left:  $C - V$  characteristic for different temperatures. Capacitance curves are vertically shifted for clarity. Right: Sheet resistance as function of gate voltage for the same temperature range. Black arrows indicate direction of sweep. The lines connecting the measurement data points are a guide to the eye.

When the temperature is increased from 10 K to 90 K, we start to observe hysteresis as well in the capacitance as in resistance gate sweeps, cf. Fig. 6.9, especially for gate voltages close to the Dirac point, i.e. the capacitance minimum. We shall not discuss this hysteresis quantitatively here, but observe that – similar to HgTe – the main effect of meta-stability in our sample is a horizontal shift in both resistance and capacitance. We note that all curve features are shifted towards more negative gate values, when the gate voltage is swept from negative to positive gate voltages and vice-versa.

In the capacitance, we note that the minimum in capacitance shifts to more negative gate voltages when increasing the temperature. However, the mean value of capacitance (averaged over the explored gate voltage range) does not depend on temperature. This suggests that the top-TSS charge carrier density at  $V_g = 0$  is generally increasing with temperature, while the back-ground capacitance does not change. A similar observation was reported by Kim *et al.* in ref. [262]. In this paper, the authors attribute the increased surface carrier concentration to a charge transfer of thermally activated bulk electrons to the topological surface states.

For the sheet resistance, we observe a metallic temperature dependence, i.e. a positive slope in the  $R - T$  relation. Such a temperature dependence is likely to be due to electrons scattering off acoustic phonons.

We also note that the maximum in conductivity, heralding sub-band scattering, disappears for temperatures higher than 50 K. It is therefore likely that – as for HgTe – the acoustic phonon scattering rate surpasses the inter sub-band scattering rate at higher temperatures, cf. Fig. 5.19.

Fig. 6.10 a) shows the sheet resistivity as a function of temperature for several gate voltages. We note that away from the Dirac point, i.e. for high carrier densities

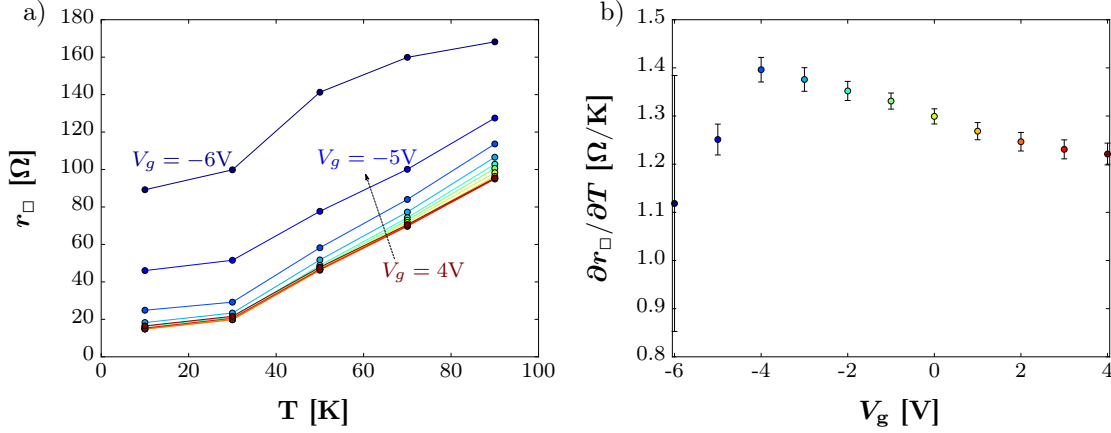


FIGURE 6.10: a) Sheet resistivity as a function of temperature for different gate voltages between  $-6V$  and  $+4V$  in steps of  $1V$  as indicated by the black arrow. b) Slopes of  $R(T)$  for  $T > 30K$  as a function of gate voltage.

( $V_g > -3V$ ) the resistivity shows a rather universal temperature behavior, with a slope  $\partial r_{\square} / \partial T \approx 1.3 \Omega/K$ , Fig. 6.10.

According to Kim *et al.* [262], the phonon limited resistivity in the high-temperature regime is given by

$$\rho \sim \frac{D^2 k_B T}{2e^2 \hbar v_F^2 v_{ph}^2 \rho_m}. \quad (6.7)$$

Given the sound velocity  $v_{ph} = 2900 \text{ m/s}$  and the (surface) mass density of a single quintuple layer of  $\text{Bi}_2\text{Se}_3$   $\rho_m = 7.68 \cdot 10^{-6} \text{ kg/m}^2$ , we find an effective deformation potential  $D = 17 \text{ eV}$ . We note that the high temperature regime is defined by  $T > T_{BG}$  with the Bloch-Grüneisen temperature  $T_{BG} = 2\varepsilon_F v_{ph} / (k_B v_F)$ . For a Fermi level  $\varepsilon_F = 100 \text{ meV}$  with respect to the Dirac point, we find  $T_{BG} \approx 12 \text{ K}$ , i.e. most data points correspond indeed to the high-temperature limit.

We note that – similar to ref. [262] – the linear relation between resistivity and temperature is altered for gate voltages close to the Dirac point. The lack of a sufficient number of data points at low temperatures, rules out a more quantitative understanding of the crossover and the low-temperature resistivity laws. For the low-temperature regime, a  $T^4 \rightarrow T$  or  $T^5 \rightarrow T$  crossover in the temperature dependence of the sheet resistivity as a function of carrier density and depending on the number of quintuple layers has been predicted [247, 263, 264]. As the RF admittance measurements yield not only the resistivity as a function of temperature, but also the compressibility, a more comprehensive study of the low-temperature behavior might lead to a better understanding of the different phonon-scattering regimes.

## 6.4 Dual-gated room temperature measurements

Our low-temperature measurements suggest a combined electronic response of top-TSS (most sensitive to the top gate) and a background carrier density, either due to bulk or to bottom-TSS carriers. In order to substantiate this interpretation, we investigated the sample's response to an additional application of a back-gate. Therefore the Si substrate with the insulating SiO<sub>2</sub> was used to deplete the Bi<sub>2</sub>Se<sub>3</sub>-flake "from the back". In order to avoid confusion, we introduce the subscripts *bg* and *tg* for back-gate and top-gate, respectively. Based on the geometrical and dielectric properties of the SiO<sub>2</sub> covering the waver, the associated geometrical capacitance per unit area of this remote back-gate is estimated to be  $c_{bg} \approx 0.1 \text{ fF}/\mu\text{m}^2$ .

**Reliability of back-gate measurements** There are several important remarks about using the global back gate: First, as mentioned above, the Si-substrate is too resistive at low temperatures, therefore this technique is only possible at room temperature. Second, the charging of the substrate with respect to the sample causes charge accumulation under the CPW electrodes at the Si/SiO<sub>2</sub> interface. This charge layer is conductive and therefore changes the overall electro-magnetic environment of our RF measurements. This renders the careful de-embedding using the dummy structure particularly important at room temperature. As an example, the stray capacitance extracted from dummy measurements at low temperatures is on the order of  $\sim 6 \text{ fF}$ , i.e. rather small when compared to the measured total sample's capacitance on the order of  $\sim 120 \text{ fF}$  as determined from a de-embedded spectrum, cf. Fig. 6.3. For the presented room temperature measurements in this section, the parasitic capacitance – determined from the dummy – rises to  $\sim 20 \text{ fF}$ . With the dielectric parameters of the SiO<sub>2</sub> back-gate oxide, cf. chapter 4, this corresponds to an effective area of  $\sim 170 \mu\text{m}^2$ , consistent with the approximate sizes of the electrodes close to the Bi<sub>2</sub>Se<sub>3</sub>-flake. In order to account for these parasitic contributions, dummy and thru were also measured for all explored back-gate voltages and de-embedding on the device-measurements was performed using the corresponding data sets. We also checked that the parasitic contribution *does not* depend on the applied top-gate voltage  $V_{tg}$ .

Third, as the back-gate oxide is much thicker than the top-gate hBN layer,  $V_{bg}$  is varied on a much larger scale in order to obtain – theoretically – similar doping variations. We monitored the leak-current of top and back-gate continuously. While no significant top-gate leakage could be detected over all explored top-gate voltages, the back-gate leakage current remained below 1 nA for back-gate voltages  $|V_{bg}| < 120 \text{ V}$ . At higher

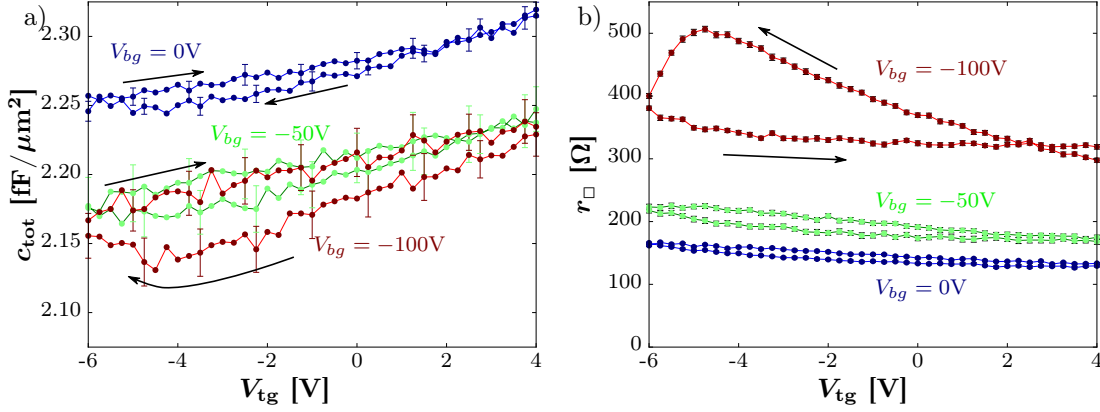


FIGURE 6.11: Capacitance per unit area (a) and sheet resistivity (b) as a function of top-gate voltage for different backgate voltages. The top-gate was swept from  $V_g = 4$  V to  $V_g = -6$  V and back as indicated by the black arrows. For better visibility only some error-bars are shown for the capacitance. The errors on the resistance are on the order of the dot size.

values of back-gate voltage, the SiO<sub>2</sub> layer suffered from a dielectric breakdown, yielding  $I_{leak} > 5$  nA (compliance setting). Unfortunately, this breakdown was irreversible, resulting in a rather limited set of back-gate dependent data points.

**Reduction of background carrier density by back-gating** In Fig. 6.11, I show capacitance per unit area and sheet resistivity as a function of top-gate voltage  $V_{tg}$  for three different back-gate voltages  $V_{bg}$ . The capacitance data is rather noisy, but shows that the overall capacitance *decreases* for larger (negative) back-gate voltages. This suggests that the background quantum capacitance indeed decreases when the sample’s bottom-TSS/bulk-bands are depleted. We also note that the  $V_{bg} = 0$  V  $C - V$  characteristic does not feature a clear minimum. This suggests that the thermal activation mentioned above indeed increases the top-TSS carrier density. For  $V_{bg} = -100$  V, we observe however a minimum-like feature in capacitance around  $V_{tg} = -4$  V, close to the  $T = 10$  K result presented above. This observation suggests that the back-gate not only depletes the bottom but also affects the top-TSS. We can estimate the total change of charge carrier density due to the back-gate from  $c_{bg} \cdot V_{bg}$ , and find  $\Delta n_{bg} \approx 6 \cdot 10^{12}/\text{cm}^2$ .

The most striking effect of the back-gate is however visible in the resistance data, Fig. 6.11 b). We observe a  $\sim 3$ -fold increase in the sheet resistance when  $V_{bg}$  is varied between 0 and  $-100$  V. This observation is in full agreement of our interpretation of “back-ground” carriers contributing to electron transport. We also note that whereas – even at low temperatures – the resistance did not show a maximum for most measurements, we observe a maximum in the “forward” (i.e.  $+4 \rightarrow -6$  V sweep) at  $V_{bg} = -100$  V. We highlight that the resistance maximum occurs in close vicinity to the minimum in capacitance for

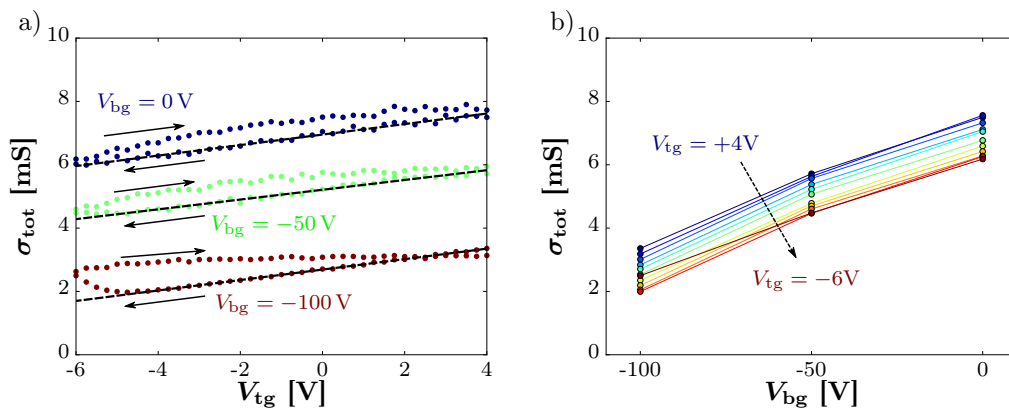


FIGURE 6.12: Total sample conductivity as a function of top-gate  $V_{tg}$  (a) and  $V_{bg}$  (b). The black arrows in (a) indicate the sweep-direction. The dashed black lines are linear fits to  $\sigma_{tot}(V_{tg})$  when  $V_{tg}$  is swept from 4 V to  $-6$  V. The colored lines in (b) are a guide to the eye.

this sweep, indicating that the corresponding minimum in conductivity is associated to a minimum in the electron compressibility.

**Meta-stability** We note a rather large difference between “forward” ( $V_{tg} = +4 \rightarrow -6$  V) and backward sweep ( $V_{tg} = -6 \rightarrow +4$  V) as well in capacitance as in resistivity, cf. Fig. 6.11, where the direction of sweep is indicated by the black arrows. Qualitatively, the observable hysteresis continues to show the horizontal shift already observed at lower temperatures: The lines of the forward sweep can be seen as shifted to the right with respect to the backwards sweep. However, the shift here is much larger than at low temperatures and extends over the full range of gate voltages. A charge transfer mechanism as presented in chapter 5 might also explain the observed hysteresis here. However, at room-temperature, slow displacement of ions in the SiO<sub>2</sub> or in the formation of an electronic layer at the SiO<sub>2</sub> interface might also lead to hysteresis. The precise origin remain thus a little obscure. In the following, we shall assume that the system remains in a well defined state during the forward sweep and concentrate our analysis on this sweep.

### Mobility differences from dual-gate dependent conductivity measurements

A more quantitative understanding of the sample conductivity can be gained by investigating  $\sigma_{tot}$  as a function of back- and top-gate, shown in Fig. 6.12. Interestingly, we find that the conductivity varies linearly (on the electron side) with the top-gate voltage independently of the applied back-gate voltage. This is illustrated by the dashed black lines in Fig. 6.12 a). We find  $\partial\sigma_{tot}/\partial V_{tg} = 160 \pm 5 \mu\text{S}/\text{V}$ . If we trace the conductivity as a function of  $V_{bg}$  for different  $V_{tg}$  we also find linear variation<sup>2</sup> independent of the

<sup>2</sup>As we measured only three different back-gate voltages, this statement must be handled with care.

applied top-gate voltage (an exception occurs for  $V_{tg} = -6$  V). We find experimentally  $\partial\sigma_{tot}/\partial V_{bg} = 40 \pm 3 \mu\text{S}/\text{V}$ . From these observations, we conclude that at least two electronic fluids “top” and “bottom” are unequally affected by the two gates. A minimal model to describe the observed phenomenology consists in writing

$$\sigma_{tot} = \sigma_{top} + \sigma_{bot}. \quad (6.8)$$

Within a Drude model we have

$$\sigma_{top/bot} = n_{top/bot} e \mu_{top/bot}, \quad (6.9)$$

where  $\mu_{top/bot}$  designates effective electron mobilities for the corresponding fluid.

Both gates are likely to not exclusively affect the closest electron fluid, however, we can assume that the top (bottom) gate *mainly* affects the charge carrier density of the top (bottom) fluid. Thus, we shall assume

$$en_{top/bot} \approx c_{top/bot}(V_{tg/bg} - V_{CNP}). \quad (6.10)$$

where  $V_{CNP}$  is the voltage corresponding to minimal carrier density. Anyway we concentrate on the electron side, and therefore the exact value of  $V_{CNP}$  does not play a role in the following discussion. Combining eqs. (6.9) and (6.10), we find from the slopes in Fig. 6.12  $\mu_{top} \approx 650 \text{ cm}^2/(\text{Vs})$  and  $\mu_{bot} \approx 4000 \text{ cm}^2/(\text{Vs})$ . Consequently, we conclude that the bottom electronic fluid has a much higher mobility than the top-fluid.

Although our measurements cannot yield information about the existence and relative contribution to the total conductivity of bulk carriers, it seems unphysical to assume that top and bottom gate affect bulk carriers differently. Hence, the bulk carriers might lead to constant offsets in the conductivity but not change the slope of the  $\sigma(V)$  relations. Thus, we can conclude from our observations at room temperature that the top-TSS electrons show a  $\sim 6$ -times lower mobility than the bottom-TSS. This situation is actually expected from the device fabrication details: The SVD-growth on hBN is known to be epitaxial [157, 216], and the exfoliated hBN-crystals are atomically flat. This leads to a very clean bottom surface of the investigated  $\text{Bi}_2\text{Se}_3$ -flakes. The AFM scan, Fig. 6.1, reveals that this does not hold for the top surface. Furthermore, the bottom-surface in close contact to the bottom-BN is never exposed to air during fabrication process, whereas the top-surface is exposed until top-BN deposition. The rougher top-surface and a possible surface degradation due to e.g. surface oxidation [218] is thus likely to cause enhanced electron scattering for top-TSS electrons.

We highlight the extremely high field-effect mobility for the bottom-TSS at room temperature that we found on the present sample. This illustrates the importance of clean neighboring surfaces for the electronic properties of topological surface states in Bi<sub>2</sub>Se<sub>3</sub>.

## 6.5 Conclusions and outlook

We have fabricated encapsulated hBN-Bi<sub>2</sub>Se<sub>3</sub>-hBN metal-insulator-topological insulator capacitors via a fabrication process that minimizes Bi<sub>2</sub>Se<sub>3</sub>-exposure to photo- or e-beam resists and solvents. Furthermore, the direct growth of Bi<sub>2</sub>Se<sub>3</sub> on hBN exfoliated thin flakes results in a atomically flat and clean substrate for the Bi<sub>2</sub>Se<sub>3</sub>-growth.

Our radio-frequency admittance measurements at low temperatures revealed a part of the quantum capacitance to vary linearly with chemical potential, indicating topological surface states with a Fermi velocity of  $v_F \approx 5.4 \cdot 10^5$  m/s. We also observe indications of a massive sub-band for high doping concentrations and finite electric fields. This observation is very similar to the results presented for HgTe. The main indicator for the appearance of a sub-band is an inversion in the  $\sigma(V_g)$  characteristic (changing from a positive to a negative slope) at positive gate voltages, i.e. relatively high carrier concentration. This feature is however much broader than for the case of HgTe which is due to the lower TSS mobility ( $< 16.000$  cm<sup>2</sup>/(Vs) at 10 K) of Bi<sub>2</sub>Se<sub>3</sub>-TSS.

The temperature dependence in a low-temperature regime of capacitance and sheet resistance features signatures of (TSS-)electron scattering off acoustic phonons, with an experimentally determined deformation potential  $D \approx 17$  eV. Following the arguments of Kim *et al.* [262], the evolution of charge carrier density at  $V_g = 0$  with temperature indicates an increase in (TSS) charge carrier density via thermal activation of bulk carriers transferred to the surfaces.

Combining top- and backgate measurements at room temperature (300K) on the Bi<sub>2</sub>Se<sub>3</sub>-flake, we found a  $\sim 6$ -times enhanced field-effect mobility of the bottom-TSS as compared to the top-TSS. We attribute this to an increased electronic scattering rates for the top-TSS due to growth-induced surface roughness and surface oxidation. Our observations illustrate clearly the advantages of growing Bi<sub>2</sub>Se<sub>3</sub>-flakes epitaxially on hBN for room-temperature applications.

As an outlook, we aim at fabricating encapsulated Bi<sub>2</sub>Se<sub>3</sub>-flakes on top of pre-patterned *local* back-gates. Such a design would allow us to probe the quantum capacitance of the (higher mobility) bottom-TSS quantitatively and reduce parasitic contributions from charges at the back-gate's metal-insulator interface. Furthermore, in such a dual local

gate design, we plan to investigate the role of electric fields and changes in chemical potential independently.

## Chapter 7

# Conclusions and Outlook

In this thesis we have investigated the AC electronic compressibility of three-dimensional HgTe and Bi<sub>2</sub>Se<sub>3</sub> topological insulators. Particular attention was given to the influence of high electric fields.

We have presented experimental evidence of topological surface states with a Dirac-like dispersion via capacitance spectroscopy on high quality strained HgTe TI samples from Würzburg University (Germany). We have shown that in this experimental situation, the TSS dominate the spectrum on the electron side over a large range of chemical potentials, exceeding by far the bulk transport band gap. This “Dirac screening”-regime is limited to a certain range of phase space spanned by chemical potential, electric field and charge carrier density. These phase boundaries can be calculated in a simple model, developed by our collaborators from Orsay University (Paris-Saclay). The boundary between an inverted (topological) and a normal gap (trivial) insulator is modeled as a gradual junction over which the gap varies smoothly. This model predicts i) the existence of topologically confined massive surface states in addition to the well-known massless Dirac surface states, ii) an explicit electric field dependence of the excitation gap of these states, iii) a reduction of the effective Fermi velocities for all types of surface states at large electric fields and iv) the existence of a critical electric field. The critical electric field corresponds to the limit of vanishing Fermi velocity and a gap-closing for all massive surface states. Experimentally, we presented four-fold indications for these massive subbands: i) a highly effective inter-sub band scattering mechanism, ii) a bump in electronic compressibility, iii) a non-linearity in magneto-transport and iv) the appearance of charge metastability.

We have thus established a first step towards a reinterpretation of the surface physics of TI-normal insulator boundaries. The rich surface spectrum and the identification of electric field and charge carrier density as relevant variables raise the question how this

surface spectrum evolves under the influence of other external parameters like magnetic fields, temperature, etc. Furthermore, the electric field-dependent expressions for the surface spectrum constitute a first step towards the calculation of a surface energy correction associated to topological confinement. Such a description is yet to be done, but it might address the question of “topological surface tension”.

As a more practical outlook, the theoretical part of this thesis might be complemented by numeric calculations based on  $\mathbf{k} \cdot \mathbf{P}$  theory, while explicitly taking the interface width  $\xi$  into account. During the preparation of this manuscript, first preliminary  $\mathbf{k} \cdot \mathbf{P}$  calculations by David Carpentier and Victor Jouffrey (ENS Lyon) seem to back the existence of massive surface states in the absence of electric fields if a finite interface region is considered. As a second step, electric fields should be incorporated via a self-consistent treatment similar to Baum *et al.* [41].

On the experimental side, some results could be complemented by further analysis and measurements. As an example, the temperature dependent capacitance and resistivity in the HgTe and the Bi<sub>2</sub>Se<sub>3</sub> samples might provide further insight into the electron-phonon scattering mechanisms in these systems. In particular, electron-phonon scattering at low temperatures (i.e. below the Bloch-Grüneisen temperature) is predicted to yield either a  $T^4$  or a  $T^5$  law for the TSS resistivity, depending on sample thickness, cf. Refs. [247, 264].

As a more technological aspect of this work, in particular for the Bi<sub>2</sub>Se<sub>3</sub>-samples, we have presented evidence that the bottom surface of epitaxially grown Bi<sub>2</sub>Se<sub>3</sub> on hBN has better electron mobilities than the top-surface due to its protection from surface oxidation or lithography induced contamination. We plan to use a local bottom-gate technique, developed by Q. Wilmart at LPA [225, 241], to locally address the bottom-TSS of Bi<sub>2</sub>Se<sub>3</sub>. This approach might pave the way for room temperature Dirac electronics, including high-frequency transistors (due to high electron mobility), or coupling to magnetic contacts for spintronics (helical TSS), etc. On a more fundamental level, the implementation of combined local back- and top-gates will allow us to disentangle the electric-field and charge carrier density dependencies of TSS and MSS properties.

On the experimental side, the techniques used in this thesis can be adapted to the study of a large number of other systems: As a first example, Riley *et al.* have reported on negative electron compressibilities in WSe<sub>2</sub> [265]. However, in Ref. [265], the conclusions were drawn rather indirectly based on the interpretation of ARPES data. Our capacitance measurement technique might shed further light on this phenomenon driven by electron-electron interactions. Such a study might constitute a part of Romaric Legoff’s PhD at LPA.

As a second example, we might study (2D) HgTe quantum wells close to the critical thickness for the trivial to topological insulator phase transition. At this point, the formation of domains of topological trivial and normal regions, i.e. positive and negative gaps might occur. Such a mixed state might result in so-called Dirac mass disorder. Such a type of disorder was previously reported by our group in the case of graphene [15]. Combined measurements of quantum capacitance and conductivity in a RF-capacitor design are thus expected to shed further light on the details of this topological phase transition. This experimental prospect constitutes a generalization of the present thesis towards a lower-dimensional system.

Furthermore a generalization to a higher (i.e. 3D) topological system seems to be an interesting alternative path. Indeed as a 3D Dirac system (“3D Graphene”) the emergence of Weyl [266] semi-metals caused considerable theoretical and experimental effort [267–274] (see also Refs. [275–277]). In contrast to topological insulators, the bulk of Weyl semi-metals is not gapped, but features (an even number of) non-degenerate Dirac points, called Weyl nodes protected by symmetries (time-reversal, inversion, etc.). Similar to the calculation of other topological invariants, e.g. Chern or  $\mathbb{Z}_2$  indexes, a chirality  $\chi$  can be associated to each Weyl node. Depending on the underlying symmetry, Weyl nodes appear in pairs or in quadruples such that the *total* chirality is always zero [275, 278, 279]. At the sample surfaces however, the projection of Weyl points of different chirality are connected by so-called Fermi-arcs, i.e. the Fermi surface of the 2D surfaces is an (open) 1D line. These Fermi arcs have been observed in ARPES measurements [268, 269, 280] and quasi-particle interference [281]. To my knowledge, no experimental data on electron compressibility of Weyl semi-metals exists up to date. Protogenov *et al.* predicted a logarithmic divergence of the surface density of states in Weyl semi-metals around a saddle point in the surface spectrum [282]<sup>1</sup>. Strain engineering of 3D HgTe is predicted to drive HgTe into the Weyl phase [283]. Leubner *et al.* recently demonstrated in Würzburg that strain-engineering of HgTe quantum wells is indeed possible [284]. Hence, strain-engineering Weyl semi-metals in the HgTe material family are within experimental reach. Extending the existing collaboration between LPA and the Würzburg group to this new class of materials might thus constitute a first step towards an experimental determination of their compressibility in an electron transport experiment. A promising alternative platform for studying Weyl semi-metals might be realized in Heusler compounds, cf. Ref. [285] for an overview. Especially GdPtBi seems a promising candidate for experimental studies on *magnetic* Weyl semi-metals due to a phase transition at  $T_C = 9.0$  K available in our experimental setup between a TI and a magnetic Weyl semi-metal phase (anti-ferromagnetic phase) [285, 286].

<sup>1</sup>unpublished reference. The logarithmic divergence in this work is based on a surface dispersion relation featuring a saddle point. Unfortunately, the origin (and robustness) of such a saddle point seems to be badly referenced in Ref. [282].

One of the most exciting properties of topological matter, particularly appealing in Weyl semi-metals is the so-called chiral anomaly due to an axionic term in the electromagnetic Lagrangian [287, and references therein]. This feature shall be quickly discussed here. Indeed, capacitor structures in the large electric field limit, could be used to investigate such axion electrodynamics. The theory of axion electrodynamics was originally developed by Wilczek [131], who introduced an axionic term  $\mathcal{L}_\theta = \theta \mathbf{E} \cdot \mathbf{B}$  to the electromagnetic Lagrangian. Here,  $\theta$  is the so-called *axion* field. It has been shown [132] that the action describing a TI takes the same form under the identification of  $\theta \leftrightarrow P_3$  with  $P_3$  the topological magneto-electric polarization. Adding this  $\mathcal{L}_\theta$ -term leads to additional terms in Maxwell's equations [82, 134]:

$$\text{modified Gau\ss}' \text{ law : } \quad \nabla \cdot \mathbf{E} = \frac{\rho}{\varepsilon_0} + 2c\alpha \nabla \left( \frac{\theta}{2\pi} \right) \cdot \mathbf{B}, \quad (7.1)$$

$$\text{modified Amp\`ere's law : } \quad \nabla \times \mathbf{B} = \mu_0 \mathbf{j} + \frac{2\alpha}{c} \left[ \mathbf{B} \frac{\partial}{\partial t} \left( \frac{\theta}{2\pi} \right) + \nabla \left( \frac{\theta}{2\pi} \right) \times \mathbf{E} \right]. \quad (7.2)$$

Already in the original paper from 1987, Wilczek pointed out that axion electrodynamics might be observable in a solid-state context. Importantly, axion electrodynamics are important not only for Weyl semi-metals but also for topological insulators. Qi *et al.* [132] showed that the axion parameter  $\theta$  (i.e.  $P_3$ ) varies between  $\pi$  in a TI and zero in a trivial insulator<sup>2</sup>. Hence, the surface of a TI is a natural realization of a non-vanishing  $\nabla\theta$ . As a possible consequence of the axionic terms in Maxwell's equations, (induced) magnetic monopoles were proposed [133]. Moreover, the theory implies the existence of crossed terms in the magneto-electric polarizability, i.e. magnetic fields induce electric dipoles and electric fields induce magnetic dipoles. This ‘‘topological magneto-electric effect’’ leads eventually to quantized Kerr and Faraday rotations if polarized (terahertz) radiation is incident on topological insulator samples [288, 289]. First signatures of (strong) Kerr rotations due to topological surface states in  $\text{Bi}_2\text{Se}_3$  were reported by Vald\`ez Aguilar *et al.* [290]. Recently, a quantization has been reported in  $\text{Bi}_2\text{Se}_3$  by Armitage's group in Baltimore [134] and in Vienna by Dziom *et al.* on strained HgTe-samples from W\`urzburg [82]. This quantization might be interesting for metrology under further experimental improvements. We note that for the observation of these quantization effects, rather large magnetic fields ( $\sim 7$  T) are required. To my knowledge, less attention has been spent to the effects of large electric fields in the context of axion electrodynamics. Due to the symmetric role occupied by  $\mathbf{E}$  and  $\mathbf{B}$  in the axion Lagrangian, studying topological materials under this new perspective in the high electric field limit seems thus to be a promising route.

---

<sup>2</sup>In a time-reversal symmetric system, it can be shown that  $\theta$  can only be zero or  $\pi$  (up to  $2\pi$ ).

## Appendix A

# Finite temperature expressions for 2D Quantum capacitances

### A.1 Linear dispersion - Graphene-like systems

For a 2D conductor with linear band dispersion

$$\varepsilon(\mathbf{k}) = \pm \hbar v_F |k| \quad (\text{A.1})$$

and a degeneracy factor  $g$ , the density of states is given by

$$c_Q = e^2 \frac{g|\varepsilon|}{2\pi(\hbar v_F)^2}. \quad (\text{A.2})$$

One obtains thus an electron compressibility that is proportional to the Fermi level. Note, that interestingly, the numeric value of the prefactor is similar for graphene or TI surface states. In fact, the degeneracy factor of four for graphene (one for a topological surface state) is compensated by a factor of approximately one half in the Fermi velocity ( $\sim 10^6$  m/s for graphene vs  $\sim 5 \cdot 10^5$  m/s for most TIs.). In this particular case of a perfect Dirac cone, an analytic expression at finite temperatures exist, cf. [10]:

$$c_Q = e^2 \frac{gk_B T}{2\pi(\hbar v_F)^2} \ln \left[ 2 + 2 \cosh \left( \frac{\mu}{k_B T} \right) \right]. \quad (\text{A.3})$$

## A.2 Quadratic Dispersion - Quantum well - 2DEG-like systems

It is well known, that at the interface of two semiconductors, quantum wells can form and (trivial) interface states emerge. The most widely used type of these interface states occurs in epitaxially grown GaAs/GaAlAs heterostructures, cf. [85] for an overview. Typically these interface states are called two-dimensional electron gases (2DEG). In order to fix the notation, a small remark shall be made here: Although graphene and the surface states of a TI naturally constitute 2D electronic systems, their intriguing ‘‘Dirac’’-properties led to the linguistic convention of not calling these systems ‘‘2DEG’’. Throughout this thesis, the acronym ‘‘2DEG’’ is used for a trivial and massive two-dimensional electron gas. The electronic properties of these gases in two dimensions are typically described by a massive dispersion relation

$$\varepsilon = \frac{\hbar^2 k^2}{2m^*}, \quad (\text{A.4})$$

where  $m^*$  is the effective mass.

The density of states at zero temperature is given by

$$c_Q = e^2 \frac{gm^*}{2\pi\hbar^2} \Theta(\varepsilon - \varepsilon_{\text{BE}}), \quad (\text{A.5})$$

where  $\varepsilon_{\text{BE}}$  is the band-edge and  $\Theta$  is the Heaviside step-function.

Note, that once the system starts to be populated the density of states is constant. The effect of finite temperature on the 2DEG’ compressibility is simply a broadening of the step feature following a Fermi-Dirac distribution:

$$c_Q = \frac{gm^*}{2\pi\hbar^2} \frac{1}{1 + e^{\beta(\varepsilon - \mu)}}. \quad (\text{A.6})$$

## A.3 Massive Dirac system

If a Dirac cone is gapped which can be achieved for example in ultra-thin 3D TIs [291], the spectrum is described by a so-called massive Dirac model, yielding the following dispersion relation

$$\varepsilon = \sqrt{\Delta^2 + (\hbar v_{\text{F}} k)^2}, \quad (\text{A.7})$$

where  $\Delta$  corresponds to half the gap. Note that for simplicity we restrict the discussion here to the conduction band. At large  $k$ , i.e. high Fermi levels, the system recovers a gap-less dispersion of a perfect Dirac cone, whereas at low energies close to the band

gap, the electrons obey (in second order approximation) a massive band-structure with a mass equal to  $m^* = \Delta/v_F^2$ . Interestingly the density of states for such a massive Dirac combines the features of a massless Dirac system and that of a parabolic band: At the band-edge, the density of states is discontinuous and jumps from zero to the value that the massless system would have at the same energy if the Dirac point was at mid-gap, see also fig. 3.3 from the main text. For  $E > \Delta$ , the density of states follows exactly the same law as the massless system. Its zero-temperature expression is given by

$$c_Q = e^2 \frac{g\varepsilon}{2\pi(\hbar v_F)^2} \Theta(\varepsilon - \Delta). \quad (\text{A.8})$$

One can also calculate the electron compressibility at finite temperature for the massive Dirac system:

$$c_Q = e^2 \frac{g}{2\pi(\hbar v_F)^2} \left\{ \varepsilon - \Delta \left[ \frac{e^{\beta(\Delta-\varepsilon)}}{1 + e^{\beta(\Delta-\varepsilon)}} \right] + k_B T \ln \left[ 1 + e^{\beta(\Delta-\varepsilon)} \right] \right\}. \quad (\text{A.9})$$

Analogous formula apply to the hole side.



## Appendix B

# Capacitance in depletion regime

In the depletion region Gauss' law writes:

$$V'' = -\frac{e}{\varepsilon}N_D. \quad (\text{B.1})$$

Therefore

$$V'(z) = -\frac{eN_D}{\varepsilon}z + V'(0) = -\frac{eN_D}{\varepsilon}z + \frac{eN_D}{C_Q}. \quad (\text{B.2})$$

Here I explicitly used the “general” relation (3.28). Furthermore, we have  $C_Q^0 = C_Q(V = V_{\text{CBE}}) = eN_D/V'(\delta)$ . Hence

$$\frac{1}{C_Q} = \frac{1}{C_Q^0} + \frac{\delta}{\varepsilon}. \quad (\text{B.3})$$

We can integrate (B.2) once more to find

$$V(z) = -\frac{eN_D}{2\varepsilon}z^2 + \frac{eN_D}{C_Q}z + V(0). \quad (\text{B.4})$$

It is interesting to evaluate this equation in  $z = \delta$ , i.e.  $V(\delta) = V_{\text{CBE}}$  when  $V(0) = V_{\text{VBE}}$ . We obtain

$$\Delta_{\text{Gap}} = -\frac{e^2N_D}{2\varepsilon}\delta_m^2 + \frac{e^2N_D}{C_Q}\delta_m \quad (\text{B.5})$$

$$= -\frac{e^2N_D}{2\varepsilon}\delta_m^2 + \frac{e^2N_D}{C_Q^0}\delta_m + \frac{e^2N_D}{\varepsilon}\delta_m^2 \quad (\text{B.6})$$

$$= \frac{e^2N_D}{2\varepsilon}\delta_m^2 + \frac{e^2N_D}{C_Q^0}\delta_m, \quad (\text{B.7})$$

which allows us to calculate the maximal depletion width

$$\delta_m = \frac{\varepsilon}{C_Q^0} \left( \sqrt{1 + 2\frac{\Delta_{\text{Gap}}C_Q^0{}^2}{e^2N_D\varepsilon}} - 1 \right). \quad (\text{B.8})$$

The python code for finite temperature evaluation of the bulk's quantum capacitance at finite temperature is given in the following:

---

```

'''The full temperature dependent screening problem.'''
from RFLPA.fundconst import e,hbar,kB,eps0 # Defines e, hbar, etc.
import numpy as np
from numpy import sqrt,abs,pi
import matplotlib.pyplot as plt

#-----
# Model paramters (for a "massive Dirac" bulk).
# The Delta parameter and the band extrema can be chosen indepentently.
#-----
Delta_e = 0.05*e # Delta parameter for electrons.
Delta_h = Delta_e # Delta parameter for holes.
E_C = 0.018*e # Electron band minimum.
E_V = -0.012*e # Hole band maximum.
vFe = 1.6e6 # Fermi velocity electron side.
vFh = 0.5e6 # Fermi velocity hole side.
eps_r = 21. # bulk dielectric constant.

#-----
# Specify "external" paramters.
#-----
T = 10 # Temperature in Kelvin.
mu_inf = 0.170*e # Chemical potential deep in the bulk (in Joule).

#-----
# Definition of functions.
#-----
def heaviside(x):
    '''Heaviside step function'''
    return 0.5*(np.sign(x)+1)

def DoS_e(en):
    '''electronic (3D) T=0 density of states calculated at energy en.'''
    e_s = en+Delta_e-E_C #Shifted spectrum for correct band offset
    a = e_s**2.-Delta_e**2.
    return heaviside(en-E_C)*abs(e_s)*sqrt(abs(a))/(pi**2*(hbar*vFe)**3.)

def DoS_h(en):
    '''hole (3D) T=0 density of states calculated at energy en.'''
    e_s = en-Delta_h-E_V #Shifted spectrum for correct band offset
    a = (e_s)**2.-Delta_h**2.
    return (heaviside(E_V-en)*abs(e_s)*sqrt(abs(a))
            /(pi**2*(hbar*vFh)**3.))

def fFD(en,mu,T):
    '''Fermi-Dirac distribution. Evaluated in natural units.'

    Parameters
    -----
    en: A numpy array of energies (in J).
    mu: chemical potential (in J)
    T: temperature (in K)

```

```

'''
e_adim = en/e
mu_adim = mu/e
beta = e/(kB*T) # reduced inverse temperature.
res = np.empty(len(en))
res[en-mu>=100*kB*T] = 0 # Avoid numerical overflow
res[en-mu<=-100*kB*T] = 1 # Avoid numerical overflow
mask = np.logical_and(en-mu>-100*kB*T, en-mu<100*kB*T)
res[mask]=1./(1.+np.exp(beta*(e_adim[mask]-mu_adim)))
return res

def n(T,mu):
'''Electron density at given chemical potential and temperature.

Parameters
-----
mu: An array or a float for the chemical potential in Joule.
T: temperature (in K).

Returns
-----
res: the 3D electron density in 1/m^3.
'''
b_p = np.linspace(-5*e,5*e,20000) # base points for numerical integration
func = lambda x: DoS_e(x)*fFD(x,mu,T) # finite T DoS.
return np.trapz(func(b_p),x=b_p)# Numerical integration

def p(T,mu):
'''Hole density at given chemical potential and temperature.

Parameters
-----
mu: An array or a float for the chemical potential in Joule.
T: temperature (in K).

Returns
-----
res: the 3D hole density in 1/m^3.
'''
b_p = np.linspace(-5*e,5*e,20000) # base points for numerical integration
func = lambda x: DoS_h(x)*(1.-fFD(x,mu,T)) # finite T DoS.
return np.trapz(func(b_p),x=b_p) # Numerical integration

def CQ(mu_s, N,P,all_ens):
'''Calculate CQ for a given surface chemical potential.
Element-wise calculation.
Use CQ_it for calculation over vectors of mu_s.'''
mu_inf_i = np.argmin(abs(all_ens-mu_inf))
mu_s_i = np.argmin(abs(all_ens-mu_s))
Ninf = N[mu_inf_i]-P[mu_inf_i] # Finite T "intrinsic" carrier density.
Rho = e*(Ninf-N+P) # Total charge density for all energies.
if mu_s_i == mu_inf_i:
# Treats the "problematic point" and avoids numerical issue.
dndmu = (Rho[mu_inf_i+1]/e)/(all_ens[mu_inf_i+1]-all_ens[mu_inf_i])
return sqrt(eps0*eps_r/(e**2*abs(dndmu))) # Thomas-Fermi result.

```

---

```

elif mu_s>mu_inf:
    mask = np.logical_and(all_ens>=mu_inf,all_ens<=mu_s)
    sign = -1
else:
    mask = np.logical_and(all_ens<=mu_inf,all_ens>=mu_s)
    sign = +1
b_p = all_ens[mask] # base points for numerical integration
integral = np.trapz(Rho[mask],x=b_p)*sign # numerical integration
under_root = 2.*integral/(eps0*eps_r*e) # argument of sqrt.
return abs(Rho[mu_s_i])/(sqrt(under_root))

def CQ_it(mu_s,N,P,all_ens):
    '''Calculate CQ for a list of surface chemical potentials.
    For mu_s == mu_inf, numerical divergencies are likely to occur.
    This point is treated separately.
    '''
    res = np.array([CQ(m,N,P,all_ens) for m in mu_s]) # contains problematic point!
    index =np.argmax(abs(mu_s-mu_inf)) # Index of mu_s = mu_inf.
    res[index] = (res[index+1]+res[index-1])/2. # mean of neighbouring points.
    return res

p = np.vectorize(p) # vectorize functions
n = np.vectorize(n) # vectorize functions

#=====
# Begin main program.
#=====
# "Long" list of surface chemical potentials for numerical evaluation below:
all_ens = np.linspace(-1.*e,1.*e,20001) # in Joule
N = n(T,all_ens) # Electron densities for all these energies (finite T)
P = p(T,all_ens) # Hole densities for all these energies (finite T)
mu_s_list = np.linspace(-0.4,0.4,501)*e # List of surface potential for plot.
cQbulk = CQ_it(mu_s_list,N,P,all_ens) # Calculate quantum capacitance.
# Plot cQ(mu_surface).
plt.figure('Plot cq bulk')
plt.plot(mu_s_list/e*1e3,cQbulk*1e3,
         label = r'T=%2.1fK, $\mu_{\infty}$ = %2.1f meV'%(T,mu_inf/e*1e3))
plt.xlabel('mu surface [meV]')
plt.ylabel('cQ bulk [fF/mu m^2]')
plt.legend()
plt.show()

```

---

## Appendix C

# 1D model for the RF-admittance of a distributed RC-line

For clarity in this appendix the complex unit will be noted  $j$  ( $j^2 = -1$ ) whereas currents are denoted by  $i$ . In order to calculate the admittance of a distributed RC line presented in Fig. C.1, the Kirchoff's circuit rules for an infinitesimal circuit element of length  $dx$  read (in frequency space):

$$V(x + dx) - V(x) = -i(x)r(x)dx, \quad (\text{C.1})$$

$$i(x + dx) - i(x) = -V(x)j\omega c(x)dx. \quad (\text{C.2})$$

Currents are measured in the resistive elements with a positive sign from left to right. In the simplest case of a TI channel with constant width,  $r$  and  $c$  are length-independent. The system of coupled differential equations is solved by differentiating eq. (C.1) again and inserting into eq. (C.2):

$$V''(x) = jV(x)rc\omega, \quad (\text{C.3})$$

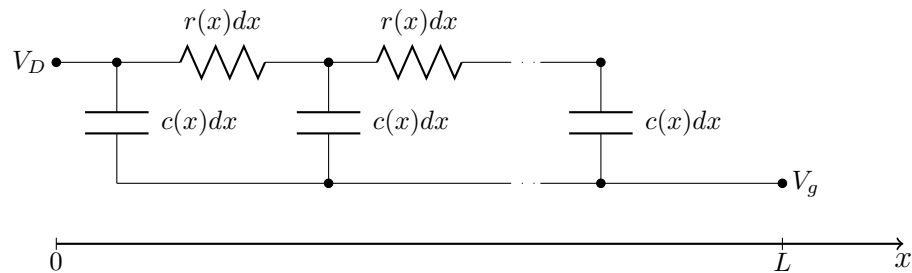


FIGURE C.1: Small signal equivalent circuit of a metal-insulator-TI capacitor without access resistance. The circuit diagram is rotated with respect to Fig. 4.6 in the main text. This simplifies the notations.

with the general solutions

$$V(x) = V_+ e^{jkx} + V_- e^{-jkx}, \quad (\text{C.4})$$

$$i(x) = \frac{jk}{r} (V_- e^{-jkx} - V_+ e^{jkx}), \quad (\text{C.5})$$

with the complex wave vector  $k = \sqrt{j\omega cr}$ . The current in the TI channels vanishes at  $x = L$  in Fig. C.1 leading to

$$V(x) = V_0 \cosh(jk(x - L)), \quad (\text{C.6})$$

$$i(x) = -\frac{jk}{r} V_0 \sinh(jk(x - L)). \quad (\text{C.7})$$

The admittance is thus given by

$$Y(\omega) = \frac{i(0)}{V(0)} = \frac{jk}{r} \tanh(jkL). \quad (\text{C.8})$$

Assume now a trapezoidal shaped channel for an x-capacitor. The sample shall be connected on the right (at  $x = L$ ), where the channel is broader, with a contact (right end) width  $W_R$ . The width at the beginning of the channel ( $x = 0$ ) shall be denoted  $W_L$ . The capacitance and the resistance per unit length become then position dependent:

$$c(x) = c_{\square} \cdot W(x), \quad (\text{C.9})$$

$$r(x) = r_{\square} / W(x). \quad (\text{C.10})$$

where  $c_{\square}(r_{\square})$ , denote the standard capacitance (resistivity) per square. In the trapezoidal geometry, one has thus

$$W(x) = W_L + \frac{x}{L} (W_R - W_L). \quad (\text{C.11})$$

As always, the constitutive relations for the voltage/current waves in frequency space read

$$V'(x) = -r(x)i(x), \quad (\text{C.12})$$

$$i'(x) = -j\omega c(x)V(x), \quad (\text{C.13})$$

with the difference to the rectangular case that now the resistance and capacitance depend on the position. Taking the derivative of (C.12) gives

$$V''(x) = -r'(x)i(x) - r(x)i'(x) = \frac{r_{\square} W'(x)}{W(x)^2} i(x) + j\omega c_{\square} r_{\square} V(x), \quad (\text{C.14})$$

where one can identify eq. (C.12):

$$V''(x) = -\frac{W'(x)}{W(x)}V'(x) + i\omega c_{\square}r_{\square}V(x). \quad (\text{C.15})$$

With the explicit form of  $W(x)$ , eq. (C.11), one finds

$$V''(x) = -\frac{A}{1+Ax}V'(x) + jBV(x), \quad (\text{C.16})$$

where

$$A = \frac{W_R - W_L}{W_L L}, \quad B = \omega c_{\square}r_{\square} \quad (\text{C.17})$$

Eq. (C.16) is a so-called Sturm-Liouville equation and admits solutions of the form

$$V(x) = V_1 J_0 \left( (-1)^{3/4} \sqrt{B}(x + 1/A) \right) + V_2 Y_0 \left( -(-1)^{3/4} \sqrt{B}(x + 1/A) \right), \quad (\text{C.18})$$

where  $J$  and  $Y$  are Bessel function of first and second kind, respectively. Using (C.12), one finds

$$I(x) = -\frac{1}{r(x)}V'(x) \quad (\text{C.19})$$

$$= \frac{(-1)^{3/4} \sqrt{B}}{r(x)} \left[ V_1 J_1 \left( (-1)^{3/4} \sqrt{B}(x + 1/A) \right) - V_2 Y_1 \left( -(-1)^{3/4} \sqrt{B}(x + 1/A) \right) \right]. \quad (\text{C.20})$$

One has now the following boundary condition:

$$I(x = L) = 0, \quad (\text{C.21})$$

This allows us to eliminate  $V_2$ :

$$V_2 = V_1 \frac{J_1 \left( (-1)^{3/4} \sqrt{B}(L + 1/A) \right)}{Y_1 \left( -(-1)^{3/4} \sqrt{B}(L + 1/A) \right)}. \quad (\text{C.22})$$

I introduce further

$$f(x) = \sqrt{B}(x + 1/A) \quad (\text{C.23})$$

and  $K = (-1)^{3/4} \sqrt{B}/A$ . Then, one can calculate the admittance

$$Y(\omega) = \frac{I(0)}{V(0)} = \frac{(-1)^{3/4} \sqrt{B} W_L}{r_{\square}} \frac{(Y_1(-K) J_1((-1)^{3/4} f(L)) - J_1(K) Y_1(-(-1)^{3/4} f(L)))}{(Y_0(-K) J_1((-1)^{3/4} f(L)) + J_0(K) Y_1(-(-1)^{3/4} f(L)))}. \quad (\text{C.24})$$

Of course, it is difficult to develop an intuition for this function. It is therefore important to have a look at the low frequency development:

$$Y(\omega) \approx i\omega C + \alpha R(C\omega)^2 + \mathcal{O}(\omega^3), \quad (\text{C.25})$$

where

$$C = c_{\square} L \bar{W}, \quad (\text{C.26})$$

$$R = r_{\square} \frac{L}{\bar{W}}, \quad (\text{C.27})$$

with the mean width  $\bar{W} = (W_R + W_L)/2$ . The correction factor  $\alpha$  reads

$$\alpha = \frac{W_L^4 - 4W_L^2W_R^2 + 4W_R^4 \log\left(\frac{W_L}{W_R}\right) + 3W_R^4}{8(W_L - W_R)^3(W_L + W_R)}. \quad (\text{C.28})$$

One can check, that in the limit  $W_L \rightarrow W_R$ ,  $\alpha \rightarrow 1/3$ . It is remarkable (yet not very surprising), that in the low frequency development, it is always the total capacitance that enters. This can even be seen as a general law. At low frequencies, the resistance effects do not play a role and the system behaves as a “mathematical” capacitor.

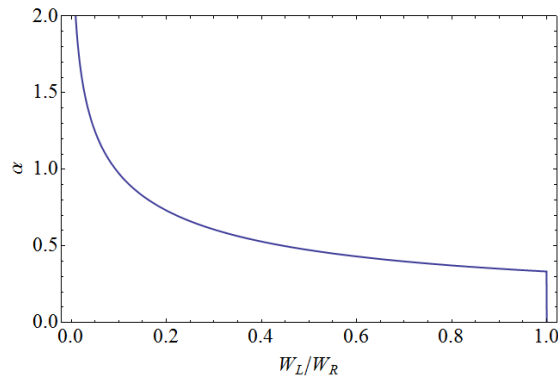


FIGURE C.2:  $\alpha$  as a function of the width ratio  $W_L/W_R$ .

## Appendix D

# Y matrix corrections due to wave propagation and cross-talk

S-parameters and ABCD-parameters are related via [239, p. 187]:

$$\begin{aligned} S_{11} &= \frac{A + B/Z_0 - CZ_0 - D}{A + B/Z_0 + CZ_0 + D}, & S_{12} &= \frac{2(AD - BC)}{A + B/Z_0 + CZ_0 + D}, \\ S_{21} &= \frac{2}{A + B/Z_0 + CZ_0 + D}, & S_{22} &= \frac{-A + B/Z_0 - CZ_0 + D}{A + B/Z_0 + CZ_0 + D} \end{aligned}$$

and

$$\begin{aligned} A &= \frac{(1 + S_{11})(1 - S_{22}) + S_{12}S_{21}}{2S_{21}}, & B &= Z_0 \frac{(1 + S_{11})(1 + S_{22}) - S_{12}S_{21}}{2S_{21}}, \\ C &= \frac{1}{Z_0} \frac{(1 - S_{11})(1 - S_{22}) - S_{12}S_{21}}{2S_{21}}, & D &= \frac{(1 - S_{11})(1 + S_{22}) + S_{12}S_{21}}{2S_{21}}. \end{aligned}$$

The procedure described in section 4.2 can best be understood by checking figures D.1 and D.2. Although the requirements  $Y_{11} = Y_{22}$  and  $Y_{12} = Y_{21}$  are met on the raw spectra, the relation between off-diagonal elements and diagonal elements, eq. (4.13), is clearly not fulfilled. However, after correcting the THRU, all four matrix elements are equal (up to the sign change required by eq. (4.13)).

Generally, the parasitic contribution due to cross talk between the metal pads is rather small. A typical dummy spectrum (after THRU de-embedding) is shown in Fig.D.4.

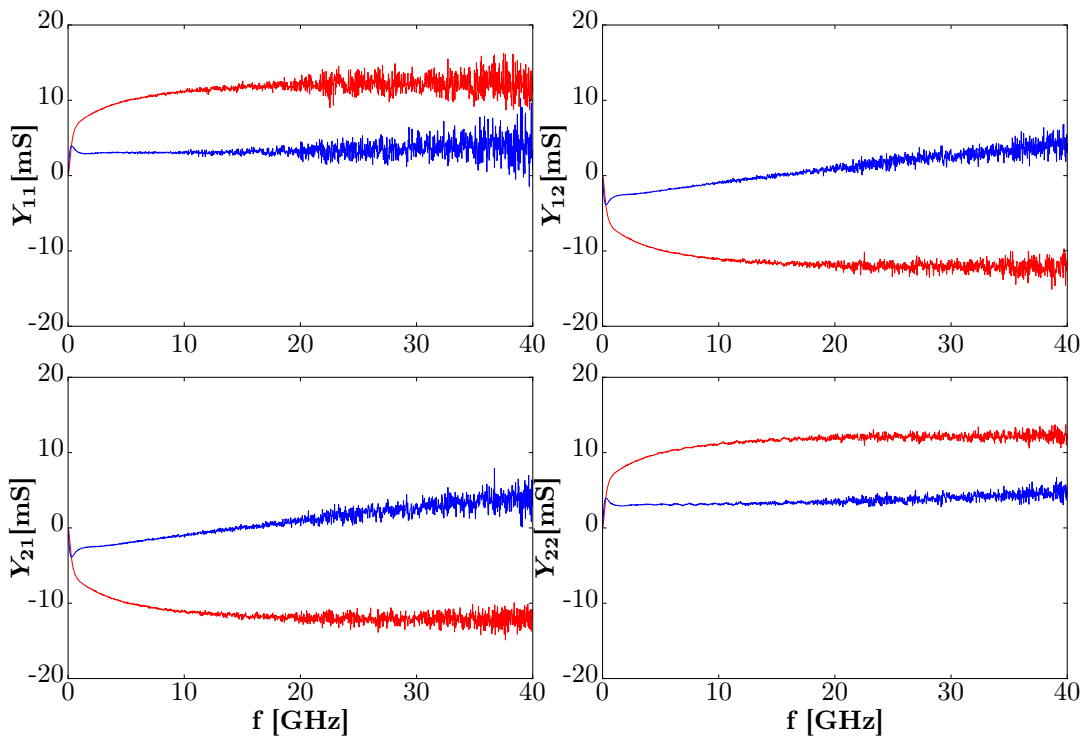


FIGURE D.1: Raw Y parameters of a typical HgTe sample. The real (imaginary) part of the Y parameters are represented in blue (red). Note, that the imaginary part changes sign as a function of frequency for the off-diagonal elements whereas it does not for the diagonal elements. This is an obvious qualitative violation of eq.(4.13).

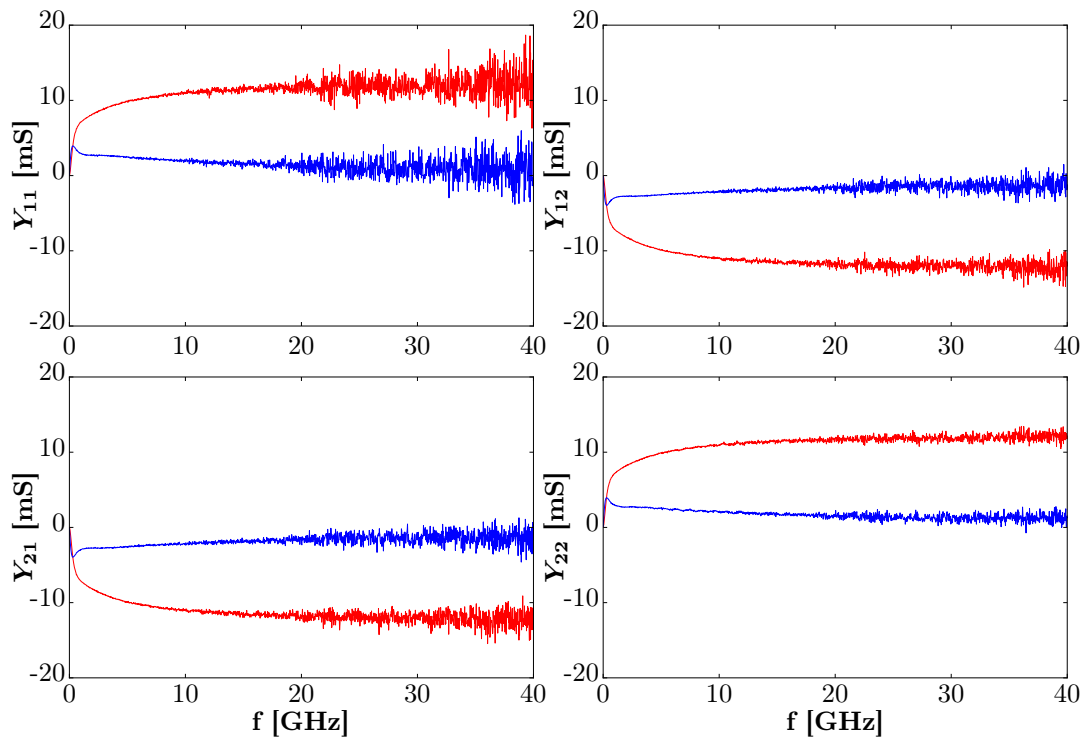


FIGURE D.2: The Y parameters of Fig. D.1 after de-embedding the THRU propagation. The real (imaginary) part of the Y parameters are represented in blue (red). The symmetries of the matrix required by eq.(4.13) are now clearly respected.

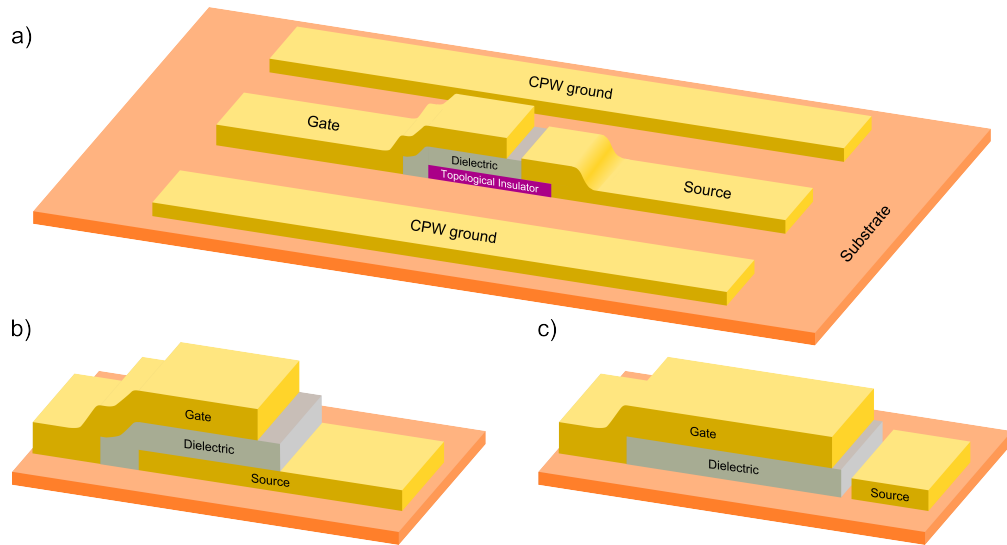


FIGURE D.3: a) Artist view of the MOTI-Capacitor embedded in a coplanar waveguide. b) For the metal-oxide-metal (MOM) structure, the TI material is replaced by a metallic electrode. This device allows us to determine the geometric capacitance of the insulating layer independently. c) The dummy structure. Here, the TI is completely removed or left out during sample fabrication. It allows us to determine the parasitic coupling (“cross-talk”) between gate and source electrode.

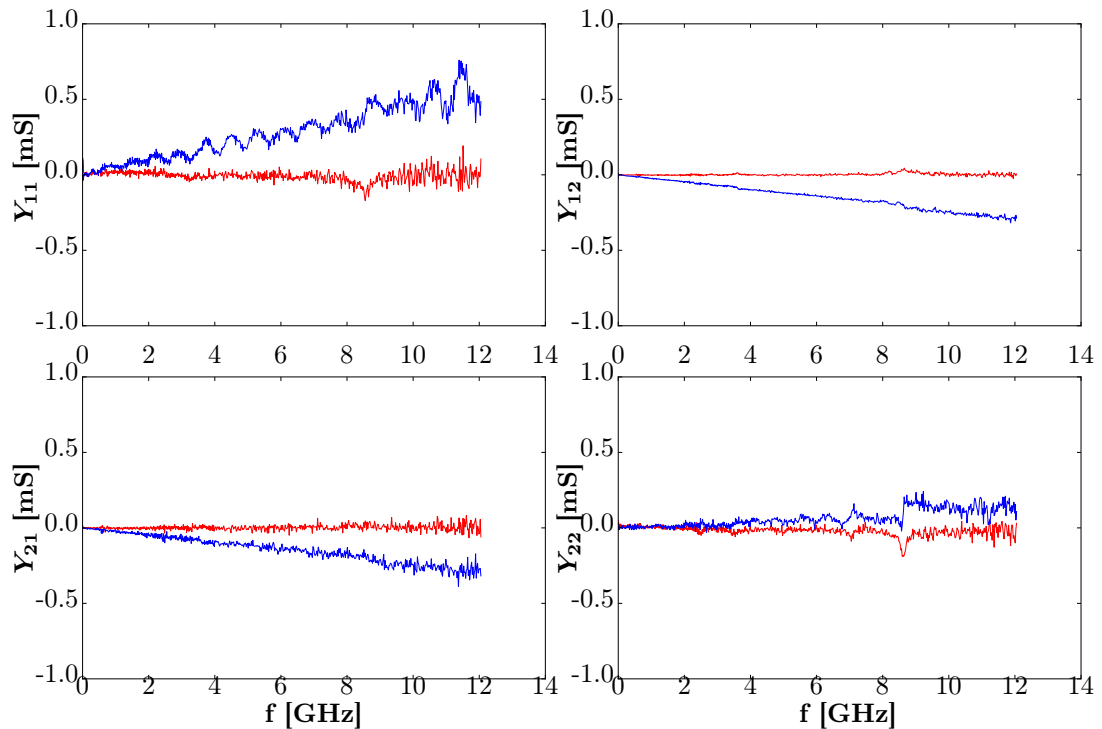


FIGURE D.4: The Y parameters of a dummy device. The admittances are typically on the order of  $\lesssim 1 \text{ mS}$ . Therefore the subtraction of the dummy is a rather small correction to the sample spectra.



## Appendix E

# Supplementary (low frequency) measurements for the HgTe samples

### Intrinsic sample

We checked that the phase of the Lock-in measurements remained constant when the gate is swept over a large gate range. This is shown in Fig. E.1.

The meta-oxide-metal (M-O-M) control structure allows us to obtain an estimate of the HfO<sub>2</sub> capacitance (see also Fig. D.3 for an artist view of this structure). When sweeping the DC gate voltage over  $V_g = \pm 10$  V, it shows a weak gate dependence on the order of  $\lesssim 1.5\%$  as shown in Fig. E.2. This minor correction is not taken into account in the main text. We also observed no gate leakage on the M-O-M structure for gate voltages up to  $\pm 10$  V. Given the approximate thickness of 10 nm for the HfO<sub>2</sub>-layer, this corresponds to a dielectric strength of at least 1.0 V/nm.

Further we checked that the capacitance-voltage characteristics (per unit area) are device independent. In the main text of this thesis, we focus on measurements on a sample with length  $L = 44 \mu\text{m}$  and width  $W = 20 \mu\text{m}$ . In Fig. E.3, the capacitance-voltage characteristic of a sample with the same width but length  $L = 59 \mu\text{m}$  is shown. It shows the same features as the shorter sample in Fig. 5.2.

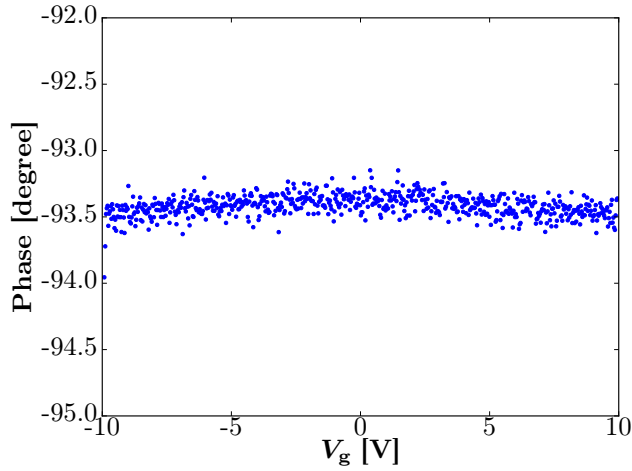


FIGURE E.1: Lock-in phase of capacitance measurement on the intrinsic sample for large gate voltage range.  $f = 10$  kHz,  $T = 10$  K.

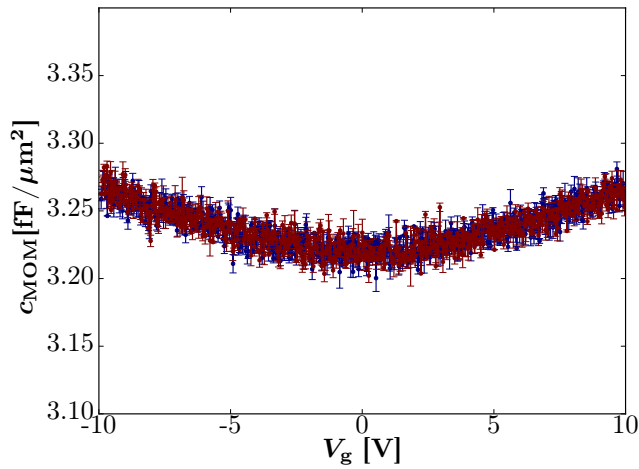


FIGURE E.2: The low-frequency capacitance of the metal-oxide-metal reference structure of the intrinsic HgTe sample over the largest explored gate range.  $f = 10$  kHz,  $T = 10$  K. Red and blue points correspond to forward and backwards sweeps, respectively.

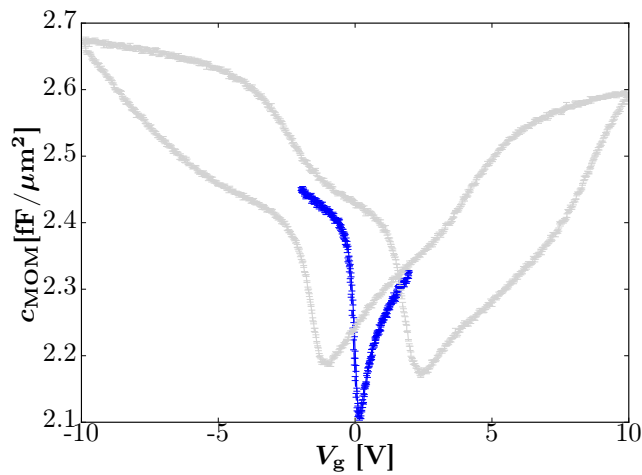


FIGURE E.3: The low-frequency capacitance of an intrinsic (strained) HgTe MITI-Capacitor with length  $L = 59$   $\mu\text{m}$  and width  $W = 20$   $\mu\text{m}$ . The blue line corresponds to the first sweep after cooldown in the reversible regime ( $V_g = \pm 2$  V). The gray line is a  $V_g = \pm 10$  V sweep.  $f = 10$  kHz,  $T = 10$  K.

## Hysteresis of n-type sample

Similar to the results presented for the intrinsic sample in section 5.5, we carried out a systematic study of hysteresis on the n-type sample. These results are shown in Fig. E.4. The opening of hysteresis is quantified by measuring the distance between forward and backward sweeps defined at the point where  $c(V)$ -line crosses  $c = 3.8 \text{ fF}/\mu\text{m}^2$  on the hole side. This is illustrated in Fig. E.4 (b). The crossing is reached only when the gate voltage range is larger than  $\pm 2 \text{ V}$ . Therefore only these sweeps are considered here. We observe in Fig. E.4 (c), that the hysteresis opens only for a gate voltage range larger than  $\gtrsim 3 \text{ V}$ . In Fig. E.4 (d), I show the minimal capacitance and the corresponding gate voltage for all investigated sweeps. The fact that the capacitance minimum *decreases* first when the gate voltage range is extended to negative values (sweep  $V_g = -3 \dots 3 \text{ V}$ ) supports the (metastable) surface to bulk charge transfer mechanism explained in the main text.

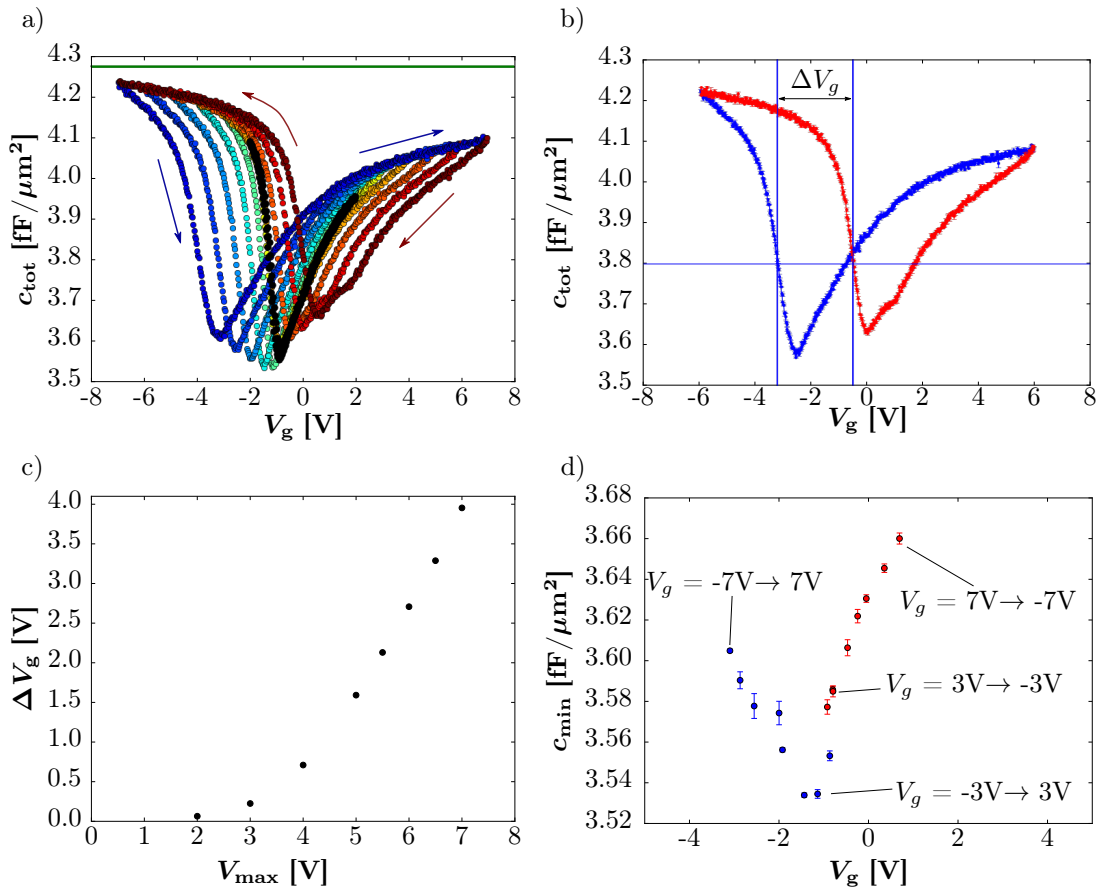


FIGURE E.4: a)  $c(V)$  data for gate voltage sweeps with varying amplitude, ranging from  $|V_g| \leq 2 \text{ V}$  to  $|V_g| \leq 7 \text{ V}$ . The reversible  $|V_g| \leq 2 \text{ V}$  sweep is highlighted in black. Warm (cold) colors represent backwards (forward) sweeps. b) Example of how the opening of hysteresis  $\Delta V_g$  is quantified on the  $|V_g| \leq 6 \text{ V}$ -sweep. c) Amplitude of hysteresis as a function of maximal gate voltage for the corresponding sweep. d) Position of capacitance minima (capacitance value and corresponding gate voltage) for different sweeps. Forward (backward) sweeps in blue (red).



## Appendix F

# Change of variables in the model

Our collaborators developed a theory based on a pseudo-relativistic Lorentz boost, transforming the interface Hamiltonian to a frame such that the electric field is canceled and a pseudo-magnetic field gives rise to a Landau level like spectrum, described in the main text. The natural variables of this theory are chemical potential and electric field. Experimentally, we access the electron number directly via the integration of the capacitance-voltage characteristic. In order to compare theory and experiment, we develop here this change of variables. As in the main text, we measure all energies with respect to the Dirac point, i.e. terms in  $\beta\Delta_1$  are neglected (c.f. main text).

Starting from the density of states,

$$\text{DoS}(\mu) = \frac{\mu}{2\pi(\hbar v_F)^2(1-\beta^2)} \cdot (l+1), \quad (\text{F.1})$$

where  $l$  is defined via  $\mu_{l+1} > \mu > \mu_l$  with the band-minimum energies

$$\mu_l = \sqrt{2e\mathcal{E}_I\hbar v_F(1-\beta^2)^{3/2}l}. \quad (\text{F.2})$$

We identify a natural scale for the energies

$$\tilde{\mu} := \sqrt{2e\mathcal{E}_I\hbar v_F}, \quad (\text{F.3})$$

such that

$$\mu_l = \tilde{\mu}\sqrt{(1-\beta^2)^{3/2}l}. \quad (\text{F.4})$$

The charge carrier density is given by the energy-integrated density of states. First we calculate the charge carrier densities  $n_l$  at the sub-band energies. We find the recursive

relation

$$n_{l+1} - n_l = \frac{\tilde{N}}{(1 - \beta^2)} (1 - \beta^2)^{3/2} [(l + 1) - l] (l + 1) \quad (\text{F.5})$$

$$= \tilde{N} \sqrt{1 - \beta^2} (l + 1). \quad (\text{F.6})$$

with the scale for the charge carrier density

$$\tilde{N} := \frac{e\mathcal{E}_I}{2\pi\hbar v_F}. \quad (\text{F.7})$$

For  $l = 1$  the calculation of  $n$  is particularly simple (it corresponds to the graphene case):

$$n_1 = \tilde{N} \sqrt{1 - \beta^2}. \quad (\text{F.8})$$

From the recursive relation and the value of  $n_1$  we deduce

$$n_l = \frac{l(l + 1)}{2} \frac{e\mathcal{E}_I}{2\pi\hbar v_F} \sqrt{1 - \beta^2}. \quad (\text{F.9})$$

We can further show, that for  $n_{l+1} > n > n_l$ , the quantum capacitance is given by

$$c_Q = \frac{e^2}{2} \frac{\tilde{N}}{\tilde{\mu}} \sqrt{\frac{l + 1}{1 - \beta^2} \frac{n + n_l}{\tilde{N}}}. \quad (\text{F.10})$$

# Bibliography

- [1] Felix Bloch. Über die Quantenmechanik der Elektronen in Kristallgittern. *Zeitschrift für Physik*, 52(7-8):555–600, jul 1929.
- [2] Neil W. Ashcroft and N. David Mermin. *Solid State Physics*. Brooks/Cole, 1976.
- [3] Gerald D. Mahan. *Many-Particle Physics*. Kluwer Academic/Plenum Publishers, New York, 3 edition, 2000. ISBN 0-306-46338-5.
- [4] M. Kaplit and J. N. Zemel. Capacitance Observations of Landau Levels in Surface Quantization. *Physical Review Letters*, 21(4):212–215, jul 1968. ISSN 0031-9007. doi: 10.1103/PhysRevLett.21.212. URL <http://link.aps.org/doi/10.1103/PhysRevLett.21.212>.
- [5] T. P. Smith, B. B. Goldberg, P. J. Stiles, and M. Heiblum. Direct measurement of the density of states of a two-dimensional electron gas. *Physical Review B*, 32(4):2696–2699, aug 1985.
- [6] Serge Luryi. Quantum capacitance devices. *Applied Physics Letters*, 52(6):501, 1988. ISSN 00036951. doi: 10.1063/1.99649. URL <http://link.aip.org/link/APPLAB/v52/i6/p501/s1{&}Agg=doi>.
- [7] J. P. Eisenstein, L. N. Pfeiffer, and K. W. West. Negative compressibility of interacting two-dimensional electron and quasiparticle gases. *Physical Review Letters*, 68(5):674–677, feb 1992. ISSN 0031-9007. doi: 10.1103/PhysRevLett.68.674. URL <http://link.aps.org/doi/10.1103/PhysRevLett.68.674>.
- [8] J. P. Eisenstein, L. N. Pfeiffer, and K. W. West. Compressibility of the two-dimensional electron gas: Measurements of the zero-field exchange energy and fractional quantum Hall gap. *Physical Review B*, 50(3):1760–1778, jul 1994. ISSN 0163-1829. doi: 10.1103/PhysRevB.50.1760. URL <http://link.aps.org/doi/10.1103/PhysRevB.50.1760>.
- [9] S. Ilani, L. a. K. Donev, M. Kindermann, and P. L. McEuen. Measurement of the quantum capacitance of interacting electrons in carbon nanotubes. *Nature*

- Physics*, 2(10):687–691, oct 2006. URL <http://www.nature.com/doi/10.1038/nphys412>.
- [10] Tian Fang, Aniruddha Konar, Huili Xing, and Debdeep Jena. Carrier statistics and quantum capacitance of graphene sheets and ribbons. *Applied Physics Letters*, 91(9):092109, 2007. ISSN 00036951. doi: 10.1063/1.2776887. URL <http://link.aip.org/link/APPLAB/v91/i9/p092109/s1{&}Agg=doihttp://scitation.aip.org/content/aip/journal/apl/91/9/10.1063/1.2776887>.
- [11] Zhihong Chen and Joerg Appenzeller. Mobility extraction and quantum capacitance impact in high performance graphene field-effect transistor devices. In *2008 IEEE International Electron Devices Meeting*, number L in IEDM, pages 1–4. IEEE, dec 2008. ISBN 978-1-4244-2377-4. doi: 10.1109/IEDM.2008.4796737. URL <http://ieeexplore.ieee.org/document/4796737/>.
- [12] Jilin Xia, Fang Chen, Jinghong Li, and Nongjian Tao. Measurement of the quantum capacitance of graphene. *Nature nanotechnology*, 4(8):505–9, aug 2009. URL <http://www.ncbi.nlm.nih.gov/pubmed/19662012>.
- [13] S. Droescher, P. Roulleau, F. Molitor, P. Studerus, C. Stampfer, K. Ensslin, and T. Ihn. Quantum capacitance and density of states of graphene. *Applied Physics Letters*, 96(15):152104, 2010.
- [14] L. A. Ponomarenko, R. Yang, R. V. Gorbachev, P. Blake, A. S. Mayorov, K. S. Novoselov, M. I. Katsnelson, and A. K. Geim. Density of States and Zero Landau Level Probed through Capacitance of Graphene. *Physical Review Letters*, 105(13):136801, sep 2010. URL <http://link.aps.org/doi/10.1103/PhysRevLett.105.136801>.
- [15] E. Pallecchi, a. C. Betz, J. Chaste, G. Fève, B. Huard, T. Kontos, J.-M. Berroir, and B. Plaçais. Transport scattering time probed through rf admittance of a graphene capacitor. *Physical Review B*, 83(12):125408, mar 2011. ISSN 1098-0121. doi: 10.1103/PhysRevB.83.125408. URL <http://link.aps.org/doi/10.1103/PhysRevB.83.125408>.
- [16] D. A. Kozlov, D. Bauer, J. Ziegler, R. Fischer, M. L. Savchenko, Z. D. Kvon, N. N. Mikhailov, S. A. Dvoretzky, and D. Weiss. Probing Quantum Capacitance in a 3D Topological Insulator. *Physical Review Letters*, 116(16):166802, apr 2016. ISSN 0031-9007. doi: 10.1103/PhysRevLett.116.166802. URL <http://arxiv.org/abs/1511.00606http://link.aps.org/doi/10.1103/PhysRevLett.116.166802>.

- [17] R. K. Goodall, R. J. Higgins, and J. P. Harrang. Capacitance measurements of a quantized two-dimensional electron gas in the regime of the quantum Hall effect. *Physical Review B*, 31(10):6597–6608, may 1985.
- [18] S.M. Sze and K.K. Ng. *Physics of Semiconductor Devices*. Wiley, 2006. ISBN 9780470068304.
- [19] Faxian Xiu, Nicholas Meyer, Xufeng Kou, Liang He, Murong Lang, Yong Wang, Xinxin Yu, Alexei V Fedorov, Jin Zou, and Kang L Wang. Quantum capacitance in topological insulators. *Scientific reports*, 2:669, jan 2012. ISSN 2045-2322. doi: 10.1038/srep00669. URL <http://www.pubmedcentral.nih.gov/articlerender.fcgi?artid=3444751&tool=pmcentrez&rendertype=abstract>.
- [20] M. Tahir and U. Schwingenschlögl. Quantum capacitance in topological insulators under strain in a tilted magnetic field. *Applied Physics Letters*, 101(23):10–14, 2012.
- [21] M Tahir, K Sabeeh, and U Schwingenschlögl. Quantum capacitance of an ultrathin topological insulator film in a magnetic field. *Scientific Reports*, 3:1261, feb 2013.
- [22] D. S L Abergel and S. Das Sarma. Two-dimensional compressibility of surface states on three-dimensional topological insulators. *Physical Review B*, 87(4):041407, jan 2013.
- [23] Anirudha Menon, Debashree Chowdhury, and Banasri Basu. Effect of perturbative hexagonal warping on quantum capacitance in ultra-thin topological insulators. *Journal of Physics D: Applied Physics*, 49(13):135003, apr 2016.
- [24] T. Kernreiter, M. Governale, and U. Zülicke. Quantum capacitance of an HgTe quantum well as an indicator of the topological phase. *Physical Review B*, 93(24):241304, jun 2016.
- [25] Eduardo V. Castro, K. S. Novoselov, S. V. Morozov, N. M R Peres, J. M. B. Lopes dos Santos, Johan Nilsson, F. Guinea, A. K. Geim, and A. H Castro Neto. Biased Bilayer Graphene: Semiconductor with a Gap Tunable by the Electric Field Effect. *Physical Review Letters*, 99(21):216802, nov 2007. URL <http://link.aps.org/doi/10.1103/PhysRevLett.99.216802>.
- [26] Kin Fai Mak, Chun Hung Lui, Jie Shan, and Tony F. Heinz. Observation of an electric-field-induced band gap in bilayer graphene by infrared spectroscopy. *Physical Review Letters*, 102(25):100–103, 2009.
- [27] Edward McCann. Interlayer asymmetry gap in the electronic band structure of bilayer graphene. *physica status solidi (b)*, 244(11):4112–4117, nov 2007.

- [28] Hongyan Guo, Ning Lu, Jun Dai, Xiaojun Wu, and Xiao Cheng Zeng. Phosphorene nanoribbons, phosphorus nanotubes, and van der waals multilayers. *The Journal of Physical Chemistry C*, 118(25):14051–14059, 2014. doi: 10.1021/jp505257g.
- [29] Yan Li, Shengxue Yang, and Jingbo Li. Modulation of the electronic properties of ultrathin black phosphorus by strain and electrical field. *The Journal of Physical Chemistry C*, 118(41):23970–23976, 2014. doi: 10.1021/jp506881v.
- [30] Bingchen Deng, Vy Tran, Hao Jiang, Cheng Li, Yujun Xie, Qiushi Guo, Xiaomu Wang, He Tian, Han Wang, Judy J Cha, Qiangfei Xia, Li Yang, and Fengnian Xia. Efficient Electrical Control of Thin-Film Black Phosphorus Bandgap. *ArXiv*, dec 2016. URL <http://arxiv.org/abs/1612.04475>.
- [31] Qihang Liu, Xiuwen Zhang, L. B. Abdalla, Adalberto Fazzio, and Alex Zunger. Switching a normal insulator into a topological insulator via electric field with application to phosphorene. *Nano Letters*, 15(2):1222–1228, 2015. doi: 10.1021/nl5043769. PMID: 25607525.
- [32] Jonas Anversa, Paulo Piquini, Adalberto Fazzio, and Tome M. Schmidt. First-principles study of HgTe/CdTe heterostructures under perturbations preserving time-reversal symmetry. *Physical Review B*, 90(19):195311, nov 2014.
- [33] Parijat Sengupta, Tillmann Kubis, Yaohua Tan, Michael Povolotskyi, and Gerhard Klimeck. Design principles for HgTe based topological insulator devices. *Journal of Applied Physics*, 114(4):043702, 2013. URL <http://scitation.aip.org/content/aip/journal/jap/114/4/10.1063/1.4813877>.
- [34] Jun Li and Kai Chang. Electric field driven quantum phase transition between band insulator and topological insulator. *Applied Physics Letters*, 95(22):222110, 2009.
- [35] Sergey S Krishtopenko, Wojciech Knap, and Frédéric Teppe. Phase transitions in two tunnel-coupled HgTe quantum wells: Bilayer graphene analogy and beyond. *Scientific Reports*, 6(August):30755, aug 2016.
- [36] Anton Quelle, Emilio Cobanera, and Cristiane Morais Smith. Thermodynamic signatures of edge states in topological insulators. *Physical Review B*, 94(7):075133, aug 2016. ISSN 2469-9950. doi: 10.1103/PhysRevB.94.075133. URL <http://arxiv.org/abs/1601.03745><http://link.aps.org/doi/10.1103/PhysRevB.94.075133>.
- [37] S. N. Kempkes, A. Quelle, and C. Morais Smith. Universalities of thermodynamic signatures in topological phases. *Scientific Reports*, 6(November):38530, dec 2016.

- ISSN 2045-2322. doi: 10.1038/srep38530. URL <http://arxiv.org/abs/1607.03373><http://www.nature.com/articles/srep38530>.
- [38] David Nozadze and Nandini Trivedi. Compressibility as a probe of quantum phase transitions in topological superconductors. *Physical Review B*, 93(6):064512, feb 2016. ISSN 2469-9950. doi: 10.1103/PhysRevB.93.064512. URL <http://link.aps.org/doi/10.1103/PhysRevB.93.064512>.
- [39] Kangjun Seo, Chuanwei Zhang, and Sumanta Tewari. Thermodynamic signatures for topological phase transitions to Majorana and Weyl superfluids in ultracold Fermi gases. *Physical Review A*, 87(6):063618, jun 2013. ISSN 1050-2947. doi: 10.1103/PhysRevA.87.063618. URL <http://link.aps.org/doi/10.1103/PhysRevA.87.063618>.
- [40] Xiao-Gang Wen. Quantum orders and symmetric spin liquids. *Physical Review B*, 65(16):165113, 2002. ISSN 0163-1829. doi: 10.1103/PhysRevB.65.165113. URL <http://arxiv.org/abs/cond-mat/0107071><http://link.aps.org/doi/10.1103/PhysRevB.65.165113>.
- [41] Yuval Baum, Jan Böttcher, Christoph Brüne, Cornelius Thienel, Laurens W Molenkamp, Ady Stern, and Ewelina M. Hankiewicz. Self-consistent  $k \cdot p$  calculations for gated thin layers of three-dimensional topological insulators. *Physical Review B*, 89(24):245136, jun 2014.
- [42] B. Andrei Bernevig and Taylor L. Hughes. *Topological insulators and topological superconductors*. Princeton University Press, 1st edition, 2013.
- [43] Andreas P. Schnyder, Shinsei Ryu, Akira Furusaki, and Andreas W. W. Ludwig. Classification of topological insulators and superconductors in three spatial dimensions. *Physical Review B*, 78(19):195125, nov 2008. ISSN 1098-0121. doi: 10.1103/PhysRevB.78.195125. URL <http://link.aps.org/doi/10.1103/PhysRevB.78.195125>.
- [44] Shinsei Ryu, Andreas P Schnyder, Akira Furusaki, and Andreas W W Ludwig. Topological insulators and superconductors: tenfold way and dimensional hierarchy. *New Journal of Physics*, 12(6):065010, jun 2010. ISSN 1367-2630. doi: 10.1088/1367-2630/12/6/065010. URL <http://stacks.iop.org/1367-2630/12/i=6/a=065010?key=crossref.8100f885f6d94a261914942850e92d50>.
- [45] M. Z. Hasan and C. L. Kane. Colloquium : Topological insulators. *Reviews of Modern Physics*, 82(4):3045–3067, nov 2010.

- [46] Xiao-Liang Qi and Shou-Cheng Zhang. Topological insulators and superconductors. *Reviews of Modern Physics*, 83(4):1057–1110, oct 2011. URL <http://link.aps.org/doi/10.1103/RevModPhys.83.1057>.
- [47] Andreas Inhofer. *Time-dependent quantum dot coupled to the edges of a two-dimensional topological insulator*. Master thesis, Albert-Ludwig-Universität Freiburg, August 2013.
- [48] Louis Veyrat. *Quantum-Transport Study of Spin-Helical Dirac Fermions in 3D Topological Insulator Nanostructures*. Dissertation, Technische Universität Dresden, February 2016.
- [49] C. L. Kane and E. J. Mele. Quantum Spin Hall Effect in Graphene. *Physical Review Letters*, 95(22):226801, nov 2005. doi: 10.1103/PhysRevLett.95.226801. URL <http://link.aps.org/doi/10.1103/PhysRevLett.95.226801>.
- [50] C. L. Kane and E. J. Mele.  $Z_2$  Topological Order and the Quantum Spin Hall Effect. *Physical Review Letters*, 95(14):146802, sep 2005. ISSN 0031-9007. doi: 10.1103/PhysRevLett.95.146802. URL <http://link.aps.org/doi/10.1103/PhysRevLett.95.146802>.
- [51] Liang Fu and C. Kane. Topological insulators with inversion symmetry. *Physical Review B*, 76(4):045302, jul 2007. ISSN 1098-0121. doi: 10.1103/PhysRevB.76.045302. URL <http://link.aps.org/doi/10.1103/PhysRevB.76.045302>.
- [52] Liang Fu, C. L. Kane, and E. J. Mele. Topological Insulators in Three Dimensions. *Physical Review Letters*, 98(10):106803, mar 2007. doi: 10.1103/PhysRevLett.98.106803.
- [53] D. J. Thouless, M. Kohmoto, M. P. Nightingale, and M. den Nijs. Quantized Hall Conductance in a Two-Dimensional Periodic Potential. *Physical Review Letters*, 49(6):405–408, aug 1982.
- [54] Shinsei Ryu and Yasuhiro Hatsugai. Topological Origin of Zero-Energy Edge States in Particle-Hole Symmetric Systems. *Physical Review Letters*, 89(7):077002, jul 2002.
- [55] Carpentier, D. and Levy, L. Un nouvel état de la matière. *Dossier pour la science*, 79:42–48, april 2013.
- [56] W. P. Su, R. Schrieffer, and A. J. Heeger. Solitons in Polyacetylene. *Physical Review Letters*, 42(25):1698–1701, 1979.

- [57] K. Klitzing, G. Dorda, and M. Pepper. New Method for High-Accuracy Determination of the Fine-Structure Constant Based on Quantized Hall Resistance. *Physical Review Letters*, 45(6):494–497, aug 1980. URL <http://link.aps.org/doi/10.1103/PhysRevLett.45.494>.
- [58] Daijiro Yoshioka. *The Quantum Hall Effect*, volume 133 of *Springer Series in Solid-State Sciences*. Springer Berlin Heidelberg, Berlin, Heidelberg, 2002. ISBN 978-3-642-07720-3. doi: 10.1007/978-3-662-05016-3. URL <http://link.springer.com/10.1007/978-3-662-05016-3>.
- [59] M. V. Berry. Quantal Phase Factors Accompanying Adiabatic Changes. *Proceedings of the Royal Society A: Mathematical, Physical and Engineering Sciences*, 392(1802):45–57, mar 1984. ISSN 1364-5021. doi: 10.1098/rspa.1984.0023. URL <http://rspa.royalsocietypublishing.org/cgi/doi/10.1098/rspa.1974.0120><http://rspa.royalsocietypublishing.org/cgi/doi/10.1098/rspa.1984.0023>.
- [60] J.M. Lee. *Riemannian Manifolds: An introduction to Curvature*. Springer, 1997.
- [61] C. Nash and S. Sen. *Topology and Geometry for Physicists*. Dover Publications Inc., 2011.
- [62] B Andrei Bernevig, Taylor L Hughes, and Shou-Cheng Zhang. Quantum spin Hall effect and topological phase transition in HgTe quantum wells. *Science (New York, N.Y.)*, 314(5806):1757–61, dec 2006. ISSN 1095-9203. doi: 10.1126/science.1133734. URL <http://www.ncbi.nlm.nih.gov/pubmed/17170299>.
- [63] Markus König, Steffen Wiedmann, Christoph Brüne, Andreas Roth, Hartmut Buhmann, Laurens W Molenkamp, Xiao-Liang Qi, and Shou-Cheng Zhang. Quantum spin hall insulator state in HgTe quantum wells. *Science (New York, N.Y.)*, 318(5851):766–70, nov 2007. ISSN 1095-9203. doi: 10.1126/science.1148047. URL <http://www.ncbi.nlm.nih.gov/pubmed/17885096>.
- [64] F. D. M. Haldane. Model for a Quantum hall Effect without Landau Levels: Condensed-Matter Realization of the "Parity Anomaly". *Physical Review Letters*, 61(18):2015–2018, 1988.
- [65] B. Andrei Bernevig and Shou-cheng Zhang. Quantum Spin Hall Effect. *Physical Review Letters*, 96(10):106802, mar 2006. ISSN 0031-9007. doi: 10.1103/PhysRevLett.96.106802. URL <http://link.aps.org/doi/10.1103/PhysRevLett.96.106802><http://link.aps.org/doi/10.1103/PhysRevLett.96.106401><http://www.ncbi.nlm.nih.gov/pubmed/>

- 19659109<http://link.aps.org/doi/10.1103/PhysRevLett.96.106401><http://link.aps.org/doi/10.1103/PhysRevLett.96.106802>.
- [66] J. Boettger and S. Trickey. First-principles calculation of the spin-orbit splitting in graphene. *Physical Review B*, 75(12):121402, mar 2007. ISSN 1098-0121. doi: 10.1103/PhysRevB.75.121402. URL <http://link.aps.org/doi/10.1103/PhysRevB.75.121402>.
- [67] M. Gmitra, S. Konschuh, C. Ertler, C. Ambrosch-Draxl, and J. Fabian. Band-structure topologies of graphene: Spin-orbit coupling effects from first principles. *Physical Review B*, 80(23):235431, dec 2009.
- [68] a. Castro Neto and F. Guinea. Impurity-Induced Spin-Orbit Coupling in Graphene. *Physical Review Letters*, 103(2):026804, jul 2009.
- [69] Christoph Brüne, Andreas Roth, Hartmut Buhmann, Ewelina M. Hankiewicz, Laurens W. Molenkamp, Joseph Maciejko, Xiao-Liang Qi, and Shou-Cheng Zhang. Spin polarization of the quantum spin Hall edge states. *Nature Physics*, 8(6):486–491, may 2012. ISSN 1745-2473. doi: 10.1038/nphys2322. URL <http://www.nature.com/doi/10.1038/nphys2322>.
- [70] Haijun Zhang, Chao-xing Liu, Xiao-liang Qi, Xi Dai, Zhong Fang, and Shou-cheng Zhang. Topological insulators in Bi<sub>2</sub>Se<sub>3</sub>, Bi<sub>2</sub>Te<sub>3</sub> and Sb<sub>2</sub>Te<sub>3</sub> with a single Dirac cone on the surface. *Nature Physics*, 5(6):438–442, may 2009. ISSN 1745-2473. doi: 10.1038/nphys1270. URL <http://dx.doi.org/10.1038/nphys1270><http://www.nature.com/doi/10.1038/nphys1270>.
- [71] D Hsieh, D Qian, L Wray, Y Xia, Y S Hor, R J Cava, and M Z Hasan. A topological Dirac insulator in a quantum spin Hall phase. *Nature*, 452(7190):970–4, apr 2008. ISSN 1476-4687. doi: 10.1038/nature06843. URL <http://www.ncbi.nlm.nih.gov/pubmed/18432240>.
- [72] Y. Xia, D. Qian, D. Hsieh, L. Wray, A. Pal, H. Lin, A. Bansil, D. Grauer, Y. S. Hor, R. J. Cava, and M. Z. Hasan. Observation of a large-gap topological-insulator class with a single Dirac cone on the surface. *Nature Physics*, 5(6):398–402, may 2009. ISSN 1745-2473. doi: 10.1038/nphys1274. URL <http://www.nature.com/doi/10.1038/nphys1274>.
- [73] Y L Chen, J G Analytis, J-H Chu, Z K Liu, S-K Mo, X L Qi, H J Zhang, D H Lu, X Dai, Z Fang, S C Zhang, I R Fisher, Z Hussain, and Z-X Shen. Experimental realization of a three-dimensional topological insulator, Bi<sub>2</sub>Te<sub>3</sub>. *Science (New York, N. Y.)*, 325(5937):178–81, jul 2009. ISSN 1095-9203. doi: 10.1126/science.1173034. URL <http://www.ncbi.nlm.nih.gov/pubmed/19520912>.

- [74] D. Hsieh, Y. Xia, D. Qian, L. Wray, F. Meier, J. H. Dil, J. Osterwalder, L. Patthey, A. V. Fedorov, H. Lin, A. Bansil, D. Grauer, Y. S. Hor, R. J. Cava, and M. Z. Hasan. Observation of Time-Reversal-Protected Single-Dirac-Cone Topological-Insulator States in  $\text{Bi}_2\text{Te}_3$  and  $\text{Sb}_2\text{Te}_3$ . *Physical Review Letters*, 103(14):146401, sep 2009. ISSN 0031-9007. doi: 10.1103/PhysRevLett.103.146401. URL <http://link.aps.org/doi/10.1103/PhysRevLett.103.146401>.
- [75] C. Brüne, C. X. Liu, E. G. Novik, E. M. Hankiewicz, H. Buhmann, Y. L. Chen, X. L. Qi, Z. X. Shen, S. C. Zhang, and L. W. Molenkamp. Quantum Hall effect from the topological surface states of strained bulk HgTe. *Physical Review Letters*, 106(12):126803, mar 2011. ISSN 00319007. doi: 10.1103/PhysRevLett.106.126803. URL <http://link.aps.org/doi/10.1103/PhysRevLett.106.126803>.
- [76] a. H. Castro Neto, F. Guinea, N. M. R. Peres, K. S. Novoselov, and a. K. Geim. The electronic properties of graphene. *Reviews of Modern Physics*, 81(1):109–162, jan 2009. ISSN 0034-6861. doi: 10.1103/RevModPhys.81.109. URL <http://link.aps.org/doi/10.1103/RevModPhys.81.109>.
- [77] M. I. Katsnelson, K. S. Novoselov, and A. K. Geim. Chiral tunnelling and the klein paradox in graphene. *Nature Physics*, 2:620, 2006.
- [78] Congjun Wu, B. Andrei Bernevig, and Shou-Cheng Zhang. Helical Liquid and the Edge of Quantum Spin Hall Systems. *Physical Review Letters*, 96(10):106401, mar 2006. doi: 10.1103/PhysRevLett.96.106401. URL <http://link.aps.org/doi/10.1103/PhysRevLett.96.106401>.
- [79] Cenke Xu and J. Moore. Stability of the quantum spin Hall effect: Effects of interactions, disorder, and Z2 topology. *Physical Review B*, 73(4):045322, jan 2006. URL <http://link.aps.org/doi/10.1103/PhysRevB.73.045322>.
- [80] Xiao-Liang Qi and Shou-Cheng Zhang. The quantum spin Hall effect and topological insulators. *Physics Today*, 63(1):33, 2010. URL <http://link.aip.org/link/PHTOAD/v63/i1/p33/s1{&}Agg=doi>.
- [81] D. A. Kozlov, Z. D. Kvon, E. B. Olshanetsky, N. N. Mikhailov, S. A. Dvoretzky, and D. Weiss. Transport Properties of a 3D Topological Insulator based on a Strained High-Mobility HgTe Film. *Physical Review Letters*, 112(19):196801, may 2014. ISSN 0031-9007. doi: 10.1103/PhysRevLett.112.196801. URL <http://link.aps.org/doi/10.1103/PhysRevLett.112.196801>.
- [82] V. Dziom, A. Shuvaev, A. Pimenov, G. V. Astakhov, C. Ames, K. Bendias, J. Böttcher, G. Tkachov, E. M. Hankiewicz, C. Brüne, H Buhmann, and L. W.

- Molenkamp. Observation of the universal magnetoelectric effect in a 3D topological insulator. *ArXiv*, 3:7, mar 2016. URL <http://arxiv.org/abs/1603.05482>.
- [83] Liang Fu. Hexagonal warping effects in the surface states of the topological insulator Bi<sub>2</sub>Te<sub>3</sub>. *Physical Review Letters*, 103(26):1–4, 2009.
- [84] Tsuneya Ando, Alan B. Fowler, and Frank Stern. Electronic properties of two-dimensional systems. *Reviews of Modern Physics*, 54(2):437–672, apr 1982.
- [85] Gérald Bastard. *Wave mechanics applied to semiconductor heterostructures*. Les éditions de Physique - Monographies de Physique, 1996.
- [86] V. L. Berezinskii. Destruction of Long-range Order in One-dimensional and Two-dimensional Systems having a Continuous Symmetry Group I. Classical Systems. *Soviet Journal of Experimental and Theoretical Physics*, 32:493, 1971.
- [87] V. L. Berezinskii. Destruction of Long-range Order in One-dimensional and Two-dimensional Systems Possessing a Continuous Symmetry Group. II. Quantum Systems. *Soviet Journal of Experimental and Theoretical Physics*, 34:610, 1972.
- [88] J M Kosterlitz and D J Thouless. Ordering, metastability and phase transitions in two-dimensional systems. *Journal of Physics C: Solid State Physics*, 6(7):1181–1203, apr 1973. URL <http://stacks.iop.org/0022-3719/6/i=7/a=010?key=crossref.f2d443370878b9288c142e398ad429b1>.
- [89] F.D.M. Haldane. Continuum dynamics of the 1-D Heisenberg antiferromagnet: Identification with the O(3) nonlinear sigma model. *Physics Letters A*, 93(9):464–468, feb 1983. doi: 10.1016/0375-9601(83)90631-X. URL <http://linkinghub.elsevier.com/retrieve/pii/037596018390631X>.
- [90] F. D M Haldane. Nonlinear Field Theory of Large-Spin Heisenberg Antiferromagnets: Semiclassically Quantized Solitons of the One-Dimensional Easy-Axis Néel State. *Physical Review Letters*, 50(15):1153–1156, apr 1983. URL <http://link.aps.org/doi/10.1103/PhysRevLett.50.1153>.
- [91] Ettore Majorana. Teoria simmetrica dell’elettrone e del positrone. *Il Nuovo Cimento*, 14(4):171–184, apr 1937. URL <http://link.springer.com/10.1007/BF02961314>.
- [92] E Majorana. A symmetric theory of electrons and positrons. *Soryushiron Kenkyu*, 63(3):149–162, 1981.
- [93] Frank Wilczek. Majorana returns. *Nature Physics*, 5(9):614–618, sep 2009. URL <http://dx.doi.org/10.1038/nphys1380http://www.nature.com/doi/10.1038/nphys1380>.

- [94] N. Read and Dmitry Green. Paired states of fermions in two dimensions with breaking of parity and time-reversal symmetries and the fractional quantum Hall effect. *Physical Review B*, 61(15):10267–10297, apr 2000.
- [95] G E Volovik. Fermion zero modes on vortices in chiral superconductors. *Journal of Experimental and Theoretical Physics Letters*, 70(9):609–614, nov 1999. doi: 10.1134/1.568223.
- [96] Andrew Peter Mackenzie and Yoshiteru Maeno. The superconductivity of  $\text{Sr}_2\text{RuO}_4$  and the physics of spin-triplet pairing. *Reviews of Modern Physics*, 75(2):657–712, 2003. ISSN 00346861. doi: 10.1103/RevModPhys.75.657. URL <http://link.aps.org/doi/10.1103/RevModPhys.75.657>[http://rmp.aps.org/pdf/RMP/v75/i2/p657\\_1](http://rmp.aps.org/pdf/RMP/v75/i2/p657_1).
- [97] N. Lütke-Entrup, R. Blaauwgeers, B. Plaçais, A. Huxley, S. Kambe, M. Krusius, P. Mathieu, and Y. Simon. Flux-flow resistivity in  $\text{UPt}_3$ : Evidence for nonsingular vortex-core structure. *Physical Review B*, 64(2):020510, jun 2001. ISSN 0163-1829. doi: 10.1103/PhysRevB.64.020510. URL <http://link.aps.org/doi/10.1103/PhysRevB.64.020510>.
- [98] J.A. Sauls. The order parameter for the superconducting phases of  $\text{UPt}_3$ . *Advances in Physics*, 43(1):113–141, feb 1994. ISSN 0001-8732. doi: 10.1080/00018739400101475. URL <http://www.tandfonline.com/doi/abs/10.1080/00018739400101475>.
- [99] Robert Joynt and Louis Taillefer. The superconducting phases of  $\text{UPt}_3$ . *Reviews of Modern Physics*, 74(January):235–294, 2002. ISSN 0034-6861. doi: 10.1103/RevModPhys.74.235. URL <http://link.aps.org/doi/10.1103/RevModPhys.74.235>[http://rmp.aps.org/abstract/RMP/v74/i1/p235\\_1](http://rmp.aps.org/abstract/RMP/v74/i1/p235_1)[http://rmp.aps.org/pdf/RMP/v74/i1/p235\\_1](http://rmp.aps.org/pdf/RMP/v74/i1/p235_1).
- [100] Dieter Vollhardt and Peter Wölfle, editor. *The Superfluid Phases of Helium 3*. Taylor and Francis, 1990. ISBN 0-85066-412-8.
- [101] Jay D. Sau, Roman M. Lutchyn, Sumanta Tewari, and S. Das Sarma. Generic new platform for topological quantum computation using semiconductor heterostructures. *Physical Review Letters*, 104(4):1–4, 2010.
- [102] V Mourik, K Zuo, S M Frolov, S R Plissard, E P a M Bakkers, and L P Kouwenhoven. Signatures of Majorana fermions in hybrid superconductor-semiconductor nanowire devices. *Science (New York, N.Y.)*, 336(6084):1003–7, may 2012. URL <http://www.ncbi.nlm.nih.gov/pubmed/22499805>.

- [103] Chetan Nayak, Steven H. Simon, Ady Stern, Michael Freedman, and Sankar Das Sarma. Non-Abelian anyons and topological quantum computation. *Reviews of Modern Physics*, 80(3):1083–1159, sep 2008. ISSN 0034-6861. doi: 10.1103/RevModPhys.80.1083. URL <http://link.aps.org/doi/10.1103/RevModPhys.80.1083>.
- [104] Sankar Das Sarma, Michael Freedman, and Chetan Nayak. Majorana zero modes and topological quantum computation. *npj Quantum Information*, 1(December 2014):15001, oct 2015. URL <http://arxiv.org/abs/1501.02813><http://www.nature.com/articles/npjqi20151>.
- [105] Anindya Das, Yuval Ronen, Yonatan Most, Yuval Oreg, Moty Heiblum, and Hadas Shtrikman. Zero-bias peaks and splitting in an Al–InAs nanowire topological superconductor as a signature of Majorana fermions. *Nature Physics*, 8(12):887–895, nov 2012. ISSN 1745-2473. doi: 10.1038/nphys2479. URL <http://www.nature.com/nphys/journal/v8/n12/abs/nphys2479.html><http://arxiv.org/abs/1205.7073><http://www.nature.com/doi/10.1038/nphys2479>.
- [106] S M Albrecht, A P Higginbotham, M Madsen, F Kuemmeth, T S Jespersen, J. Nygård, P Krogstrup, and C M Marcus. Exponential protection of zero modes in Majorana islands. *Nature*, 531(7593):206–209, mar 2016. ISSN 0028-0836. doi: 10.1038/nature17162. URL <http://dx.doi.org/10.1038/nature17162><http://www.nature.com/doi/10.1038/nature17162>.
- [107] M T Deng, S. Vaitiekėnas, E B Hansen, J Danon, M Leijnse, K Flensberg, J. Nygård, P Krogstrup, and C M Marcus. Majorana bound state in a coupled quantum-dot hybrid-nanowire system. *Science*, 354(6319):1557–1562, dec 2016. ISSN 0036-8075. doi: 10.1126/science.aaf3961. URL <http://www.sciencemag.org/lookup/doi/10.1126/science.aaf3961>.
- [108] Falko Pientka, Leonid I. Glazman, and Felix von Oppen. Topological superconducting phase in helical Shiba chains. *Physical Review B*, 88(15):155420, oct 2013. ISSN 1098-0121. doi: 10.1103/PhysRevB.88.155420. URL <http://link.aps.org/doi/10.1103/PhysRevB.88.155420>.
- [109] Jelena Klinovaja, Peter Stano, Ali Yazdani, and Daniel Loss. Topological Superconductivity and Majorana Fermions in RKKY Systems. *Physical Review Letters*, 111(18):186805, nov 2013. ISSN 0031-9007. doi: 10.1103/PhysRevLett.111.186805. URL <http://link.aps.org/doi/10.1103/PhysRevLett.111.186805>.
- [110] Stevan Nadj-Perge, Ilya K. Drozdov, Jian Li, Hua Chen, Sangjun Jeon, Jungpil Seo, Allan H. MacDonald, B. Andrei Bernevig, and Ali Yazdani. Observation of

- majorana fermions in ferromagnetic atomic chains on a superconductor. *Science*, 2014. ISSN 0036-8075. doi: 10.1126/science.1259327. URL <http://science.sciencemag.org/content/early/2014/10/01/science.1259327>.
- [111] Jian Li, Hua Chen, Ilya K. Drozdov, A. Yazdani, B. Andrei Bernevig, and A. H. MacDonald. Topological superconductivity induced by ferromagnetic metal chains. *Physical Review B*, 90(23):235433, dec 2014. ISSN 1098-0121. doi: 10.1103/PhysRevB.90.235433. URL <http://link.aps.org/doi/10.1103/PhysRevB.90.235433>.
- [112] Rémy Pawlak, Marcin Kisiel, Jelena Klinovaja, Tobias Meier, Shigeki Kawai, Thilo Glatzel, Daniel Loss, and Ernst Meyer. Probing atomic structure and Majorana wavefunctions in mono-atomic Fe chains on superconducting Pb surface. *npj Quantum Information*, 2:16035, nov 2016. ISSN 2056-6387. doi: 10.1038/npjqi.2016.35. URL <http://www.nature.com/articles/npjqi201635>.
- [113] Michael Ruby, Falko Pientka, Yang Peng, Felix von Oppen, Benjamin W. Heinrich, and Katharina J. Franke. End States and Subgap Structure in Proximity-Coupled Chains of Magnetic Adatoms. *Physical Review Letters*, 115(19):197204, nov 2015. ISSN 0031-9007. doi: 10.1103/PhysRevLett.115.197204. URL <http://link.aps.org/doi/10.1103/PhysRevLett.115.197204>.
- [114] Rahul Roy. Topological superfluids with time reversal symmetry. *arXiv*, 0803.2868: 1–5, mar 2008. URL <http://arxiv.org/abs/0803.2868>.
- [115] S. Das Sarma, Jay D. Sau, and Tudor D. Stanescu. Splitting of the zero-bias conductance peak as smoking gun evidence for the existence of the Majorana mode in a superconductor-semiconductor nanowire. *Physical Review B*, 86(22):220506, dec 2012. ISSN 1098-0121. doi: 10.1103/PhysRevB.86.220506. URL <http://link.aps.org/doi/10.1103/PhysRevB.86.220506>.
- [116] H.-J. Kwon, K. Sengupta, and V. M. Yakovenko. Fractional ac Josephson effect in p- and d-wave superconductors. *The European Physical Journal B - Condensed Matter*, 37(3):349–361, feb 2003. ISSN 1434-6028. doi: 10.1140/epjb/e2004-00066-4. URL <http://www.springerlink.com/openurl.asp?genre=article&id=doi:10.1140/epjb/e2004-00066-4>.
- [117] A Yu Kitaev. Unpaired Majorana fermions in quantum wires. *Physics-Uspekhi*, 44 (10S):131–136, oct 2001. URL <http://stacks.iop.org/1063-7869/44/i=10S/a=S29?key=crossref.8adaeb1befda6574f9e1617c47e8ae35>.

- [118] Erwann Bocquillon, Russell S. Deacon, Jonas Wiedenmann, Philipp Leubner, Teunis M. Klapwijk, Christoph Brüne, Koji Ishibashi, Hartmut Buhmann, and Laurens W. Molenkamp. Gapless Andreev bound states in the quantum spin Hall insulator HgTe. *Nature Nanotechnology*, page 16, aug 2016. ISSN 1748-3387. doi: 10.1038/nnano.2016.159. URL <http://arxiv.org/abs/1601.08055><http://www.nature.com/doifinder/10.1038/nnano.2016.159>.
- [119] Russell S. Deacon, Jonas Wiedenmann, Erwann Bocquillon, Fernando Domínguez, Teun M. Klapwijk, Philipp Leubner, Christoph Brüne, Ewelina M. Hankiewicz, Seigo Tarucha, Koji Ishibashi, Hartmut Buhmann, and Laurens W. Molenkamp. Josephson radiation from gapless Andreev bound states in HgTe-based topological junctions. *Condensed Matter - Mesoscale and Nanoscale Physics*, pages 1–19, mar 2016. URL <http://arxiv.org/abs/1603.09611>.
- [120] Jonas Wiedenmann, Erwann Bocquillon, Russell S. Deacon, Simon Hartinger, Oliver Herrmann, Teun M. Klapwijk, Luis Maier, Christopher Ames, Christoph Brüne, Charles Gould, Akira Oiwa, Koji Ishibashi, Seigo Tarucha, Hartmut Buhmann, and Laurens W. Molenkamp.  $4\pi$ -periodic Josephson supercurrent in HgTe-based topological Josephson junctions. *Nature Communications*, 7:10303, jan 2016. URL <http://arxiv.org/abs/1503.05591><http://www.nature.com/doifinder/10.1038/ncomms10303>.
- [121] Liang Fu. Topological Crystalline Insulators. *Physical Review Letters*, 106(10):106802, mar 2011. ISSN 0031-9007. doi: 10.1103/PhysRevLett.106.106802. URL <http://link.aps.org/doi/10.1103/PhysRevLett.106.106802>.
- [122] Timothy H Hsieh, Hsin Lin, Junwei Liu, Wenhui Duan, Arun Bansil, and Liang Fu. Topological crystalline insulators in the SnTe material class. *Nature communications*, 3:982, 2012. ISSN 2041-1723. doi: 10.1038/ncomms1969. URL <http://www.ncbi.nlm.nih.gov/pubmed/22864575>.
- [123] S. Safaei, P. Kacman, and R. Buczko. Topological crystalline insulator (Pb,Sn)Te: Surface states and their spin polarization. *Physical Review B*, 88(4):045305, jul 2013. ISSN 1098-0121. doi: 10.1103/PhysRevB.88.045305. URL <http://link.aps.org/doi/10.1103/PhysRevB.88.045305>.
- [124] B. M. Wojek, P. Dziawa, B. J. Kowalski, A. Szczerbakow, A. M. Black-Schaffer, M. H. Berntsen, T. Balasubramanian, T. Story, and O. Tjernberg. Band inversion and the topological phase transition in (Pb,Sn)Se. *Physical Review B - Condensed Matter and Materials Physics*, 90(16):5–9, 2014. ISSN 1550235X. doi: 10.1103/PhysRevB.90.161202.

- [125] P Dziawa, B J Kowalski, K Dybko, R Buczko, A Szczerbakow, M Szot, E Łusakowska, T Balasubramanian, B M Wojek, M H Berntsen, O Tjernberg, and T Story. Topological crystalline insulator states in  $\text{Pb}_{1-x}\text{Sn}_x\text{Se}$ . *Nature Materials*, 11(12):1023–7, sep 2012. ISSN 1476-1122. doi: 10.1038/nmat3449. URL <http://dx.doi.org/10.1038/nmat3449><http://www.nature.com/doifinder/10.1038/nmat3449>.
- [126] B.A. Assaf, T. Phuphachong, V.V. Volobuev, A. Inhofer, G. Bauer, G. Springholz, L.A. de Vaulchier, and Y. Guldner. Massive and massless Dirac fermions in  $\text{Pb}_{1-x}\text{Sn}_x\text{Te}$  topological crystalline insulator probed by magneto-optical absorption. *Scientific Reports*, 6(February):20323, 2016. ISSN 2045-2322. doi: 10.1038/srep20323. URL <http://arxiv.org/abs/1510.01081><http://www.nature.com/articles/srep20323>.
- [127] Badih a Assaf, Thanyanan Phuphachong, Valentine V Volobuev, Günther Bauer, Gunther Springholz, Louis-Anne De Vaulchier, and Yves Guldner. Universal relation between velocity and topological character of Dirac fermions through a topological phase transition. *arXiv*, page 1608.08912, 2016.
- [128] Maxim Dzero, Jing Xia, Victor Galitski, and Piers Coleman. Topological Kondo Insulators. *arXiv*, 106408(March):1–26, 2015. ISSN 1947-5454. doi: 10.1146/). URL <http://arxiv.org/abs/1406.3533><http://arxiv.org/abs/1506.05635>.
- [129] G. Li, Z. Xiang, F. Yu, T. Asaba, B. Lawson, P. Cai, C. Tinsman, A. Berkley, S. Wolgast, Y. S. Eo, Dae-Jeong Kim, C. Kurdak, J. W. Allen, K. Sun, X. H. Chen, Y. Y. Wang, Z. Fisk, and Lu Li. Two-dimensional fermi surfaces in kondo insulator  $\text{SmB}_6$ . *Science*, 346(6214):1208–1212, 2014. ISSN 0036-8075. doi: 10.1126/science.1250366. URL <http://science.sciencemag.org/content/346/6214/1208>.
- [130] Dominik Gresch, Gabriel Autès, Oleg V. Yazyev, Matthias Troyer, David Vanderbilt, B. Andrei Bernevig, and Alexey A. Soluyanov. Z2Pack: Numerical Implementation of Hybrid Wannier Centers for Identifying Topological Materials. *Arxiv*, pages 1–26, oct 2016. URL <http://arxiv.org/abs/1610.08983>.
- [131] Frank Wilczek. Two applications of axion electrodynamics. *Physical Review Letters*, 58(18):1799–1802, 1987. ISSN 00319007. doi: 10.1103/PhysRevLett.58.1799.
- [132] Xiao-Liang Qi, Taylor L. Hughes, and Shou-Cheng Zhang. Topological field theory of time-reversal invariant insulators. *Physical Review B*, 78(19):195424, nov 2008. ISSN 1098-0121. doi: 10.1103/PhysRevB.78.195424. URL <http://link.aps.org/doi/10.1103/PhysRevB.78.195424>.

- [133] Xiao-Liang Qi, Rundong Li, Jiadong Zang, and Shou-Cheng Zhang. Inducing a magnetic monopole with topological surface States. *Science (New York, N.Y.)*, 323(5918):1184–7, 2009. ISSN 1095-9203. doi: 10.1126/science.1167747. URL <http://www.ncbi.nlm.nih.gov/pubmed/19179491>.
- [134] Liang Wu, M. Salehi, N. Koirala, J. Moon, S. Oh, and N. P. Armitage. Quantized Faraday and Kerr rotation and axion electrodynamics of a 3D topological insulator. *Science*, 354(6316):1124–1127, dec 2016. ISSN 0036-8075. URL <http://arxiv.org/abs/1603.04317><http://www.sciencemag.org/cgi/doi/10.1126/science.aaf5541>.
- [135] Christoph Brüne, Cornelius Thienel, Michael Stuiber, Jan Böttcher, Hartmut Buhmann, Elena G. Novik, Chao Xing Liu, Ewelina M. Hankiewicz, and Laurens W. Molenkamp. Dirac-screening stabilized surface-state transport in a topological insulator. *Physical Review X*, 4(4):1–6, 2014.
- [136] according to isi web of knowledge, sep. 2016, 2016. URL [http://apps.webofknowledge.com/CitationReport.do?product=WOS&search\\_mode=CitationReport&SID=V19KSM8u2AYIILwtFSv&page=1&cr\\_pqid=1&viewType=summary&colName=WOS](http://apps.webofknowledge.com/CitationReport.do?product=WOS&search_mode=CitationReport&SID=V19KSM8u2AYIILwtFSv&page=1&cr_pqid=1&viewType=summary&colName=WOS).
- [137] G. Bastard. Superlattice band structure in the envelope-function approximation. *Physical Review B*, 24(10):5693–5697, nov 1981. URL <http://link.aps.org/doi/10.1103/PhysRevB.24.5693>.
- [138] G. Bastard. Theoretical investigations of superlattice band structure in the envelope-function approximation. *Physical Review B*, 25(12):7584–7597, jun 1982. URL <http://link.aps.org/doi/10.1103/PhysRevB.25.7584>.
- [139] Klaus Capelle. A bird’s-eye view of density-functional theory. *Brazilian Journal of Physics*, 36(4a):1318–1343, dec 2006. ISSN 0103-9733. doi: 10.1590/S0103-97332006000700035. URL [http://www.scielo.br/scielo.php?script=sci\\_arttext&pid=S0103-97332006000700035&lng=en&nrm=iso&tlng=en](http://www.scielo.br/scielo.php?script=sci_arttext&pid=S0103-97332006000700035&lng=en&nrm=iso&tlng=en).
- [140] M. P. Seah and W. A. Dench. Quantitative electron spectroscopy of surfaces: A standard data base for electron inelastic mean free paths in solids. *Surface and Interface Analysis*, 1(1):2–11, feb 1979. doi: 10.1002/sia.740010103. URL <http://doi.wiley.com/10.1002/sia.740010103>.
- [141] E. H. Hall. On a New Action of the Magnet on Electric Currents. *American Journal of Mathematics*, 2(3):287, sep 1879.

- [142] Yang Xu, Ireneusz Miotkowski, Chang Liu, Jifa Tian, Hyoungdo Nam, Nasser Alidoust, Jiuning Hu, Chih-Kang Shih, M. Zahid Hasan, and Yong P. Chen. Observation of topological surface state quantum Hall effect in an intrinsic three-dimensional topological insulator. *Nature Physics*, 10(December), 2014.
- [143] G Eguchi and S Paschen. New scheme for magnetotransport analysis in topological insulators. *arXiv*, 1:1–6, sep 2016. URL <http://arxiv.org/abs/1609.04134>.
- [144] S. Datta. *Electronic transport in mesoscopic Systems*. Cambridge University Press, 1995.
- [145] M. O. Goerbig, G Montambaux, and F Piéchon. Measure of Diracness in two-dimensional semiconductors. *EPL (Europhysics Letters)*, 105(5):57005, mar 2014.
- [146] Louis Veyrat, Fabrice Iacovella, Joseph Dufouleur, Christian Nowka, Hannes Funke, Ming Yang, Walter Escoffier, Michel Goiran, Barbara Eichler, Oliver G. Schmidt, Bernd Büchner, Silke Hampel, and Romain Giraud. Band Bending Inversion in Bi<sub>2</sub>Se<sub>3</sub> Nanostructures. *Nano Letters*, 15(11):7503–7507, nov 2015. ISSN 1530-6984. doi: 10.1021/acs.nanolett.5b03124. URL <http://pubs.acs.org/doi/10.1021/acs.nanolett.5b03124>.
- [147] Fanming Qu, Chi Zhang, Rui-Rui Du, and Li Lu. Coexistence of Bulk and Surface Shubnikov-de Haas Oscillations in Bi<sub>2</sub>Se<sub>3</sub>. *Journal of Low Temperature Physics*, 170(5-6):397–402, mar 2013.
- [148] Hai Zhou Lu, Junren Shi, and Shun Qing Shen. Competition between weak localization and antilocalization in topological surface states. *Physical Review Letters*, 107(7):1–5, 2011.
- [149] S. Hikami, A. I. Larkin, and Y. Nagaoka. Spin-Orbit Interaction and Magnetoresistance in the Two Dimensional Random System. *Progress of Theoretical Physics*, 63(2):707–710, feb 1980.
- [150] Huichao Wang, Haiwen Liu, Cui-Zu Chang, Huakun Zuo, Yanfei Zhao, Yi Sun, Zhengcai Xia, Ke He, Xucun Ma, X C Xie, Qi-Kun Xue, and Jian Wang. Crossover between Weak Antilocalization and Weak Localization of Bulk States in Ultrathin Bi<sub>2</sub>Se<sub>3</sub> Films. *Scientific reports*, 4:5817, jan 2014. ISSN 2045-2322. doi: 10.1038/srep05817. URL <http://www.pubmedcentral.nih.gov/articlerender.fcgi?artid=4108910&tool=pmcentrez&rendertype=abstract>.
- [151] Yong Seung Kim, Matthew Brahlek, Namrata Bansal, Eliav Edrey, Gary A Kapilevich, Keiko Iida, Makoto Tanimura, Yoichi Horibe, Sang-wook Cheong, and Seongshik Oh. Thickness-dependent bulk properties and weak antilocalization effect in topological insulator Bi<sub>2</sub>Se<sub>3</sub>. *Physical Review B*, 84(7):073109, aug 2011.

- [152] J Chen, H J Qin, F. Yang, J Liu, T Guan, F M Qu, G H Zhang, J R Shi, X C Xie, C L Yang, K H Wu, Y Q Li, and L Lu. Gate-Voltage Control of Chemical Potential and Weak Antilocalization in  $\text{Bi}_2\text{Se}_3$ . *Physical Review Letters*, 105(17):176602, oct 2010. URL <http://link.aps.org/doi/10.1103/PhysRevLett.105.176602>.
- [153] B. A. Assaf, T. Cardinal, P. Wei, F. Katmis, J. S. Moodera, and D. Heiman. Linear magnetoresistance in topological insulator thin films: Quantum phase coherence effects at high temperatures. *Applied Physics Letters*, 102(1):012102, jan 2013. ISSN 0003-6951. doi: 10.1063/1.4773207. URL <http://aip.scitation.org/doi/10.1063/1.4773207>.
- [154] P. Adroguer, Weizhe E. Liu, D. Culcer, and E. M. Hankiewicz. Conductivity corrections for topological insulators with spin-orbit impurities: Hikami-Larkin-Nagaoka formula revisited. *Physical Review B*, 92(24):241402, dec 2015.
- [155] Hailin Peng, Keji Lai, Desheng Kong, Stefan Meister, Yulin Chen, Xiao-liang Qi, Shou-Cheng Zhang, Zhi-Xun Shen, and Yi Cui. Aharonov-Bohm interference in topological insulator nanoribbons. *Nature materials*, 9(3):225–9, mar 2010. ISSN 1476-1122. doi: 10.1038/nmat2609. URL <http://dx.doi.org/10.1038/nmat2609><http://www.ncbi.nlm.nih.gov/pubmed/20010826>.
- [156] J. Dufouleur, L. Veyrat, A. Teichgräber, S. Neuhaus, C. , S. Hampel, J. Cayssol, J. Schumann, B. Eichler, O. G. Schmidt, B. Büchner, and R. Giraud. Quasiballistic Transport of Dirac Fermions in a  $\text{Bi}_2\text{Se}_3$  Nanowire. *Physical Review Letters*, 110(18):186806, apr 2013. ISSN 0031-9007. doi: 10.1103/PhysRevLett.110.186806. URL <http://link.aps.org/doi/10.1103/PhysRevLett.110.186806>.
- [157] Shuigang Xu, Yu Han, Xiaolong Chen, Zefei Wu, Lin Wang, Tianyi Han, Weiguang Ye, Huanhuan Lu, Gen Long, Yingying Wu, Jiangxiazhi Lin, Yuan Cai, K. M. Ho, Yuheng He, and Ning Wang. Van der Waals Epitaxial Growth of Atomically Thin  $\text{Bi}_2\text{Se}_3$  and Thickness-Dependent Topological Phase Transition. *Nano Letters*, 15(4):2645–2651, 2015. ISSN 15306992. doi: 10.1021/acs.nanolett.5b00247.
- [158] Jinsong Zhang, Cui-Zu Chang, Zuocheng Zhang, Jing Wen, Xiao Feng, Kang Li, Minhao Liu, Ke He, Lili Wang, Xi Chen, Qi-Kun Xue, Xucun Ma, and Yayu Wang. Band structure engineering in  $(\text{Bi}_{1-x}\text{Sb}_x)_2\text{Te}_3$  ternary topological insulators. *Nature Communications*, 2:574, dec 2011.
- [159] Kouji Segawa, Zhi Ren, Satoshi Sasaki, Tetsuya Tsuda, Susumu Kuwabata, and Yoichi Ando. Ambipolar transport in bulk crystals of a topological insulator by gating with ionic liquid. *Physical Review B*, 86(7):075306, aug 2012. ISSN 1098-0121. doi: 10.1103/PhysRevB.86.075306. URL <http://link.aps.org/doi/10.1103/PhysRevB.86.075306>.

- [160] Yuichiro Ando, Takahiro Hamasaki, Takayuki Kurokawa, Kouki Ichiba, Fan Yang, Mario Novak, Satoshi Sasaki, Kouji Segawa, Yoichi Ando, and Masashi Shiraishi. Electrical Detection of the Spin Polarization Due to Charge Flow in the Surface State of the Topological Insulator  $\text{Bi}_{1.5}\text{Sb}_{0.5}\text{Te}_{1.7}\text{Se}_{1.3}$ . *Nano Letters*, 14(11):6226–6230, nov 2014. ISSN 1530-6984. doi: 10.1021/nl502546c. URL <http://pubs.acs.org/doi/abs/10.1021/nl502546c>.
- [161] Stanislav Chadov, Xiaoliang Qi, Jürgen Kübler, Gerhard H Fecher, Claudia Felser, and Shou Cheng Zhang. Tunable multifunctional topological insulators in ternary Heusler compounds. *Nature Materials*, 9(7):541–545, jul 2010. ISSN 1476-1122. doi: 10.1038/nmat2770. URL <http://www.ncbi.nlm.nih.gov/pubmed/20512154><http://www.nature.com/doi/10.1038/nmat2770>.
- [162] Shi Yuan Lin, Ming Chen, Xiao Bao Yang, Yu Jun Zhao, Shu Chun Wu, Claudia Felser, and Binghai Yan. Theoretical search for half-heusler topological insulators. *Physical Review B - Condensed Matter and Materials Physics*, 91(9):1–6, 2015. ISSN 1550235X. doi: 10.1103/PhysRevB.91.094107.
- [163] Su-Yang Xu, Chang Liu, Nasser Alidoust, M. Neupane, D. Qian, I. Belopolski, J.D. Denlinger, Y.J. Wang, H. Lin, L.A. Wray, G. Landolt, B. Slomski, J.H. Dil, A. Marcinkova, E. Morosan, Q. Gibson, R. Sankar, F.C. Chou, R.J. Cava, A. Bansil, and M.Z. Hasan. Observation of a topological crystalline insulator phase and topological phase transition in  $\text{Pb}_{1-x}\text{Sn}_x\text{Te}$ . *Nature Communications*, 3(November):1192, nov 2012. ISSN 2041-1723. doi: 10.1038/ncomms2191. URL <http://www.nature.com/doi/10.1038/ncomms2191>.
- [164] J. Navrátil, J. Horák, T. Plecháček, S. Kamba, P. Lošt'ák, J.S. Dyck, W. Chen, and C. Uher. Conduction band splitting and transport properties of  $\text{Bi}_2\text{Se}_3$ . *Journal of Solid State Chemistry*, 177(4-5):1704–1712, apr 2004. ISSN 00224596. doi: 10.1016/j.jssc.2003.12.031. URL <http://linkinghub.elsevier.com/retrieve/pii/S0022459604000179>.
- [165] Y. S. Hor, A. Richardella, P. Roushan, Y. Xia, J. G. Checkelsky, A. Yazdani, M. Z. Hasan, N. P. Ong, and R. J. Cava. p-type  $\text{Bi}_2\text{Se}_3$  for topological insulator and low-temperature thermoelectric applications. *Physical Review B*, 79(19):195208, may 2009. ISSN 1098-0121. doi: 10.1103/PhysRevB.79.195208. URL <http://link.aps.org/doi/10.1103/PhysRevB.79.195208>.
- [166] Chandler Downs and Thomas Vandervelde. Progress in Infrared Photodetectors Since 2000. *Sensors*, 13(4):5054–5098, apr 2013. URL <http://www.mdpi.com/1424-8220/13/4/5054/>.

- [167] G L Hansen. Energy gap versus alloy composition and temperature in  $\text{Hg}_{1-x}\text{Cd}_x\text{Te}$ . *Journal of Applied Physics*, 53(10):7099, 1982. ISSN 00218979. doi: 10.1063/1.330018. URL <http://scitation.aip.org/content/aip/journal/jap/53/10/10.1063/1.330018>.
- [168] Yves Guldner. *Etude magnétooptique des alliages  $\text{Hg}_{1-x}\text{Cd}_x\text{Te}$* . Thèse d'état, Université Pierre et Marie Curie, 1979.
- [169] W.D. Lawson, S Nielsen, E.H. Putley, and A.S. Young. Preparation and properties of  $\text{HgTe}$  and mixed crystals of  $\text{HgTe-CdTe}$ . *Journal of Physics and Chemistry of Solids*, 9(3-4):325–329, mar 1959. ISSN 00223697. doi: 10.1016/0022-3697(59)90110-6. URL <http://linkinghub.elsevier.com/retrieve/pii/0022369759901106>.
- [170] Evan O. Kane. Band structure of indium antimonide. *Journal of Physics and Chemistry of Solids*, 1(4):249–261, jan 1957. ISSN 00223697. doi: 10.1016/0022-3697(57)90013-6. URL <http://linkinghub.elsevier.com/retrieve/pii/0022369757900136>.
- [171] T.C. Harman, W.H. Kleiner, A.J. Strauss, G.B. Wright, J.G. Mavroides, J.M. Honig, and D.H. Dickey. Band structure of  $\text{HgTe}$  and  $\text{HgTe-CdTe}$  alloys. *Solid State Communications*, 2(10):305–308, oct 1964. ISSN 00381098. doi: 10.1016/0038-1098(64)90531-9.
- [172] John D. Wiley and R. N. Dexter. Helicons and Nonresonant Cyclotron Absorption in Semiconductors. II.  $\text{Hg}_{1-x}\text{Cd}_x\text{Te}$ . *Physical Review*, 181(3):1181–1190, may 1969. ISSN 0031-899X. doi: 10.1103/PhysRev.181.1181. URL <http://journals.aps.org/pr/abstract/10.1103/PhysRev.181.1181>  
<http://link.aps.org/doi/10.1103/PhysRev.181.1181>.
- [173] M. W. Scott. Energy gap in  $\text{Hg}_{1-x}\text{Cd}_x\text{Te}$  by optical absorption. *Journal of Applied Physics*, 40(10):4077–4081, 1969. ISSN 00218979. doi: 10.1063/1.1657147.
- [174] Y. Guldner, C Rigaux, M. Grynberg, and A. Mycielski. Interband  $\Gamma_6 \rightarrow \Gamma_8$  Magnetoabsorption in  $\text{HgTe}$ . *Physical Review B*, 8(8):3875–3883, oct 1973. doi: 10.1103/PhysRevB.8.3875. URL <http://link.aps.org/doi/10.1103/PhysRevB.8.3875>.
- [175] J. M. Berroir, Y. Guldner, J P Vieren, M. Voos, and J. P. Faurie. Magneto-optical determination of the  $\text{HgTe-CdTe}$  superlattice band structure. *Physical Review B*, 34(2):891–894, jul 1986. doi: 10.1103/PhysRevB.34.891. URL <http://link.aps.org/doi/10.1103/PhysRevB.34.891>.
- [176] Chang Liu, Guang Bian, Tay-Rong Chang, Kedong Wang, Su-Yang Xu, Ilya Belopolski, Irek Miotkowski, Helin Cao, Koji Miyamoto, Chaoqiang Xu, Christian E.

- Matt, Thorsten Schmitt, Nasser Alidoust, Madhab Neupane, Horng-Tay Jeng, Hsin Lin, Arun Bansil, Vladimir N. Strocov, Mark Bissen, Alexei V. Fedorov, Xudong Xiao, Taichi Okuda, Yong P. Chen, and M. Zahid Hasan. Tunable spin helical Dirac quasiparticles on the surface of three-dimensional HgTe. *Physical Review B*, 92(11):115436, sep 2015. doi: 10.1103/PhysRevB.92.115436.
- [177] Jean-Marc Berroir. *Propriétés électroniques des superréseaux HgTe-CdTe*. Thèse de doctorat, Université Pierre et Marie Curie, 1988.
- [178] B. A. Volkov and O. A. Pankratov. Two-dimensional massless electrons in an inverted contact. *JETP Letters*, 42(4):179, 1985.
- [179] J.M. Berroir and J.A. Brum. Band structure of iii-v and ii-vi superlattices. *Superlattices and Microstructures*, 3(3):239–245, jan 1987. ISSN 07496036. doi: 10.1016/0749-6036(87)90065-6. URL <http://linkinghub.elsevier.com/retrieve/pii/0749603687900656>.
- [180] O. A. Pankratov. Electronic properties of band-inverted heterojunctions: supersymmetry in narrow-gap semiconductors. *Semiconductor Science and Technology*, 5:S204–S209, 1990. ISSN 0268-1242. doi: 10.1088/0268-1242/5/3S/045.
- [181] J P Faurie, K C Woo, and S Rafol. Recent Developments in MBE Growth and Properties of Hg<sub>1-x</sub>Cd<sub>x</sub>Te/CdTe Superlattices. In G. Bauer, F. Kuchar, and H. Heinrich, editors, *Two-dimensional Systems: Physics and New Devices: Proceedings of the International Winter School, Mauterndorf, Austria, February 24-28*, chapter 3, pages 24–32. Springer Berlin Heidelberg, 1986. doi: 10.1007/978-3-662-02470-6\_3. URL [http://link.springer.com/10.1007/978-3-662-02470-6\\_{ }3](http://link.springer.com/10.1007/978-3-662-02470-6_{ }3).
- [182] Xi Dai, Taylor L. Hughes, Xiao-Liang Qi, Zhong Fang, and Shou-Cheng Zhang. Helical edge and surface states in HgTe quantum wells and bulk insulators. *Physical Review B*, 77(12):125319, mar 2008. ISSN 1098-0121. doi: 10.1103/PhysRevB.77.125319. URL <http://link.aps.org/doi/10.1103/PhysRevB.77.125319>.
- [183] F. Teppe, M. Marcinkiewicz, S. S. Krishtopenko, S. Ruffenach, C. Consejo, A. M. Kadykov, W. Desrat, D. But, W. Knap, J. Ludwig, S. Moon, D. Smirnov, M. Orlita, Z. Jiang, S. V. Morozov, V.I. Gavrilenko, N. N. Mikhailov, and S. A. Dvoretiskii. Temperature-driven massless Kane fermions in HgCdTe crystals. *Nature Communications*, 7:12576, aug 2016. doi: 10.1038/ncomms12576.
- [184] Olivier Crauste, Yoshiyuki Ohtsubo, Philippe Ballet, Pierre André Louis Delplace, David Carpentier, Clément Bouvier, Tristan Meunier, Amina Taleb-Ibrahimi, and Laurent Lévy. Topological surface states of strained Mercury-Telluride probed by ARPES. *Arxiv.Org*, pages 1–5, jul 2013. URL <http://arxiv.org/abs/1307.2008>.

- [185] P. Ballet. Mbe-growth of hgte/cdte topological insulator structures. *Talk at the conference Topolyon2016*, 2016.
- [186] Clément Bouvier, Tristan Meunier, Philippe Ballet, Xavier Baudry, Roman Bernd Günter Kramer, and Laurent Lévy. Strained HgTe: a textbook 3D topological insulator. *arXiv preprint*, page 1112.2092, dec 2011. URL <http://arxiv.org/abs/1112.2092>.
- [187] S. Urazhdin, D. Bilc, S. D. Mahanti, S. H. Tessmer, Theodora Kyratsi, and M. G. Kanatzidis. Surface effects in layered semiconductors Bi<sub>2</sub>Se<sub>3</sub> and Bi<sub>2</sub>Te<sub>3</sub>. *Physical Review B*, 69(8):085313, feb 2004. ISSN 1098-0121. doi: 10.1103/PhysRevB.69.085313. URL <http://link.aps.org/doi/10.1103/PhysRevB.66.161306><http://link.aps.org/doi/10.1103/PhysRevB.69.085313>.
- [188] K. S. Novoselov, A. K. Geim, S. V. Morozov, D. Jiang, Y. Zhang, S. V. Dubonos, I. V. Grigorieva, and A. A. Firsov. Electric field effect in atomically thin carbon films. *Science (New York, N.Y.)*, 306(5696):666–9, oct 2004. ISSN 1095-9203. doi: 10.1126/science.1102896. URL <http://www.ncbi.nlm.nih.gov/pubmed/15499015>.
- [189] M.S. Bahrany, P.D.C King, A de la Torre, J Chang, M Shi, L Patthey, G Balakrishnan, Ph Hofmann, R Arita, N Nagaosa, and F Baumberger. Emergent quantum confinement at topological insulator surfaces. *Nature Communications*, 3:1159, oct 2012.
- [190] Marco Bianchi, Dandan Guan, Shining Bao, Jianli Mi, Bo Brummerstedt Iversen, Philip D.C. King, and Philip Hofmann. Coexistence of the topological state and a two-dimensional electron gas on the surface of Bi<sub>2</sub>Se<sub>3</sub>. *Nature Communications*, 1(8):128, nov 2010. doi: 10.1038/ncomms1131.
- [191] James G Analytis, Ross D. McDonald, Scott C Riggs, Jiun-haw Chu, G S Boebinger, and Ian R Fisher. Two-dimensional surface state in the quantum limit of a topological insulator. *Nature Physics*, 6(12):960–964, nov 2010. ISSN 1745-2473. doi: 10.1038/nphys1861. URL <http://dx.doi.org/10.1038/nphys1861><http://www.nature.com/doifinder/10.1038/nphys1861>.
- [192] Hadar Steinberg, Dillon R Gardner, Young S Lee, and Pablo Jarillo-Herrero. Surface State Transport and Ambipolar Electric Field Effect in Bi(2)Se(3) Nanodevices. *Nano letters*, pages 5032–5036, nov 2010. URL <http://www.ncbi.nlm.nih.gov/pubmed/21038914>.

- [193] Benjamin Sacépé, Jeroen B. Oostinga, Jian Li, Alberto Ubaldini, Nuno J.G. Couto, Enrico Giannini, and Alberto F. Morpurgo. Gate-tuned normal and superconducting transport at the surface of a topological insulator. *Nature Communications*, 2: 575, dec 2011. ISSN 2041-1723. doi: 10.1038/ncomms1586.
- [194] J. G. Checkelsky, Y. S. Hor, R. J. Cava, and N. P. Ong. Bulk Band Gap and Surface State Conduction Observed in Voltage-Tuned Crystals of the Topological Insulator  $\text{Bi}_2\text{Se}_3$ . *Physical Review Letters*, 106(19):196801, may 2011. ISSN 0031-9007. doi: 10.1103/PhysRevLett.106.196801. URL <http://link.aps.org/doi/10.1103/PhysRevLett.106.196801>.
- [195] Haim Beidenkopf, Pedram Roushan, Jungpil Seo, Lindsay Gorman, Ilya Drozdov, Yew San Hor, R J Cava, and Ali Yazdani. Spatial fluctuations of helical Dirac fermions on the surface of topological insulators. *Nature Physics*, 7(12):939–943, oct 2011.
- [196] Chao-Xing Liu, HaiJun Zhang, Binghai Yan, Xiao-Liang Qi, Thomas Frauenheim, Xi Dai, Zhong Fang, and Shou-Cheng Zhang. Oscillatory crossover from two-dimensional to three-dimensional topological insulators. *Physical Review B*, 81(4):041307, jan 2010. ISSN 1098-0121. doi: 10.1103/PhysRevB.81.041307. URL <http://link.aps.org/doi/10.1103/PhysRevB.81.041307>.
- [197] Ke He, Yi Zhang, Cui-zu Chang, Can-li Song, Li-li Wang, Xi Chen, Jin-feng Jia, Zhong Fang, Xi Dai, Wen-yu Shan, Shun-qing Shen, Qian Niu, Xiao-liang Qi, Shou-cheng Zhang, Xu-Cun Ma, and Qi-Kun Xue. Crossover of the three-dimensional topological insulator  $\text{Bi}_2\text{Se}_3$  to the two-dimensional limit. *Nature Physics*, 6(8): 584–588, jun 2010. ISSN 1745-2473. doi: 10.1038/nphys1689. URL <http://www.nature.com/doi/10.1038/nphys1689>.
- [198] K.-M. Dantscher, D. A. Kozlov, P. Olbrich, C. Zoth, P. Faltermeier, M. Lindner, G. V. Budkin, S. A. Tarasenko, V. V. Bel'kov, Z. D. Kvon, N. N. Mikhailov, S. A. Dvoretzky, D. Weiss, B. Jenichen, and S. D. Ganichev. Cyclotron-resonance-assisted photocurrents in surface states of a three-dimensional topological insulator based on a strained high-mobility HgTe film. *Physical Review B*, 92(16):165314, oct 2015. URL <http://arxiv.org/abs/1503.06951><http://scitation.aip.org/content/aip/journal/pop/22/3/10.1063/1.4914933><http://dx.doi.org/10.1103/PhysRevB.92.165314><http://link.aps.org/doi/10.1103/PhysRevB.92.165314>.
- [199] Zhi Ren, A. A. Taskin, Satoshi Sasaki, Kouji Segawa, and Yoichi Ando. Fermi level tuning and a large activation gap achieved in the topological insulator  $\text{Bi}_2\text{Te}_2\text{Se}$  by

- Sn doping. *Physical Review B*, 85(15):155301, apr 2012. doi: 10.1103/PhysRevB.85.155301. URL <http://link.aps.org/doi/10.1103/PhysRevB.85.155301>.
- [200] N. P. Butch, K. Kirshenbaum, P. Syers, a. B. Sushkov, G. S. Jenkins, H. D. Drew, and J. Paglione. Strong surface scattering in ultrahigh-mobility Bi<sub>2</sub>Se<sub>3</sub> topological insulator crystals. *Physical Review B*, 81(24):241301, jun 2010. URL <http://link.aps.org/doi/10.1103/PhysRevB.81.241301>.
- [201] Matthew Brahlek, Nikesh Koirala, Namrata Bansal, and Seongshik Oh. Transport properties of topological insulators: Band bending, bulk metal-to-insulator transition, and weak anti-localization. *Solid State Communications*, 215:54–62, 2014. ISSN 00381098. doi: 10.1016/j.ssc.2014.10.021. URL <http://www.sciencedirect.com/science/article/pii/S0038109814004426>.
- [202] M. Orlita, B. A. Piot, G. Martinez, N. K. Sampath Kumar, C. Faugeras, M. Potemski, C. Michel, E. M. Hankiewicz, T. Brauner, Č. Drašar, S. Schreyeck, S. Grauer, K. Brunner, C. Gould, C. Brüne, and L. W. Molenkamp. Magneto-Optics of Massive Dirac Fermions in Bulk Bi<sub>2</sub>Se<sub>3</sub>. *Physical Review Letters*, 114(18):186401, may 2015. URL <http://link.aps.org/doi/10.1103/PhysRevLett.114.186401>.
- [203] Liang He, Faxian Xiu, Xinxin Yu, Marcus Teague, Wanjun Jiang, Yabin Fan, Xufeng Kou, Murong Lang, Yong Wang, Guan Huang, Nai-Chang Yeh, and Kang L Wang. Surface-dominated conduction in a 6 nm thick Bi<sub>2</sub>Se<sub>3</sub> thin film. *Nano letters*, 12(3):1486–90, mar 2012. URL <http://www.ncbi.nlm.nih.gov/pubmed/22316380>.
- [204] J.L. Moll. Variable capacitance with large capacitance change. *Wescon Conv. Rec.*, 1959.
- [205] W. G. Pfann and Garrett. Semiconductor varactor using space-charge layers. *Proc. IRE*, 47, 1959.
- [206] S. H. Barnes and J.E. Mann. Patent: Voltage sensitive semiconductor capacitor, 1961. URL <http://tinyurl.com/jn66opx>.
- [207] N Arora. *MOSFET Models for VLSI Circuit Simulation: Theory and Practice*. Springer-Verlag / Wien, 1st edition, 1993.
- [208] C. N. Berglund. Surface states at steam-grown silicon-silicon dioxide interfaces. *IEEE Transactions on Electron Devices*, 13(10):701–705, Oct 1966. ISSN 0018-9383. doi: 10.1109/T-ED.1966.15827.
- [209] Y L Chen, J.-H. Chu, J G Analytis, Z K Liu, K Igarashi, H.-H. Kuo, X L Qi, S K Mo, R G Moore, D H Lu, M Hashimoto, T Sasagawa, S C Zhang, I R Fisher,

- Z Hussain, and Z X Shen. Massive Dirac Fermion on the Surface of a Magnetically Doped Topological Insulator. *Science*, 329(5992):659–662, aug 2010. ISSN 0036-8075. doi: 10.1126/science.1189924. URL <http://www.sciencemag.org/cgi/doi/10.1126/science.1189924>.
- [210] Dohun Kim, Sungjae Cho, Nicholas P Butch, Paul Syers, Kevin Kirshenbaum, Shaffique Adam, Johnpierre Paglione, and Michael S Fuhrer. Surface conduction of topological Dirac electrons in bulk insulating Bi<sub>2</sub>Se<sub>3</sub>. *Nature Physics*, 8(6):459–463, 2012.
- [211] Jacob Linder, Takehito Yokoyama, and Asle Sudbø. Anomalous finite size effects on surface states in the topological insulator Bi<sub>2</sub>Se<sub>3</sub>. *Physical Review B*, 80(20):205401, nov 2009.
- [212] Kush Saha and Ion Garate. Theory of bulk-surface coupling in topological insulator films. *Physical Review B*, 90(24):245418, dec 2014. ISSN 1098-0121. doi: 10.1103/PhysRevB.90.245418. URL <http://arxiv.org/abs/1409.6291><http://link.aps.org/doi/10.1103/PhysRevB.90.245418>.
- [213] Jun Xiong, Yuehaw Khoo, Shuang Jia, R. J. Cava, and N. P. Ong. Tuning the quantum oscillations of surface Dirac electrons in the topological insulator Bi<sub>2</sub>Te<sub>2</sub>Se by liquid gating. *Physical Review B*, 88(3):035128, jul 2013. ISSN 1098-0121. doi: 10.1103/PhysRevB.88.035128. URL <http://link.aps.org/doi/10.1103/PhysRevB.88.035128>.
- [214] Serguei Tchoumakov, Marcello Civelli, and Mark O. Goerbig. Magnetic-Field-Induced Relativistic Properties in Type-I and Type-II Weyl Semimetals. *Physical Review Letters*, 117(8):086402, aug 2016. ISSN 0031-9007. doi: 10.1103/PhysRevLett.117.086402. URL <http://arxiv.org/abs/1605.00994><http://link.aps.org/doi/10.1103/PhysRevLett.117.086402>.
- [215] Christian Nowka, Louis Veyrat, Sandeep Gorantla, Udo Steiner, Barbara Eichler, Oliver G. Schmidt, Hannes Funke, Joseph Dufouleur, Bernd Büchner, Romain Giraud, and Silke Hampel. Catalyst-free Growth of Single Crystalline Bi<sub>2</sub>Se<sub>3</sub> Nanostructures for Quantum Transport Studies. *Crystal Growth & Design*, 15(9):4272–4278, 2015. doi: 10.1021/acs.cgd.5b00566. URL <http://dx.doi.org/10.1021/acs.cgd.5b00566>.
- [216] J. Duffy. Operating procedure for mti furnace. Technical report, Département de Physique, Ecole Normale Supérieure de Paris, 2016.

- [217] V. A. Golyashov, K. A. Kokh, S. V. Makarenko, K. N. Romanyuk, I. P. Prosvirin, A. V. Kalinkin, O. E. Tereshchenko, A. S. Kozhukhov, D. V. Sheglov, S. V. Ere-meev, S. D. Borisova, and E. V. Chulkov. Inertness and degradation of (0001) sur-face of Bi<sub>2</sub>Se<sub>3</sub> topological insulator. *Journal of Applied Physics*, 112(11):113702, 2012. ISSN 00218979. doi: 10.1063/1.4767458. URL <http://scitation.aip.org/content/aip/journal/jap/112/11/10.1063/1.4767458>.
- [218] Desheng Kong, Judy J Cha, Keji Lai, Hailin Peng, James G Analytis, Stefan Meister, Yulin Chen, Hai-Jun Zhang, Ian R Fisher, Zhi-Xun Shen, and Yi Cui. Rapid surface oxidation as a source of surface degradation factor for Bi<sub>2</sub>Se<sub>3</sub>. *ACS nano*, 5(6):4698–703, jun 2011. ISSN 1936-086X. doi: 10.1021/nm200556h. URL <http://www.ncbi.nlm.nih.gov/pubmed/21568290>.
- [219] Mahmoud Eddrief, Paola Atkinson, Victor Etgens, and Bernard Jusserand. Low-temperature Raman fingerprints for few-quintuple layer topological insulator Bi<sub>2</sub>Se<sub>3</sub> films epitaxied on GaAs. *Nanotechnology*, 25(24):245701, jun 2014.
- [220] M. Eddrief, T. Phuphachong, F. Vidal, B. Jusserand, S. Hidki, Y. Zheng, D. De-maille, L. Largeau, M. Marangolo, P. Atkinson, L.-A. De Vaultier, and Y. Guld-ner. Growth, structure, electronic and vibrational properties of epitaxial bi<sub>2</sub>se<sub>3</sub> topological insulator films on gaas(111) substrates. In *The 17th International Con-ference on II-VI Compounds and Related Materials*, 2015. Poster.
- [221] a. Richardella, D. M. Zhang, J. S. Lee, A. Koser, D. W. Rench, a. L. Yeats, B. B. Buckley, D. D. Awschalom, and N. Samarth. Coherent heteroepitaxy of Bi[sub 2]Se[sub 3] on GaAs (111)B. *Applied Physics Letters*, 97(26):262104, 2010. doi: 10.1063/1.3532845. URL <http://scitation.aip.org/content/aip/journal/apl/97/26/10.1063/1.3532845>.
- [222] Christopher Ames. *Molecular Beam Epitaxy of 2D and 3D HgTe, a Topological Insulator*. Dissertation, Julius-Maximilians-Universität Würzburg, December 2015.
- [223] AZO Materials. Cadmium telluride semiconductors, 2013.
- [224] Andreas Betz. *Elastic and inelastic scattering in graphene studied by microwave transport and noise*. Thesis, Université Pierre et Marie Curie - Paris VI, September 2012. URL <https://tel.archives-ouvertes.fr/tel-00784346>.
- [225] Quentin Wilmart. *Engineering doping profiles in graphene: from Dirac fermion optics to high frequency electronics*. Thèse de doctorat, Ecole Normale Supérieure, December 2015.

- [226] C R Dean, a F Young, I Meric, C Lee, L Wang, S Sorgenfrei, K Watanabe, T Taniguchi, P Kim, K L Shepard, and J Hone. Boron nitride substrates for high-quality graphene electronics. *Nature nanotechnology*, 5(10):722–6, oct 2010.
- [227] Andres Castellanos-Gomez, Michele Buscema, Rianda Molenaar, Vibhor Singh, Laurens Janssen, Herre S J van der Zant, and Gary a Steele. Deterministic transfer of two-dimensional materials by all-dry viscoelastic stamping. *2D Materials*, 1(1):011002, apr 2014. URL <http://stacks.iop.org/2053-1583/1/i=1/a=011002?key=crossref.4a11185bed3e80db2f125d0422bf4c4b>.
- [228] P. J. Zomer, S. P. Dash, N. Tombros, and B. J. van Wees. A transfer technique for high mobility graphene devices on commercially available hexagonal boron nitride. *Applied Physics Letters*, 99(23):232104, 2011. URL <http://scitation.aip.org/content/aip/journal/apl/99/23/10.1063/1.3665405>.
- [229] Yoshiaki Hattori, Takashi Taniguchi, Kenji Watanabe, and Kosuke Nagashio. Layer-by-Layer Dielectric Breakdown of Hexagonal Boron Nitride. *ACS Nano*, 9(1):916–921, jan 2015.
- [230] Kenji Natori, Daijiro Otani, and Nobuyuki Sano. Thickness dependence of the effective dielectric constant in a thin film capacitor. *Applied Physics Letters*, 73(5):632–634, 1998.
- [231] Di Wu, Alexander J. Pak, Yingnan Liu, Yu Zhou, Xiaoyu Wu, Yihan Zhu, Min Lin, Yu Han, Yuan Ren, Hailin Peng, Yu-Hao Tsai, Gyeong S. Hwang, and Keji Lai. Thickness-Dependent Dielectric Constant of Few-Layer In<sub>2</sub>Se<sub>3</sub> Nanoflakes. *Nano Letters*, 15(12):8136–8140, dec 2015. URL <http://pubs.acs.org/doi/10.1021/acs.nanolett.5b03575>.
- [232] Takashi Taniguchi and Kenji Watanabe. Synthesis of high-purity boron nitride single crystals under high pressure by using Ba–BN solvent. *Journal of Crystal Growth*, 303(2):525–529, may 2007.
- [233] Jiro Yota, Hong Shen, and Ravi Ramanathan. Characterization of atomic layer deposition HfO<sub>2</sub>, Al<sub>2</sub>O<sub>3</sub>, and plasma-enhanced chemical vapor deposition Si<sub>3</sub>N<sub>4</sub> as metal–insulator–metal capacitor dielectric for GaAs HBT technology. *Journal of Vacuum Science & Technology A: Vacuum, Surfaces, and Films*, 31(1):01A134, 2013.
- [234] John Robertson. Band offsets of wide-band-gap oxides and implications for future electronic devices. *Journal of Vacuum Science & Technology B: Microelectronics and Nanometer Structures*, 18(3):1785, 2000.

- URL <http://link.aip.org/link/JVTBD9/v18/i3/p1785/s1{&}Agg=doihttp://scitation.aip.org/content/avs/journal/jvstb/18/3/10.1116/1.591472>.
- [235] J Robertson. High dielectric constant oxides. *The European Physical Journal Applied Physics*, 28(3):265–291, dec 2004.
- [236] F. Yang. *Characterization of HFO2 Capacitors*. Master thesis, University of Maine, 2003.
- [237] Neumaier, D. (Advanced Microelectronic Center Aachen, AMO GmbH). Graphene transistors: Process technology and its implication on the performance. Internal communication, 2014.
- [238] Steven M. George. Atomic Layer Deposition: An Overview. *Chemical Reviews*, 110(1):111–131, jan 2010. ISSN 0009-2665. doi: 10.1021/cr900056b. URL <http://pubs.acs.org/doi/abs/10.1021/cr900056b>.
- [239] David M. Pozar. *Microwave engineering*. Wiley, 3rd (international) edition, 2005.
- [240] Peter Capper and James Garland, editors. *Mercury Cadmium Telluride: Growth, Properties and Applications*. Wiley, 2010.
- [241] Q. Wilmart, A. Inhofer, M. Boukhicha, W. Yang, M. Rosticher, P. Morfin, N. Garroum, G. Fève, J.-M. Berroir, and B. Plaçais. Contact gating at GHz frequency in graphene. *Scientific Reports*, 6(November 2015):21085, feb 2016. ISSN 2045-2322. doi: 10.1038/srep21085. URL <http://www.nature.com/articles/srep21085>.
- [242] Rui-Lin Chu, Wen-Yu Shan, Jie Lu, and Shun-Qing Shen. Surface and edge states in topological semimetals. *Physical Review B*, 83(7):075110, feb 2011. ISSN 1098-0121. doi: 10.1103/PhysRevB.83.075110. URL <http://link.aps.org/doi/10.1103/PhysRevB.83.075110>.
- [243] Shu-chun Wu, Binghai Yan, and Claudia Felser. Ab initio study of topological surface states of strained HgTe. *EPL (Europhysics Letters)*, 107(5):57006, sep 2014. doi: 10.1209/0295-5075/107/57006. URL <http://stacks.iop.org/0295-5075/107/i=5/a=57006?key=crossref.4c4290ff73b20bf0d718afb916838ebd>.
- [244] J. Baars and F. Sorger. Reststrahlen spectra of HgTe and CdxHg1-xTe. *Solid State Communications*, 10(9):875–878, may 1972.
- [245] S. Das Sarma, Shaffique Adam, E. H. Hwang, and Enrico Rossi. Electronic transport in two-dimensional graphene. *Reviews of Modern Physics*, 83(2):407–470, may 2011. ISSN 0034-6861. doi: 10.1103/RevModPhys.83.407. URL <http://link.aps.org/doi/10.1103/RevModPhys.83.407>.

- [246] Dimitrie Culcer, E. H. Hwang, Tudor D. Stanescu, and S. Das Sarma. Two-dimensional surface charge transport in topological insulators. *Phys. Rev. B*, 82:155457, 2010. ISSN 1098-0121. doi: 10.1103/PhysRevB.82.155457. URL <http://arxiv.org/abs/1005.4931>.
- [247] Sébastien Giraud and Reinhold Egger. Electron-phonon scattering in topological insulators. *Physical Review B*, 83(24):245322, jun 2011. ISSN 1098-0121. URL <http://link.aps.org/doi/10.1103/PhysRevB.83.245322>.
- [248] S. Mori and T. Ando. Intersubband scattering effect on the mobility of a Si (100) inversion layer at low temperatures. *Physical Review B*, 19(12):6433–6441, jun 1979. ISSN 0163-1829. doi: 10.1103/PhysRevB.19.6433. URL <http://link.aps.org/doi/10.1103/PhysRevB.19.6433>.
- [249] Shojiro Mori and Tsuneya Ando. Electronic Properties of a Semiconductor Superlattice II. Low Temperature Mobility Perpendicular to the Superlattice. *Journal of the Physical Society of Japan*, 48(3):865–873, mar 1980. ISSN 0031-9015. doi: 10.1143/JPSJ.48.865. URL <http://journals.jps.jp/doi/10.1143/JPSJ.48.865>.
- [250] Seungchan Woo, E. H. Hwang, and Hongki Min. Large negative transconductance in multilayer graphene: The role of intersubband scattering. *arXiv*, pages 1–14, oct 2016. URL <http://arxiv.org/abs/1610.07006>.
- [251] L Andrew Wray, Suyang Xu, Madhab Neupane, Yuqi Xia, David Hsieh, Dong Qian, Alexei V Fedorov, Hsin Lin, Susmita Basak, Yew San Hor, Robert J Cava, Arun Bansil, and M Zahid Hasan. Electron dynamics in topological insulator based semiconductor-metal interfaces (topological p-n interface based on Bi<sub>2</sub>Se<sub>3</sub> class). *Arxiv*, page 14, may 2011. URL <http://arxiv.org/abs/1105.4794>.
- [252] Vinu Lukose, R. Shankar, and G. Baskaran. Novel Electric Field Effects on Landau Levels in Graphene. *Physical Review Letters*, 98(11):116802, mar 2007. ISSN 0031-9007. doi: 10.1103/PhysRevLett.98.116802. URL <http://link.aps.org/doi/10.1103/PhysRevLett.98.116802>.
- [253] Torsten Karzig, Gil Refael, and Felix von Oppen. Boosting Majorana Zero Modes. *Physical Review X*, 3(4):041017, nov 2013.
- [254] Serguei Tchoumakov, Marcello Civelli, and Mark O. Goerbig. Magnetic description of the Fermi arc in type-I and type-II Weyl semimetals. *ArXiv*, pages 1–19, dec 2016. URL <http://arxiv.org/abs/1612.07693>.
- [255] William Shockley. On the Surface States Associated with a Periodic Potential. *Physical Review*, 56(4):317–323, aug 1939.

- [256] E. G. Novik, a. Pfeuffer-Jeschke, T. Jungwirth, V. Latussek, C. R. Becker, G. Landwehr, H. Buhmann, and L. W. Molenkamp. Band structure of semimagnetic Hg<sub>1-y</sub>Mn<sub>y</sub>Te quantum wells. *Physical Review B*, 72:035321, 2005. ISSN 10980121. doi: 10.1103/PhysRevB.72.035321.
- [257] C. R. Becker, V. Latussek, A. Pfeuffer-Jeschke, G. Landwehr, and L. W. Molenkamp. Band structure and its temperature dependence for type-III HgTe/Hg(1-x)Cd(x)Te superlattices and their semimetal constituent. *Physical Review B*, 62(15):10353–10363, oct 2000.
- [258] Eric Bersch, Sylvie Rangan, Robert Allen Bartynski, Eric Garfunkel, and Elio Vescovo. Band offsets of ultrathin high- $\kappa$  oxide films with si. *Phys. Rev. B*, 78:085114, Aug 2008. doi: 10.1103/PhysRevB.78.085114. URL <http://link.aps.org/doi/10.1103/PhysRevB.78.085114>.
- [259] Yanping Liu, Kyle Tom, Xi Wang, Chunming Huang, Hongtao Yuan, Hong Ding, Changhyun Ko, Joonki Suh, Lawrence Pan, Kristin A. Persson, and Jie Yao. Dynamic Control of Optical Response in Layered Metal Chalcogenide Nanoplates. *Nano Letters*, 16(1):488–496, 2016.
- [260] L. Leontie, M. Caraman, M. Alexe, and C. Harnagea. Structural and optical characteristics of bismuth oxide thin films. *Surface Science*, 507-510:480–485, jun 2002.
- [261] C. E. ViolBarbosa, Chandra Shekhar, Binghai Yan, S. Ouardi, Eiji Ikenaga, G. H. Fecher, and C. Felser. Direct observation of band bending in the topological insulator Bi<sub>2</sub>Se<sub>3</sub>. *Physical Review B*, 88(19):195128, nov 2013.
- [262] Dohun Kim, Qiuzi Li, Paul Syers, Nicholas P Butch, Johnpierre Paglione, S Das Sarma, and Michael S Fuhrer. Intrinsic Electron-Phonon Resistivity of Bi<sub>2</sub>Se<sub>3</sub> in the Topological Regime. *Physical Review Letters*, 109(16):166801, oct 2012.
- [263] Qiuzi Li, E. Rossi, and S. Das Sarma. Two-dimensional electronic transport on the surface of three-dimensional topological insulators. *Physical Review B*, 86(23):235443, dec 2012.
- [264] Sébastien Giraud, Arijit Kundu, and Reinhold Egger. Electron-phonon scattering in topological insulator thin films. *Physical Review B*, 85(3):035441, jan 2012.
- [265] J M Riley, W Meevasana, L Bawden, M Asakawa, T Takayama, T Eknapakul, T K Kim, M Hoesch, S-K Mo, H Takagi, T Sasagawa, M S Bahramy, and P D C King. Negative electronic compressibility and tunable spin splitting in WSe<sub>2</sub>.

- Nature Nanotechnology*, 10(12):1043–1047, 2015. URL <http://www.nature.com/doifinder/10.1038/nano.2015.217>.
- [266] Hermann Weyl. Elektron und Gravitation. I. *Zeitschrift für Physik*, 56(5-6):330–352, may 1929. ISSN 1434-6001. doi: 10.1007/BF01339504. URL <http://link.springer.com/10.1007/BF01339504>.
- [267] Bohm-jung Yang and Naoto Nagaosa. Classification of stable three-dimensional Dirac semimetals with nontrivial topology. *Nature Communications*, 5:4898, 2014. URL <http://dx.doi.org/10.1038/ncomms5898><http://www.nature.com/doifinder/10.1038/ncomms5898>.
- [268] B. Q. Lv, H. M. Weng, B. B. Fu, X. P. Wang, H. Miao, J. Ma, P. Richard, X. C. Huang, L. X. Zhao, G. F. Chen, Z. Fang, X. Dai, T. Qian, and H. Ding. Experimental Discovery of Weyl Semimetal TaAs. *Physical Review X*, 5(3):031013, jul 2015. URL <http://link.aps.org/doi/10.1103/PhysRevX.5.031013>.
- [269] Su-Yang Xu, Nasser Alidoust, Ilya Belopolski, Zhujun Yuan, Guang Bian, Tay-Rong Chang, Hao Zheng, Vladimir N. Strocov, Daniel S. Sanchez, Guoqing Chang, Chenglong Zhang, Daixiang Mou, Yun Wu, Lunan Huang, Chi-Cheng Lee, Shin-Ming Huang, BaoKai Wang, Arun Bansil, Horng-Tay Jeng, Titus Neupert, Adam Kaminski, Hsin Lin, Shuang Jia, and M. Zahid Hasan. Discovery of a Weyl fermion state with Fermi arcs in niobium arsenide. *Nature Physics*, 11(9):748–754, aug 2015. URL <http://arxiv.org/abs/1504.01350><http://www.nature.com/doifinder/10.1038/nphys3437><http://www.nature.com/doifinder/10.1038/nphys3437>.
- [270] Philip J. W. Moll, Nityan L. Nair, Toni Helm, Andrew C. Potter, Itamar Kimchi, Ashvin Vishwanath, and James G. Analytis. Transport evidence for Fermi-arc-mediated chirality transfer in the Dirac semimetal Cd<sub>3</sub>As<sub>2</sub>. *Nature*, 535(7611):266–270, jul 2016. URL <http://arxiv.org/abs/1505.02817><http://www.nature.com/doifinder/10.1038/nature18276><http://www.nature.com/doifinder/10.1038/nature18276>.
- [271] Zhijun Wang, A. Alexandradinata, R. J. Cava, and B. Andrei Bernevig. Hourglass Fermions. *Nature*, 532(7598):189, 2016. ISSN 0028-0836. doi: 10.1038/nature17410. URL <http://arxiv.org/abs/1602.05585>.
- [272] Hongming Weng, Chen Fang, Zhong Fang, B. Andrei Bernevig, and Xi Dai. Weyl Semimetal Phase in Noncentrosymmetric Transition-Metal Monophosphides. *Physical Review X*, 5(1):011029, mar 2015. ISSN 2160-3308. doi: 10.1103/PhysRevX.5.011029. URL <http://link.aps.org/doi/10.1103/PhysRevX.5.011029>.

- [273] Stefanos Kourtis, Jian Li, Zhijun Wang, Ali Yazdani, and B. Andrei Bernevig. Universal signatures of Fermi arcs in quasiparticle interference on the surface of Weyl semimetals. *Physical Review B - Condensed Matter and Materials Physics*, 93(4):1–5, 2016. ISSN 1550235X. doi: 10.1103/PhysRevB.93.041109.
- [274] Chenlu Wang, Yan Zhang, Jianwei Huang, Simin Nie, Guodong Liu, Aiji Liang, Yuxiao Zhang, Bing Shen, Jing Liu, Cheng Hu, Ying Ding, Defa Liu, Yong Hu, Shaolong He, Lin Zhao, Li Yu, Jin Hu, Jiang Wei, Zhiqiang Mao, Youguo Shi, Xiaowen Jia, Fengfeng Zhang, Shenjin Zhang, Feng Yang, Zhimin Wang, Qinjun Peng, Hongming Weng, Xi Dai, Zhong Fang, Zuyan Xu, Chuangtian Chen, and X J Zhou. Observation of Fermi arc and its connection with bulk states in the candidate type-II Weyl semimetal WTe<sub>2</sub>. *Physical Review B*, 241119:1–8, 2016. doi: 10.1103/PhysRevB.94.241119.
- [275] Pavan Hosur and Xiaoliang Qi. Recent developments in transport phenomena in Weyl semimetals. *Comptes Rendus Physique*, 14(9-10):857–870, 2013.
- [276] Ashvin Vishwanath. Where the Weyl Things Are. *Physics*, 8:84, sep 2015. ISSN 1943-2879. doi: 10.1103/Physics.8.84. URL <http://link.aps.org/doi/10.1103/Physics.8.84>.
- [277] S. Rao. Weyl semi-metals : a short review. *ArXiv e-prints*, March 2016. URL <https://arxiv.org/abs/1603.02821>.
- [278] H.B. Nielsen and M. Ninomiya. Absence of neutrinos on a lattice I. *Nuclear Physics B*, 185(1):20–40, jul 1981.
- [279] H.B. Nielsen and M. Ninomiya. Absence of neutrinos on a lattice II. *Nuclear Physics B*, 193(1):173–194, dec 1981.
- [280] Su-Yang Xu, Ilya Belopolski, Nasser Alidoust, Madhab Neupane, Guang Bian, Chenglong Zhang, Raman Sankar, Guoqing Chang, Zhujun Yuan, Chi-Cheng Lee, Shin-Ming Huang, Hao Zheng, Jie Ma, Daniel S. Sanchez, BaoKai Wang, Arun Bansil, Fangcheng Chou, Pavel P. Shibayev, Hsin Lin, Shuang Jia, and M. Zahid Hasan. Discovery of a weyl fermion semimetal and topological fermi arcs. *Science*, 349(6248):613–617, 2015. ISSN 0036-8075. doi: 10.1126/science.aaa9297. URL <http://science.sciencemag.org/content/349/6248/613>.
- [281] Hiroyuki Inoue, András Gyenis, Zhijun Wang, Jian Li, Seong Woo Oh, Shan Jiang, Ni Ni, B. Andrei Bernevig, and Ali Yazdani. Quasiparticle interference of the fermi arcs and surface-bulk connectivity of a weyl semimetal. *Science*, 351(6278):1184–1187, 2016. ISSN 0036-8075. doi: 10.1126/science.aad8766. URL <http://science.sciencemag.org/content/351/6278/1184>.

- [282] Alexander P Protogenov, Valery A Verbus, and Evgueni V Chulkov. The Density of Surface States in Weyl Semimetals. *arXiv*, pages 4–6, jun 2014. URL <http://arxiv.org/abs/1406.1507>.
- [283] Jiawei Ruan, Shao-Kai Jian, Hong Yao, Haijun Zhang, Shou-Cheng Zhang, and Dingyu Xing. Symmetry-protected ideal Weyl semimetal in HgTe-class materials. *Nature Communications*, 7:11136, apr 2016. URL <http://arxiv.org/abs/1511.08284><http://www.nature.com/doi/10.1038/ncomms11136>.
- [284] Philipp Leubner, Lukas Lunczer, Christoph Brüne, Hartmut Buhmann, and Laurens W. Molenkamp. Strain Engineering of the Band Gap of HgTe Quantum Wells Using Superlattice Virtual Substrates. *Physical Review Letters*, 117(8):1–5, 2016. ISSN 10797114. doi: 10.1103/PhysRevLett.117.086403.
- [285] Binghai Yan and Claudia Felser. Topological Materials: Weyl Semimetals. *arXiv e-Preprints*, pages 1–19, nov 2016. URL <http://arxiv.org/abs/1611.04182>.
- [286] Chandra Shekhar, Ajaya K. Nayak, Sanjay Singh, Nitesh Kumar, Shu-Chun Wu, Yang Zhang, Alexander C. Komarek, Erik Kampert, Yurii Skourski, Jochen Wosnitza, Walter Schnelle, Alix McCollam, Uli Zeitler, Jurgen Kubler, S. S. P. Parkin, Binghai Yan, and C. Felser. Observation of chiral magneto-transport in RPtBi topological Heusler compounds. *arXiv*, page 1604.01641, apr 2016. URL <http://arxiv.org/abs/1604.01641>.
- [287] A. A. Zyuzin and A. A. Burkov. Topological response in Weyl semimetals and the chiral anomaly. *Physical Review B - Condensed Matter and Materials Physics*, 86(11):1–8, 2012.
- [288] Wang Kong Tse and A. H. MacDonald. Giant magneto-optical kerr effect and universal faraday effect in thin-film topological insulators. *Physical Review Letters*, 105(5):1–4, 2010. ISSN 00319007. doi: 10.1103/PhysRevLett.105.057401.
- [289] Wang Kong Tse and A. H. MacDonald. Magneto-optical and magnetoelectric effects of topological insulators in quantizing magnetic fields. *Physical Review B - Condensed Matter and Materials Physics*, 82(16):1–4, 2010. ISSN 10980121. doi: 10.1103/PhysRevB.82.161104.
- [290] R. Valdés Aguilar, A V Stier, W Liu, L S Bilbro, D K George, N Bansal, L Wu, J. Cerne, A. G. Markelz, S. Oh, and N. P. Armitage. Terahertz Response and Colossal Kerr Rotation from the Surface States of the Topological Insulator Bi<sub>2</sub>Se<sub>3</sub>. *Physical Review Letters*, 108(8):087403, feb 2012. ISSN 0031-9007. doi: 10.1103/PhysRevLett.108.087403. URL <http://link.aps.org/doi/10.1103/PhysRevLett.108.087403>.

- [291] Hai-Zhou Lu, Wen-Yu Shan, Wang Yao, Qian Niu, and Shun-Qing Shen. Massive Dirac fermions and spin physics in an ultrathin film of topological insulator. *Physical Review B*, 81(11):115407, mar 2010. ISSN 1098-0121. doi: 10.1103/PhysRevB.81.115407. URL <http://link.aps.org/doi/10.1103/PhysRevB.81.115407>.

## Résumé

Dans cette thèse, j'étudie la compressibilité électronique de deux isolants topologiques tridimensionnels : Le tellure de mercure (HgTe) sous contrainte et le sélénure de bismuth ( $\text{Bi}_2\text{Se}_3$ ).

Je présente des mesures d'admittance électronique à basse température résolues en phase sur une large gamme de fréquence. Cela permet d'extraire la capacité quantique associée à la densité d'états et la résistivité des matériaux étudiés.

Nous montrons qu'un isolant topologique intrinsèque présente une réponse dominée par les états de surface topologiques sur une large gamme d'énergie qui s'étend au-delà du gap de transport du matériau massif. Ce régime, appelé « écrantage de Dirac », est caractérisé par une compressibilité électronique proportionnelle à l'énergie de surface et une haute mobilité.

Dans la suite, nous nous intéressons à la limite de ce régime. Nous observons qu'à haute énergie et sous l'influence de forts champs électriques perpendiculaires, des états excités massifs de surface sont peuplés ce qui se manifeste expérimentalement de différentes façons : Une chute dans la constante de diffusion électronique, un pic de conductivité ainsi que l'apparition d'un deuxième type de porteurs en magnéto-transport et de métastabilité dans la relation charge-tension. Un modèle théorique basé sur un traitement quasi-relativiste du Hamiltonien de surface est présenté. Il permet d'identifier la dépendance en énergie et champ électrique des états massifs de surface.

Cette thèse est complétée par des résultats expérimentaux sur  $\text{Bi}_2\text{Se}_3$  obtenu par croissance sur nitrure de bore mettent en évidence l'importance de la pureté des interfaces d'isolants topologiques.

## Mots Clés

Isolants topologiques, Compressibilité électronique, radiofréquence, tellure de mercure, sélénure de bismuth, Fermions de Dirac

## Abstract

This thesis discusses the electronic compressibility of two representative three dimensional topological insulators: Strained mercury telluride (HgTe) and bismuth selenide ( $\text{Bi}_2\text{Se}_3$ ).

I present low temperature phase-sensitive electron admittance data over a broad frequency range. This allows to extract the quantum capacitance related to the density of states and the resistivity of the investigated materials.

We show that the response of an intrinsic topological insulator is dominated by topological surface states over a large energy range exceeding the bulk material's transport gap. This regime, named "Dirac screening" is characterized by an electron compressibility proportional to the surface Fermi level and a high mobility.

Subsequently, we investigate the limits of this regime. At high energy and large perpendicular electric fields we observe the population of excited massive surface states. Experimentally, these manifest themselves in multiple signatures: A drop in the electronic diffusion constant, a peak in the conductivity, appearance of a second carrier type in magneto-transport and meta-stability in the charge-voltage relation.

A theoretical model based on a quasi-relativistic treatment of the surface Hamiltonian is presented. It allows to identify the electric field and energy dependence of the massive surface states.

This thesis is complemented by experimental results on  $\text{Bi}_2\text{Se}_3$  grown on boron nitride, where we demonstrate the importance of clean surfaces for the study of electronic properties in topological insulators.

## Keywords

Topological insulators, Electron compressibility, Radio-frequency, Mercury telluride, Bismuth selenide, Dirac Fermions